High resolution electron microscopy of biological molecules

Berriman, John A.

Award date:
1988

Awarding institution:
University of Bath

HIGH RESOLUTION ELECTRON MICROSCOPY OF BIOLOGICAL MOLECULES.

submitted by John A. Berriman

for the degree of Ph.D.

of the University of Bath

1988

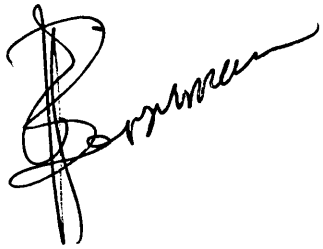

ProQuest LLC
789 East Eisenhower Parkway
P.O. Box 1346
Ann Arbor, MI 48106-1346

This thesis is submitted under the terms of the regulation: Staff Candidature - Method A, for the Degree of Doctor of Philosophy. The research work which forms the basis for this submission is the result of collaboration with different research groups. The majority of presented material is the author's own original work. Publications that have been obtained during the period of registration and which are based on the material in the thesis are included as an appendix.

ACKNOWLEDGEMENTS

I am very grateful for the help and guidance I have received from my supervisor Dr.W. Whish. I am also indebted to the Schools of Biological Science and Materials Science at the University of Bath for the various facilities made available to me during this work.

I wish to acknowledge Dr. Kevin Leonard at the European Molecular Biology Laboratory, Heidelberg, West Germany, for his continued assistance in the development of my research.

My thanks also go to Dr. John Trinick at the Agriculture and Food Research Council Institute, (Langford, Bristol), Dr. Roger Vincent (Department of Physics, University of Bristol) and Dr. Richard Henderson (Medical Research Council Laboratory of Molecular Biology, Cambridge) for many helpful discussions and suggestions, and the use of electron microscope and computer facilities.

Lastly, I am truly grateful to my wife and children for their patience, help and understanding through the course of this work.

SUMMARY

The methods of low dose electron microscopy are shown to provide high resolution detail in the specimens investigated in this study. The results reveal detail of protein molecular structure which would not be obtainable by conventional microscopy.

The construction of an optical diffractometer is described with details of alignment. The use of this apparatus for practical analysis of electron micrographs is outlined with examples.

A specimen of the lipoprotein from Escherichia coli cell envelopes gave electron diffraction patterns that revealed a coiled-coil alpha-helix structure for the protein part of the molecule. Low dose images showed a side-by-side packing which supported a trimer arrangement of molecules.

The restriction enzyme Eco RV ,complexed with short DNA fragments, gave crystals which produced electron diffraction patterns of potentially atomic resolution. A 3-dimensional model of the enzyme is reconstructed from electron microscope images and electron diffraction indicates the orientation of bound DNA.

A derivatised form of the high resolution crystal is analysed which gives important clues of the packing of the molecules within the crystal.

The investigation of protein crystals by electron diffraction revealed a reduction in thickness which was induced by electron irradiation. This is shown to be a general phenomenon of negatively stained specimens producing a reduction in thickness of 50%.

In the light of these findings the advantages of frozen specimen preparation is described within the context of perfect specimen preparation.

CONTENTS

1. Introduction.....1

2. Structural Studies by Electron Microscopy.....4

2.1 General aspects.....4

2.2 Radiation damage.....8

2.3 Preparative methods.....19

2.4 Image analysis.....30

2.4.1 Contrast in bright field images.....30

2.4.2 Two-dimensional analysis.....34

2.4.3 Three-dimensional analysis.....37

3. Experimental Procedures.....39

3.1 Specimen preparation.....39

3.2 Electron microscopy.....40

3.2.1 Low dose imaging.....41

3.2.2 Dosimetry.....45

3.2.3 Electron diffraction.....46

3.3 Optical diffraction.....48

3.3.1 The optical bench.....48

(a) Construction.....50

(b) Alignment.....53

(c) Recording.....54

3.3.2 Image assessment.....55

(a) Calibration of magnification.....55

(b) Effect of focus.....57
(c) Effect of drift.....58
(d) Effect of resolution.....59
(e) Effect of coherence.....61

4. The Ultrastructure of the Lipoprotein from Escherichia coli Envelopes.....62
4.1 Introduction.....63
4.2 Materials and methods.....66
4.3 Results.....68
4.4 Discussion.....74

5. Structural study of Restriction Enzyme-DNA complexes
5.1 Introduction.....84
5.2 Materials and methods.....87
5.2.1 Specimen preparation.....87
(a) Growth of culture.....87
(b) Purification of enzyme.....90
(c) Crystallisation with Oligonucleotides.....93
5.2.2 Electrophoresis.....95
5.2.3 Electron microscopy.....97
5.2.4 Computing.....97
5.3 Results.....98
5.3.1 Enzyme purification.....98

5.3.2 Electron microscopy.....101
(a) Non-specific binding.....101
(b) Crystals with a specific decanucleotide.....102
(c) Crystals with a non-specific octanucleotide.....106
(d) Crystallisation with the specific decanucleotide containing a tri-osmium cluster.....112
5.4 Discussion.....116

6. A Determination of Specimen Collapse.....122
6.1 Introduction.....123
6.2 Materials and methods.....124
6.2.1 Determination of 'c'
(a) Goniometric measurements.....125
(b) Laue zone measurements.....127
6.2.2 The accuracy of the goniometer.....129
6.2.3 Preparation of low temperature specimens.....131
6.2.4 Determination of the thickness of single particles.....132
6.2.5 Partly supported crystals.....134
6.3 Results.....134

6.3.1 Thickness change in negatively stained specimens

(a) For thin crystals.....134

(b) For single particles.....139

(c) For unsupported crystals.....142

6.3.2 Absolute thickness determination.....145

6.3.3 Accuracy of the goniometer.....151

6.4 Discussion.....152

7. General Discussion and Conclusions.....157

8. References.....165

9. Publications.....171

1. Ultrastructure of Native Lipoprotein from Escherichia coli Envelopes. D.J.Manstein, J.Berriman K.Leonard and J.P.Rosenbusch.

J. Mol. Biol. 189 701-707 (1986).....172

2. Structural studies of Eco RV endonuclease and of it's complexes with short DNA fragments.

F.K.Winkler. R.S.Brown, K.Leonard and J.Berriman.

In: Crystallography in Molecular Biology. Ed. D.Moras, Plenum Press, New York.....179

3. Methods for Specimen Thickness Determination in Electron Microscopy. J.Berriman, R.K.Bryan, R.Freeman and K.R.Leonard, Ultramicroscopy 13 351-364 (1984)....187

4. Methods for Specimen Thickness Determination in Electron Microscopy, Part II, Changes in thickness with dose. J.Berriman and K.R.Leonard, Ultramicroscopy 19 349-366 (1986)...201

ABBREVIATIONS

Å	Ångstrom unit = 0.1 nm = 10^{-10} metres
DTT	DL-Dithiothreitol
EDTA	Ethylenediamine-tetra-acetic acid
HEPES	N-2-Hydroxyethylpiperazine-N'-2-etanesulphonic acid
IPTG	Isopropyl -D-thiogalactopyranoside
kev	kilo electron volts
Octyl-POE	Octyl-oligo$_{(3 \text{ to } 12)}$-oxyethylene
PAGE	Polyacrylamide gel electrophoresis
PMSF	Phenyl methyl sulfonyl fluoride
PTA	Phosphotungstic acid
SDS	Sodium dodecyl sulphate
STEM	Scanning transmission electron microscope
TMV	Tobacco Mosaic Virus
Tris	Tris(hydroxymethyl)aminomethane

1. INTRODUCTION

Structure determination is at the heart of biological research. How an organism is organised is the key to understanding the processes of life. This investigation is constantly demanding finer detail and the techniques of microscopy have developed correspondingly.

Molecular Biology requires structural analysis at the atomic level and electron microscopy has a unique place among the physical methods available. The instrument can produce a direct image of the specimen with, potentially, atomic resolution. Frequently, suitable samples can not be prepared for X-ray and neutron diffraction. These methods also require large quantities of material and the results are obtained only after lengthy data collection and processing.

The deleterious effects of the vacuum and radiation levels to biological specimens were, until recently, serious obstacles to high resolution electron microscopy. This thesis deals with the application of methods to sustain the specimen against dehydration and minimize the contribution of radiation damage to the image.

In Chapter 2 a literature survey is presented of a number of theoretical and practical developments in the electron microscopy of biological molecules. The

techniques of image analysis such as optical diffraction, 3-dimensional reconstruction and a description of image processing computer programs are described in Chapter 3.

Chapter 4 is a study of the structure of the lipoprotein purified from the envelope of the Gram-negative bacterium Escherichia coli. The sample gives diffraction data which support the idea that the molecule forms coiled-coil alpha-helices. A model is constructed of its organisation and aspects of the relation to function considered. The crystalline order of this specimen was however, not good enough to allow investigation at higher resolution. In Chapter 5 a specimen is investigated with very high order and the possibility of atomic resolution. The restriction enzyme Eco RV, complexed with small DNA fragments, forms thin crystals showing electron diffraction to better than 0.3 nm. The morphology of the dimeric enzyme and the orientation of the DNA bound to it is determined.

The development of electron crystallographic methods, necessary to acquiring the high resolution information, leads to the discovery of a significant reduction in thickness of the specimen caused by radiation damage. This finding is extensively investigated in Chapter 6 and is shown to be a general phenomenon raising serious implications to the interpretation of 3-dimensional reconstructions from negatively-stained specimens.

Finally, Chapter 7 is a discussion of the results and their place among those of other researchers in this field. An overview is given of current trends and an outlook made of immediate challenges and possible future developments.

2. STRUCTURAL STUDIES BY ELECTRON MICROSCOPY

2.1 General Aspects

The drawings made by the early microscopist Leeuwenhoek (1632-1723) show that with his single lens microscope he was able to discern detail down to 1.5 μm [1]. The resolution of the subsequent designs of instrument improved over the next two centuries. However, by 1870 it became apparent that a limit existed to this progress, at a resolution of about 0.2 μm. This was determined by using, as a test object, a glass microscope slide with bands of finely scribed lines [2]. In 1873 Abbe, the scientific manager of the Carl Zeiss microscope firm, showed that, because of diffraction effects, a barrier to resolution was set by the wavelenght of the illumination and the collecting angle of the objective lens [3]. (It should be noted that, although Abbe is credited with establishing this relationship, Helmholtz concurrently published a theory of image formation in the microscope containing the same conclusion [4]). The microscopes of the time had already reached the predicted limit and the only advance that could be made was to go down in wavelength and construct, with quartz lenses and fluorescent screen, an ultra-violet microscope [5].

In 1912 Friedrich, Knipping and Laue showed by diffraction that X-rays (discovered in 1895 by Roentgen) were a radiant energy of wavelength comparable to the separation of atoms in solids [6]. This discovery had far-reaching implications for structure research. The development of X-ray crystallography by W.H.Bragg and his son W.L.Bragg led to, as they put it, " Microscopy on an atomic scale " [7]. This was unlike optical microscopy in that X-rays could not be focussed with a lens. The method relied on irradiating crystals with a narrow collimated beam. The diffraction pattern produced, was measured in terms of the spatial coordinates of the maxima and their relative intensities. This 'reciprocal lattice' was then used to determine the real lattice of the crystal. The function of a lens to form an image from the diffracted intensities (deconvolute) was performed mathematically. The development of computers and the application of Fourier analysis caused rapid progress and increasingly complex structures were solved [8].

Louis de Broglie, in 1924, suggested that, just as there is a duality in the nature of light (wave /corpuscle), there is wave-like quality to the propagation of atomic particles [9].

Electron wavelength = Planck's constant / Electron Momentum

$$= 1.226 / [V(1+0.9788\times10^{-6}V)]^{\frac{1}{2}} \text{ nm.}$$

with V =Electron voltage

For a 100 kev electron beam the wavelength is 0.0037 nm.

This calculation was soon experimentally verified by crystal diffraction [10].

As electrons are of very low mass and carry an electrostatic charge their trajectories are strongly affected by magnetic or electrostatic fields. When it was shown that a cylindrical electromagnet would act as a focussing lens to electrons moving along its axis [11], the design of an electron microscope was begun.

Ruska and Knoll, in 1931, produced the first electron microscope [12]. This was the prototype of all transmission instruments to follow, including the present day. As the subject of his Ph.D. research work at The Technological University of Berlin, Ruska developed the microscope and, by 1933, demonstrated a resolution of 50 nm [13]. This was four times better than possible with an optical microscope and, unlike X-ray diffraction, the image required no calculation, it was displayed on a fluorescent screen.

To many physicists at the time this invention was considered to be of little practical use because of the very strong interaction of electrons with matter. The extremely high energy densities deposited within the specimen would, it was thought, either melt or drastically alter it. This, after all ,is the principle of electron beam welding. To the biologist such objections were secondary, the barrier to increased magnification had been removed and there were so many questions to be answered.

In gaining support for further research and development, not least financial backing, it was a significant advantage to Ruska that his brother Helmut was a medical student with an appreciation for the potential of electron microscopy to biological science. He enlisted the support of Siebeck, the head of the Berlin Medical University Clinic at which he studied. Siebeck believed that methods of specimen preparation could be developed and that considerable gains could be made with a microscope that exceeded the resolution of optical microscopes by a factor of ten. In a letter to the Siemens and Zeiss manufacturers in 1936 [14], urging sponsorship, he outlined particular needs in normal and pathological microscopical anatomy. 'The structure of cell walls, membranes and nerve fibrils; the nature of protoplasm, centrosomes and colloids; the chromosome; the filtratable virus; these would be investigations of not just theoretical importance in aetiology, but to provide a new practical method for clinical diagnosis'.

After 50 years of development the resolution of the electron microscope, at 0.2 nm, now exceeds that of an optical microscope by three orders of magnitude. Many of Siebeck's predictions have been realised and electron microscopy is an important tool in medical research. The goal of atomic resolution of a biological specimen has only recently been achieved [15]. This was through the application of methods to reduce radiation damage, techniques to protect hydrated molecules against the

microscope's vacuum and computer methods to correct distortions in the image.

2.2 Radiation Damage

The first biological specimen examined in an electron microscope was most probably cotton thread. This Ruska used because he found that, after an initial disruption into fine fibres, once stable they were a useful test object [13]. The effect of radiation was of great interest to the early researchers investigating methods of preparation. The transition from light to electron microscopy gave initially very disappointing results. The standard techniques produced sections that were much too thick. The paraffin wax in which the samples were embedded bubbled on exposure to the beam and caused distortion [16]. In a study of the effects of electron irradiation Hillier determined the dose to which the specimen was exposed from the intensity on the viewing screen and the operating magnification [17]. Bacteria were stained and fixed for electron microscopy by exposure to osmium tetroxide vapour. Irradiation at low levels completely stopped this effect. The nitrocellulose supporting film of the grid became insoluble in amyl acetate and stable to heat treatment above 600 ^{o}C. Electron irradiation produced an increase

in melting point and reductions in solubility and chemical reactivity. In the image below the effect is shown of electron irradiation to a section of an ion-exchange resin membrane embedded in Araldite. The section was examined, a small area at a time, in short 'hops'. The micrograph was taken just after moving and shows (to the left) an area previously irradiated and (to the right) an area exposed for the first time. Since the section was of even thickness the change in grey levels relative to the Araldite show that the specimen has lost mass on irradiation.

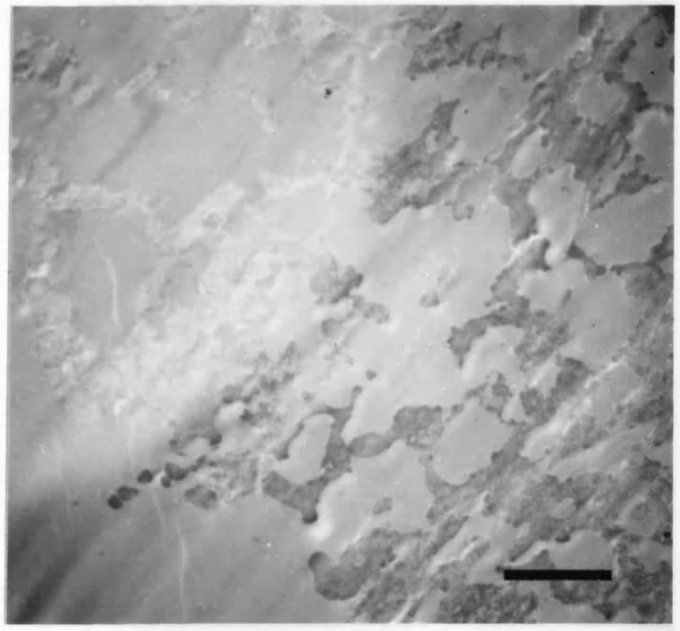

Scale bar represents 100 nm.

The section was then stained and re-examined. The areas pre-exposed showed no chemical reactivity to the stain. In the image on this page, the area of irradiation came from the top left in one 'hop'. The amino groups of the ion-exchange resin have evidently been strongly stained by the lead stain but the irradiated zone remains light in contrast to the Araldite.

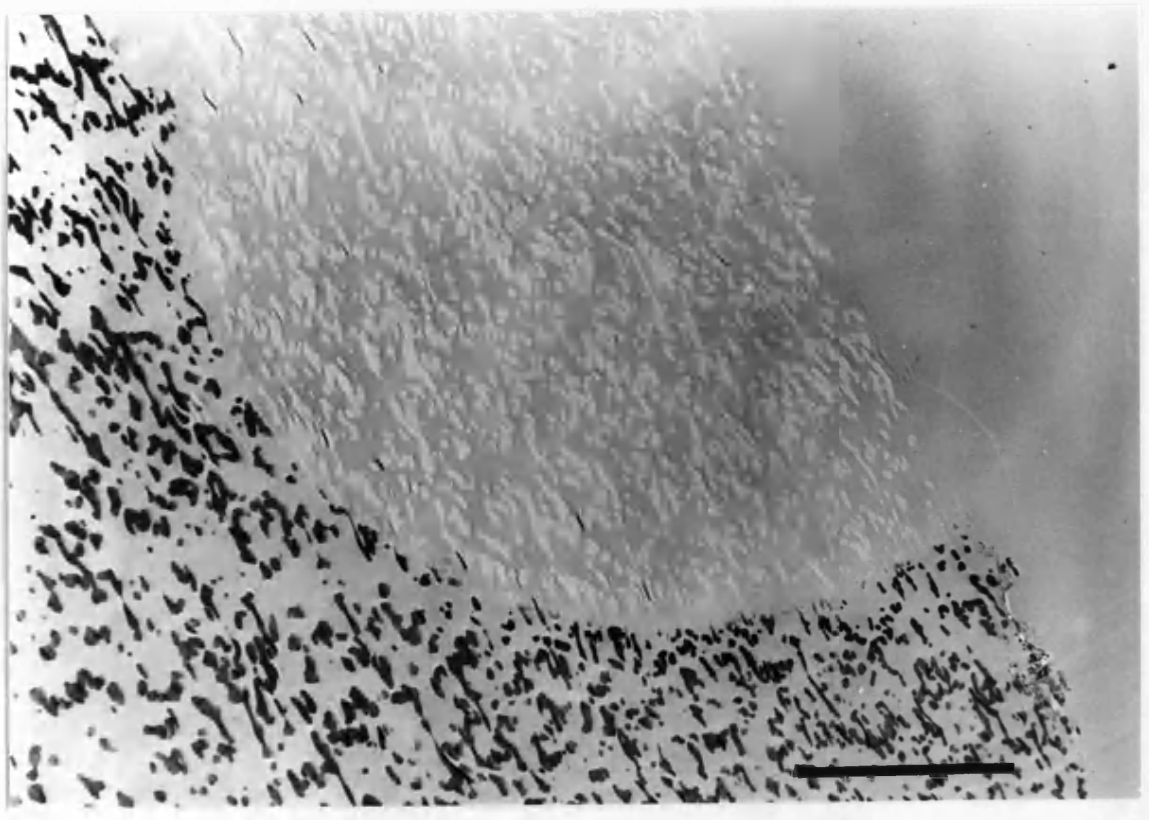

Scale bar represents 1 μm.

This change in the physico-chemical properties was consistent with the crosslinking and polymerisation of organic material found when it was exposed to other sources of radiation, such as after months within a nuclear pile [18].

Viruses, Siebeck wrote, would, because they were just below the resolution of the light microscope, provide new important discoveries very quickly. With the invention of a heavy metal shadowing technique by Williams and Wyckoff in 1945 [19], images of viruses were obtained with 10 nm resolution. This was at the limit of the instruments available then. Over the next few years improvements in the microscopes failed to evince new detail in the images. In an examination of the effects of radiation damage to Tobacco Mosaic Virus (TMV) particles by Williams , they were found to become flattened [20]. Parts of a specimen grid of viruses, were pre-irradiated in the microscope. The grid was then shadowed and examined. Non-irradiated areas showed particles whose shadow length indicated a thickness, confirming the cylindrical construction of the virus. Those regions pre-irradiated had no clear shadow. This suggested that the virus was drastically altered by irradiation and this would be bound to lower the observed resolution.

Introduced in 1954, the Siemens Elmiskop-1 microscope was to dominate research work over the next twenty years. It gave investigators 1.0 nm resolution and had an improved vacuum at the sample. Poor vacuum

caused carbon contamination to build up at alarming rates on the specimens in the early microscopes. In fact this problem was suggested as the reason for the lack of shadow in Williams' TMV work. The pre-irradiated particles being embedded in contamination of cracked vacuum pump oil. As well as a biased electron gun the microscope had two condenser lenses. This allowed great control of brightness, or dose rate. At the same time the preparation of thin carbon films was demonstrated by Bradbury [22]. Hitherto, the plastic films formvar and collodion, were used as a support for specimens. These tended to be relatively thick and to distort and cause specimen drift when irradiated. Carbon films were very thin, strong, drift-free and able to conduct away electrostatic charge.

The first lattice image was obtained with an Elmiskop in 1955 by Menter [23]. The phthalocyanine crystals he examined were able to withstand very high doses. A polymer sample with bond energies similar to biological molecules was shown to be destroyed by exposure to very low intensities of electrons by Agar et al. [24]. Small crystals of polyethylene had been grown which gave electron diffraction patterns. The intensity of the patterns faded however, and quickly disappeared. This indicated damage to the covalently bonded molecule at radiation levels markedly below that normally used in electron microscopy. The method used was to first focus on the sample at a low magnification (5000x) and the

beam was focussed to a small 3 μm spot (at this magnification 1.5 cms). Then, expanding the illumination to fill the grid square (100 μ m across), the outline of a crystal was just visible on the screen. This alteration of the second condenser lens reduced the dose rate by 1000x. By diffraction it was known that at this level of radiation the pattern from a crystal would last 20 seconds. Moving the grid across two squares a new crystal was found and an image was immediately recorded for 15 seconds. These images showed high resolution diffraction contrast effects (dark bands or bend contours running across the crystal) as found in images of metals, but only in the first recorded image. Subsequent images only showed the shape of the crystal upon which were variations of brightness corresponding to different mass-thicknesses. This effect is demonstrated below with low (left) and high dose images of KH_2PO_4 crystals.

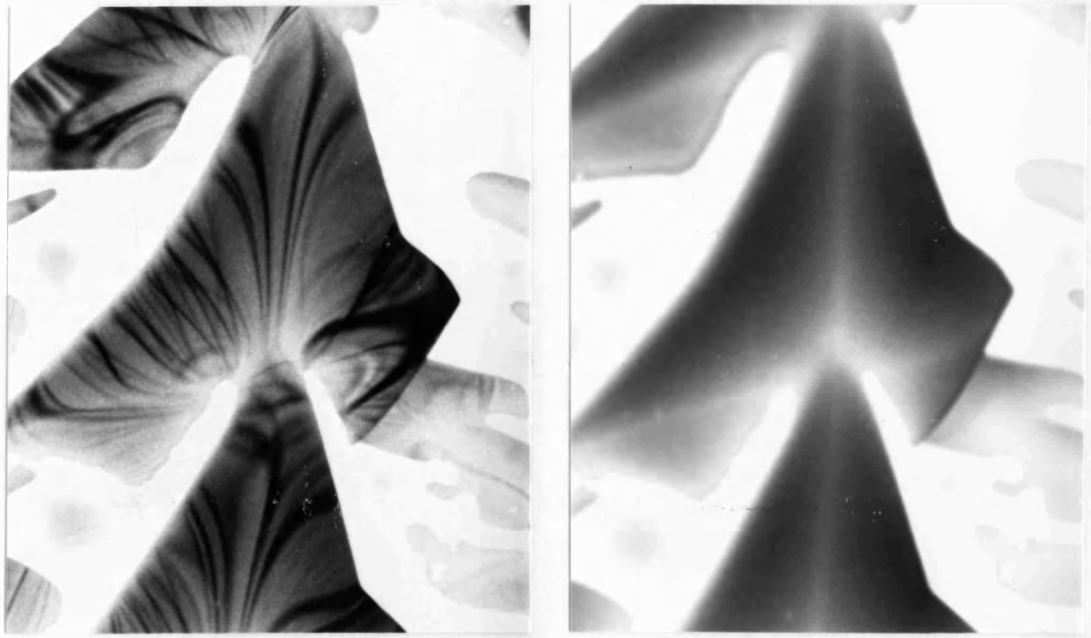

There was over the next decade an appraisal by many researchers of the nature of electron radiation damage [25, 26]. This encouraged the use of the more stable epoxy resin plastics for specimen embedding [25] and the investigation of methods to attenuate the damage. By 1970 electron microscopes such as the Philips EM301 had a resolution of 0.34 nm. This was readily demonstrated with the separation of layers of atoms in a graphitic carbon test object [27]. This is shown below with the scale bar representing 5 nm.

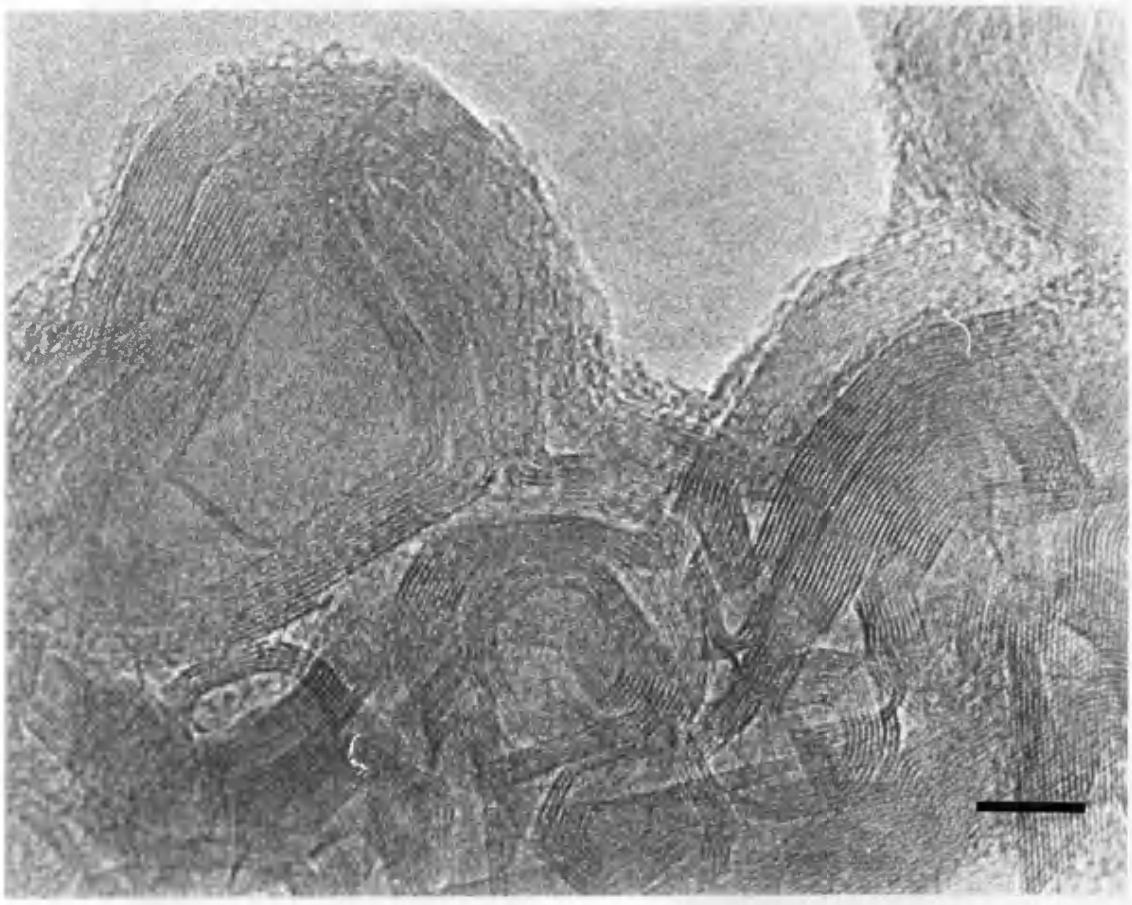

With the high resolution capability of the electron microscope the preparative technique that gave the best resolution for biological specimens, negative staining, gave detail only down to 2.5 nm. The morphology of the molecule was accessible to analysis but it was important to discover the reason for the limitation to atomic resolution.

X-ray diffraction demonstrated detail in TMV to a resolution of 0.3 nm [28]. Williams and Fisher applied low dose microscopy, as used by Agar on polyethylene crystals, to negatively stained TMV particles [29]. An example is shown below of this specimen with the low dose image to the left. The scale bar represents 50 nm.

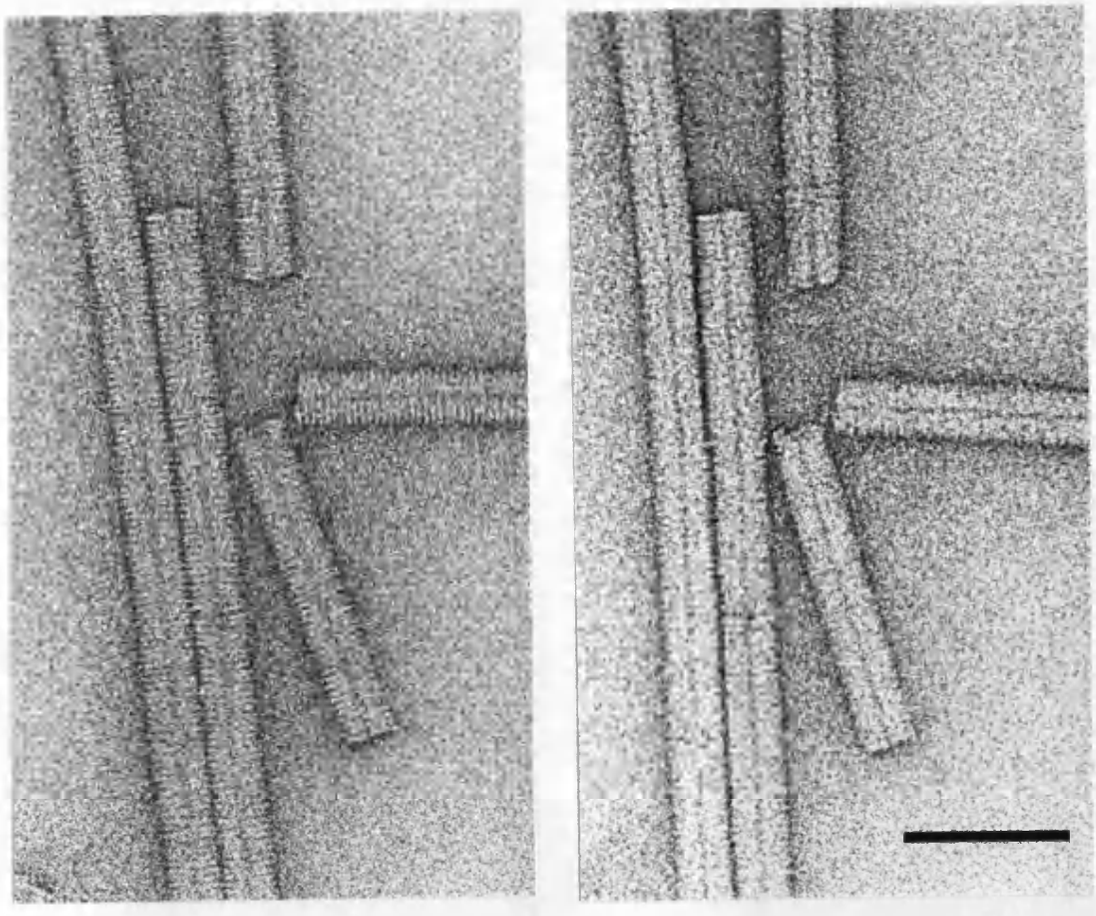

Fine detail, evidence of the helical organisation of the virus, was recorded in the initial exposure but not in subsequent images . This demonstration, of a significant improvement in image resolution through the application of a simple technique, accelerated the use of low or minimum dose methods by many research groups.

Glaeser and Thomas emphasised the use of crystals and their diffraction patterns to quantify damage [30]. Choosing crystals of the amino acid L-valine they measured the rate at which diffraction patterns faded for a given dose rate. This quantitative approach was most important in deciding the various factors which could improve the stability of the specimen. A set of diffraction patterns of an L-valine crystal is shown below. This is the hk0 projection with unit cell dimensions a= 0.97 and b= 0.53 nm. The patterns were taken after incident doses of (from left to right) 0.25, 0.5, 0.75, and 1.0 electrons per square Ångstrom unit, $e^-/Å^2$.

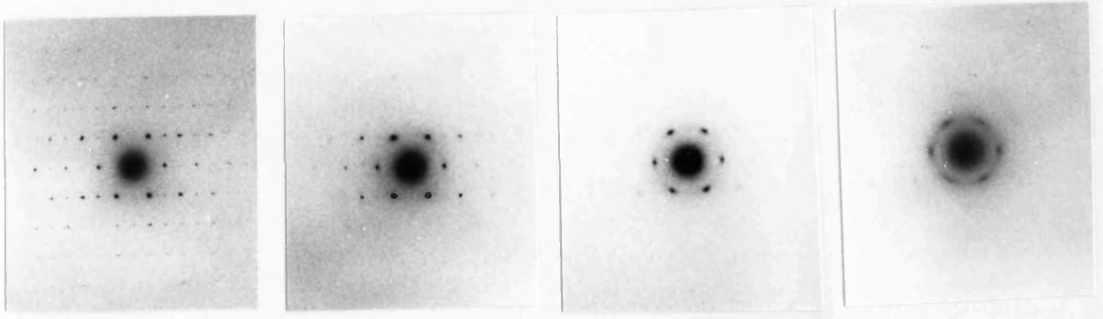

Since the effects of dose rate [31], accelerating voltage [32], metal coatings [33] and temperatures down to liquid nitrogen [34] and liquid helium [35] were examined by many research groups, this common specimen was of great integrating value.

Many biological structures are assemblies of multiple copies of identical protein subunits which are symmetrically arranged. Methods to retrieve the maximum amount of information from electron microscope images of such systems (eg. viruses and muscle proteins) were developed by Klug and collaborators in Cambridge [36]. Because of its analytical approach this had considerable consequences for both establishing better specimen preparative techniques and for reducing the effects of radiation damage.

The Rose equation [37] expresses the relationship between the number of electrons per unit object area (n) and the attainable resolution (d) for a given contrast (C) in an image:

$$Cd = 5/ [\ n\ ]^{\frac{1}{2}}$$

It can be calculated that for atomic resolution and sufficient contrast for it to be to be interpretable [38], an image would require a dose more than three orders of magnitude greater than a biological molecule could withstand. Taken with a dose low enough for

molecular integrity, an image of a single molecule would have insufficient contrast and be lost in noise. A crystal has thousands of molecules all with the same, or symmetrically related, orientation. In a low dose image of a crystal the weak contributions of the individual molecules can be added together and the limitation inposed by dose overcome [39].

2.3 PREPARATIVE METHODS

Biological research has developed three basic techniques for transmission electron microscopy. The specimen is either (a) embedded and sectioned, (b) a replica made of its surface or (c) simply applied to a thin supporting film. Additional to all these protocols is the introduction of a chemical element of high atomic weight. This 'stains' by scattering electrons and generating contrast in the image . In molecular biology the first method has failed to provide high resolution detail for two possible reasons. Firstly, the thinnest sections are necessary and these are easily distorted [40]. Secondly, to prepare a specimen it must be dehydrated and then heated to polymerize the resin, both steps which may alter the structure of a molecule. The introduction of the 'Araldite' epoxy resins [41] gave a significant increase in stability to the sections but the resolution was still limited to about 5 nm.

Surface replica methods were initially very successful. The contrasting material, normally platinum, was evaporated onto the specimen at a glancing angle to produce a shadow effect of contrast. However, the metal coating has a granular nature which limits the resolution to about 3nm. There is also the limitation that only the

surface of the specimen is observed and that has been exposed to the possibly damaging effects of drying and coating.

Absorbing the specimen onto a supporting film is a simple and easily repeated technique. There was an early interest in improving the shadowed images of viruses and the invention of negative staining must have taken place many times in different laboratories . The staining of a section can be said to be positive, where chemically reactive groups of the specimen bind the stain and unbound stain is washed away. In negative staining the stain is not washed away, the sample is dried onto the grid in it. Any attempt at preparing a positively stained sample may leave small areas inadequately washed. It was soon noticed that images from these regions gave superior resolution. The stain provided a sustaining medium, replacing the water and, having little internal structure, gave good resolution of the whole structure.

Brenner and Horne [43] used a solution of phosphotungstic acid (PTA), neutralised with potassium hydroxide, which was mixed with the bacteriophage T4 and fine droplets sprayed from a nebuliser onto a grid. Using a similar technique, Huxley and Zubay [44] negatively stained ribosomes with uranyl acetate. This was after finding that PTA disrupted the ribosomes. These have remained the most commonly used negative stains and have been found to have different advantages for different

specimens. Generally PTA has been been useful for examining lipids, membranes and vesicles and uranyl salts have given the highest resolution for protein structure. A comparison is made in the figure below of, from top to bottom, PTA, uranyl acetate and uranyl formate as negative stains for TMV. The scale bar represents 50 nm.

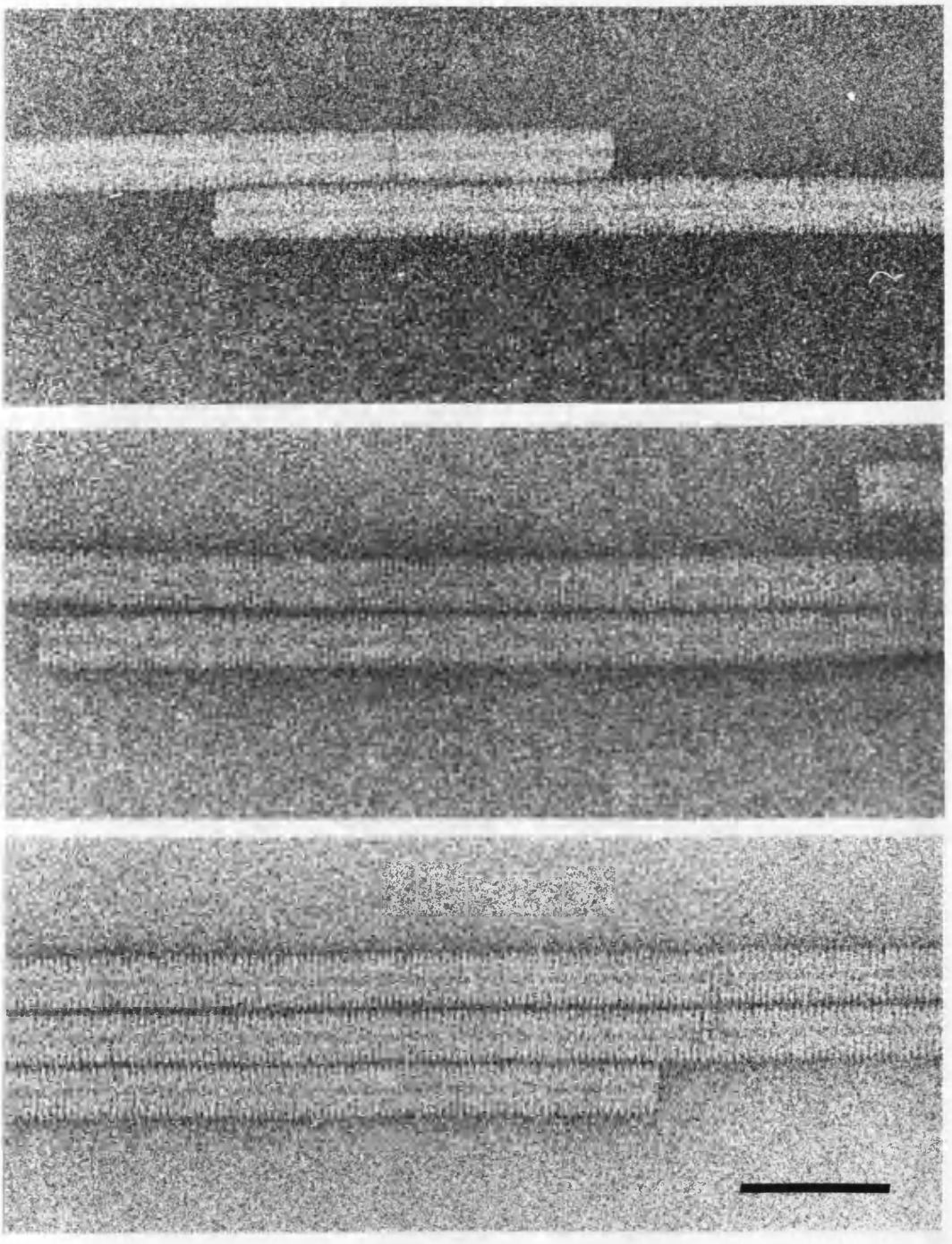

Uranyl formate, as demonstrated here, was shown to give greater contrast than the acetate [45] and hence some improvement in resolution. The figure below shows that, with the virus Semliki Forest, there may be other preparative advantages to using uranyl formate (lower image) rather than the acetate (top).

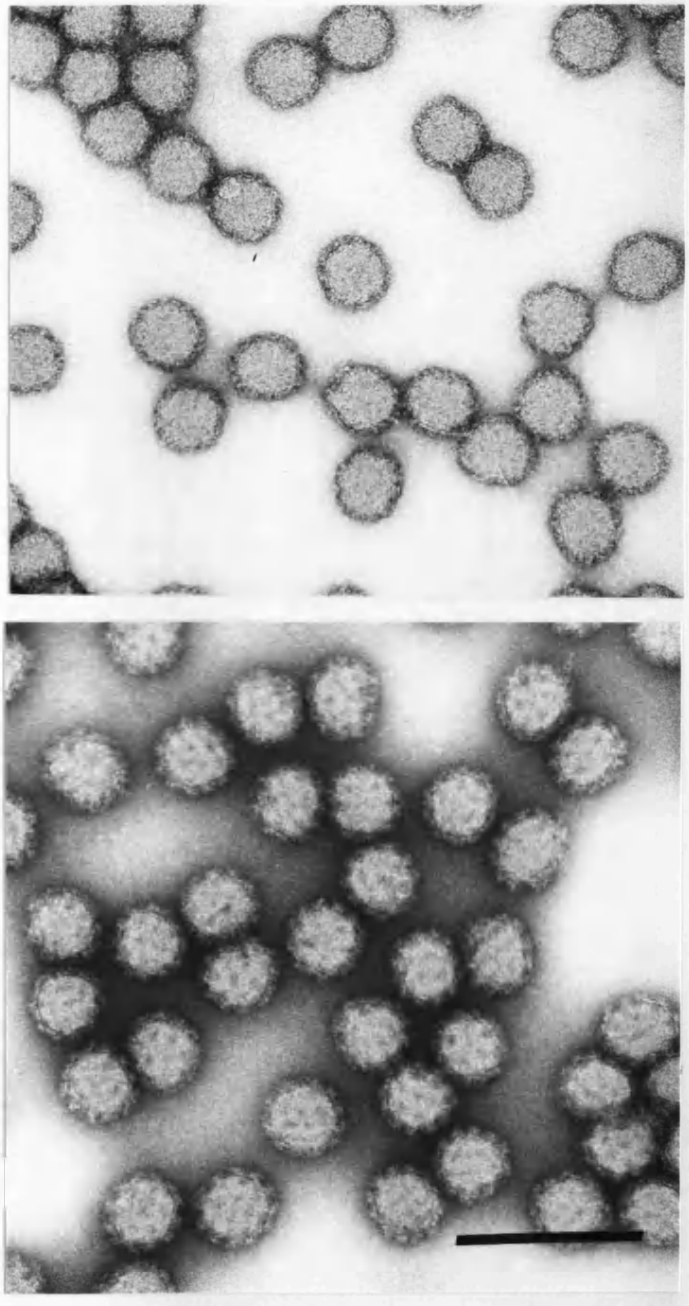

The resolution was however limited to about 2 nm. The surface of the molecule was contrasted by the stain, but for higher resolution; for information of the shape of the protein chain backbone, negative staining was not adequate.

Matricardi, Moretz and Parsons developed a wet stage for a 200 kev electron microscope. This used the high energy electron's greater penetrating ability to travel through an environmental cell in which specimens could be kept hydrated. Optimising the sensitivity of proteins and recording diffraction patterns from thin crystals of bovine catalase, they showed resolution of 0.2 nm [46]. Catalase crystals had been examined by negative staining [47] and used as a standard for magnification calibration [48]. A typical image is shown below. The scale bar represents 100 nm.

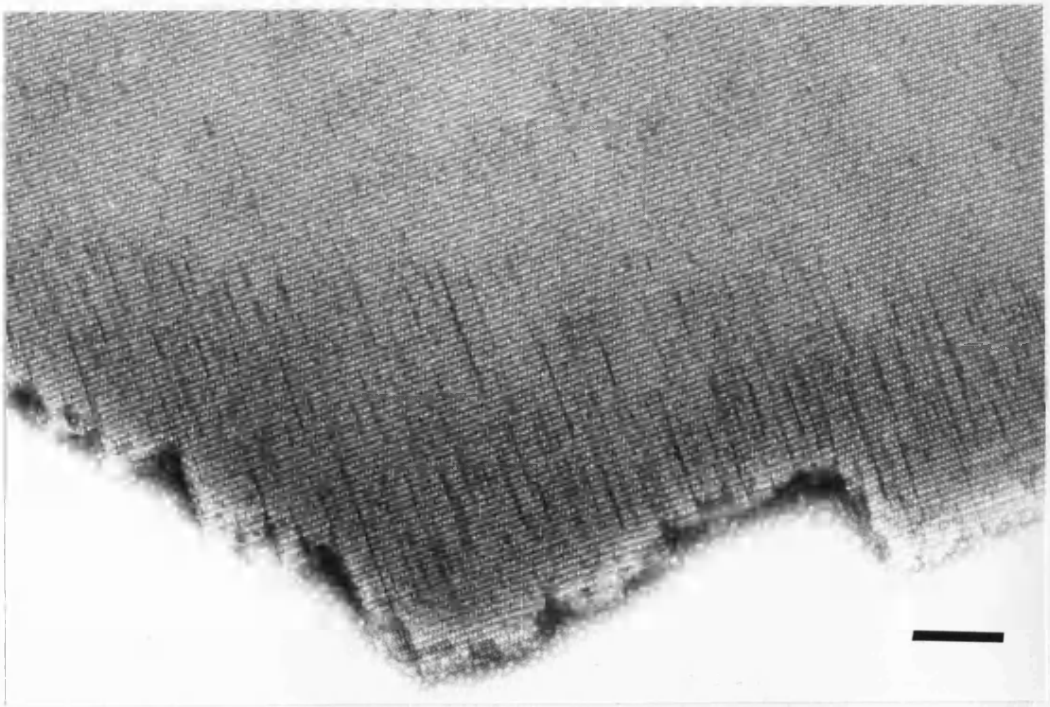

Negatively stained preparations, however, showed only 2 nm resolution at best. The low dose, hydrated patterns were as good as could be obtained from thick crystals by X-ray diffraction and contained information on the atomic organisation of the protein. This work demonstrated the preservation of structure of proteins on mounting them in the microscope and, by spreading the dose over a large crystalline area, high resolution diffraction patterns could be obtained.

Freezing and keeping the specimen at liquid nitrogen temperature was a simple method of overcoming the effect of the vacuum on wet biological samples. Taylor and Glaeser [49] obtained 0.34 nm diffraction patterns from frozen catalase crystals with an adapted 100 kev microscope. A cold stage was a more straightforward device to operate than a wet cell and lacked the problems of thermal and Brownian motion of the sample. Motion of the specimen caused by thermal drift and vibrations from the boiling coolant though, were an obstacle to obtaining high resolution images.

Unwin and Henderson [50] brought together the research on high resolution specimen preparation, application of optimal dose and the methods of image analysis and reconstruction. They elegantly overcome the problem of hydration by using a solution of glucose into which the specimen was dried. This was essentially the same as the negative staining method except that the many hydroxyls of the carbohydrate replaced the water and on

drying, the molecules were not exposed to the high ionic strengths of staining salts. Crystals of catalase dried in glucose diffracted to 0.3 nm. A comparison is shown below of diffraction patterns from negatively stained (top) and glucose embedded catalase crystals. They were taken with the same diffraction camera length. The 4th row of spots (arrowed) at about 1.7 nm resolution can just be made out in the upper pattern. The lower pattern shows the 17th row at 0.4 nm.

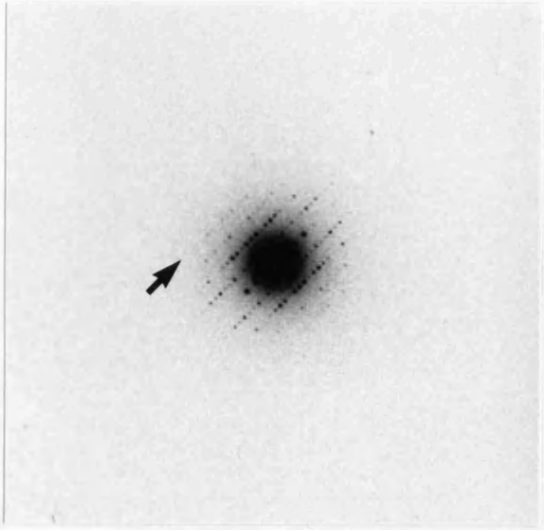

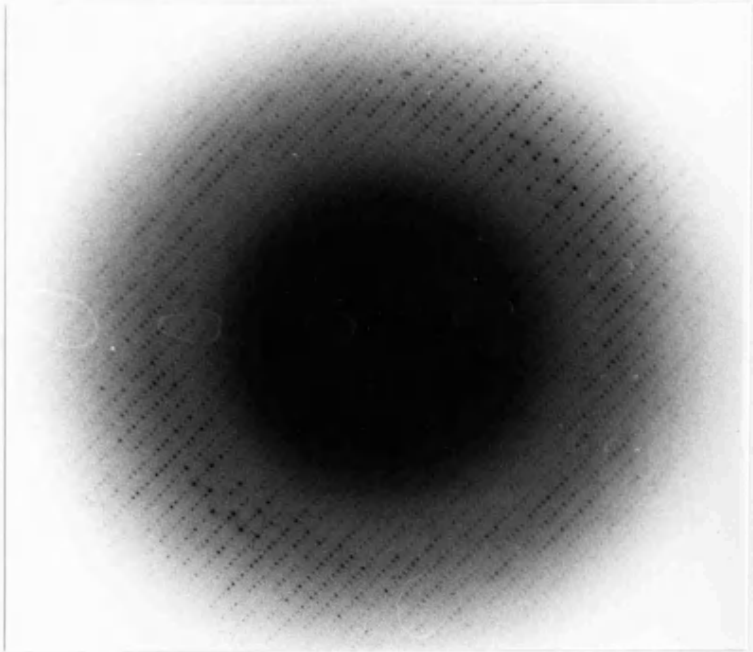

A Philips EM301 was used with a conventional room temperature specimen holder and there was no problem of specimen motion or vibration. Also, the technique was straightforward and easily repeatable. High resolution images of the purple membrane from Halobacterium halobium gave a resolution of 0.7 nm and revealed an electron density projection of the molecule's trans-membrane alpha-helices. The limit to the resolution was not because of the specimen, which showed diffraction out to 0.35 nm, or the microscope, which could resolve the graphite lattice. The loss of contrast for high resolution information was determined as being due to "some electron optical disturbance" which is more severe at the magnifications used to record low dose images than at the top magnifications used to record graphite fringes.

It was anticipated from diffraction studies with L-valine that lower temperatures would provide longer lifetimes for the specimens and therefore improved resolution in the images, provided the cold stages could be made stable. Intense interest was stimulated by Knapek and Dubochet when they published a 300x increase in lifetime for L-valine at liquid helium temperature, 4 ^{o}K. They used an electron microscope with a superconducting objective lens [51]. This had been designed because of the extreme stability of the magnetic lens and the specimen stage. The dream of non-destructive electron microscopy for biological specimens however, was not to

be. The results were later found to be erroneous [52] and the factor of improvement found to be only about 10x. The initial paper caused an increased interest in cryo-microscopy and accelerated investigations into the preparation of frozen, hydrated specimens.

Thin layers of water were frozen onto the grid and observed using a cold stage [53]. The image below shows a thin film of crystalline (hexagonal) ice, frozen by cooling the grid in liquid nitrogen. The dark bands are bend contours produced by diffraction effects from the orientation of this thin crystal.

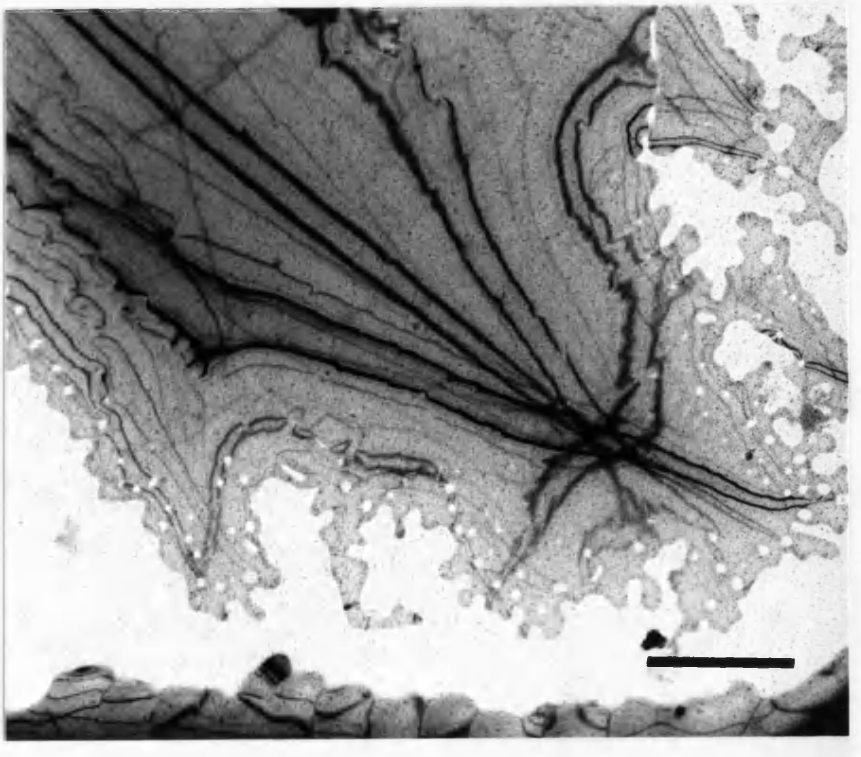

Scale bar represents 5 μm.

This preparation could be used for preparing frozen hydrated specimens which were in pure water [54]. The image below shows the virus Semliki Forest, frozen in hexagonal ice. The contrast here is phase contrast and is generated by underfocusing the microscope, the dark band is a bend contour. The scale bar represents 50 nm.

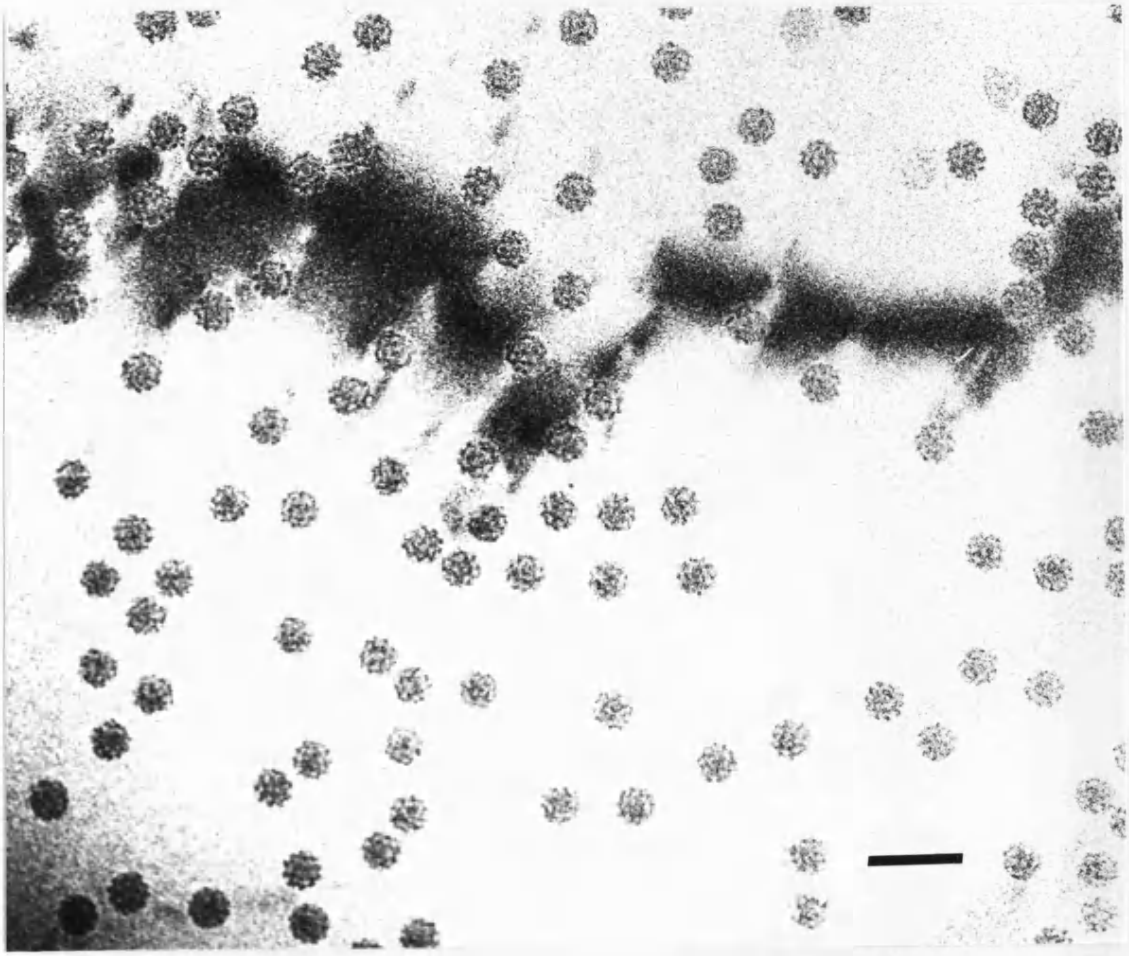

As a solution freezes the water forms pure ice and the solutes are concentrated into a eutectic phase between the ice crystals. This exposes the specimen to potentially harmful osmolarities and ionic strengths. Also, and this may be the case in the image shown above,

the growing ice crystal may expel the sample to the surface.

Freezing the sample by plunging the grid into a cryogen sufficiently fast produces amorphous ice [53]. This traps the water in a state very similar to that of the liquid and provides the electron microscopist with a specimen free of preparative artefacts. Below is an image of the bacteriophage Lambda frozen in amorphous ice. Those particles which contain DNA are darker because of the greater density, and hence electron scattering power, of DNA than water. Amorphous ice can be characterised by its diffraction pattern of two diffuse rings at 0.37 and 0.214 nm (insert). The scale bar represents 50 nm.

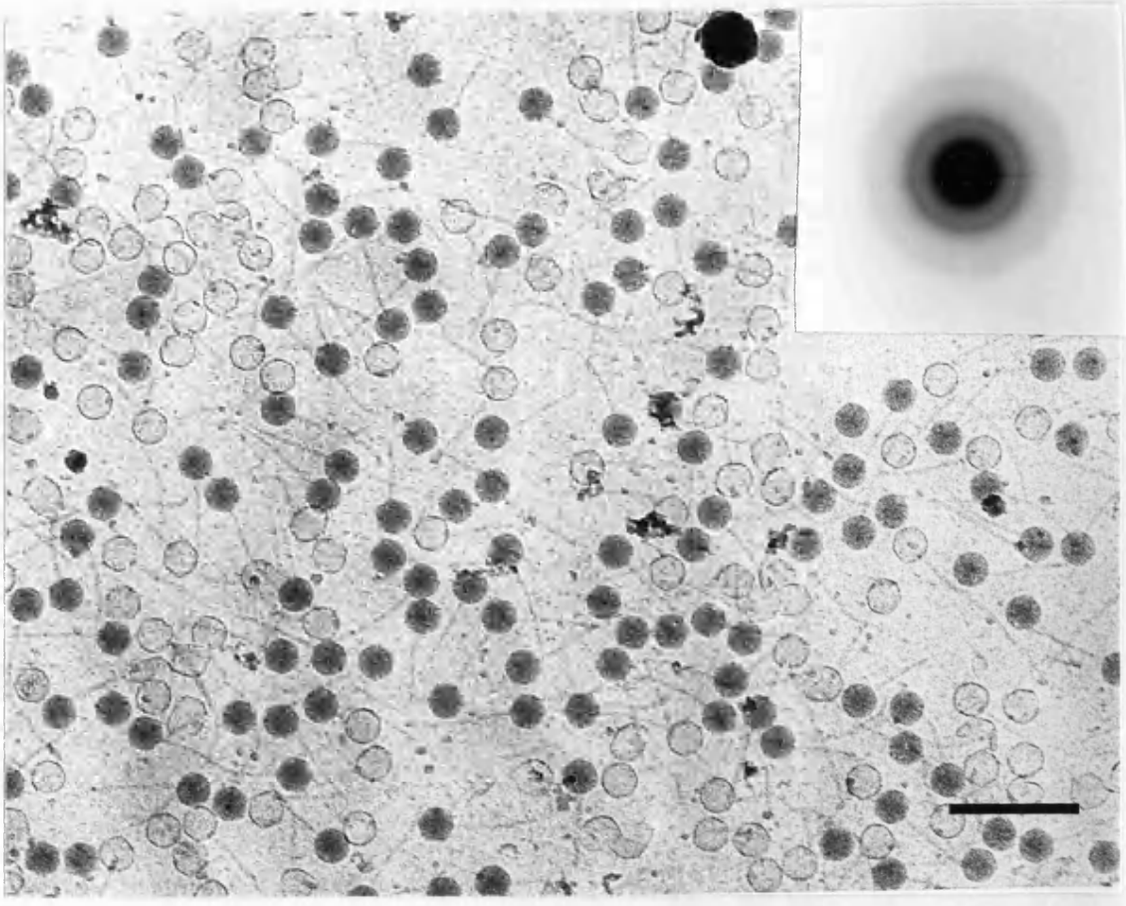

2.4 IMAGE ANALYSIS

The electron micrograph is normally first assessed by eye, often with a magnifying lens. The trained observer can find evidence of imperfections but the interpretation is quite subjective. Optical diffractometry gives an immediate ("at the speed of light" [55]) objective display of the image. Aberrations and imperfections can be found and periodicities measured in terms of size and resolution. This can also be done by computer analysis but it is normal to quickly scan images with the diffractometer and then digitise the best for computer analysis and image processing.

2.4.1 Contrast in Bright field images

In an electron microscope image two terms contribute to the final contrast. These are the amplitude contrast, which originates when electrons are scattered outside the objective aperture, and a phase contrast contribution.

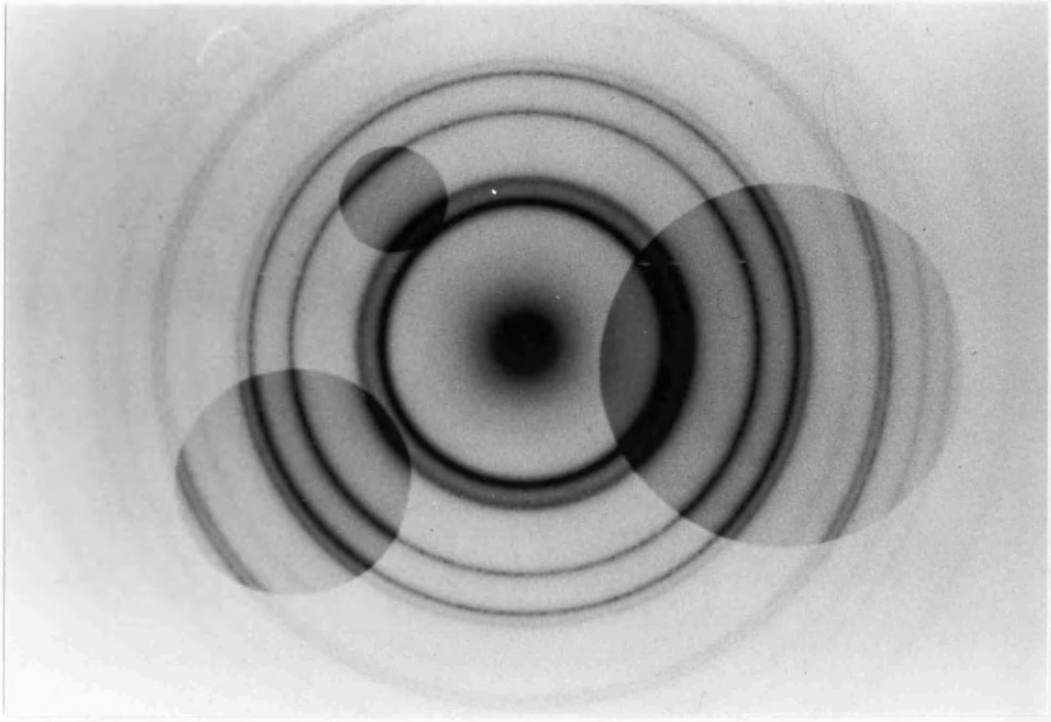

The image above shows a set of objective apertures recorded over a diffraction pattern of a gold sample. The apertures are close to the diffraction plane of the objective lens (back focal plane). An aperture is normally centred on the diffraction pattern. It can be seen that the largest would allow through the electrons scattered out into the first two rings. The smaller ones would not and would therefore generate more amplitude (also known as diffraction) contrast in the image. The gold grains, of which this specimen is composed becoming darker. At the same time as generating contrast though, the apertures remove those electrons scattered to high angles and thus remove high resolution information.

Phase contrast is produced when the scattered electrons interfere with the unscattered or background electron beam. For thin biological specimens the scattered electron wave forms a small fraction of the unscattered beam. As in light microscopy the phase difference between scattered and unscattered is very small and produces insignificant contrast itself. The Zernike phase plate of optical microscopy retards the unscattered wave by a half wavelength. Phase plates have been constructed for electron microscopy [56], but they are difficult to make and use. A simple method of generating phase contrast is by using the spherical aberration of an electron lens.

The spherical aberration of a lens causes electrons that are scattered out to higher angles to be focused more strongly. Thon demonstrated that defocusing the lens would produce phase shifts, and therefore phase contrast, for bands of spatial frequencies [57]. The position of these zones of contrast (A) changed with defocus value (dZ) according to the equation:

$$A = 1/L[\ dZ/Cs +- (\ dZ^2/Cs^2 + (\ 2N - 1)L/Cs)^{\frac{1}{2}}]^{\frac{1}{2}}$$

Where L= Electron wavelength, Cs= Spherical aberration constant and N is an integer.

The graph below shows the positions of the zones of phase contrast maxima calculated for 100 kev electrons and a lens with a Cs of 1.5 mm. The spatial frequencies, A, are on the ordinate and the value of focus on the abscissa.

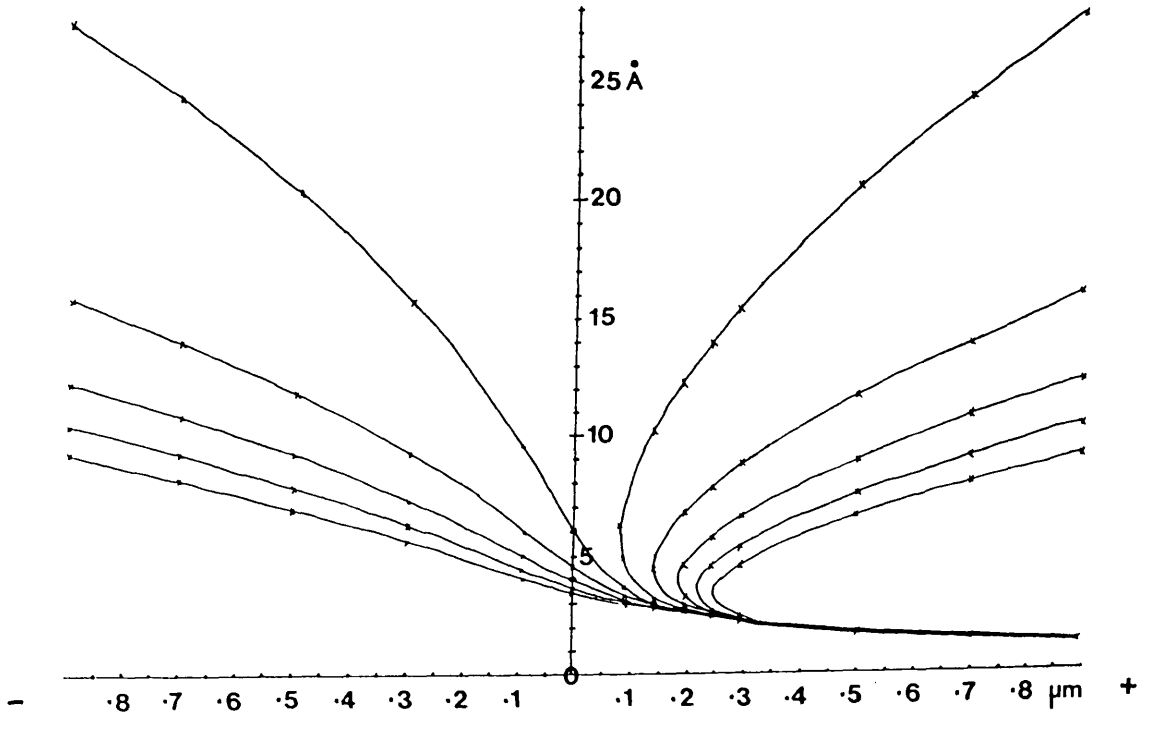

The electron microscope image is therefore potentially complex and direct interpretation can often be misleading. With low resolution specimens the image can be recorded close to focus, putting all the detail within the first maximum. At high resolution the problem is unavoidable and the image must be processed by computer to compensate for the aberration.

2.4.2 Two-dimensional analysis

By showing that diffraction limited the resolution of the optical microscope, Abbe took what had been a branch of optical physics and made it a part of perception. The important step he made was to consider the test object, a set of closely spaced lines, and then calculate the Fraunhofer diffraction pattern they would produce. It was the same construction of an array of slit sources that caused Fraunhofer to first discover the diffraction effect. The diagram below shows the formation of an image of a diffraction grating by a lens.

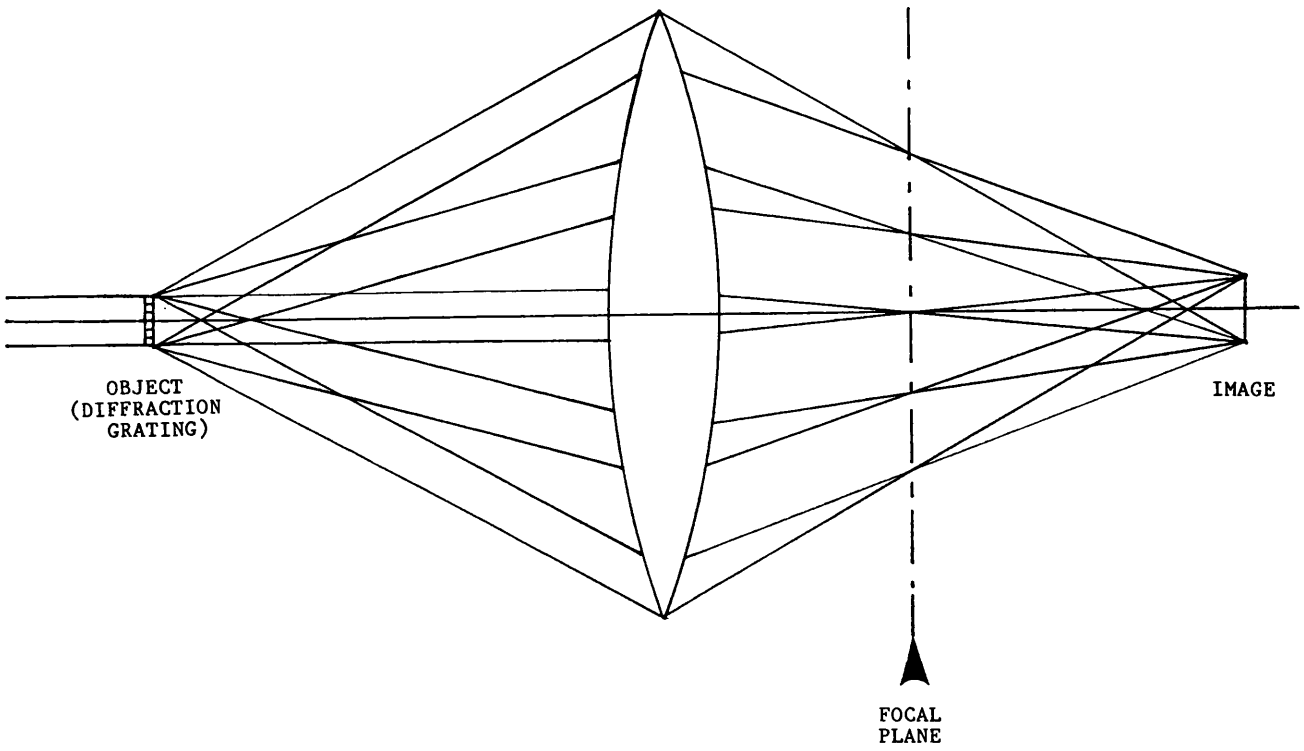

The success of X-ray diffraction was a consequence of the highly ordered nature of atoms within crystals. In analysing these patterns W.H.Bragg noticed that the relative intensities of the spots was dependent on the repeating unit within the crystal. This was identical to the differences seen between the diffraction patterns of optical diffraction gratings scribed by different machines. The shape of the repeated line, determined by the diamond cutting edge, gave rise to its own peculiar distribution of intensities along the diffraction pattern. Bragg took this investigation an important step further by showing that this convolution of the repeated unit by the lattice was mathematically described by Fourier theory [58]. This states that any periodic function can be expressed as the sum of a series of sinusoidal functions with periodicities that are integral sub-multiples or harmonics. Just as the timbre of a musical note from a particular instrument can be broken down into sets of harmonic sine waves, so an object in a repeating array is composed of sets of harmonic spatial frequencies.

A Fourier transform can be demonstrated by a lens or calculated by a computer. the advantage of the latter is that a complex system of data refinement steps can be carried out . The final result is a set of numbers that can then be used to generate, by a second Fourier transform an image of the repeating unit within the array.

The optical method was introduced by Klug and Berger [59] to give an analysis of the periodic components within an electron micrograph. The extension of this idea was to use a mask at the diffraction plane and combine the periodic diffracted rays. This synthesized a filtered image in which the aperiodic frequency contributions (noise) had been eliminated [60]. It was also possible to filter out overlapping components in an image. In the case of a helical array the 'near' and 'far' sides of the structure are superposed. Because both contributions generally have a distinguishable Fourier transform, each of them can be separately reconstructed.

Another approach in the analysis is to convert the image into a set of numbers and to perform the Fourier transformation by computer [61]. This results in a transform, in which amplitudes and phases are calculated and in which also a reverse transformation is possible. This returns the information into a 'real' space image from the 'Fourier' space pattern. The system for digitising diffraction patterns was developed for computer processing X-ray data, and it was a simple matter to acquire images with a computer driven microdensitometer.

The fast Fourier transform (FFT) computer algorithm [62] allows calculations of small arrays 128 x 128 to be made within seconds. The output can be

represented as a contour map, density plot, or simulated image, according to the computer graphics available.

2.4.3 Three-dimensional analysis

Due to the large depth of field in the electron microscope, which is several times the thickness of individual biological molecules (under normal conditions almost a micrometer), a 2-dimensional projection of the object is obtained along the electron beam direction. In order to produce a 3-dimensional density map of the structure, a number of projections have to be combined. The most successful technique to produce a 3-dimensional image from its projections is the Fourier method, originally proposed by De Rosier and Klug [63]. This is based on the fact that the Fourier transform of the 2-dimensional projection corresponds with the central section of the 3-dimensional transform of the object.

The 3-dimensional Fourier space can be built up plane by plane using different 2-dimensional projections. Images of the specimen are obtained with a stage that can be tilted. A set from 0^{o} to 60^{o} clockwise and anti-clockwise are taken in about 10^{o} steps. The images are then digitised and Fourier transformed. Using an untilted transform to start the data set the 3-dimensional transform is assembled by combining the aligned tilted

transforms at their tilt angle. This is then back-transformed into the three dimensional object.

The synthesis is very similar to X-ray crystallography, except that the phases of the X-ray pattern can not be measured but have to be derived. The data from the Fourier transform of an image contains both amplitude and phase information. A diagram of the Fourier method is shown below. From De Rosier and Klug [63] with permission.

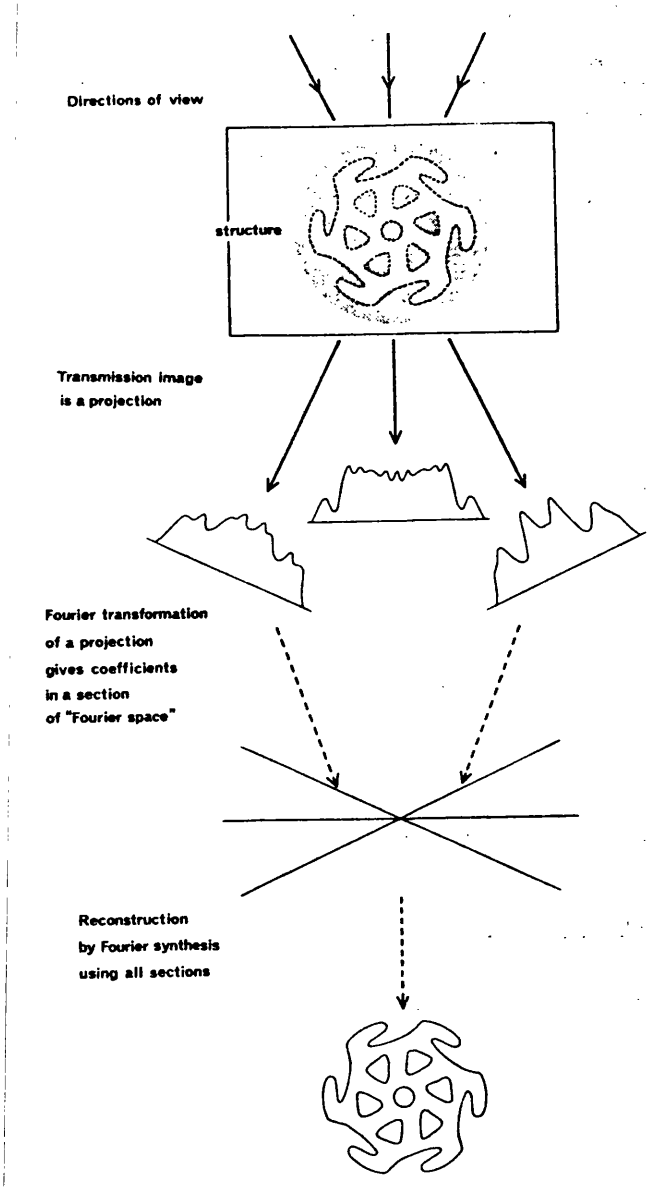

3. EXPERIMENTAL PROCEDURES

This chapter deals with specimen preparation and minimum beam techniques. In addition, the construction and operation of an optical diffractometer is detailed, together with examples of its practical use in image assessment. The isolation and preparation procedures of the biological material are described in detail in Materials and Methods sections of the following chapters.

3.1 Specimen Preparation

The specimens examined in this thesis have, for the most part, been prepared by absorption from solution onto a thin carbon film [64]. They were then either dried in a stain (negative staining), in glucose (unstained), or quickly cooled to liquid nitrogen temperature (frozen-hydrated). The surface of the carbon was rendered hydrophilic by glow discharge [65] or exposure to ultra-violet light [66].

For frozen hydrated specimens the sample was applied as a small drop onto the grid surface. The grid

was then blotted with filter paper (Whatman No.1) and quickly frozen. With a hand held tweezer the grid can be plunged into liquid nitrogen and the sample will be frozen in crystalline ice. When plunged into a suitable cryogen such as liquid ethane the freezing velocity was high enough to give amorphous ice. To ensure a high chance of this result the tweezer was clamped to an iron bar which then falls, accelerating to a velocity of over 1 metre/second, into the liquid ethane.

3.2 Electron Microscopy

In this study I have used microscopes manufactured by Philips (Eindhoven, Holland) and Jeol Ltd. (Tokyo, Japan). They were equipped with side-entry eucentric goniometer stages. This allowed simple tilting of the specimen with the tilt axis set at a constant sample height. It is noteworthy to point out that the two manufacturers design their specimen stages differently. The Philips specimen holder has the grid, loaded with the sample side up, in the microscope with the sample side down. The Jeol on the other hand, has the specimen in the microscope with the sample side up. This would not be of importance unless an investigator was using both types of microscope with an asymmetric or 'handed' specimen.

3.2.1 Low dose imaging

The three different imaging modes necessary for low dose microscopy are described.

(a) A low magnification of about 500x was used to scan the grid for suitable specimens. Going from one grid square to another across the grid until suitable specimens were found. This was examined in diffraction and the image below shows a region of a grid seen by defocusing the diffraction pattern to obtain an image with very high contrast.

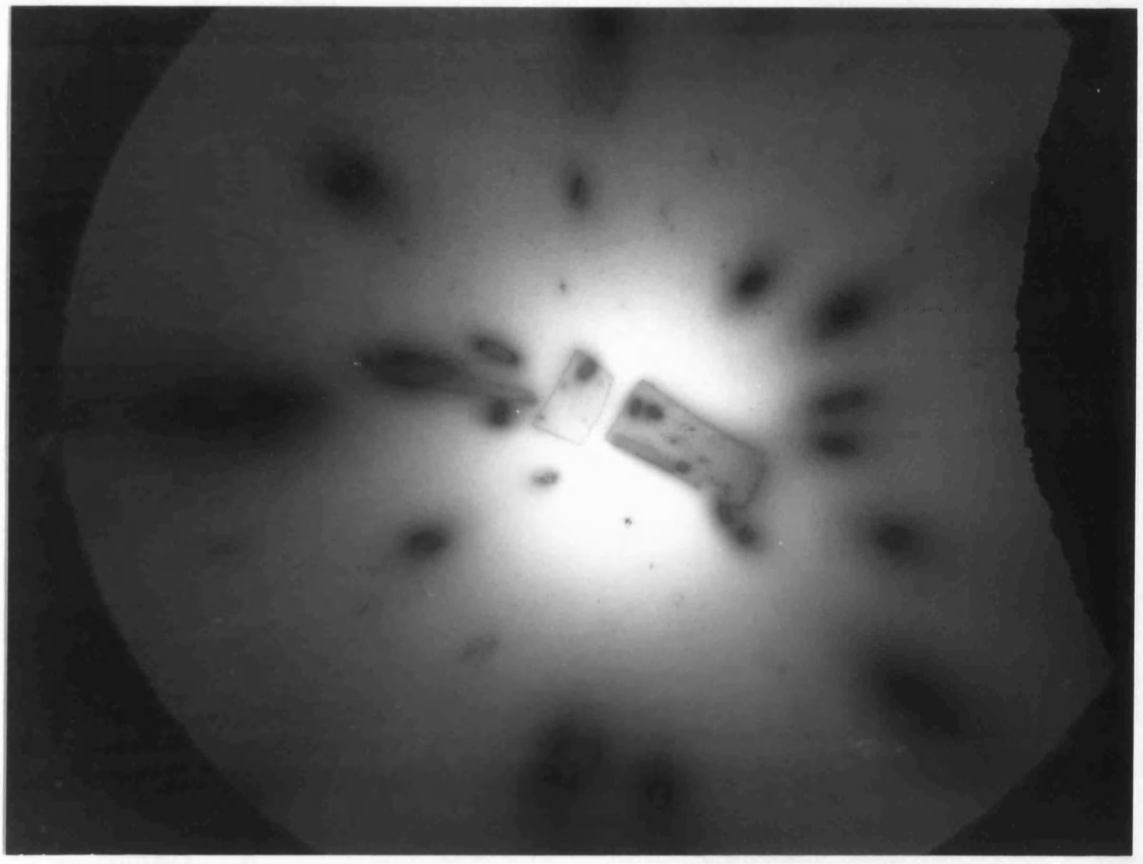

The dose received was very low in this mode. When a specimen was found, like the crystal at the centre of the image, an area selecting aperture was introduced and the specimen moved to position it inside the aperture. This aperture marks the region at the centre of the screen when the microscope was put into imaging mode. The result of this operation is shown below.

(b) A high magnification of a region of the support film adjacent to the specimen was obtained in the next mode. The region irradiated was restricted to be away from the specimen. The microscope was focussed by observing the phase contrast granularity of the background film. The minimum contrast was found and then

a small amount of underfocus applied to give optimal contrast. The image below shows (top) the granularity in this mode, scale bar represents 50 nm. The lower image reveals, by going back to the first mode, the area irradiated and its position relative to the specimen. The area is lighter because of mass-loss from the material on the grid.

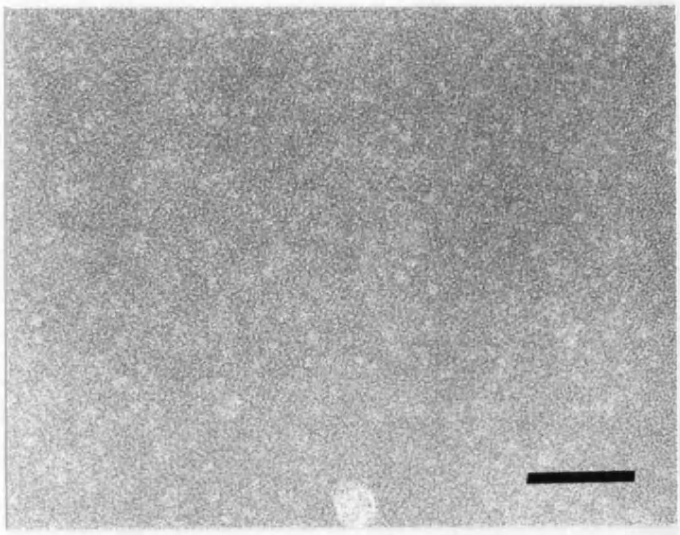

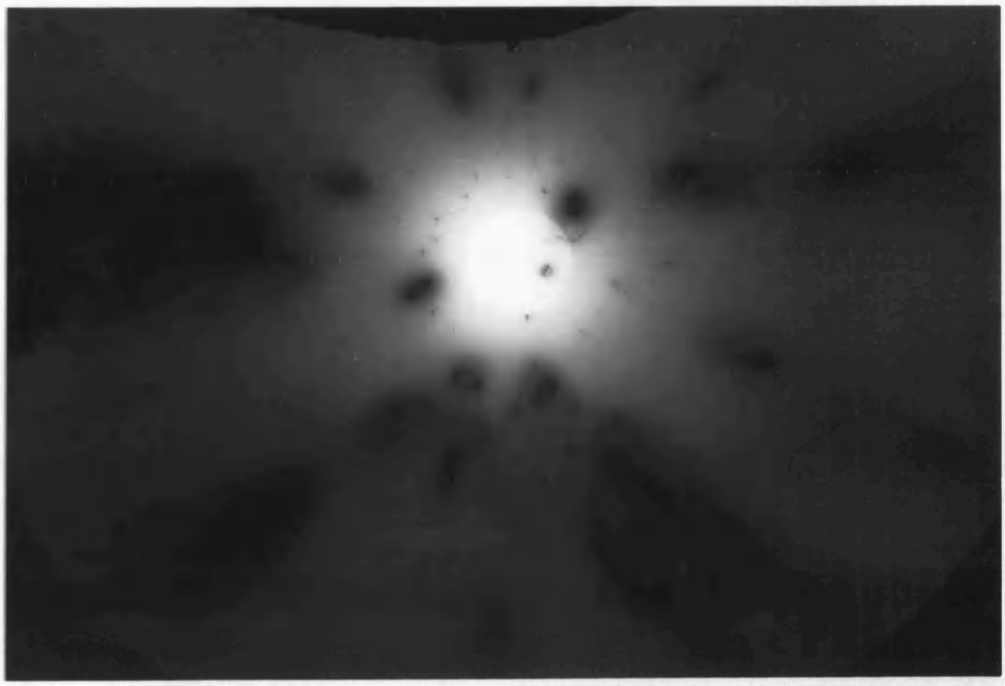

(c) A magnification was selected which optimised the sensitivity of the specimen, the speed of the film and the resolution of the film. The image was then taken of the specimen at the same time as the camera shutter opened. The image below (top) shows the low dose image of the sample; a catalase crystal negatively stained with barium acetate, the scale bar represents 100 nm. The lower image shows the effect on the crystal of irradiation by going back to the first mode.

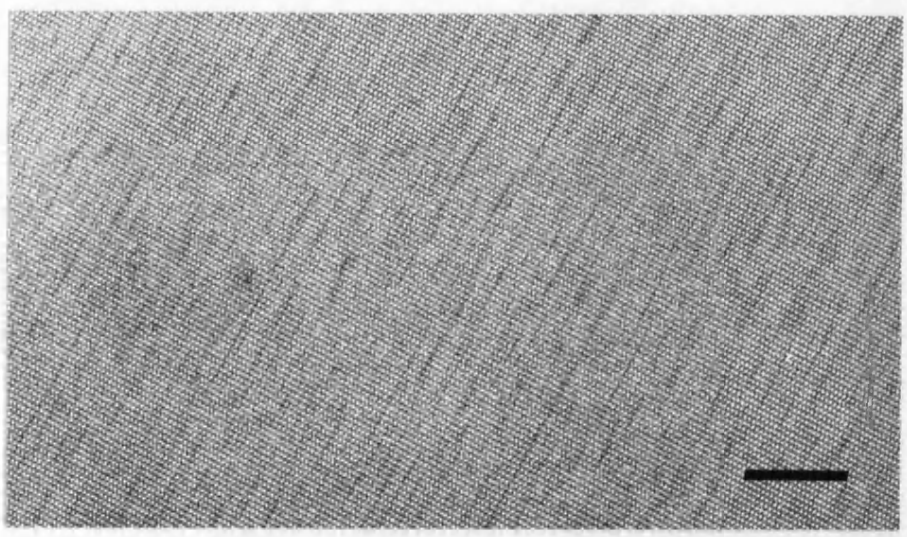

3.2.2 Dosimetry

Electron microscope film SO-163 (Eastman Kodak Co., U.S.A.) is a well characterised recording medium [67]. The electron speed of this film for 40-100 kev electrons, when developed for 12 minutes in Kodak D-19 developer (full strength), is 2.2. This means that an electron dose of 1 $e^-/\mu m^2$ at the film will produce an optical density of 2.2. This provides a simple method for calibrating the exposure meter of the viewing screen. For example, a sheet of SO-163 is exposed to a flux of electrons for 0.5 seconds when the exposure meter registers a 2 second exposure. (There must be no object in the microscope and the electron flux must be spread completely over the screen.) Should the film develop an optical density of 1.1 then for a reading of 2 seconds, 0.5 $e^-/\mu m^2$ were collected in 0.5 seconds. The dose rate at the film is $1e^-/\mu m^2/sec$ when the meter reads 2 seconds. At a reading of 1 second the dose rate is doubled, etc.

With a specimen in place, the dose that it is exposed to can be calculated by knowing the meter reading and the magnification. At a magnification of 1000x and a meter reading of 2 seconds the specimen dose rate is 1 $e^-/nm^2/sec$. At 100,000x the same meter reading indicates that the specimen dose rate is 10^4 $e^-/nm^2/sec$.

For the greatest precision a Faraday cage must be used to measure the current of the beam. However, the film method does bring the operator to an approximate awareness of the levels of irradiation to which the specimen is being exposed.

The normal working brightness of an electron microscope screen is produced by a current of approximately 1 $e^-/\mu m^2/sec$. At a magnification of 50,000x the specimen will experience a dose rate of 2,500 $e^-/nm^2/sec$. The dose that a typical biological molecule can withstand is 100 e^-/nm^2, a lifetime of only 0.04 seconds.

3.2.3. Electron Diffraction

Just as the magnification is calibrated for imaging with the microscope, so too the diffraction camera lengths are determined with standards. The actual lengths though are little used. It is the camera constant, the product of the wavelength and the camera length, that is determined and updated. This product is also the product of the spacing in the crystal and the measured distance on the film from the diffraction maximum to the origin. An unknown crystal spacing can be determined by dividing the camera constant by the measured spacing.

The image below shows the diffraction pattern of the polycrystalline diffraction standard, thallous chloride. The spacings in the crystal are accurately known and the 6th. ring out is produced by a spacing of 0.157 nm. The radius of this ring on the print is 65 mm, giving an effective camera constant of 10.2 nm x mm.

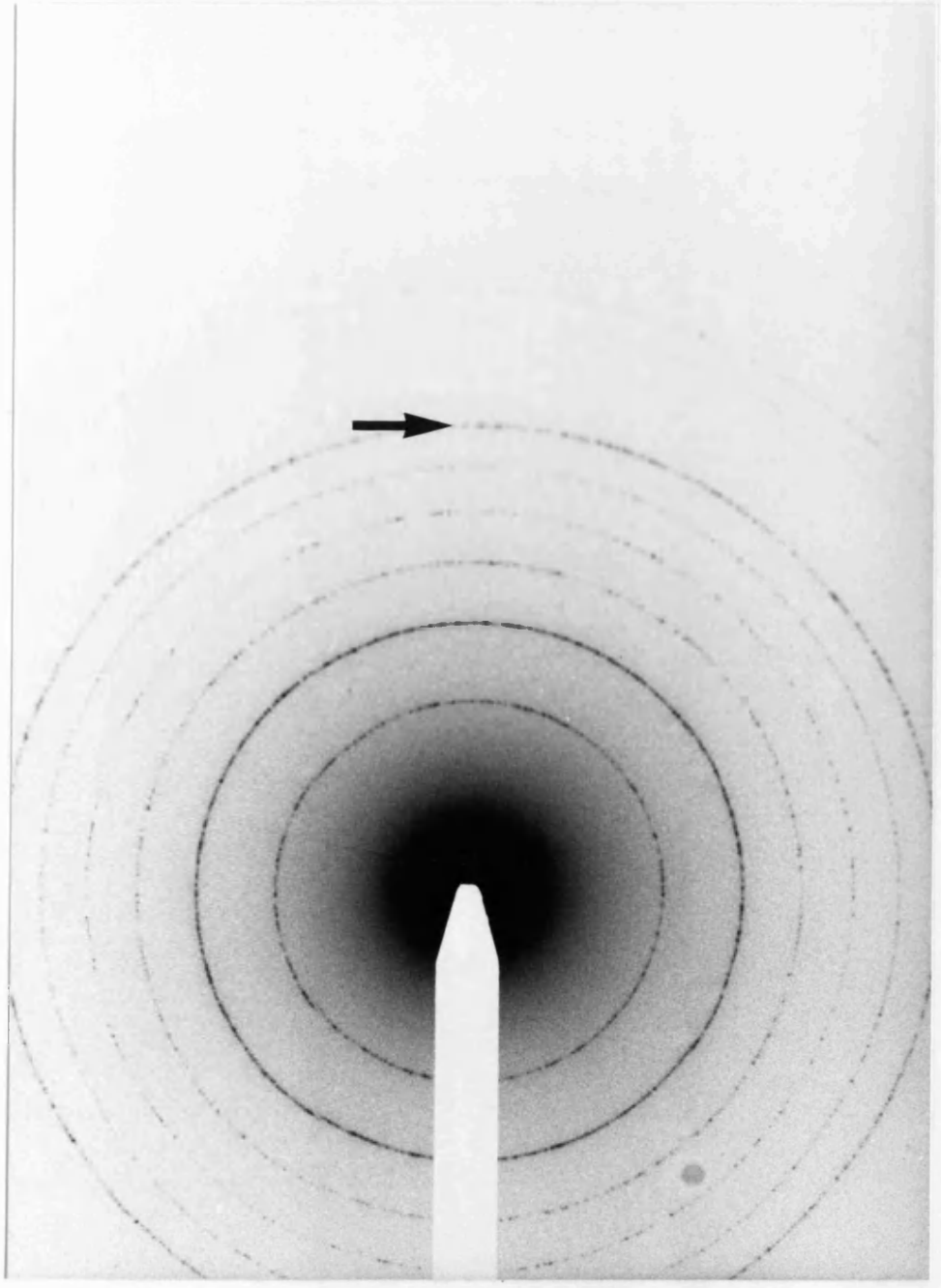

3.3 Optical Diffraction

This apparatus was designed to give a simple assessment of electron micrographs with the ability to display spacings in image down to the resolution of the film. This facility is important in high resolution microscopy where the lowest possible magnifications are used to keep radiation damage as low as possible.

3.3.1 The optical bench

It is essential to operate this instrument in a darkroom and the available space was limited to 1.5 metres of bench top. A second important consideration was to keep cost as low as possible. Since the optical bench was not to be used for image reconstruction the small amount of vibration in the wooden bench-top from nearby machinery had no effect on the diffraction pattern. This is a consequence of diffraction being translation invariant, whilst the reconstructed image is essentially a magnification of the object and very sensitive to movement.

The walls of the darkroom were found to vibrate significantly making a vertical system difficult to

secure. The doubly-folded system constructed, enabled the operator to move the micrograph around and select the required region whilst observing the diffraction pattern on the screen. The diagram below shows the layout of the Bath diffractometer.

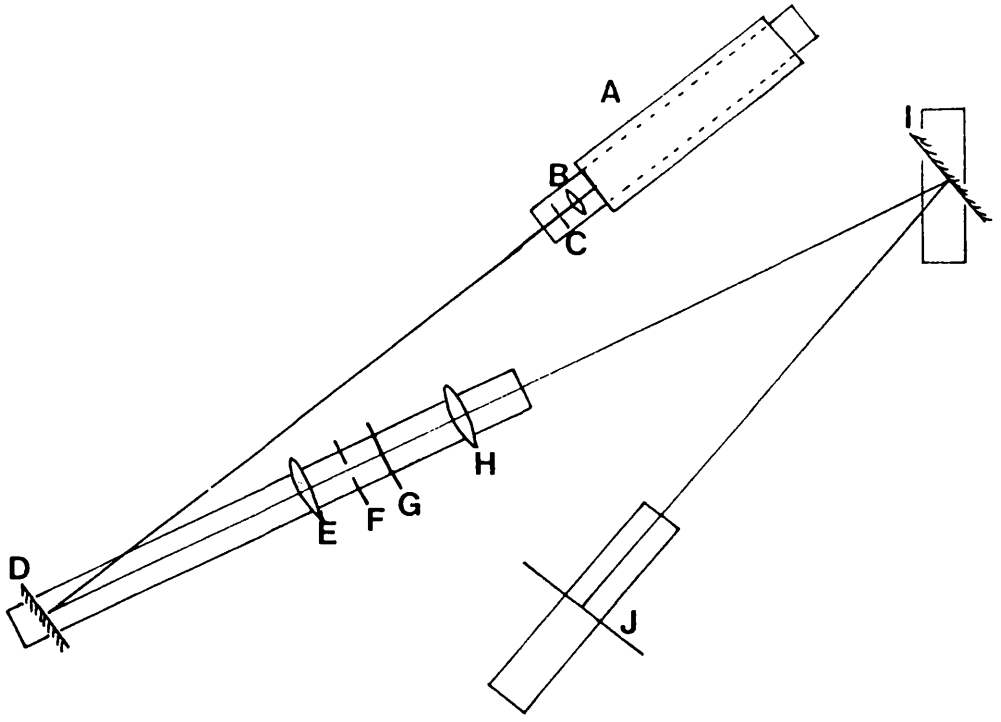

A: Laser

B: 16 mm objective lens

C: 100μm aperture

D: Front-silvered mirror

E: 1 metre focal length lens

F: Set of apertures

G: Micrograph holder

H: 1 metre focal length lens

I: Front-silvered mirror

J: Frosted-glass screen

(a) Construction

The photograph below shows the completed diffractometer. Four lengths (1 x 1 metre, 1 x ½ metre and 2 x ¼ metre) of steel optical bench [The Precision Tool and Instrument Co. Ltd. (P.T.I.), Liss, Hants.] formed the framework. A 5 mW Helium-Neon laser [Melles Girot, Aldershot, Hants.] 632.8 nm polarised, was mounted to a 0.5 metre section of bench so that the height and level of the beam could be adjusted. The clamps and saddles were all bought from P.T.I.

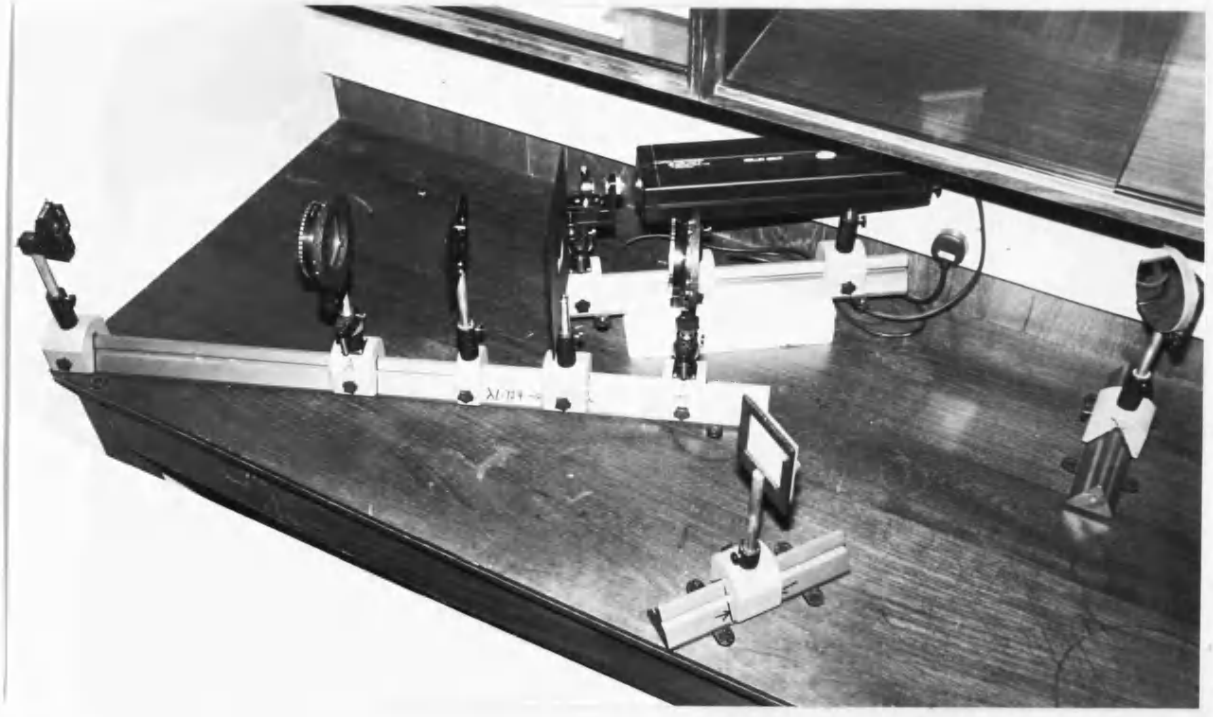

The beam was expanded with a 16 mm (6x) microscope objective. The 1 mm diameter beam coming from the laser was focused and then diverged for 1 metre to the 1 metre focal length lens. Edge effects from the exit of the laser and imperfections in the expanding lens were removed by centring a 100 μm aperture at the cross-over. The lens and aperture mount (P.T.I.) is shown in the photograph below. It was convenient to attenuate the beam with a small piece of polaroid that could be rotated in the front of this holder.

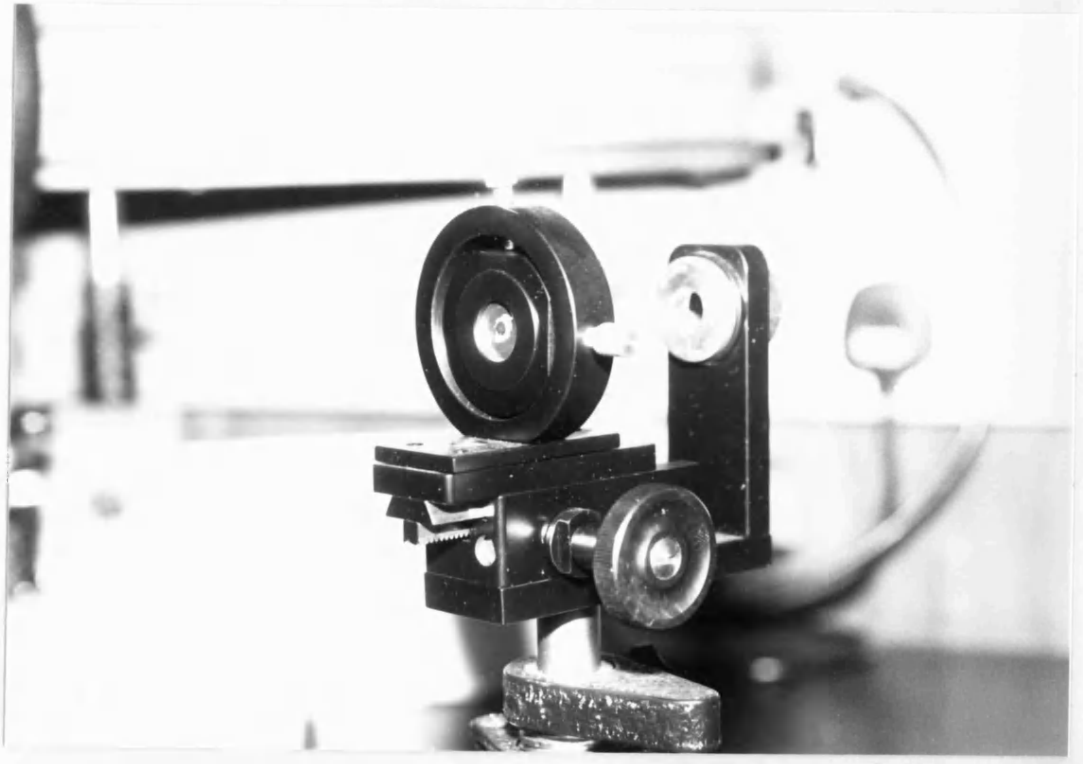

The aperture, to the left, can be centred and racked back and forth to be positioned over the expanding lens cross-over.

The expanding beam was reflected from a front silvered mirror that could be tilted (Ealing Beck Ltd., Watford, Herts.). The two 1 metre lenses [Spindler and

Hoyer UK, Tonbridge, Kent] were mounted onto lens mounts [P.T.I.] using the ring holders of the lenses which were cemented with Araldite to the mounts. This allowed fine adjustment vertically and horizontally. Tilt correction was not necessary. The micrograph was attached to a steel plate with a 6 cm hole using strips of magnetic plastic. The size of the area selected was determined with a set of circular apertures [P.T.I.]. The expanding diffraction pattern was reflected off a large, optically flat, front-silvered mirror and focused onto a ground glass screen. In the photograph below the first lens, aperture selector, micrograph holder (showing attaching strips and the region of the micrograph analysed), second lens, large mirror and screen, can be seen from left to right.

(b) Alignment

(i) The beam expander, lenses, apertures and micrograph holder were removed from the path of the beam. (Care was taken not to reflect the raw laser beam into the eye with metal surfaces). The height and level of the beam was adjusted so that the beam was of constant height and followed the optical bench. A metal plate with a crossed hole in it was used to assess this. The start of this process is shown in the photograph below.

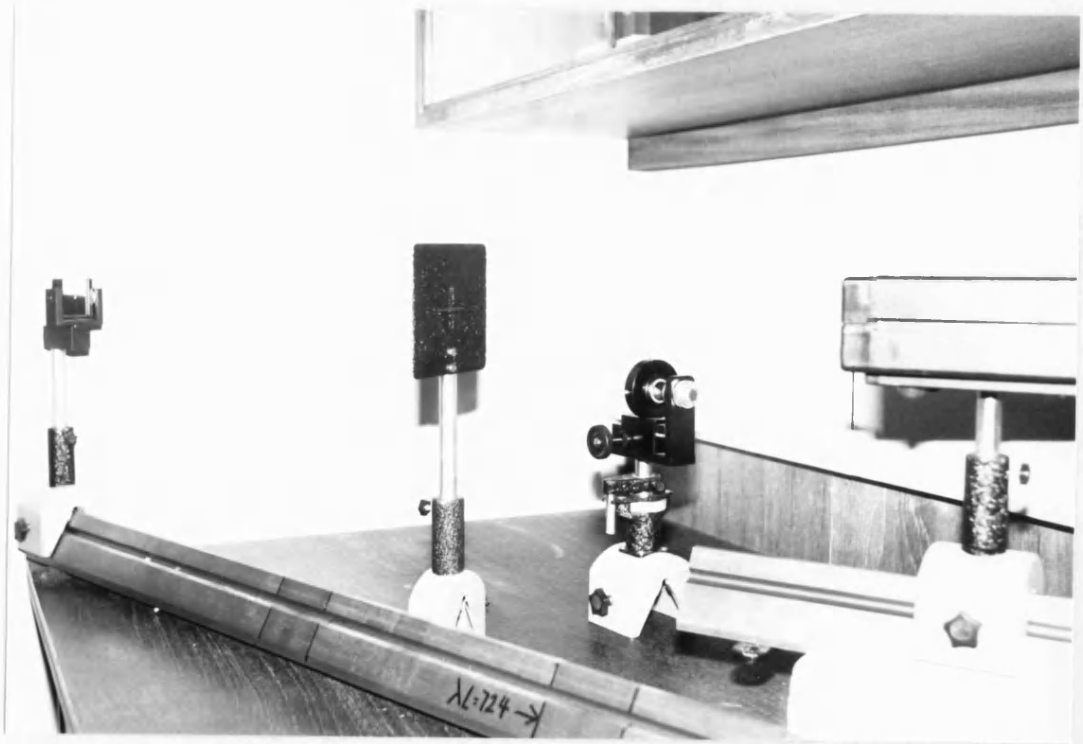

(ii) The aperture from the beam expander was removed and the lens was placed in front of the laser. A piece of white card was held in front of the first mirror

and a system of fringes were seen. The aperture was returned to the expander and it was set at the cross-over by adjusting the horizontal and vertical shifts on the aperture holder to give maximum brightness. Also the aperture was racked backwards and forwards until the fringes were minimized.

(iii) The lenses were returned to the optical bench and they were positioned so that the beam passed through their centres. This alignment was not found to be critical.

(c) Recording

The best method would be to record the pattern onto a large format (120 mm Bronica) camera. The camera being without lens and mounted on the optical bench in the place of the screen. This not being available the pattern was photographed off the screen using a 35 mm SLR camera mounted on a tripod. This was not ideal because of some internal reflections in the lenses of the camera, but produced an adequate record of results. Ilford Pan F film was used and, developed for 6 minutes in Ilford ID 11, exposure times of 1 to 4 seconds were found sufficient.

3.3.2 Image assessment

This section describes the use of the diffractometer in calibrating the magnification of the electron microscope and diagnosing defects in the micrograph.

(a) Calibration of magnification

In order to measure periodicities in the micrographs, the diffractometer was calibrated with a graticule. The figure below shows the type used, with 1.0 mm and 100 μm markings (insert), and the optical diffractogram it produced.

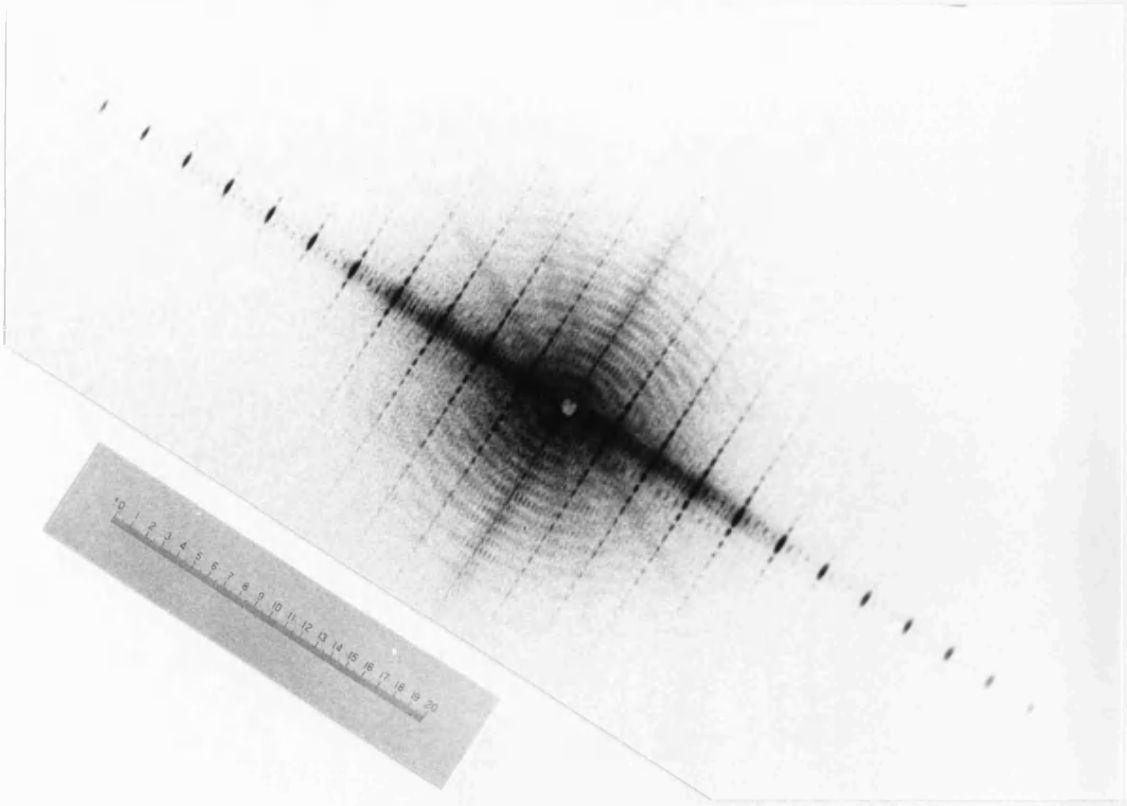

The 100 μm lines in the graticule produce the strong set of fringes in the pattern (arrowed). They are stronger than those from the 1 mm lines (the sets of 10 fine lines between the 100 μm fringes) because there are 10 times more of them. Measuring the distance between the 100 μm fringes and multiplying this by 100 μm gives the camera constant of the diffractometer. Dividing this product by any new measurement from the screen gives the periodicity in the micrograph in μm.

The diffractograms below were produced by images of negatively stained catalase crystals, taken at different magnifications. The lattice constants for this crystal are a = 17.5 nm and b = 6.9 nm. The arrows pick out 4 orders of the 6.9 nm spacing in both. The camera constant is then divided by the distance measured divided by 4, giving the spacing on the micrograph in μm. Since the spacing in the crystal is 6.9 nm, dividing the spacing on the micrograph by 6.9 gives the magnification in thousands.

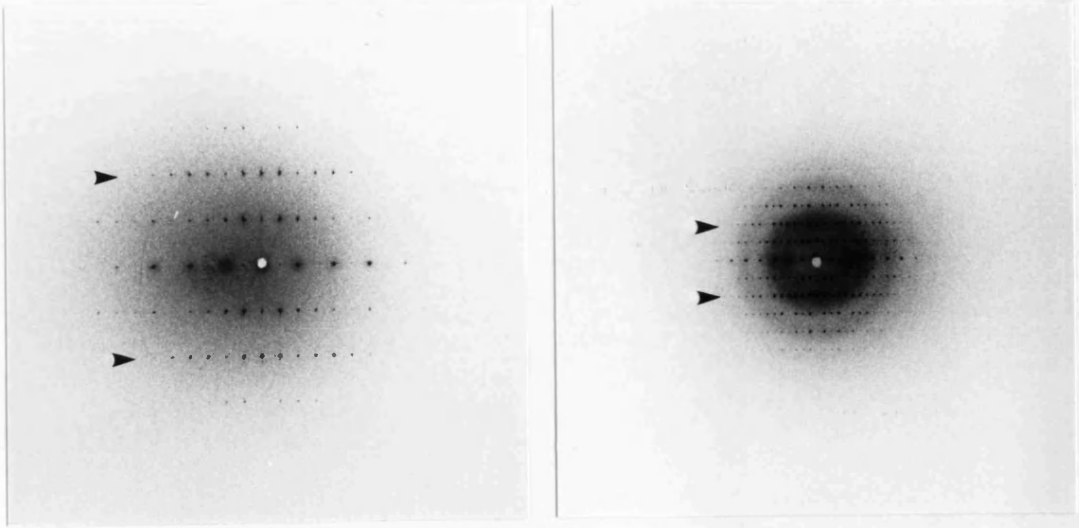

(b) Effect of focus

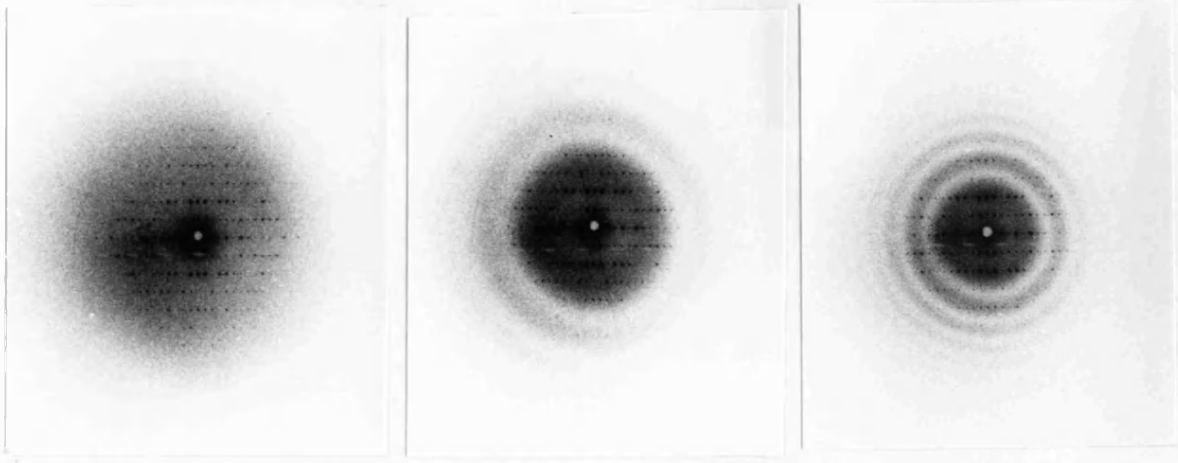

The diffractograms above show the effect on the image of underfocusing the objective lens of the microscope. The image on the left is very close to focus, with all the information of the crystal diffraction spots within the fist broad maximum. On the right the image is so underfocused that many of the diffraction spots are in the second maximum of the phase contrast rings (Thon rings). This changes the phase of the information in them and together with the loss of information at the first minimum makes direct interpretation of the image impossible.

(c) Effect of astigmatism

Objective lens astigmatism is caused by the lens not being perfectly centro-symmetric; a slightly cylindrical rather than spherical lens. This has the effect of producing a lens with two focal lengths at right angles to each other. The stigmators allow the operator to equalise these. With astigmatism present in

an image the phase contrast maxima, or Thon rings, will become elliptical because of the two orthogonal focal lengths. The diffractogram on the left below shows no astigmatism, with circular Thon rings. The middle diffractogram shows astigmatism. Horizontally it is much closer to focus than it is vertically. On the right, the 'Malteze cross' pattern is obtained when astigmatism causes the image to be both underfocused and overfocused by the two focal lengths.

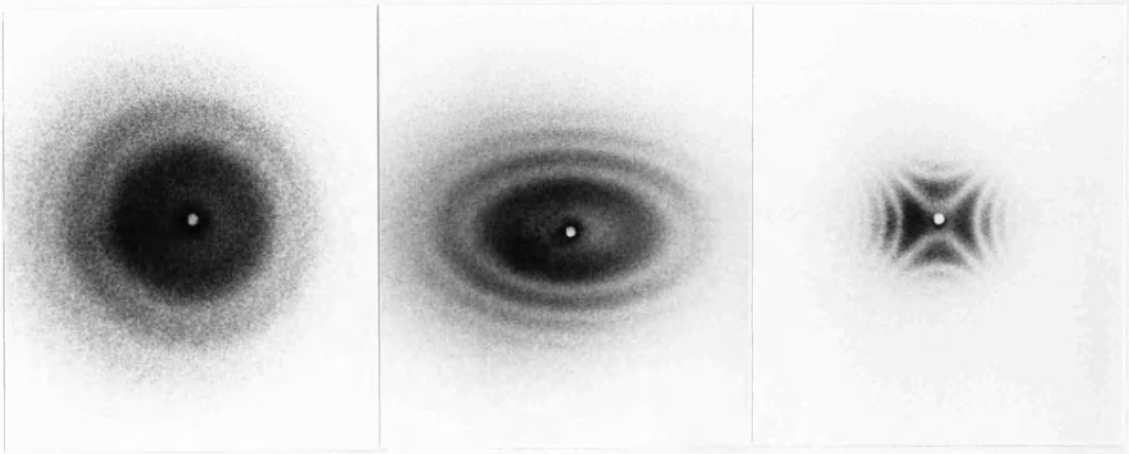

(d) Effect of drift

When a specimen moves during an exposure the information is blurred in the direction of motion. The diffractograms below were 2, 4 and 8 second exposures from specimen on a drifting cold stage.

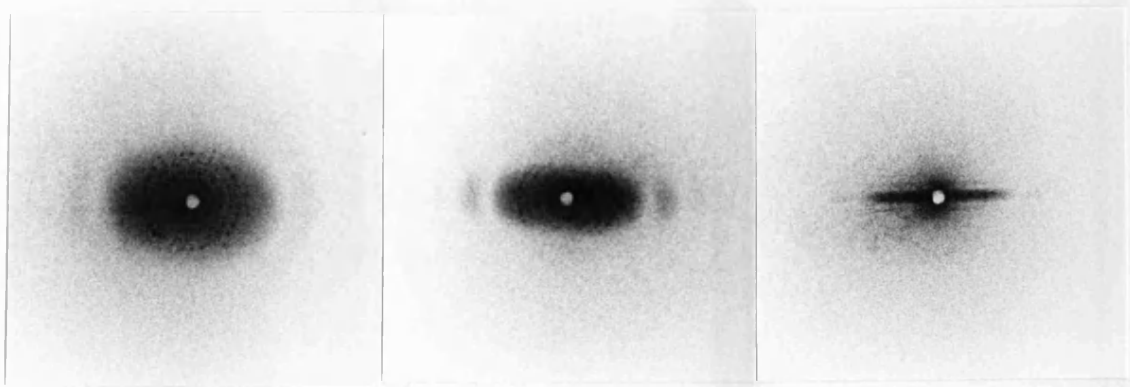

The amount of drift can be calculated by measuring the extension of the information on the pattern in that direction. The diffractograms below show the effect of the specimen moving suddenly during an exposure. The effect of a double-exposure with a displacement is to produce a set of fringes in the diffraction pattern. The amount of the displacement can be determined from the size of the fringes. Those shown below were deliberate double-exposures, taken with the drifting stage, with 2, 0.5 second exposures, 2, 4 and 8 seconds apart (from left to right).

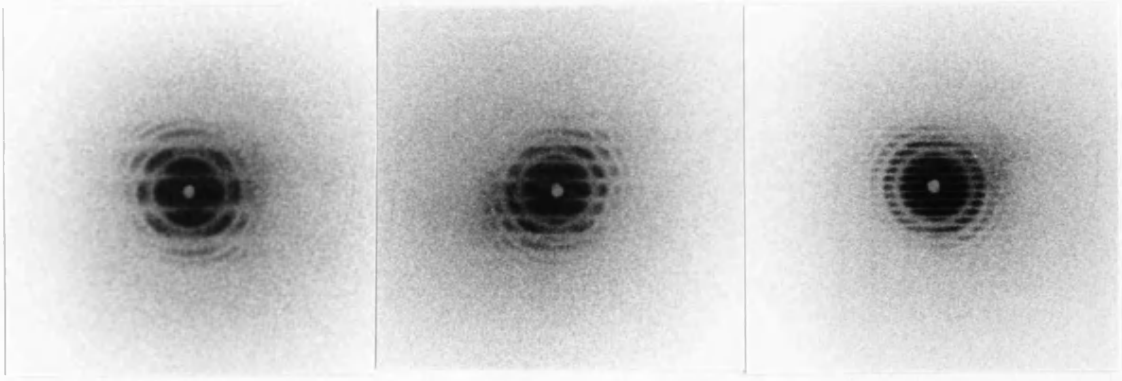

(e) Effect of resolution

The images on the next page show TMV prepared by negative staining (upper) and by unstained, frozen hydrated (lower) methods. By visual inspection the stained image is more informative because of the higher contrast. Their diffractograms however, show that the resolution of the unstained image is at least twice as good. The 6th. layer-line (arrowed) is at 1.15 nm resolution. The scale bar represents 50 nm in the images.

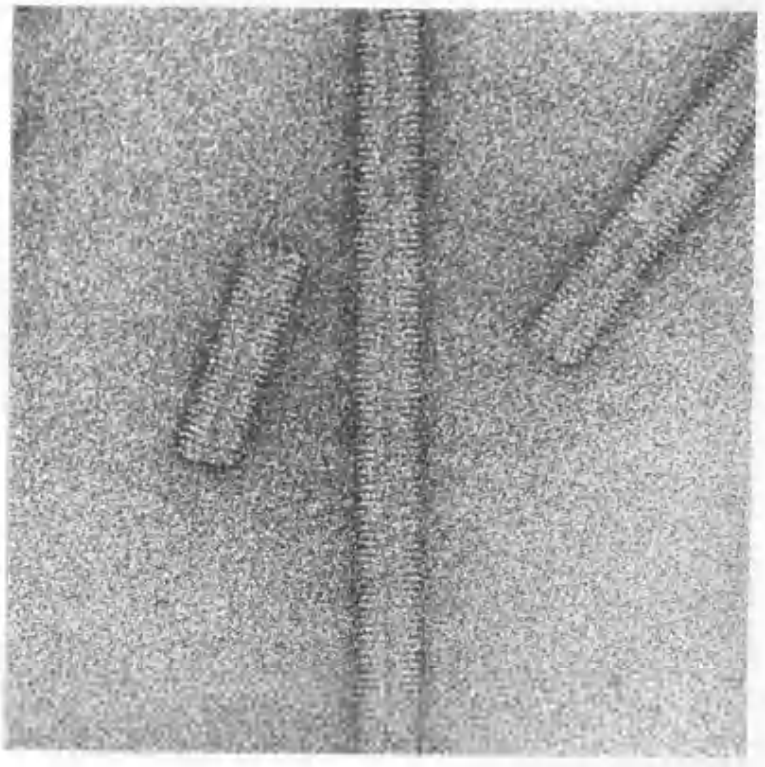

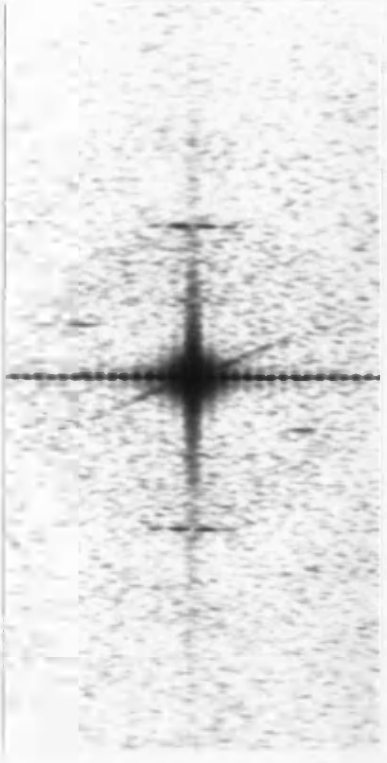

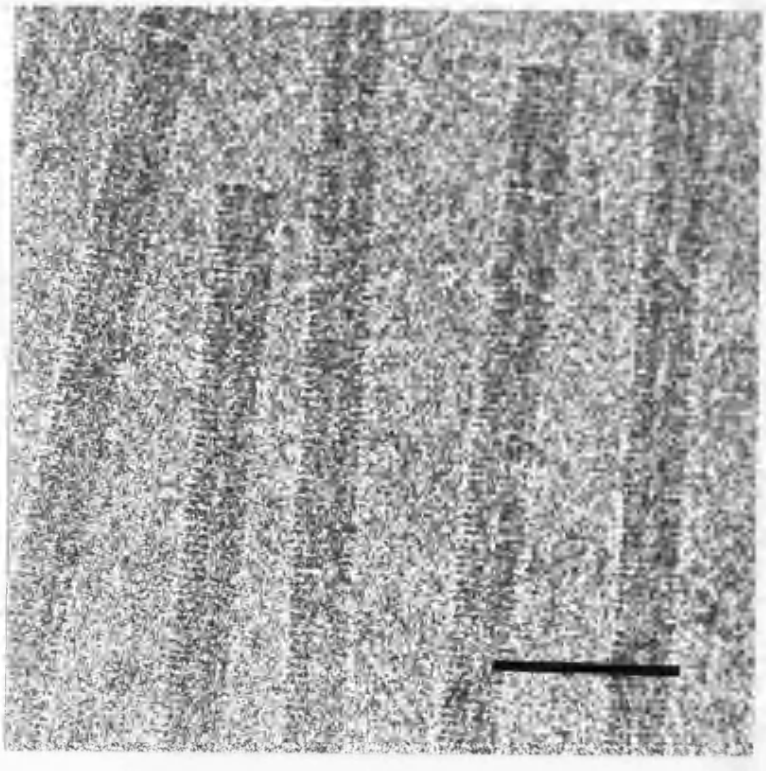

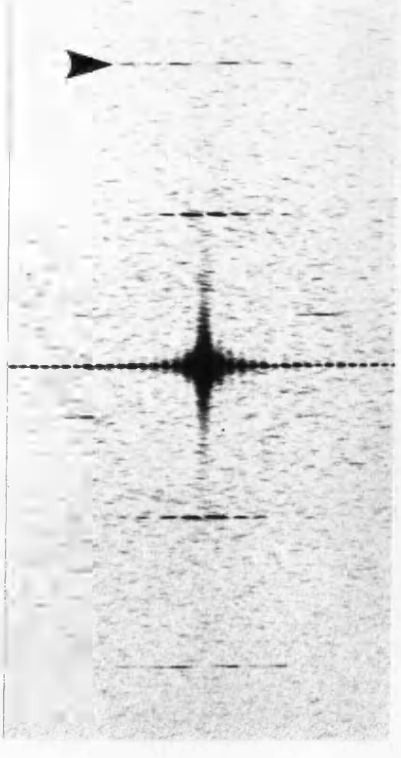

(f) Effect of coherence

The contrast in images of unstained biological specimens is almost completely phase contrast. For interference to occur between the scattered and unscattered beam the illumination must have good coherence. This is obtained by having parallel illumination. If the electrons are focused to a point on the specimen then it will be illuminated by a range of illumination angles within the converging cone. The value of this convergence angle will affect the degree of coherence of the illumination and therefore the extent of the phase contrast. The set of diffractograms shown below show the effect on the image of increasing, from left to right, the convergence of the illumination on a negatively stained catalase crystal.

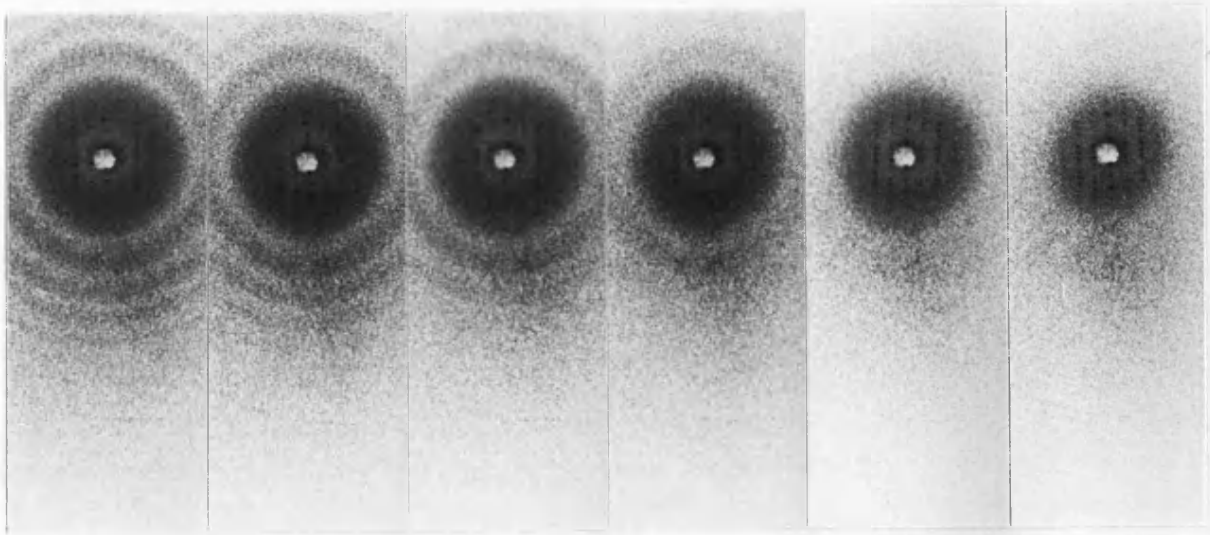

4. THE ULTRASTRUCTURE OF THE LIPOPROTEIN FROM *Escherichia coli* ENVELOPES

4.1 Introduction

The multilayered structure of the envelope of Escherichia coli was established by electron microscopy [68]. The characteristic 'tram-line' staining of a phospholipid bilayer showed that in these and other Gram-negative bacteria two enveloping membranes were present. The overall architecture of the envelope has been determined and a diagrammatic representation is shown below.

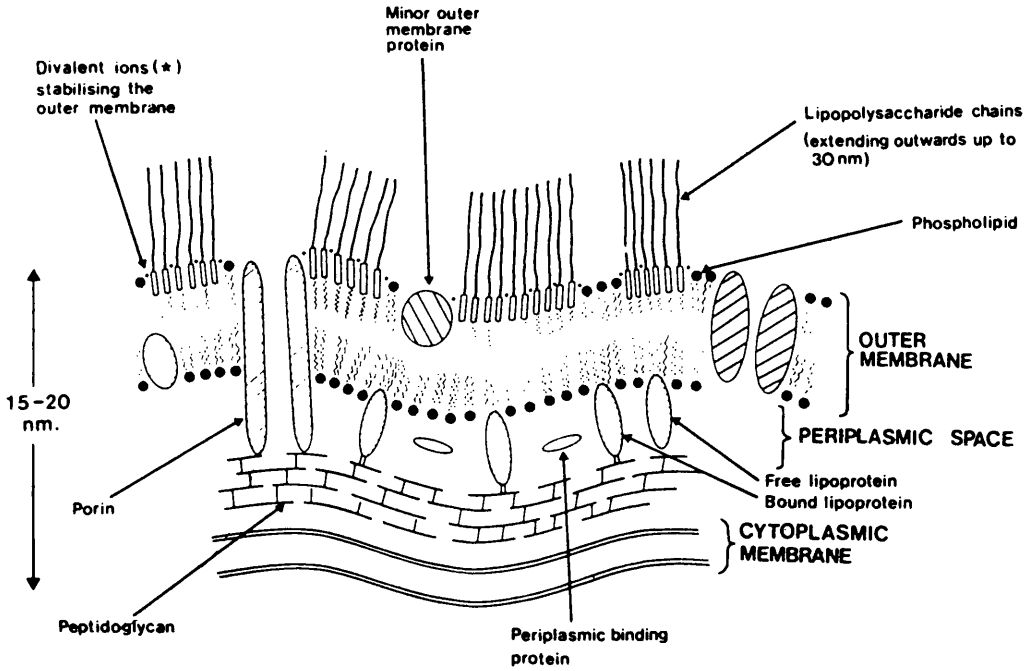

Reproduced with permission from " The Bacterial Cell Surface " by Hammond, S.M., Lambert, P.A. and Rycroft, A.N. (1984): Croom Helm, London.

The inner, or cytoplasmic, membrane provides the permeability barrier of the cell. It has proteins to control the passage of ions and molecules into and out of the cell. The apparatus for energy transduction and oxidative phosphorylation are also found in this membrane.

The outer membrane has a characteristic protein composition which is entirely different from that of the cytoplasmic membrane. It acts as a molecular sieve that allows the passage of small (up to about 600 daltons) hydrophilic molecules into the periplasmic space through channels in it made by the porin proteins.

The periplasmic space lies between the inner and outer membranes. Within this is the peptidoglycan layer, also known as the murein sacculus. Derived from murus, the Latin name for wall, this term is used as a trivial name for bacterial cell wall polymers [69]. Murein is a highly cross-linked structure, it is a complex polymer consisting of two amino sugars and at least four amino acids. The volume and shape of the cell is determined by this layer which may be considered as its skeleton and girdle. When a bacterium is put into a medium of high osmotic strength the plasmolysis that takes place shows the peptidoglycan layer remaining attached to the outer layer, whilst the inner membrane and cytoplasm shrink, unable to withstand an osmotic gradient. The peptidoglycan layer is attached to the outer membrane by covalent bonds with a lipoprotein, and

by strong ionic interactions with the porin proteins [70].

Isolated first by Braun [71], the lipoprotein is known both as Braun and murein lipoprotein. It is a small (7,200 dalton) protein that exists in a large number of copies, 7×10^5 per cell. About one-third of the population of this protein occurs in a form bound covalently to the peptidoglycan layer through the ε-amino group of its C-terminal lysine, whereas the rest occurs as free proteins. The N-terminal residue, cysteine, is modified in an unusual manner: its sulphydryl group is substituted with a di-glyceride, and its amino group is substituted with a fatty acid residue through an amide linkage. The amino acid sequence is known and a diagram of lipoprotein is shown below.

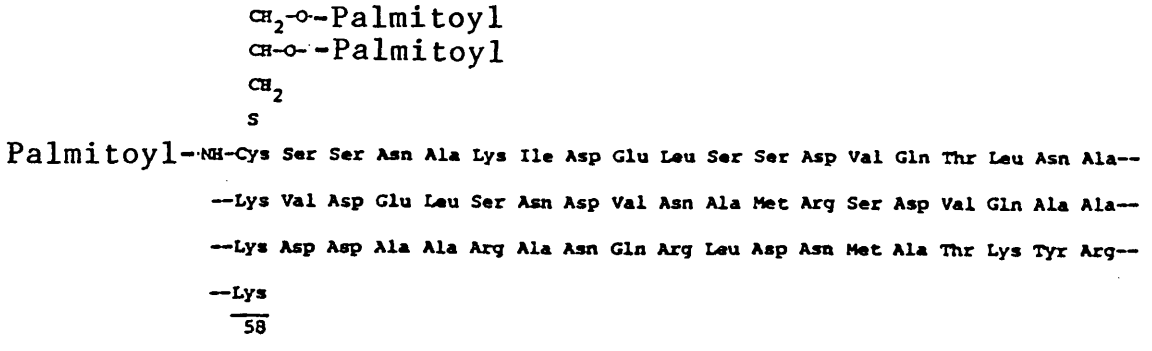

The purification methods used by earlier investigators would potentially denature the protein. They were based on extracting cell envelopes by boiling them in 4% sodium dodecyl sulphate (SDS), and fractionation with organic solvents. The purification and isolation techniques used for the lipoprotein preparation of this study [72], used the non-ionic, poly-disperse detergent octyl-oligo-oxyethylene (octyl-POE). The advantages of this were that the high critical micelle concentration (cmc) of this detergent allowed a faster removal by dialysis, the free lipoprotein was completely extracted at the relatively low temperature of 40 ^{o}C, and conventional methods of ion-exchange chromatography and gel-filtration could be used.

Paracrystals of the apparently native form were used to build a model for the molecular interactions of lipoprotein and this was related to its function in the cell envelope.

4.2 Materials and Methods

The lipoprotein was isolated from *E. coli* strain JA 221 lpp-/F' lac i^{q}/pKEN 125 [73]. The plasmid pKEN 125 contains the lipoprotein (lpp) gene under the control of lac promoter-operator fragments, and confers resistance to ampicillin. Grown to the end of the exponential phase in culture medium containing 50 μg/ml ampicillin, the lpp gene was induced with isopropyl-*beta*-D-thiogalactopyranoside (IPTG). Lipoprotein

content rose and after 15 minutes, when the cells were harvested, constituted 40% of the membrane protein.

The isolation and purification methods [72] used the detergent octyl-POE* to solubilise lipoprotein. Preparations for electron microscopy were made from a pure, 1 mg/ml (estimated by the method of Bradford [74]), solution of the protein in 1% octyl POE in water.

10 μl aliquots were dried onto carbon-collodion grids in the presence of different stains. Those used were 1% uranyl acetate, 1% PTA at pH 7.0, or 1% calcium acetate. These were examined at 80 kev.

Images were taken at a calibrated 25,000x magnification and diffraction patterns obtained with a 966 mm camera length, as determined with a thallous chloride standard. Accuracies were to within 2%. Low dose techniques were used, as described in section 3. Diffraction patterns were taken with 0.001 to 0.01 e^-/nm^2 and images with between 2 and 4 e^-/nm^2.

Computer generated patterns [75] were used to simulate positive staining at anionic and cationic sites present in the sequence of lipoprotein. Molecules were assumed to pack as extended linear molecules arranged in the paracrystal side-by-side and in register.

* The number of oxyethylene monomers in the hydrophilic residue was between 3 and 12, with a gaussian distribution peaking at 5.

4.3 Results

When dried in uranyl acetate the lipoprotein produced paracrystal as shown in the images below. The upper, low dose, image was obtained with the first 0.02 e^-/nm^2 and the lower image at high dose. The scale bar represents 100 nm.

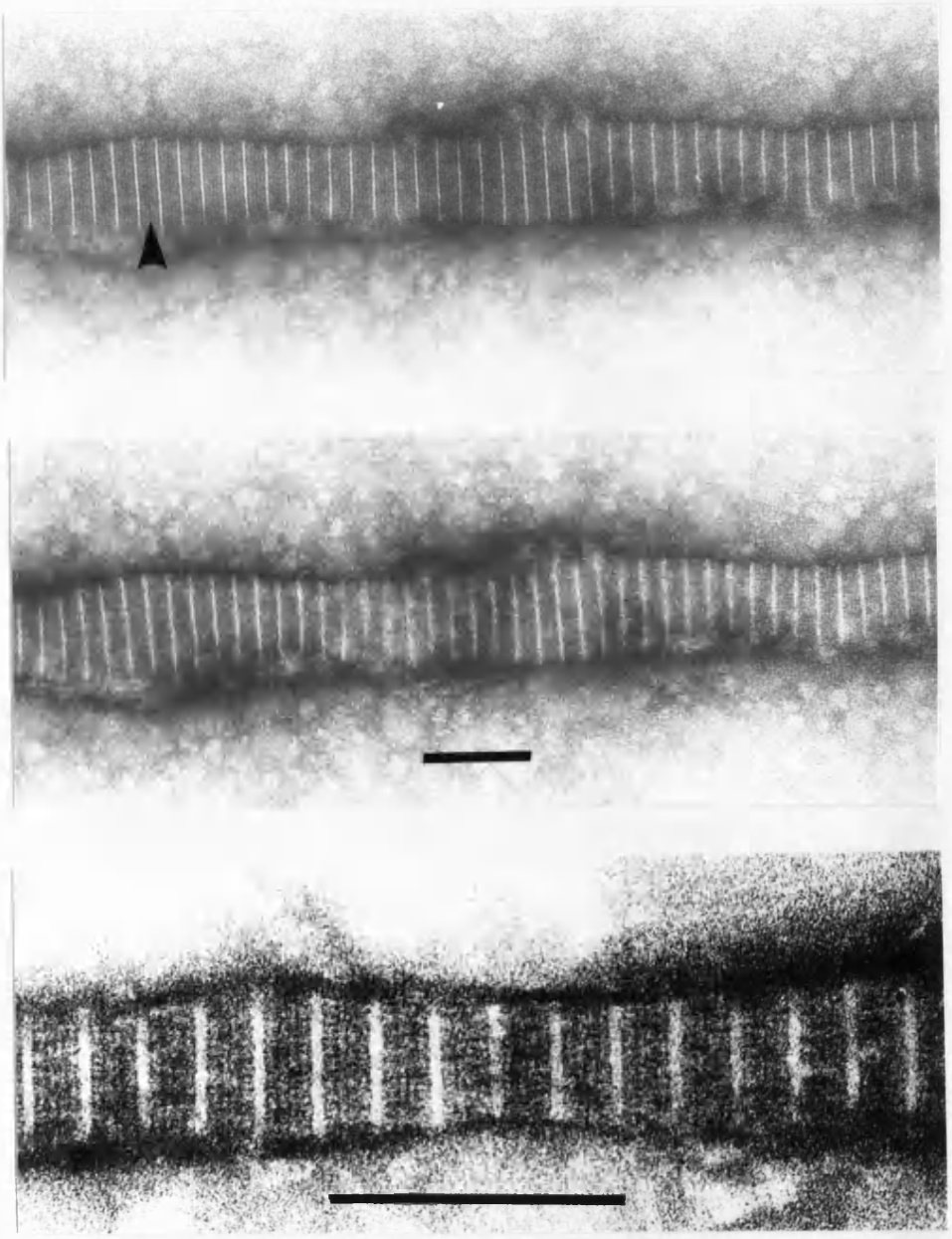

The periodicity was found to be 20 nm. The low dose image shows a bright, stain-excluding region 3nm wide, alternating with a darker banded region of 17 nm width. A thin dark line is seen at the mid position (arrowed) of this stained region, splitting the section into two 8.5 nm domains. The irradiated image shows the same periodicity, but the stain-excluding region has become wider at 4.5 nm, and the splitting of the stained band become less apparent.

The next image shows a paracrystal formed using PTA as the stain. The periodicity is also 20 nm and shows the stain-excluding region, but the pattern is different to the uranyl staining. The scale bar represents 100 nm.

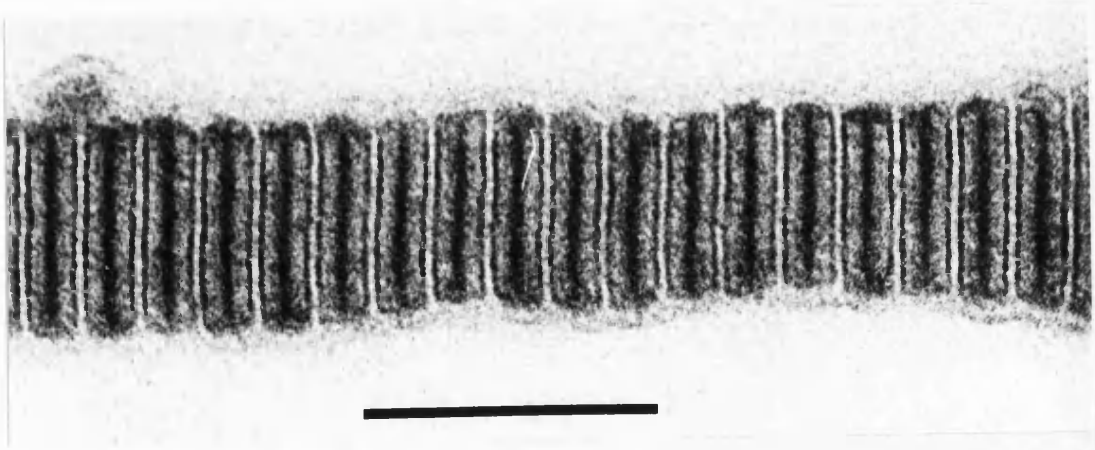

The position of the charged residues in the polypeptide was determined from the amino acid sequence [73], and a computer print out of the effect of staining on a head-to-head polarity of two molecules was made. The upper image on the next page shows the effect of an

anionic dye, such as PTA. The lower image shows the effect of a cationic dye, such as uranyl acetate.

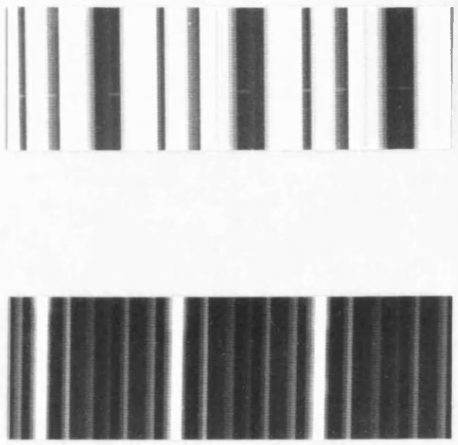

These simulations are aligned to bring the stain-excluding regions into register and were low pass filtered to reduce the effective resolution. Calculations based on other polarities of the molecules within the crystal did not reveal any similarity to the paracrystal images and were not included.

Attempts were made at drying the paracrystals into glucose, to obtain unstained images for high resolution investigation. The paracrystals were only found to form in the presence of salts and not when glucose dried or frozen-hydrated. Investigations with low atomic weight salts revealed that calcium acetate formed large paracrystals, up to 10 μm in diameter that were thin enough for electron microscopy. An area of a paracrystal is shown in the image on the next page. The

periodicity was again 20 nm with a low density region 3 nm across, but the banding pattern was less apparent. The scale bar represents 100 nm.

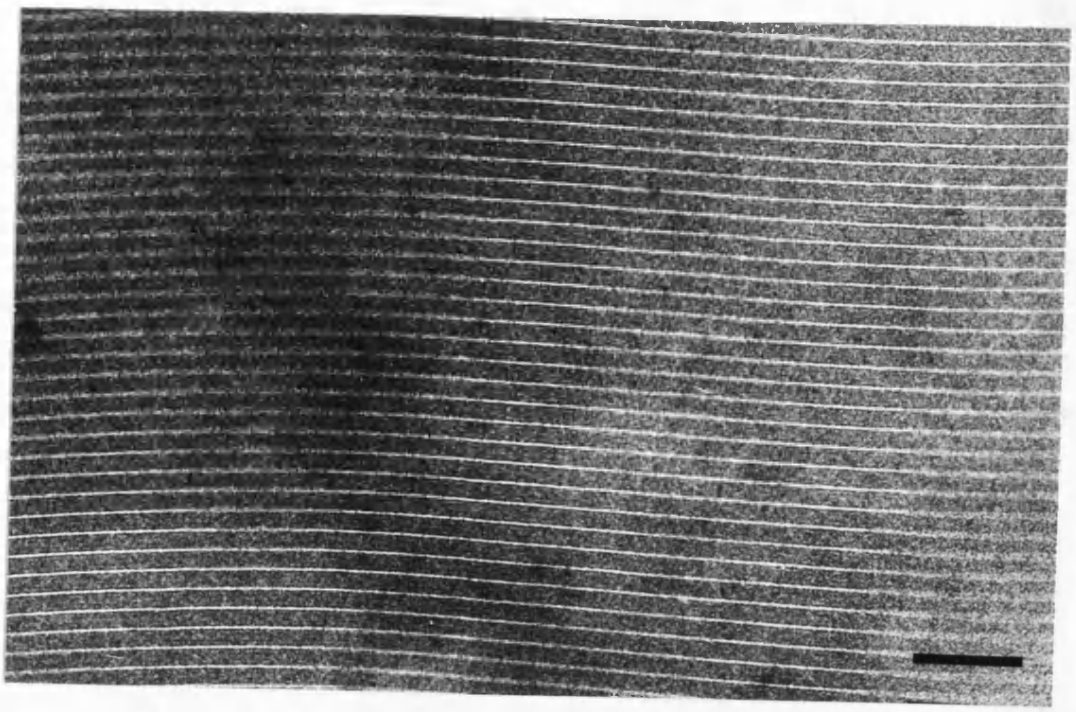

The electron diffraction patterns from such a paracrystal are shown below, aligned to the image above. At low exposure (0.001 e^-/nm^2), the pattern on the left shows the low angle 6th. order of the 20 nm repeat (arrowed) at 3.3 nm.

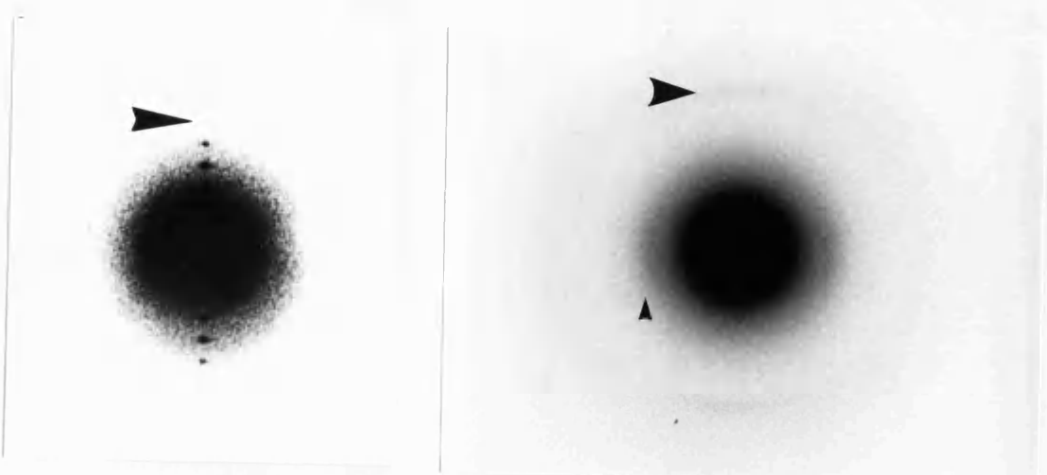

The diffraction pattern on the right (previous page) was taken after a dose of 0.075 e^-/nm^2 and is shown at a lower photographic enlargement. The dose received was optimal for high resolution information. The two sets of arcs (arrowed) measured periodicities at 1.0 nm equatorially (perpendicular to the 20 nm spacing), and 0.5 nm meridionally (parallel to the 20 nm spacing). Subsequent patterns from irradiated areas lacked the arcs.

As the calcium acetate paracrystals lacked detail in the image, a set of positive staining experiments were tried. The solution of lipoprotein was mixed with a low concentration (0.01%) of stain. After 15 minutes at room temperature the mixtures were dried with calcium acetate on the grid as before. The only stain found to give paracrystals by this method was PTA. These gave the same periodicity and pattern of staining as when the paracrystals were simply dried in this stain. They were, however, very thin. A low dose image (0.02 e^-/nm^2), as shown on the next page, revealed a 2 nm cross striation through some of the stained bands (arrowed and inset). The scale bar represents 100 nm and the inset is at 2.75x higher photographic enlargement.

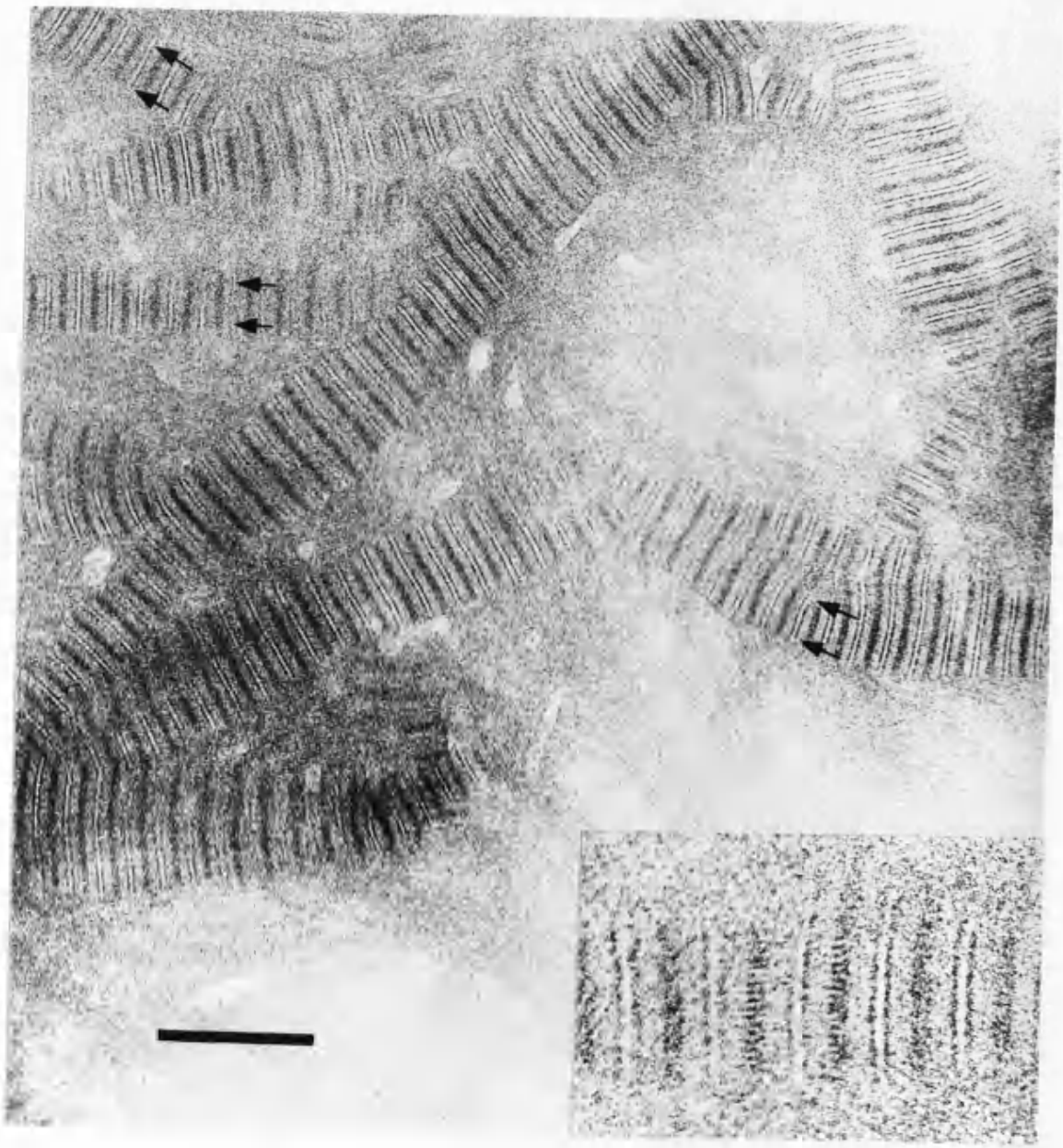

4.4 Discussion

The only direct indication of structural integrity in proteins which lack measurable biological activity, such as lipoprotein, consists in monitoring their spectral and chemical properties. Examination by circular dichroism of previously purified lipoprotein [71], indicated an alpha-helix content of over 80%. It is known that boiling in dodecyl sulphate tends to cause a shift of proteins into alpha-helicity [76], regardless of their native conformation [77]. Since the earlier purification procedure involved extraction into boiling SDS, it could not be excluded that the high alpha-helix content was artefactual and did not reflect the native configuration.

The purification procedures used for this preparation were developed to preserve membrane protein structure. They were shown not to affect the structure or function of other E.coli outer membrane proteins such as the porins [78]. This method gave, by circular dichroism, an alpha-helix content that was as high as previously found. The structural studies have revealed an organisation of the helices into coiled-coils that may have been degraded by more severe preparative methods.

Unlike earlier studies [79], the purified lipoprotein lacked the C-terminal lysine residue. The

observation appears to be of particular interest since this residue links the molecule to the peptidoglycan in the bound form. It is to be determined whether this is the result of processing in the cell by the exo- and trans-peptidases present in the bacterial envelope. Should this finding not be the result of protease activity during purification, which would be unlikely to cleave so specifically, it would reveal a significant modification of the molecule.

The negatively stained paracrystals from this preparation were very similar to those obtained by earlier methods [79] with which the overall organisation of lipoprotein molecules within the paracrystal is in good agreement. A schematic representation of the molecule as an alpha-helix of 58 amino acids and three palmitoyl acyl chains at the N-terminus is shown in (a) below.

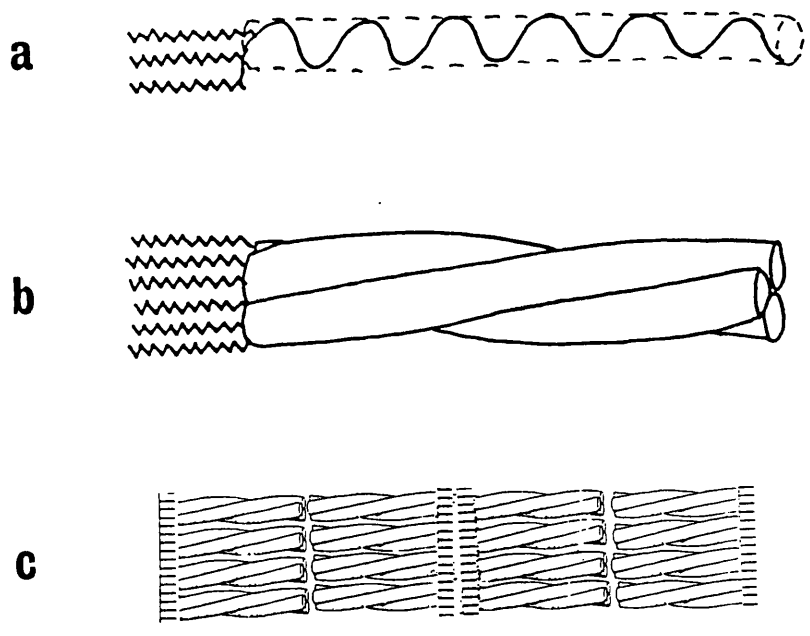

Figure (b) above shows three molecules packed in a coiled-coil, and (c) shows the head-to-head arrangement within the paracrystal. A visual summary of the computer modelled staining, with head-to-head polarity for the molecules in the paracrystal, is shown below.

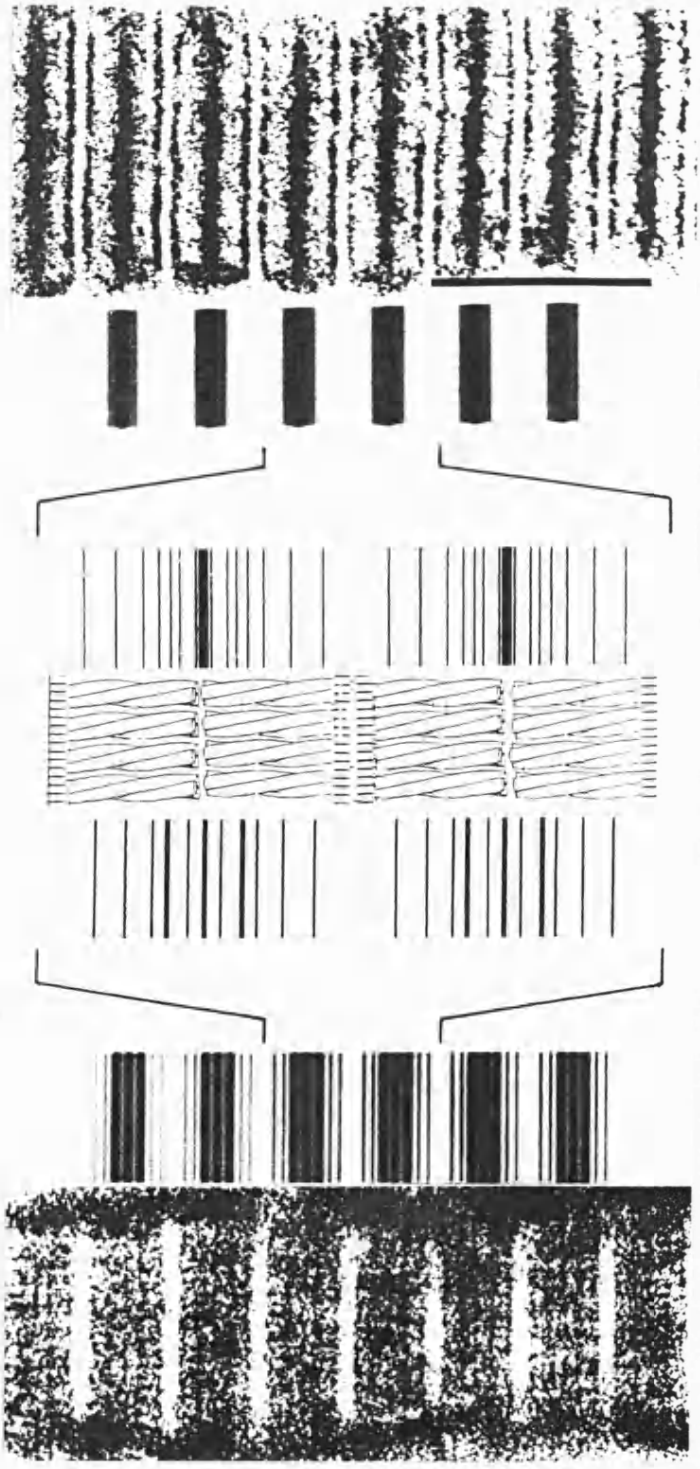

At the centre of the figure on the preceding page is the proposed model of the paracrystal. The alpha-helices are wound together as a three strand rope and arranged head-to-head with the acyl chains represented by two sets of parallel lines. The computer generated band patterns show where, on the basis of the protein sequence, amino acid residues which are negatively charged (lower half) and positively charged (upper half) would be expected to be stained with the heavy metal containing cation uranyl, or the anion phosphotungstate. The gap between the C-terminus groups as seen in the low dose images of the uranyl acetate stained paracrystals was added to the simulation 'by hand' as a negatively stained contribution to the otherwise positively stained pattern.

Further out from the centre are low pass filtered images, at about 3 nm resolution, adjacent to the correspondingly stained images for direct comparison at the same magnification.

An analysis of this type depends on the electron microscope images showing evidence of differential ionic positive staining. This was confirmed by the low concentration stain paracrystal that was formed by calcium acetate drying which showed an identical pattern to the PTA stain simulation.

The paracrystals formed in this study were different to those investigated earlier in that the periodicity was 20 rather than 22 nm [79]. This was

mainly due to the width of the stain excluding region, which was 3 nm rather than 4.6 nm. Being, presumably, a lipid/detergent phase the different detergents used, could explain the change in size. The earlier model of the paracrystal suggested a lipid bilayer structure for this region, which would be expected to produce a strong 0.42 nm equatorial intensity in the diffraction pattern [80]. That this was not found, and that the 3 nm width for the region would be too small to accommodate two palmitoyl chains in extended form in a bilayer, indicates that the fatty acyl chains are interdigitated and contain detergent.

The 0.5nm meridional arcs found in the electron diffraction patterns are at a spacing typical for coiled-coil alpha-helices [81,82]. This has been found by X-ray diffraction in a wide range of proteins such as alpha-keratin [84], paramyosin [85], tropomyosin [86], and bacterio-rhodopsin [87]. The last reference is of particular relevance here as the 0.52 nm spacing may be coming from a lipid phase. A 0.15 nm spacing would confirm a protein origin of the meridional, but this has not been observed. This, most probably, is because radiation damage removes such high resolution. The problem of displaying this reflection with X-rays is that the sample must be tilted relative to the beam. This is because of the sphere of interaction of diffraction (Ewald sphere). At the resolution obtained in most biological electron microscopy, the Ewald sphere for 80

kev electrons is satisfactorily considered as a flat plane. The maximum for a 0.15 nm reflection would, however, require a 4^{o} tilt, but the effect could only be considered as marginal.

The extension of the diffraction arcs, measured as the width at half intensity, gave a repeating unit size of 20 nm. There was no indication in the low angle patterns of any halving of the repeat that would be expected from the low dose negatively stained image and in this and the earlier models for the paracrystal. It can only be assumed that the carboxy-terminii and the predominantly positively charged end-residues form strong salt bridges, pulling the paracrystal together. This interaction may be overcome in the strongly acidic (pH 4.0) conditions of uranyl acetate paracrystal formation, allowing the entrance of stain into this zone. This may also explain the absence of a uranyl equivalent to the PTA, low concentration, calcium acetate paracrystal.

A choice exists for the number of alpha-helices which make up the complex. Two models have been advanced for lipoprotein on the basis of heptad* repeats in the amino acid sequence, a hexameric [88] and a dimeric coiled-coil [89] structure.

* This is a pattern of hydrophobic amino acid residues which occur at alternate intervals of three and four residues along the polypeptide chain. It is characteristic for alpha-helical, coiled-coil proteins.)

The 2 nm striations seen in the thin, PTA positively stained paracrystals would favour the latter, although in principle a three stranded 'rope' would also be possible. Theoretically, three and two stranded structures are equally feasible [89]. The majority of coiled-coils investigated have been found to be two stranded, e.g. tropomyosin [90], myosin [91], paramyosin [92], desmin [93], keratin [94], intermediate filament proteins [95], and the M-protein of Staphylococcus aureus [96].

The haemaglutinin glycoprotein of influenza virus has been shown by high resolution X-ray analysis to have a three stranded coiled-coil structure together with the heptad arrangement of hydrophobic residues [97]. This has also been described in serum protein fibrinogen [98], and very recently in an electron microscopy study of the GP17 tail fibre of the bacteriophage T7 [99]. These last authors point out that double stranded coiled-coil molecules are built in vivo into higher order assemblies and that in isolation they may be too flexible to give stable structures. This view is reinforced by an NMR (nuclear magnetic resonance) spectroscopy study of the mobile residues in the coiled-coils of epidermal keratins [100].

In E. coli envelopes, a stoichiometry of two free lipoproteins to one peptidoglycan bound molecule has been found [84]. This, by itself, suggests a trimeric arrangement in which one linked lipoprotein would be

associated with two in free form. A three strand arrangement would allow greater possibility for ionic cross-bridges between side chains of the alpha-helices. Evidence of the state of aggregation from gel-filtration and ultracentrifugation studies have failed because of nonspecific association caused by the hydrophobic lipid moiety. Genetic manipulation of E. coli has produced a lipoprotein devoid of 7 amino acids from the N-terminus and lacking the lipid domain [101]. This protein was localised in the periplasmic space with a minor fraction bound to the peptidoglycan. Chemical cross-linking showed that this lipoprotein existed in solution as a trimer.

A diagram of the proposed model of lipoprotein, associated with the peptidoglycan layer through the protein domain and with the outer membrane through the lipid domain, is shown below.

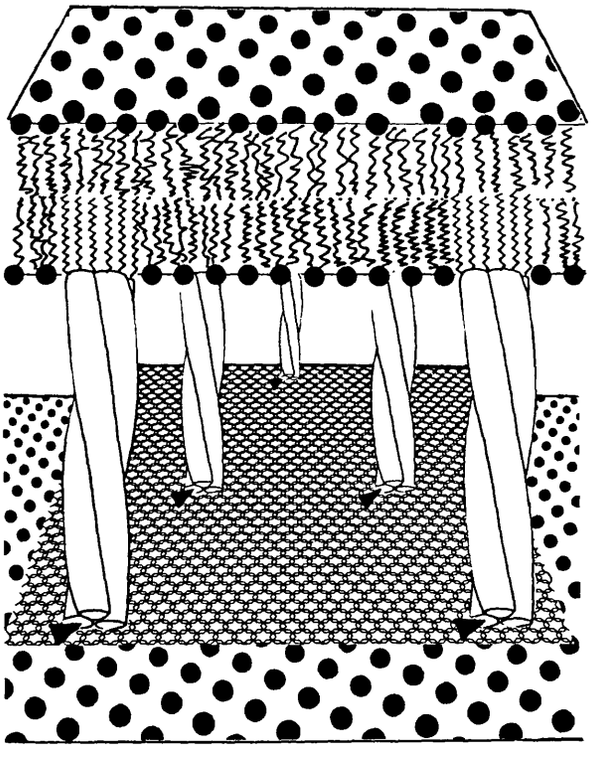

Although it was possible to make some predictions of the high resolution structure of the molecule, because the order could not be improved by using unstained methods, any further work was limited for electron microscopy. It may be possible to improve the orientation by forming the paracrystals in the presence of a high magnetic field. This method has been shown to align filamentous viruses (F. Booy, personal communication). Another approach would be to iodinate the tyrosine in the molecule. This has been shown to increase the rate of aggregation of soluble collagen and may allow crystallisation.

The next section of the thesis investigates thin 3-dimensional crystals, some of which allow high resolution determination.

5. STRUCTURAL STUDY OF RESTRICTION ENZYME-DNA COMPLEXES

5.1 Introduction

Of the recent advances made by molecular biology, gene manipulation or genetic engineering has enormous potential. The Watson-Crick model of DNA revealed the genetic information of a cell to be stored in a linear code of paired bases along the molecule [102]. The ability of a protein to recognize a specific sequence of bases along the DNA lies at the heart of many fundamental biological processes. One of the most intriguing questions in molecular biology today is whether the details of these individual recognition mechanisms will form a small number of simple patterns that will lead to a general recognition code.

The development of genetic engineering depended on a method of cutting the duplex DNA into discrete fragments, separating the fragments and attaching them to vectors which are then taken up by the host and incorporated into its genetic make-up. The discovery that bacteria could protect themselves against foreign DNA was shown by the restricted infectivity of bacteriophage on *E. coli* strain K as compared to other strains [103]. The phage DNA was shown to degraded soon after injection and the responsible enzyme is called a restriction endonuclease or restriction enzyme. The restrictive host must, of course, protect its own DNA from the effect and

so its DNA is modified. Modification involves methylation of certain bases at a very limited number of sequences within the DNA which constitute the recognition sequences for the restriction endonuclease. The enzyme of E.coli K proved to have a complicated mode of DNA scission with an initial single stranded cut being made a random distance from the recognition site and requiring a second cut to complete the double strand break [104].

A second type of restriction enzyme was first found in Haemophilus influenzae Rd which had a much simpler mode of action [105]. These type II enzymes recognize a particular target sequence and break the polynucleotide chains within, or near to, that sequence to give rise to discrete DNA fragments of defined length and sequence. This is of fundamental importance in the manipulation of DNA: the type I restriction enzymes while recognising specific nucleotide sequences, their cleavage sites are non-specific. The fragments can be studied by gel electrophoresis and the band patterns obtained can be characterised and separated.

The nomenclature of the many restriction enzymes uses the species name of the host organism identified by the first letter of genus name and the first two letters of the specific epithet to give a three-letter abbreviation in italics: for example,

Escherichia coli = Eco

Haemophilus influenzae = Hin.

The following alphabetical letter either denotes the

strain or a virus or plasmid derived origin. The final Roman numeral represents the ordering (generally chronological) of a strain that has a number of different restriction and modification systems. This should not be confused with the classification of restriction enzyme type.

Eco RV endonuclease is a type II restriction enzyme. It is a dimeric enzyme of molecular weight 2 x 29,000 daltons. It cleaves, in the presence of magnesium ions, double stranded DNA at the sequence 5'-GAT*ATC. The asterisk identifies the point of scission which produces blunt ended fragments [106]. It has very high specificity and is an attractive system for structure determination of protein-DNA interactions. Large quantities of the pure enzyme have become available through the construction of an inducible overproducing strain [107]. Crystals of the enzyme have been grown suitable for structure determination by X-ray diffraction [108].

In this study the very thin crystals that formed from complexes of the enzyme with small DNA oligonucleotides are shown to give high resolution information for the orientation of the DNA within the enzyme dimer. A comparison is made of a low resolution reconstruction of the enzyme with the X-ray map and an investigation made into a full analysis at atomic resolution of structure.

5.2 Materials and Methods

5.2.1 Specimen Preparation

(a) Growth of Culture

Escherichia coli 1100 (pRK248, pACM, pTZ115-14) cultures were obtained with the permission of their constructor (Dr. M. Zabeau, Plant Genetic Systems, Ghent, Belgium) from Dr. S. Halford (Department of Biochemistry, University of Bristol).

The three plasmids carried by this strain confer the following properties:

pRK248 has a temperature sensitive c1 repressor (C1 857) and gives tetracycline resistance.

pACM has the *Eco RV* methylase and gives chloramphenicol resistance.

pTZ115-14 has the *Eco RV* endonuclease under the *lac* promoter control and gives ampicillin resistance.

This overproducer should yield about 1 mg of endonuclease per litre of growth medium. The following method was used to provide enzyme for structural studies.

6 litres of the growth medium (L-Broth) were made up in water.

Growth medium

Bacto-Tryptone	10 g / litre
NaCl	10 g / litre
Yeast Extract	5 g / litre

5 litres of this was dispensed into 10 conical flasks (2 litre), 500 ml in each. The remaining litre was dispensed, 100 ml into 5 conical flasks (250 ml) and 100 ml into 5 screw top bottles (250 ml). 1.5 g of agar was added to each of the bottles to give 1.5 %. The flasks were stoppered and all the media were autoclaved at 15 lbs / ins^2 for 15 minutes.

Stock solutions of antibiotics were made:

Ampicillin	40 ml of	25 mg/ml	in water
Chloramphenicol	10 ml of	25 mg/ml	in ethanol
Teracycline	20 ml of	12.5mg/ml	in 1:1 water:ethanol

These were filter sterilized with a 0.2 μm Millipore filter and added to the medium which had cooled to room temperature. The volumes added were calculated to give a concentration in the medium of Ampicillin 0.1 mg/ml, Chloramphenicol 0.02 mg/ml and Tetracycline 0.005 mg/ml.

The bottles were sufficient for pouring four Petri-dishes. The cultures were streaked onto the surface of the cooled gel with a sterile platinum loop to give single colonies. They were put into a 30 ^{o}C incubator for 24 hours. The plates were stored at 4 ^{o}C for about two

months, when the colonies were transfered onto new media. Single colonies were picked off the surface with a sterile needle and used to inoculate the 250 ml flasks. They were grown with shaking at 30 °C for 24 hours. During this time the other flasks were also kept at 30 °C and the clarity of the medium checked to show that the medium and antibiotic, were sterile.

After 12 hours, 20 ml of culture was then removed from each of the flasks and transferred to empty sterile 50 ml conical flasks. They were incubated for 12 hours at 42 °C with shaking. The content of Eco RV was assessed by SDS gel electrophoresis of the whole cell extracts against an Eco RV standard.

On the basis of the enzyme content a culture was chosen and 2 ml aliquots from this flask were used to inoculate 5 of the 2 litre flasks. They were grown for 12 hours at 30 °C with shaking. The remaining culture was dispensed 1 ml at a time, aseptically, into sterilised Eppendorf tubes containing 0.25 mls of glycerol. These were sealed, shaken to mix the glycerol and frozen in liquid nitrogen. They were then stored in a -70 °C deep-freeze supervised by Dr. J. Beeching, Plant Sciences, University of Bath*.

An incubating cabinet with orbital shaker capable of taking 5, 2 litre flask was warmed to 42 °C.

* Permission must be obtained from Dr. Zabeau for the use of these colonies.

The remaining 5, 2 litre flasks were heated on a water bath to 55 ^{o}C. After the 24 hour growth the cultures had become turbid. Equal volumes of the 55 ^{o}C media were added to the culture flasks to quickly shift the temperature. They were promptly transfered to the 42 ^{o}C incubator and then grown with shaking for the next 12 hours. The cells were harvested by centrifugation at 10,000 rpm for 10 minutes. A combined cell pellet was stored in a deep-freeze at -20 ^{o}C.

(b) Purification of enzyme.

Unless otherwise stated this was performed in a cold room at 4 ^{o}C using Buffer A to which NaCl and other chemicals were added as indicated.

Buffer A : 20 mM K_2HPO_4

1 mM EDTA

10 mM Mercaptoethanol

pH 7.0

The cells were thawed and resuspended in 50 ml of Buffer A + 0.8 M NaCl and 0.05 mM PMSF. This was sonicated for 6, 2 minute periods. The cell debris was removed by spinning at 100,000 g for 30 minutes. The supernatant was added to 3 volumes of Buffer A bringing

the salt concentration to 0.2 M. (The high salt aids extraction during sonication.)

The first purification step was by phosphocellulose chromatography [109].

2 g of Whatman P11 was suspended in 100 ml of 0.2 N HCL diluted 1:1 with 95% ethanol and stirred gently for 30 minutes at room temperature. The slurry was allowed to settle and the supernatant aspirated to remove the fines. The resin was collected by vacuum filtration and washed 3 times by suspension in 100 ml of water. The pH was adjusted to near neutral with 1.0 N NaOH and the resin was suspended in 100 ml of 0.1 N NaOH. It was stirred gently for 30 minutes at room temperature, collected by filtration, and suspended in 100 ml of 1 mM EDTA. The resin was then given three cycles of stirring for 15 minutes, filtering and washing in water. The pH was adjusted to near 7 with 1 N HCL and it was filtered and resuspended in Buffer A + 0.2 M NaCl. The pH was carefully adjusted to 7.0 before pouring the column, since many column volumes of diluted buffer are required to equilibrate the pH of the packed column. A 10 ml column was prepared.

The supernatant from the centrifugation, diluted to 200 ml, as described above,was loaded onto the column at 40 ml / hour (about one drop every three seconds). The column was then washed with Buffer A + 0.2 M NaCl and samples of the supernatant were assayed by measuring the optical density at 280 nm until the level

returned to the baseline. Elution of the Eco RV was with a linear gradient of Buffer A + 0.2 M NaCl up to Buffer A + 0.8 M NaCl, 25 ml of each. Fractions were collected at 0.5 ml and assayed by SDS gel electrophoresis. The peak, around 0.5 M NaCl, was pooled (10 ml). The column was used just once and discarded.

The final chromatography step was with a blue-dextran sepharose column.

2 g Reactive Blue 2-Sepharose CL-6B (Sigma Cat. No. R-8752) was swollen in Buffer A + 0.025 M NaCl overnight. It was then filtered and washed with the same solution twice and poured into a column of about 15 ml. The pool from the phosphocellulose column was diluted with 20 volumes of Buffer A and loaded at 40 ml / hour onto the column of Blue Sepharose. After washing with the same buffer, the enzyme was eluted with a linear gradient of Buffer A + 0.025 M NaCl up to Buffer A + 0.4M NaCl, 20 ml of each, at 20 ml / hour. Fractions were collected at 0.5 ml and assayed for protein by spectrophotometry at 280 nm. The pooled peak of 5 ml was adjusted to 70% ammonium sulphate by adding the solid. This precipitated the protein and it was centrifuged with a bench minifuge for 5 minutes. The supernatant was discarded and the pellet was stored at -20 ^{o}C.

The column was washed with Buffer A + 0.001% sodium azide.

(c) Crystallisation with Oligonucleotides

Crystallisation was by the vapour diffusion method where the solution is placed within a controlled environment so that solute is either gained or lost in order to give a slow precipitation.

Square glass plates with nine circular depressions, or wells, (Polysciences Inc., U.S.A.) were cleaned and siliconised. A mark was made at the top left-hand corner to permit identification.

The stored enzyme precipitate was thawed and resuspended in 0.25 ml of following buffer:

10 mM HEPES

175 mM NaCl

1 mM EDTA

1 mM DTT

pH 7.5

This was then dialysed against 1 litre of the same buffer at 4 ^{o}C for 6 hours with Spectropore dialysis tubing No.6., having a molecular weight cutoff of 10,000. The protein concentration was adjusted to about 7 mg / ml (an optical density at 280 nm of 11.0). The restriction enzyme was dispensed as 10 μl aliquots into the crystallisation wells.

The cognate decanucleotide 5'-CCGATATCGG (recognition sequence of Eco RV underlined), 1 mg of which was obtained from Dr. B. Sproat (E.M.B.L., Heidelberg, West Germany), was used to form complex crystals. A 1 mg / ml solution was made up in water (an optical density at 260 nm of 20.0). It was added in 1 µl increments, from 1 to 9 µl, to the 10 µl of enzyme in the wells (going from left to right and down). Water was added to the wells to bring the final volume of each to 20 µl. This reduced the salt concentration to be close to that which would precipitate the enzyme. The plate was placed in a standard plastic 9 cm Petri-dish with 5 ml of water around it and the dish was sealed with silicone grease and left undisturbed at room temperature until crystals formed. A photograph of such a preparation is shown below.

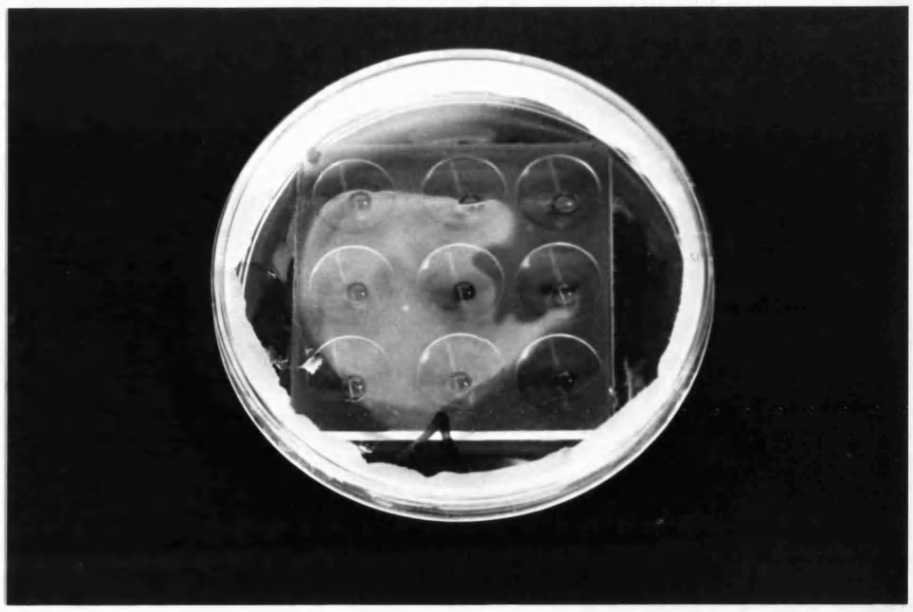

A slightly different set of conditions was used to form crystals with the non-cognate octanucleotide 5'-CGAATTCG. The salt concentration was adjusted to 150 mM and polyethylene glycol (molecular weight 10,000) was added to give a concentration of 0.8%. The vapour diffusion this time was against 100mM NaCl at room temperature.

The tri-osmium cluster compound was prepared by Dr.W.Jahn (Max Planck Institute for Medicine, Heidelberg), the specific decanucleotide was derivatised and purified by Dr.B.Sproat (EMBL, Heidelberg). The crystallisation procedure was as for the decanucleotide

5.2.2 Electrophoresis

Proteins were separated by sodium dodecyl sulphate polyacrylamide gel electrophoresis (SDS-PAGE) using a discontinuous buffer system and continuous gradient gel of 8-25 %, following the procedures of the PhastGel (Pharmacia Ltd.) system.

Whole cell extracts of the E. coli cultures were obtained by centrifuging, with a bench minifuge, 1 ml samples for 1 minute. The pellets were resuspended in 200 µl sample buffer: 10 mM Tris/Cl

1 mM EDTA

2.5 % SDS

5.0 % Mercaptoethanol

.01% Bromophenol Blue. pH 8.6

They were mixed well and heated for 5 minutes on a boiling water bath. Debris was centrifuged out with a bench minifuge. 1 µl samples were applied to the 8-25 gels together with standards. The electrophoresis took about 30 minutes and the gel was stained with Coumassie Brilliant Blue and destained in 30 % methanol/10% acetic v/v acid.

DNA was separated by agarose gel electrophoresis using a 1.1% agarose concentration. Lambda phage DNA was digested with the purified Eco RV at serial dilutions of the enzyme in

20 mM K_2HPO_4

200 mM NaCl

10 mM Mercaptoethanol

1 mM EDTA

50% Glycerol pH 7.0

1 µl of the enzyme was mixed with 1 µg of DNA in 3.5 µl to this was added 4.5 µl of water and 1 µl of the buffer

500 g/ml Bovine serum albumen (BSA)

500 mM NaCl

500 mM Tris/Cl

100 mM $MgCl_2$

10 mM DTT pH 8.0

After 1 hour at 37°C the digestion was stopped with a 5 µl sample of the buffer of 40% Sucrose, 100mM Tris/Cl (pH 8.0), 100mM EDTA and .05% Bromophenol Blue.

After a 1 minute centrifugation the sample was loaded onto the gel. The gel was run with Tris-Borate-EDTA buffer at 150 volts for 2 hours. When the electrophoresis was complete the gel was stained with a 1 µg/ml concentration of ethidium bromide for 15 minutes. The gel was destained in distilled water for 5 minutes and examined with an ultra-violet viewing box. Photography was with a Polaroid Land camera with 665 film.

5.2.3 Electron microscopy

The crystal preparations were first transfered from the wells using a 50 µl micropipette, to an Eppendorf tube. The pipette tip was used to break up the cluster of crystals by flushing the solution through it a few times. A 5 µl drop was placed on a carbon-collodion coated grid and then preparative methods as described in section 3 were used.

5.2.4 Computing

Micrographs to be processed were selected by optical diffraction. Selected areas were scanned with an Optronic P-100 rotating drum microdensitometer. Calculation of the Fourier transforms and indexing the

reciprocal lattices for peak selection was carried out by the method of Leonard et al. [111].

5.3 Results

5.3.1 Enzyme purification

The 5 litres of culture produced a wet weight of 5 g of cells. The image below shows the result of the PhastGel electrophoresis of the samples from the different starter cultures. The left hand lane shows the molecular weight standards which were, from the bottom (origin) to the top; Phosphorylase b:94,000, BSA: 67,000, Ovalbumen: 43000, Carbonic Anhydrase: 30,000, Soya Bean Trypsin Inhibitor: 20,000 and alpha-Lactalbumin: 14,400. The 4th. lane from the left shows purified Eco RV: 29,000 monomer molecular weight. The 2nd. and 3rd. lane show the proteins of a colony before and after inducing the enzyme at 42 ^{o}C. The other lanes show four other induced colonies, all of which show a strong band at 29,000 MW.

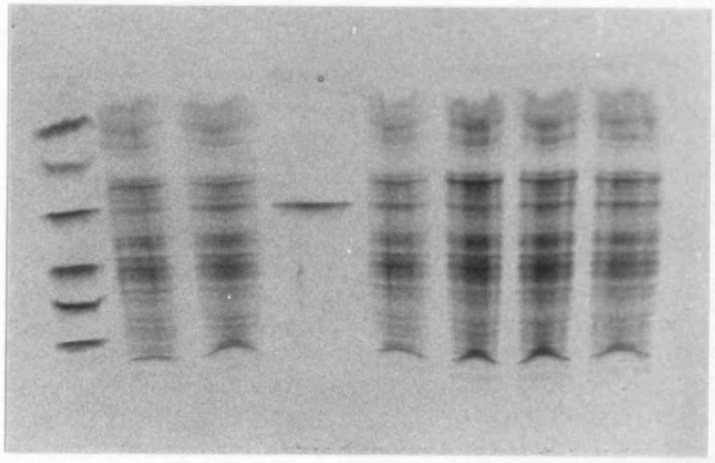

The next image shows the effect of the purification steps on the purity of the enzyme. The left lane is again the same set of standards. The 4th. lane shows the proteins present in the supernatant from the sonicated and centrifuged cells. This was loaded onto the phosphocellulose column and the peak eluent from this is shown in the 5th. lane. The eluent from the sepharose-blue column is shown in the 2nd. lane, with a 10x dilution in the 3rd. The 6th. and 7th. lanes show a 10x dilution of the 1st and 2nd.

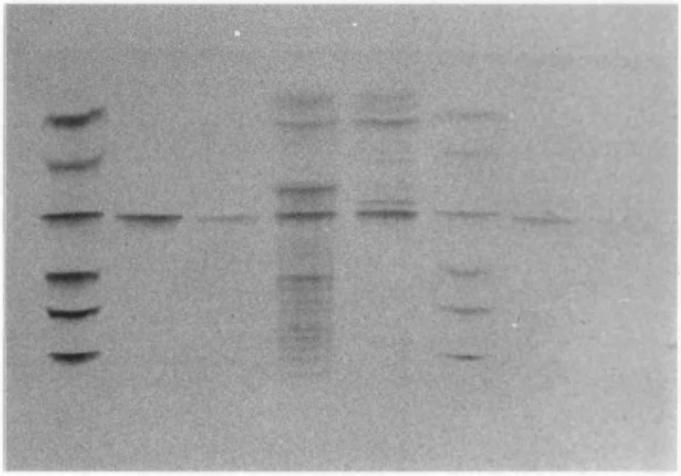

The yield of purified enzyme as estimated from the optical density was 4.5 mg. For digestion and binding studies about 1 mg of this was diluted to 0.05 mg/ml in a buffer in which the enzyme could be stored deep-frozen.

20 mM K_2HPO_4

200 mM NaCl

10 mM Mercaptoethanol

1 mM EDTA

50% Glycerol pH 7.0

The activity of the enzyme is reported to be 1 unit per 0.05 ng [112]. This gives a concentration of 10^6 units/ml for the stored solution*. The photograph below shows from right to left the digestion of Lambda DNA by successive tenfold dilutions. The extreme left is a DNA standard. The 2nd. lane from the left, a 1000x dilution shows incomplete digestion with streaking of the high molecular weight DNA at the top (origin). The 100x dilution, 3rd. lane, shows complete digestion. This indicates that the activity falls short of the optical density derived value by about a factor of three. This is in line with the observations of other investigators (S. Halford, personal communication).

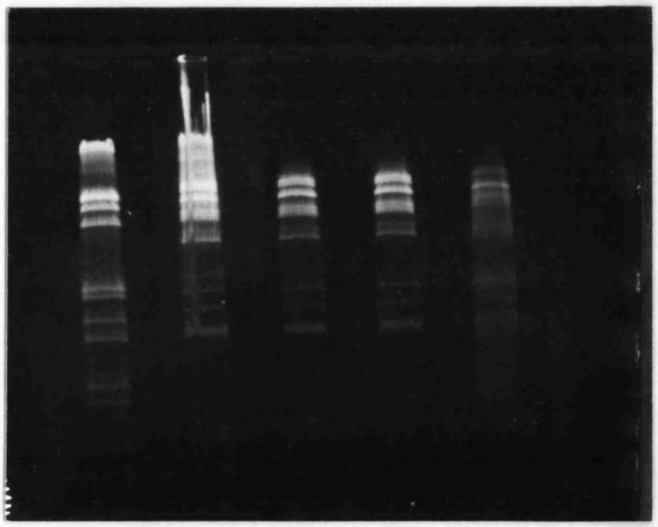

* Eppendorf tubes containing this dilution, a revised estimate of 300 units/ 1 can be found in the -70 °C deep-freeze under the supervision of DR. J. Beeching, Dpt. Plant Sciences, University of Bath.

5.3.2 Electron Microscopy

(a) Non-specific binding to DNA

Mixed with an excess of the enzyme, DNA was shown by negative staining to become coated. The first image below shows Eco RV mixed in a 20x excess, weight for weight, with Lambda DNA (The molecular weight of the dimer is approximately 100x that of a base pair. Thus a 10x excess will have the dimer spanning 10 base pairs [3.4 nm], and a 20x excess would only give a 5 base pair space for each enzyme dimer). The scale bar represents 100 nm.

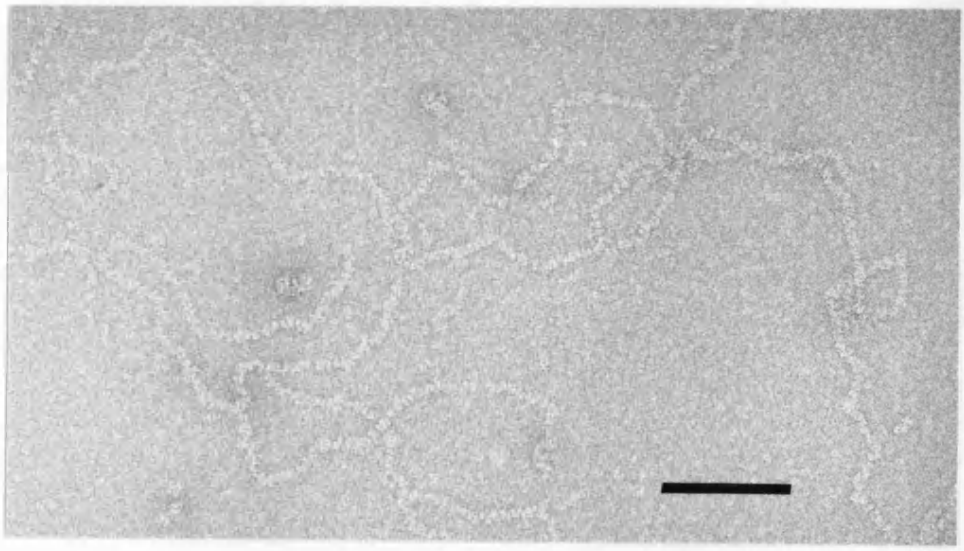

The maximum width of the coating was found to be 6 nm and the minimum spacing along the thread, 3 nm. The enzyme was mixed with a circular DNA, a plasmid pEMBL8. With the same 20x excess, the measured length of the DNA was the same as assuming a 0.34 nm base pair separation of 'B'

DNA. An image from this preparation is shown below. The scale bar represents 100 nm.

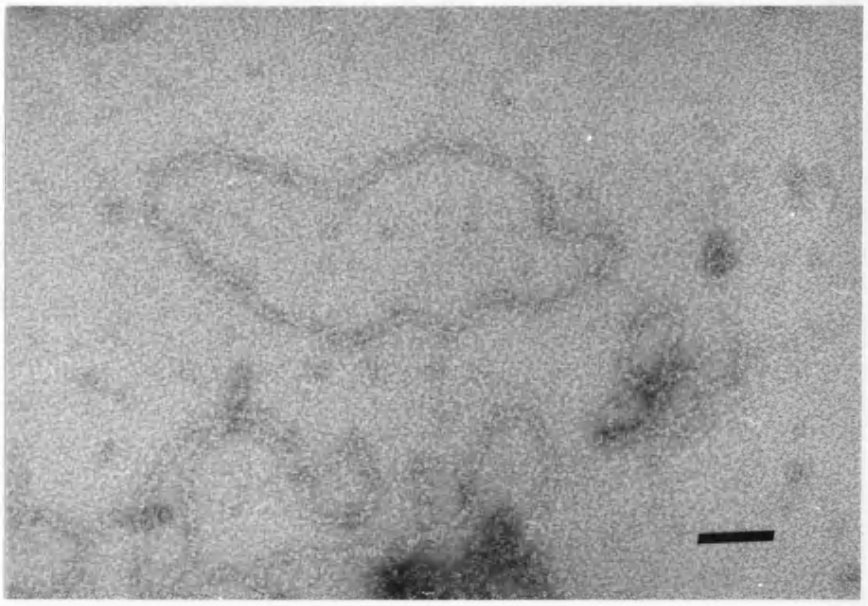

(b) Crystals with a specific decanucleotide

Eco RV complexed with 5'-CCGATATCGG gave crystals in wells with a protein to DNA weight ratio around 10:1. The crystals which formed were observed negatively stained with uranyl acetate, as shown in (a) on the next page. This projection of the crystal gave a unit cell dimension of a = 5.4 nm, b = 6.4 nm, and although the edges of the crystal were irregular the crystals were essentially rectangular, up to 5 μm across. The long dimension of the crystal was parallel with the long unit cell axis. The scale bar represents 500 nm. Figure (b) shows the optical diffractogram of (a) aligned with the crystal. The scale bar indicates a distance from the origin of a 2 nm spacing. (c) shows the computer calculated, noise filtered, image of the projection. The white areas show regions of protein, contoured to stain.

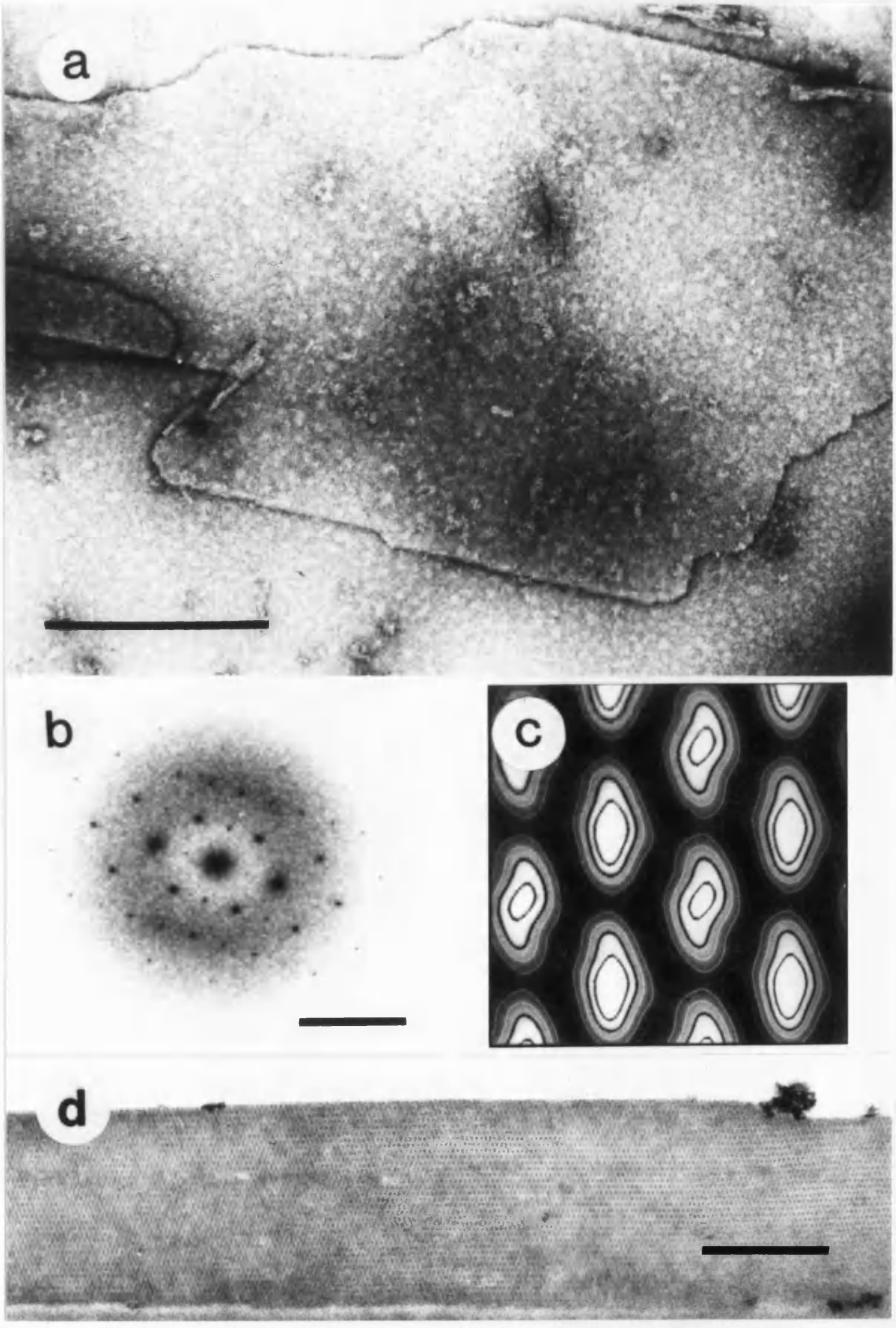
a
b
c
d

Image (d) shows a section of a plastic embedded crystal. This views the crystal from the side, along the 5.4 nm axis. The unit cell dimensions of this view are b = 6.4 nm, c = 17 nm. The scale bar represents 100 nm.

When dried in glucose the crystals gave, with a dose of 0.01 e^-/ nm^2, diffraction patterns which showed high resolution reflections out to 0.3 nm, as seen in the figure (a) on the next page. The scale bar represents a spacing of 0.5 nm. The unit cell dimensions are a = 5.6 nm and b = 6.4 nm (shown respectively, vertical and horizontal on the page) . Both axes show evidence of systematic absences on the odd orders. This would be good evidence for an asymmetric feature within the unit cell. Patterns show good mirror and Friedel symmetry.

Figure (b) on the next page shows a low dose diffraction pattern from a frozen, hydrated crystal. This shows reflections out to 0.28 nm but the mirror symmetry is broken between the top and bottom halves. A small amount of tilt about this axis would be expected to produce this. The unit cell in this case was the same as was found with the glucose preparations, a cell axis size ratio of 0.88 . The ratio found for negatively crystals was 0.84 because of a small reduction in the 'a' axis.

Attempts were made to obtain low dose images of unstained crystals but these were not successful, presumably because of movement in the multilayered crystal during the exposure.

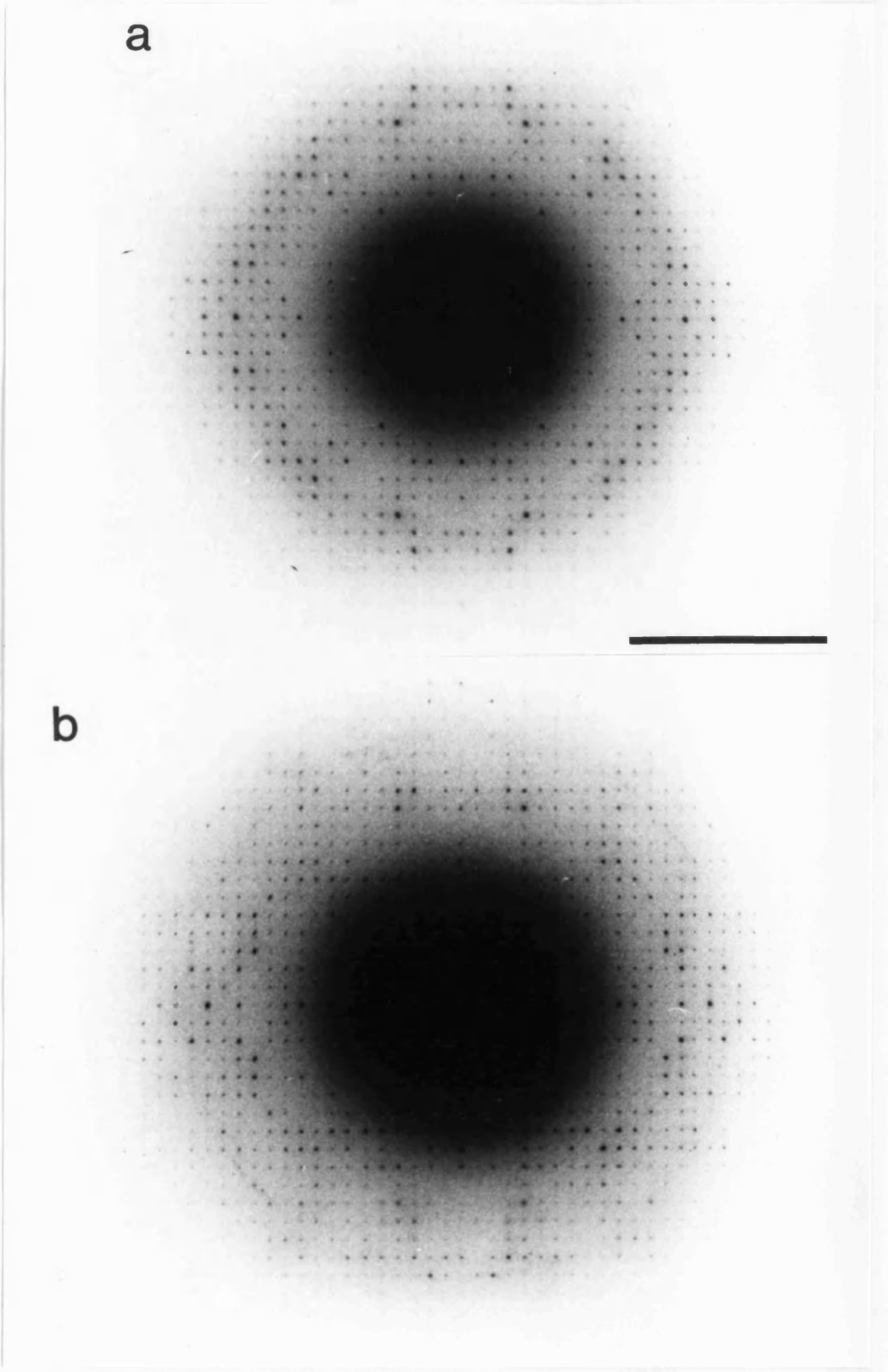
a
b

(c) Crystals with a non-specific octanucleotide.

The Eco RV complexed with 5'-CGAATTCG double stranded DNA (this contains the recognition sequence of Eco RI) also gave thin crystals. A uranyl acetate, negatively stained image of a region of one of these crystals is shown in figure (a) below. The scale bar represents 250 nm and the unit cell was a = 7.4 nm and b = 8.4 nm.

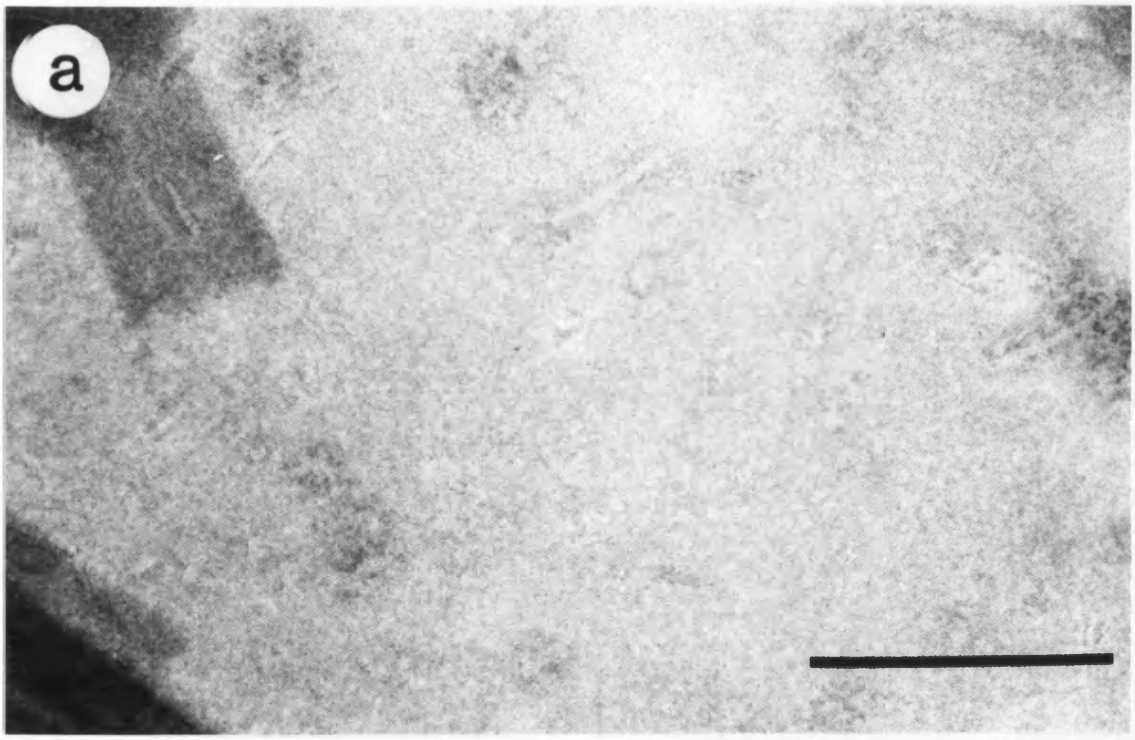

An optical diffractogram of the image is shown in (b) on the next page, with the scale bar representing a spacing of 2 nm. Figure (c) shows the computer calculated filtration of the image. The regions of stain is shown in black. The multilayered nature of the crystal make it impossible to identify the molecules because of super-positioning. In figure (a), at the top left hand corner a dark rectangular area can be seen. This is an area

of the crystal which has become detached and dried onto its surface in the stain. This property of the crystal to dissociate into sheets could be increased by diluting the crystallising medium twofold with water.

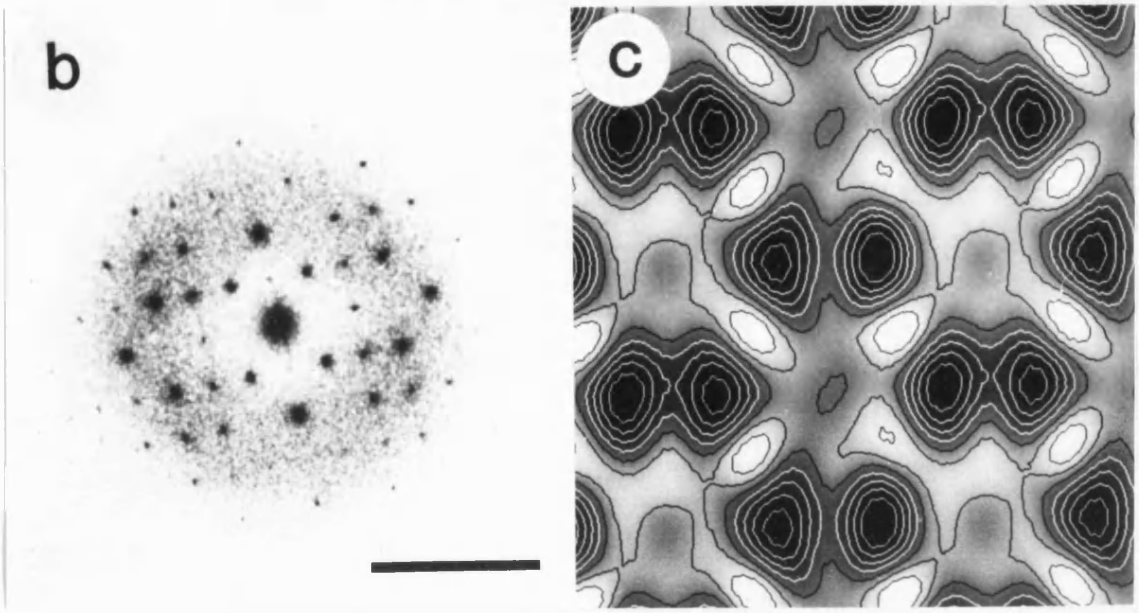

The layers were found, by negative, staining to be crystalline. Images with the best resolution were obtained from tubes and an example is shown in figure (a) on the next page. The scale bar represents 200 nm. The area analysed is marked in black and the optical diffractogram, aligned with respect to the tube, is in (b). The scale bar represents 2 nm. The contributions from the two sides of the tube can be seen in the diffractogram with the crystal axes at right angles to each other and at 45^{o} to horizontal on the page.

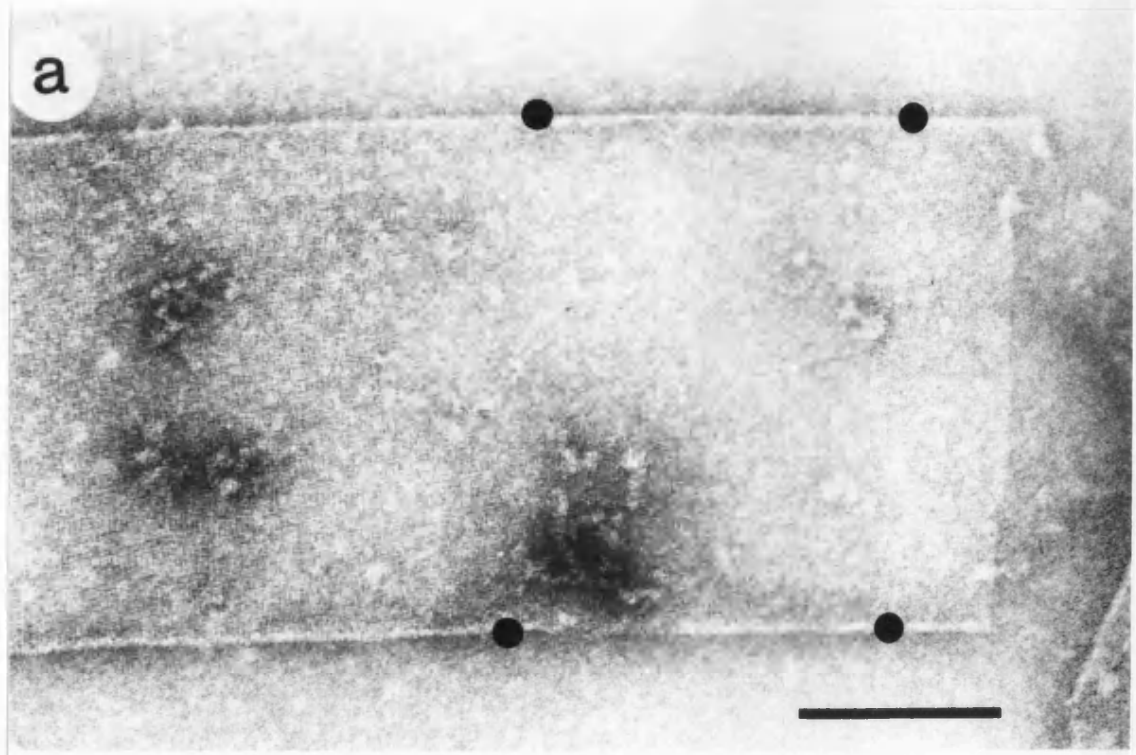
a

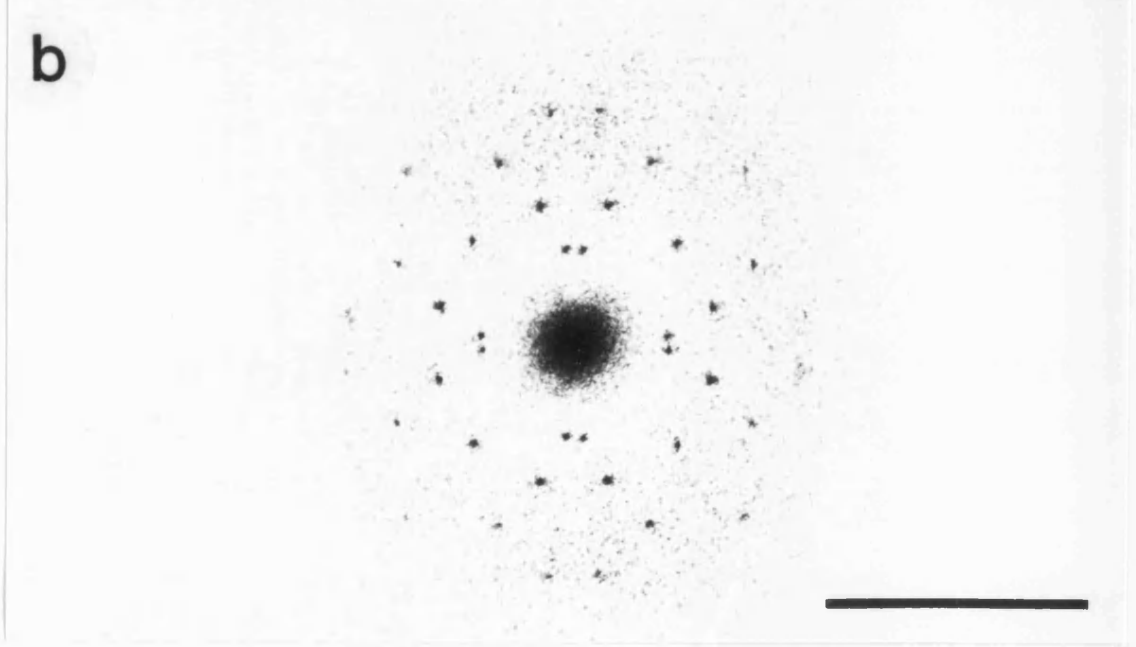
b

The figure below shows a computer filtration of one side of the tube showing that the layers are single molecule thick and revealing the dimers as light regions against the dark, contoured stain. The unit cell dimensions were the same as the crystal, a = 7.4 nm and b = 8.4 nm.

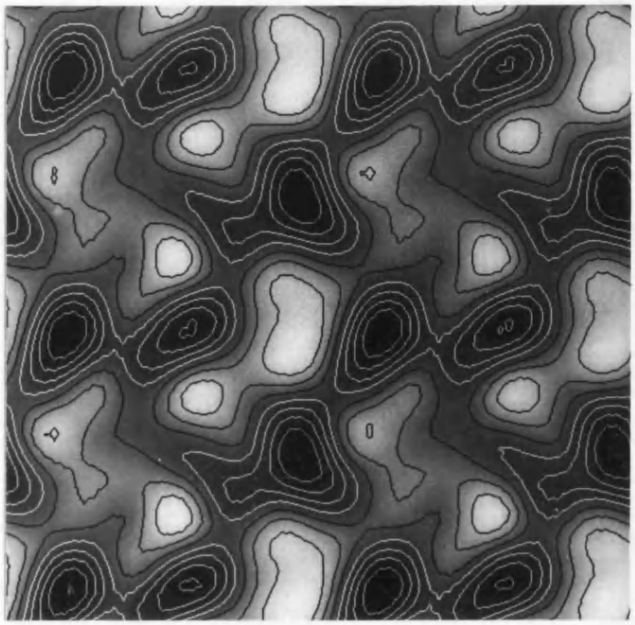

Images were obtained from the tube at different tilts, in 10^{o} steps, from -60^{o} to $+60^{o}$. The Fourier transforms of single sides of these were then combined and back transformed to give a 3-dimensional reconstruction of the enzyme dimer. The contour plots from this were taken at 1 nm slices and a Balsa wood model was built. A photograph of this is shown on the next page. The essential features were of two cylinders of 6 nm length and 3 nm diameter, positioned side by side. There was evidence of the being more closely connected at one end.

The multilayered crystals were prepared in glucose but they gave only weak diffraction patterns, as shown below. There was, however, an indication of two sets of arcs at 0.34 nm. The orientation of these arcs was at 20^{o} either side of the b, 8.4 nm axis (horizontal on the page).

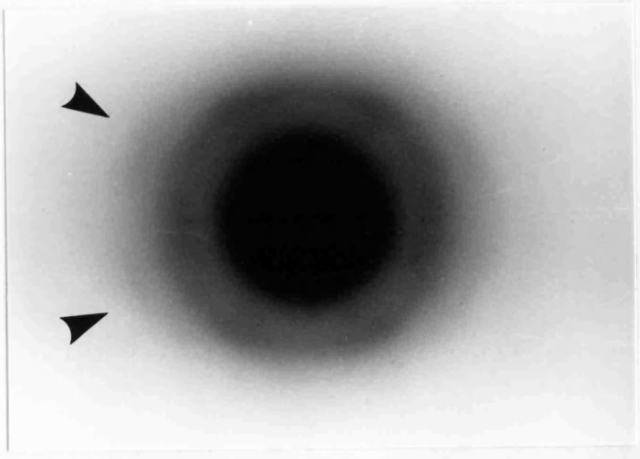

The computer filtered images of the negatively stained crystal and of the single layer of molecules are quite different, as seen below in (a) and (b). In (c) two images of (a), representing the contour plot as grey-scales, are shown superposed at one half unit cell displacement along both axes.

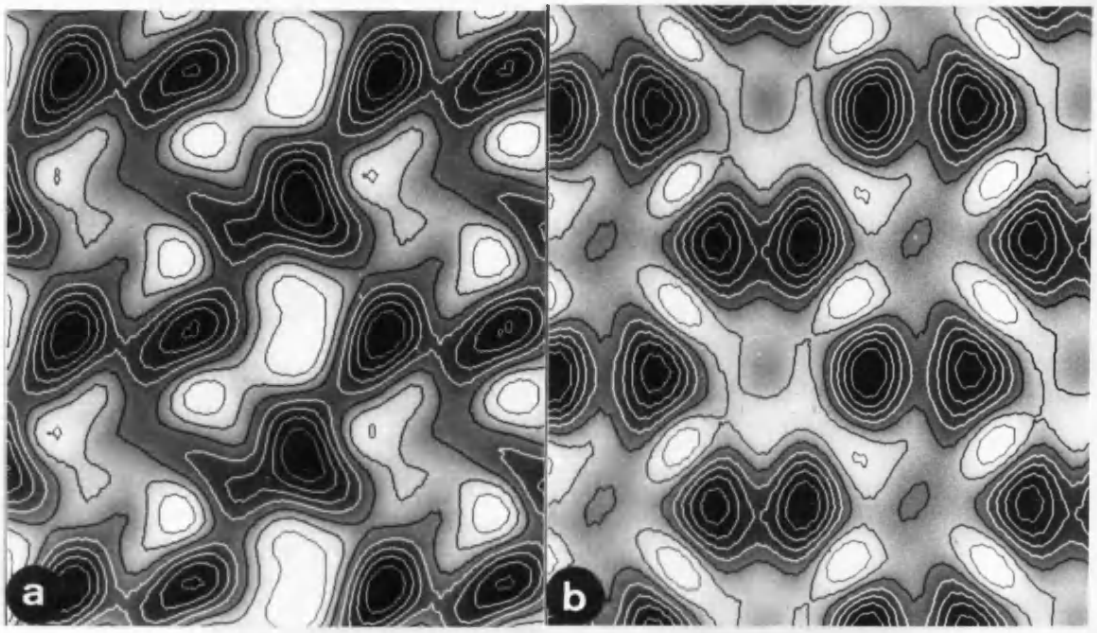

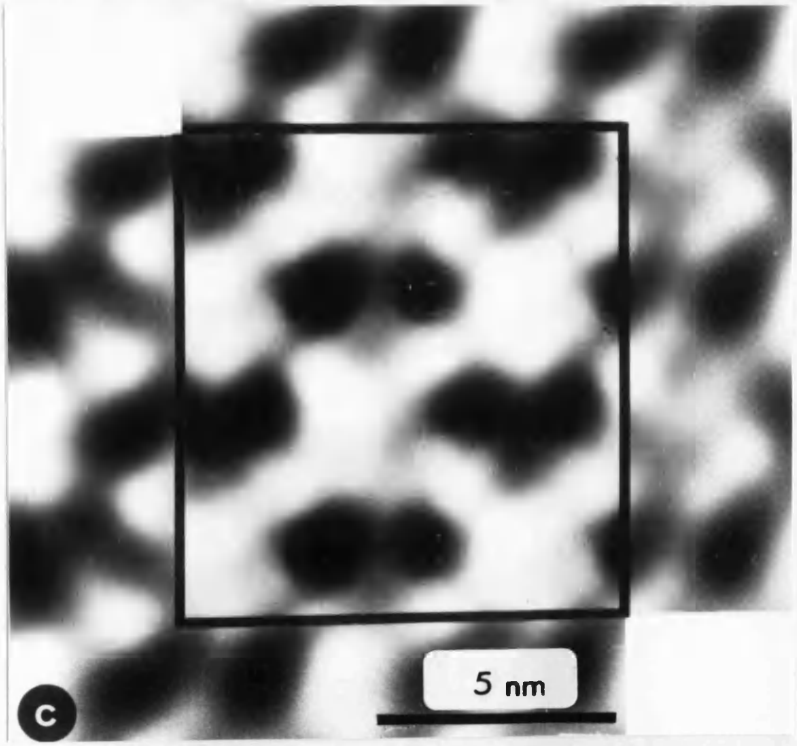

The synthesis of the image of the crystal packing indicates that there is no rotation of the molecules between different layers, only translations that do not alter their orientation. The 0.34 nm spacing is typical for 'B' form DNA and the arcs give the orientation of this to the crystal 'b' axis. Because there is only translation between layers the orientation can be related to the single layer projection and therefore to the molecule. The image below shows the two possible modes of binding of the DNA to the enzyme dimer due to the constraints of the DNA diffraction.

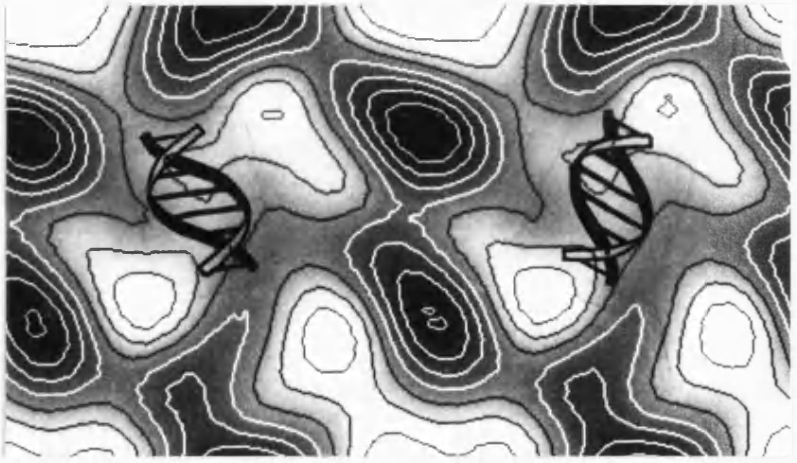

(d) Crystallisation with the specific decanucleotide containing a tri-osmium cluster.

The crystals formed with the same appearance as the non-derivatised decanucleotide. The sequence was the same as had been used before. They were prepared by drying on a grid in glucose and examined in diffraction.

The patterns below show a comparison of the non-derivatised ,upper, and the tri-osmium cluster derivative, below. They are at the same camera length and both taken with 0.01 e^-/nm^2.

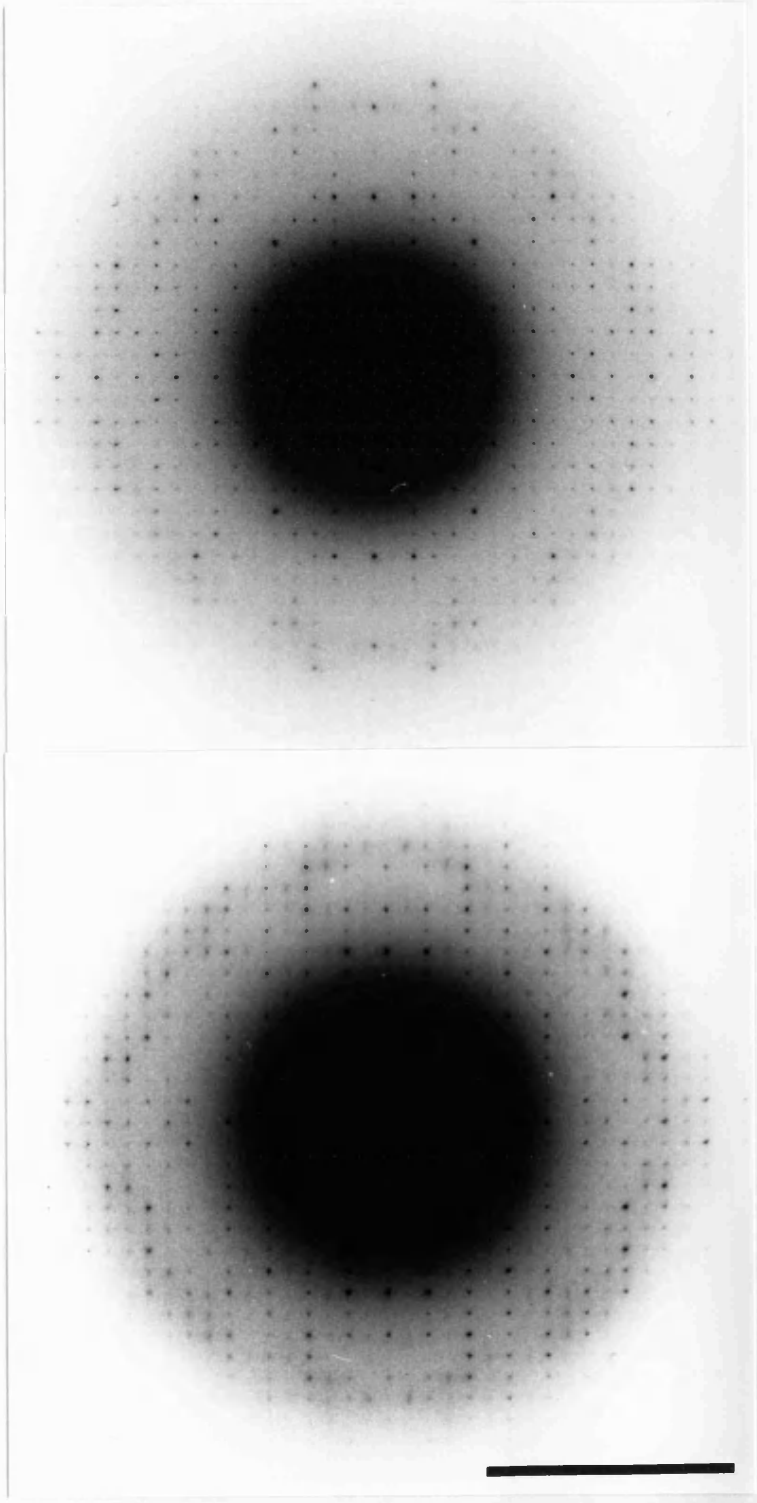

Both patterns are aligned with the axes in the same orientation, the 'a' axis is vertical and the 'b' axis is horizontal. The scale bar represents a spacing of 0.5 nm in both. The top pattern is of the non-derivatised complex crystal, and is therefore another example of the patterns obtained from specific deca-nucleotide (see page 105). The unit cell dimensions for this crystal were 'a' = 5.6 nm, 'b' = 6.4 nm and a/b = 0.88, as in the earlier patterns. The systematic absences are better preserved in this example. Along the 'a' axis only the 8th and 12th orders are strong, with a weak 10th. On the 'b' axis the even orders from the 8th to the 16th can be seen, but there is some intensity on the 11th and 13th.

The pattern of the derivatised complex has unit cell dimensions of 'a' = 6.0 nm, 'b' = 6.4 nm and a/b = 0.93. The 'b' crystal axis was the same as the non-derivatised, whilst the other axis was 7% larger. There are marked differences between the two patterns. The resolution is as good in both but the intensities show some blurring at high resolution in the derivatised. Most significant is the alternation in intensity of the rows of reflections when viewed parallel to the 'a' axis. This indicates a strong feature at half the unit cell size running along the 'b' crystal axis. The strong reflections are sharp and distinct but the weak reflections are blurred and appear streaked in the direction along the 'a' axis.

5.4 Discussion

The preparation and purification of this enzyme was straightforward and yielded sufficient material for structural studies. When a small amount of material was passed on to the molecular biologists it was received eagerly; as, in terms of commercial value, it was worth some hundreds of thousands of pounds.

The non-specific binding of the enzyme to DNA showed a high affinity. The association did not produce any stacking or contraction of the DNA length, unlike many other DNA binding proteins. The molecule could be discerned along the DNA as a string of beads with maximum and minimum projected sizes of 6 and 3 nm. This is consistent with the enzyme binding to DNA as a dimer, and confirms evidence of dimeric association by analytical centrifugation [108].

The crystallisation of the complexes was found to be most successful close to a 10:1 weight ratio of the protein to the oligonucleotide. This is consistent with the ratio of molecular weights and a 1:1 binding of one enzyme dimer to one double stranded DNA oligonucleotide. The crystals which formed grew in the wells in a spherulitic fashion, that is like a mass of plates from a central core. This is typical of fast uni-axial crystal growth. (This is frequently observed, indicating that

thin crystals grow, not because one axis grows fastest, but that one axis grows very slowly; if at all in some cases.)

The crystals that formed with the specific decanucleotide showed clear domains of protein in the computed filtration, but because of the multilayered nature of the crystal, superpositioning prevented identification of the molecule. In order to determine the packing within the unit cell, the size of the cell volume was determined. The size cell dimension in the 'c' direction, the direction of the thickness of the crystal, was first investigated by a diffraction method. The diffraction pattern of a negatively stained crystal was observed while the crystal was tilted, giving the positions of the intensities in the 3-dimensional reciprocal lattice. Knowing the tilt angles, the size of the unknown unit cell dimension could be derived. This method showed that the crystal was being radically altered by irradiation. It was shown that the thickness of negatively stained specimens was reduced by half. An extended study into this phenomenon is given in the next section of the thesis. By this method, the initial size was estimated to be between 14 and 16 nm. Using sections of plastic embedded crystals the size was measured to be 16 nm. This value gives a volume for the unit cell of 587 nm^3. The molecular weight of the enzyme dimer-DNA complex is 63,800 daltons. With four dimers packed in the unit cell the volume per dalton (V_m) is 2.3 nm^3 / kilodalton.

This value is consistent with that found for most protein crystals [113].

The high resolution diffraction patterns of the unstained preparations showed some systematic absences in the odd order positions along the principal axes. This would indicate a symmetrical arrangement of the molecules within the unit cell. However, because of the exceptions to the rule, the space group of the crystal could not be assigned. The glucose preparations showed very good Friedel (across the origin) and mirror (across the axes) symmetry of the spot intensities. The frozen specimens, although they diffracted to higher resolution, showed a loss of symmetry because of being slightly tilted. This is a problem associated with single tilt cold stages. Although the crystals were shown to contain DNA by chromatography of a washed sample the patterns show no indication of arcs at 0.34nm. This would be the spacing expected from 'B' form DNA .

The non-specific octanucleotide complex formed crystals with a different unit cell size and crystal type. The inter-molecule bonds were weak and the single molecule thick sheets and tubes, that this crystal could be induced to form, allowed the reconstruction of the enzyme dimer at low resolution. The model is shown at the top of the next page, together with a 0.6 nm resolution model obtained by X-ray crystallography of the pure (uncomplexed) enzyme [114]. The photograph shows a wire model of DNA in the 'B' form in a possible binding mode,

with the scissile phosphodiester bonds (marked P) near protrusions at the top of the molecule. The electron diffraction evidence showed that this was one of two possible alignments of the enzyme to the DNA.

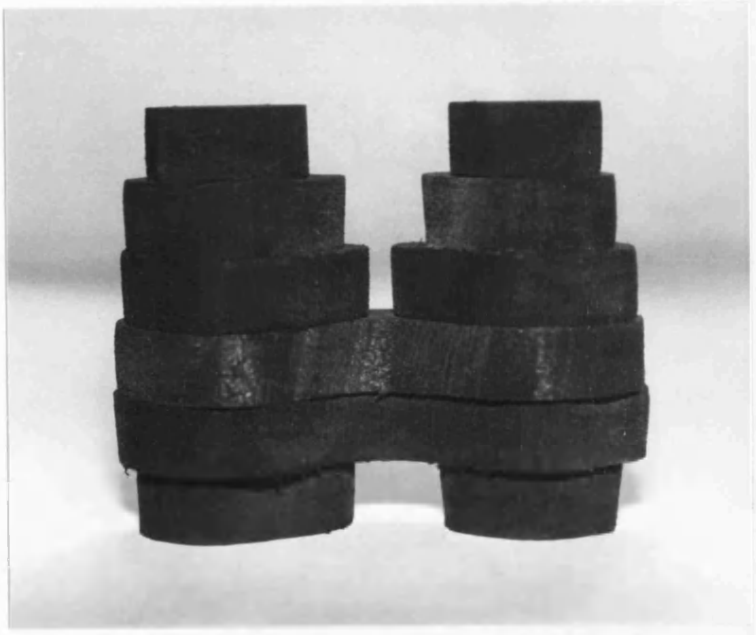

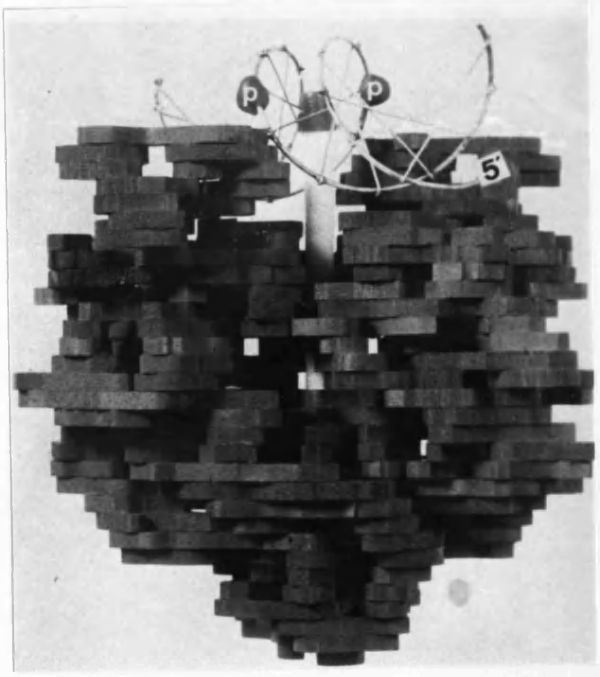

The crystals of the specific decanucleotide with tri-osmium clusters were grown in order to attempt to solve the high resolution diffraction pattern by classical X-ray crystallography techniques. The method relies on forming heavy metal derivatives and comparing the diffraction patterns [115]. A cluster of atoms was used to label the molecules because the scattering power of elements does not increase with atomic weight as quickly for electrons as it does for X-rays. There were very large differences in the relative intensities of the reflections in the two patterns. The crystal unit cell size must, however, remain the same when derivatised for this 'isomorphous' method to be possible. The 7% increase in the 'a' crystal unit cell dimension prevented such an analysis being successful and indicated that some change in the pattern may be due to a re-arrangement of the molecules within the unit cell.

The axis that was altered had been previously noted as being sensitive to different preparative methods. The 'b' axis, however, of 6.4 nm was invariable. Recent publications on the structure of protein-DNA complexes which were determined by X-ray crystallography have revealed a common feature in the organisation of the crystals [116,117]. The oligonucleotides were found to stack; to form protein-DNA rods which ran along or parallel to a crystal axis. The fact that the DNA in these structures showed a 0.326 nm base pair repeat suggests that DNA rods may run parallel to the 'b' axis

in the Eco RV-decanucleotide crystal. This view is supported by the diffraction pattern from the tri-osmium cluster derivative which shows a strong halving of the unit cell in this direction. Given that two decanucleotides span the 'b' unit cell then, placing a cluster at either end of each will, at low resolution, halve the repeat.

in the Eco RV-decanucleotide crystal. This would put two decanucleotides end-to-end across the repeat.

The model is supported by the tri-osmium crystal diffraction pattern. This shows, most strongly at lower resolution, a halving of the unit cell along the 'b' axis. With two decanucleotides spanning this repeat the clusters of osmium atoms will be at half unit cell separation and produce the observed effect to the diffraction pattern. There is still the possibility that the changes in the pattern are due to a change in the crystal packing. The alteration of relative intensities of the reflections is much larger than would be expected from the additional mass in the unit cell. Such calculations are, however, based on the effect of bulk scattering rather than the single point scattering case in this, I believe, unique example.

It can therefore be considered that, rather than providing a method of solving the diffraction pattern of the decanucleotide crystal, it has yielded an important clue. The next line of investigation will be to simulate a crystal of decanucleotides from stored computer data. They will be spaced at the separation of Eco RV-decanucleotide spacings, with the oligonucleotides stacked end-to-end along the 'b' axis. Calculating the Fourier transform of this array, the difference can be determined with the crystal diffraction pattern. The result would be a high resolution projection map of the restriction enzyme.

6. A DETERMINATION OF SPECIMEN COLLAPSE

6.1 Introduction

Radiation damage in the microscope is a subject of wide interest and of particular concern to those investigating the ultrastructure of polymers and biological macromolecules [118,119]. The application of low or minimal dose techniques has improved image resolution and made molecular (unstained) imaging possible. Investigations of unstained specimens in water, glucose and at low temperature, have concentrated on periodic arrays either in two or three dimensions. This has stimulated the use of electron diffraction which, because of its quantitative nature, allows assessment of specimen preservation with respect to preparation and radiation damage [30]. Thin protein crystals pose special problems in interpreting their diffraction patterns because of the small number of unit cells present across the crystal thickness. This problem was theoretically treated by Laue [120] and is of particular relevance to the analysis of electron diffraction patterns [121].

Proteins often produce crystals too small for X-ray diffraction crystallography. With platelet type microcrystals, electron diffraction patterns can give 0.3 nm or better resolution. The development of electron crystallography is of current interest to many researchers investigating biological structures,

complementing X-ray analysis and low resolution electron microscopy.

The analysis of the crystals from Eco RV revealed that the unit cell, in the dimension of the crystal's thickness, was becoming smaller as the specimen was observed in the electron microscope. This was attributed to a change caused by electron damage. The investigation is extended and developed to show that the volume of a negatively stained sample is reduced to about one half by electron irradiation. In this section 'c' refers to the unit cell dimension normal to the supporting film and the * superscript refers to the reciprocal lattice dimensions. The Ångstrom unit, 0.1 nm, is used because it makes expressions of radiation levels more comprehendible, the sensitivity of proteins to damage being about 1 $e^-/Å^2$.

6.2 Materials and Methods

The Eco RV-DNA crystals were made by the methods shown in the previous section (see section 5.3), catalase crystals by the method of Dorset and Parsons [122] and the yolk platelet crystals were kindly supplied by the late Dr. R.N. Lange. Single particles used were ferritin, apoferritin and glutamine synthetase (Sigma Ltd., Poole, Dorset.). They were washed and diluted into 0.9 % NaCl.

Specimens were stained with 1% aqueous solutions of uranyl acetate, uranyl formate, barium acetate and potassium phosphotungstate.

Magnification and electron diffraction camera lengths were standardised against catalase and cross-checked in diffraction with thallous chloride powder patterns.

6.2.1 The determination of the unit cell dimension 'c'.

Two methods were used to determine this spacing, both relying on the change in electron diffraction patterns on tilting the crystals.

(a) Goniometric measurements.

The figure below shows a square lattice of points. This can be taken to represent a small part of a real lattice where the points are centres of repeating motifs in a two-dimensional array.

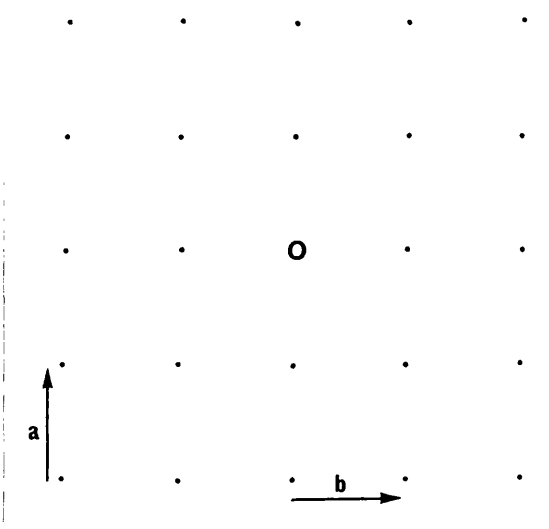

The points can also be considered to represent the reciprocal lattice or diffraction pattern of a 'real' lattice. The central point then becomes the origin or zero order of the diffraction pattern. The real (or reciprocal) lattice has been extended into three dimensions in the next figure, taking the simplest example of a cubic lattice. As a reciprocal lattice, the origin has been placed at the bottom left and two orders in $\underline{a}^*$, $\underline{b}^*$, and $\underline{c}^*$ are shown. When the diffraction plane is normal to $\underline{c}^*$ (ie. the case for an untilted specimen) the square diffraction pattern or hk0 projection is obtained, as demonstrated in the previous figure.

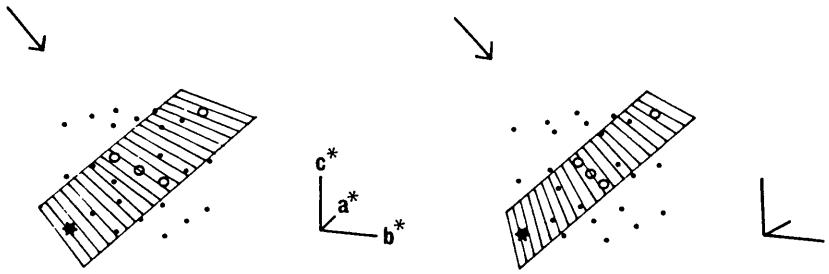

The dimensions $\underline{a}^*$ and $\underline{b}^*$ can be measured after calibration of the diffraction camera length with a compound of known lattice spacing. If the crystal is tilted with respect to the incident beam (the arrow in the figure above), diffraction will be seen only at those points in the 3-dimensional reciprocal lattice

which intersect a central plane which is normal to the incident beam. The tilt axis is parallel to the lines of the intersecting plane shown and, in this case, is shown at right angles to the diagonal between $\underline{a}^*$ and $\underline{b}^*$. The crystal (rather than the beam as shown) is rotated about the tilt axis so that the 110 reflection is lost (centre spot in the bottom plane of nine spots) and the 111 reflection found (centre spot in the intersecting plane). The tilt angle is then recorded and $\underline{c}$ is determined trigonometrically. The disadvantage of this method, over the Laue zone method (see below), is that electron irradiation of the specimen is unavoidable during the 'trial and error' procedure of adjusting the tilt angle to excite the reflections.

(b) Laue zone measurements.

As described above, a three-dimensional crystal with many unit cells in each of the lattice directions gives rise to a reciprocal lattice consisting of discrete reflections. For very thin crystals, there is an effect of crystal shape on the diffraction pattern which was considered theoretically by Laue [120] and reference made to observations obtained from electron diffraction of thin crystals. The limiting case of a thin crystal is one which is a single unit cell thick. The three-dimensional reciprocal lattice of such a two-dimensional real lattice has continuous diffraction spikes parallel to $\underline{c}^*$. This

is shown in the following figure (a). Tilting the specimen then samples the spikes at different points and reconstruction of the repeating unit can be achieved by combining the amplitude and phase data at these points from tilt sets [123].

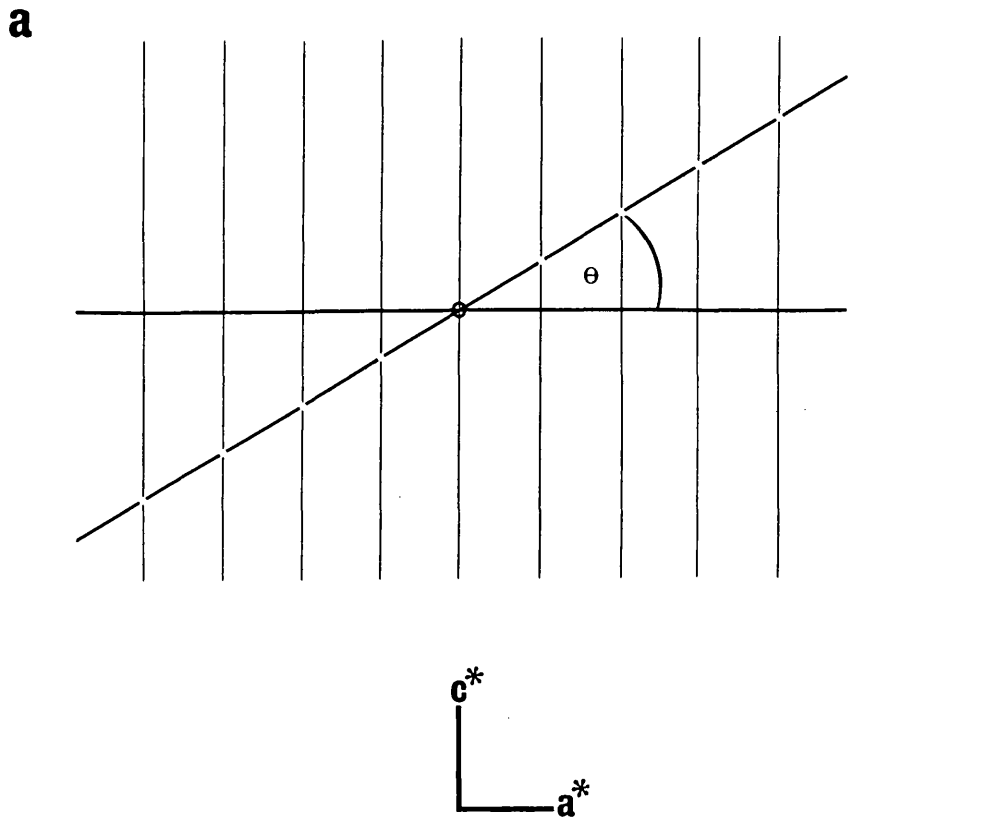

With a very thin three-dimensional crystal, containing a small number of unit cells in $\underline{c}$, an intermediate situation exists between the 2- and the 3-dimensional crystal. The diffraction points are extended into short spikes parallel to $\underline{c}^*$, as displayed in figure (b). The separation of the planes of spikes is related to the inverse of the size of the $\underline{c}$ unit cell dimension. The length of the spike being inversely related to the thickness of the crystal or the number of unit cells along $\underline{c}$. On tilting the crystal, the diffraction patterns show bands of reflections or Laue zones. Knowing the tilt angle, $\underline{c}$ can be calculated trigonometrically from the separation of the centres of these zones. The thickness of the crystal can also be calculated from the width of the zones [124]. Using this method it is possible to deduce $\underline{c}$ from tilted diffraction patterns without prior orientation of the crystal, thus permitting low dose measurements.

6.2.2 The angular accuracy of the goniometer.

As small tilt angles (up to 9^o) were used in the above measurements, it was necessary to check the accuracy and reproducibility of the goniometer specimen holder within these limits. This must be done with a crystal which is not radiation sensitive and which has a known $\underline{c}$ spacing. Protein crystals have relatively large spacings but none were found which provide a reliable standard. Thin graphite crystals were therefore used

which diffract to a resolution of 0.01 Å and which have a well-established interlayer spacing of 3.4 Å [27]. Since these measurements were made at higher resolution, the effect of the curvature of the sphere of interaction, or Ewald sphere, becomes important.

The next figure , an Ewald construction, shows a high resolution reciprocal lattice of a thin crystal and the intersections, normal and tilted, of the Ewald sphere (the radius of which is the inverse of the electron wavelength). This can be regarded as a reduction of figure (b) on page 128 (where a flat plane is a reasonable approximation) by a factor of about 20x.

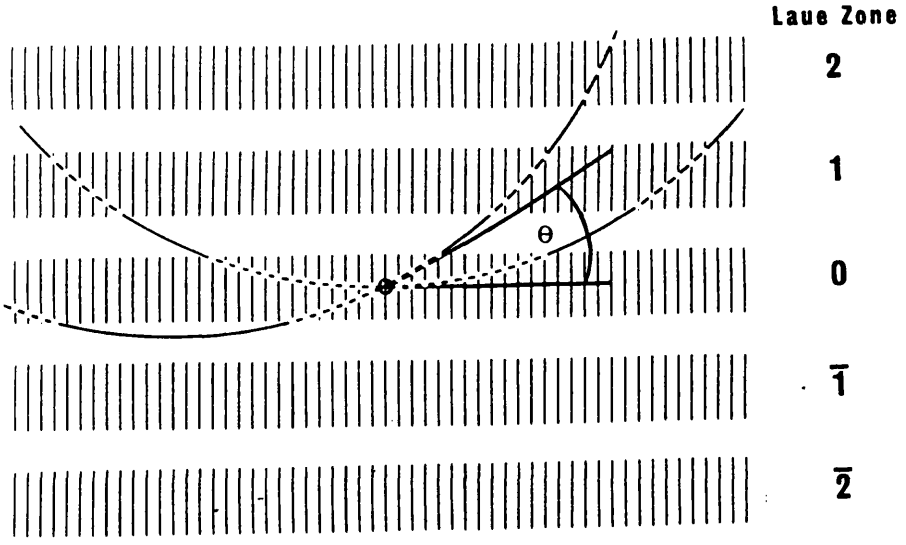

In the zero tilt the separation between the Ewald sphere and the reciprocal lattice increases with distance from the origin until reflections in this plane are no longer intersected. Eventually, with increasing reciprocal

distance, the Ewald sphere intersects the next layer of the reciprocal lattice, giving a circle of reflections known as the first order laue zone. The radius of this circle (R) is related to the unit cell dimension (c) and the electron beam wavelength (L), via the sagitta expression:

$$R = [\ 2 / Lc\ ]^{\frac{1}{2}} \qquad (\ L << c\ ).$$

At zero tilt it is possible to determine the camera length (from the projected unit cell a and b) and the c dimension (from the radius of the first order Laue zone and the electron wavelength. A tilt set at small angles then produces Laue zone patterns which can be used to verify the tilt angles.

6.2.3 Preparation of low temperature specimens

Specimens in water were applied to carbon-collodion coated copper grids, blotted quickly with filter paper and frozen in liquid nitrogen. Samples were inserted into the microscope by cold transfer with the specimen holder at liquid nitrogen temperature.

Negatively stained specimens were dried, inserted into the microscope and then cooled. In order to determine the effect of a contamination layer, dried negatively stained grids were coated with carbon on the upper surface. As an internal control one half of the grid was shielded with a metal strip put over it. To

identify the coated area a small amount of gold was sputtered on to the surface, the control half remaining shielded.

6.2.4 Determination of thickness of single particles

An area of negatively stained, approximately spherical and similar sized particles is diffracted, either directly with the electron beam or optically from an image. Each individual particle acts as a diffracting disk and a random distribution of such particles will then produce a combined Fraunhofer diffraction pattern. This ' Airy disk ' pattern has an intensity distribution which depends primarily upon the projected outline of the object. The central maximum is surrounded by a dark ring which corresponds to the first zero of the J_1 Bessel function. Thus, from such diffraction patterns the average radius of the particles can be determined using Bessel function tables.

If the specimen is tilted in the microscope, a truly spherical particle will always have a circular projection and the diffraction pattern will also be circular. Should the particle be compressed (i.e. reduced in thickness normal to the supporting film) the projection will increase in ellipticity as the angle is increased. Correspondingly, the diffraction pattern will cease to be circular and become elliptical, the major axis of the ellipse in reciprocal space being generated by the reduced thickness of the compressed particle. The

minor axis of the ellipse remains constant during tilting because there is no change in (real space) along the tilt axis around which the spheroid is being rotated. The figure below shows a spheroid on an electron microscope becoming progressively oblate, from left to right. Viewing from A (the normal direction of electron microscopy) shows no change. From C the change in thickness would be easily measured. At B the thickness change is found through the sine of the angle of observation and the projected size.

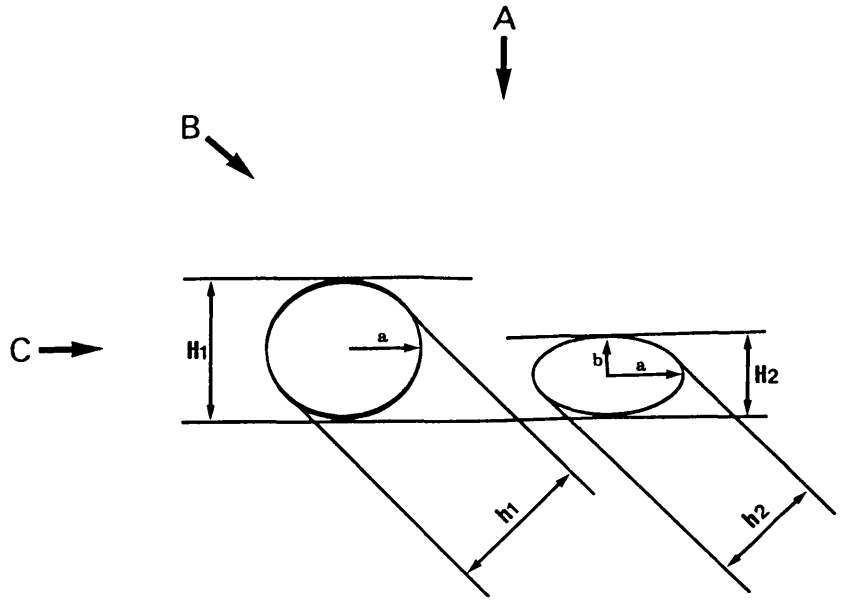

The change of height as seen from the side (H_1 - H_2) can be determined from the tilted view from B as the product of the sine of the tilt angle (from A to B) and the change in projected extension (h_1 - h_2). To measure changes in thickness with electron dose, a series of images of the same area of specimen tilted to 45° were taken, followed by a final image at 0° tilt. The images

were then analysed with an optical diffractometer and the degree of ellipticity determined for the diffraction pattern produced by each image. Alternatively, electron diffraction of a large selected area (10 μm) was carried out at 45^{o} tilt and a series of patterns were used to determine changes in specimen thickness with electron dose.

6.2.5 Experiments with partly supported crystals.

Crystals of catalase were applied to holey carbon films and negatively stained with uranyl acetate. After taking a series of micrographs with increasing electron dose, changes in the unit cell in different areas of the crystal were measured with an optical diffractometer using an aperture to sample small regions of the micrograph.

6.3 Results

6.3.1 Thickness Change in Negatively Stained Specimens

(a) For thin crystals

This was measured either by direct goniometry or by the Laue zone method. The figure on the next page shows the patterns produced by these methods on Restriction enzyme Eco RV-DNA crystals. Figure (a) shows

the electron diffraction pattern at zero tilt (down $\underline{c}^*$). The crystal was rotated round so that $\underline{b}^*$ was parallel to the tilt axis (large arrow). The crystal was then rotated about $\underline{b}^*$ until the pattern seen in (b) was obtained. Here the points along the second layer line have increased to a maximum intensity (arrowed). The tilt angle was then measured.

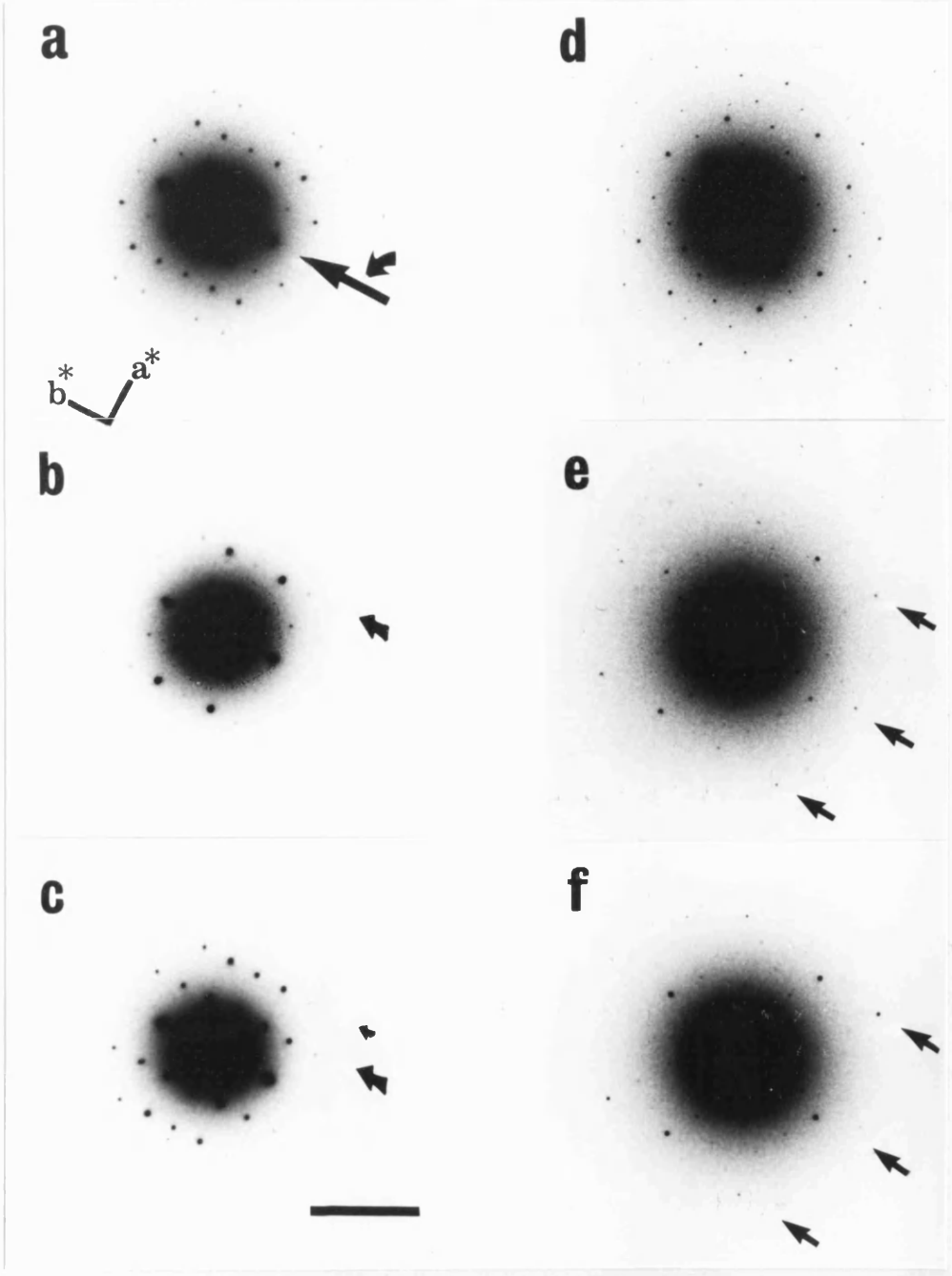

In Figure (c) the crystal was tilted further and the first layer line became excited (large arrow) coincident with a second maximum on the second layer line (small arrow). By using these angles and those obtained when tilting the specimen in the opposite direction, it was possible to correct for initial specimen tilt and to ensure that 'c' was perpendicular to 'a' and 'b'. This procedure was one of trial and error and the specimen therefore received a fairly high dose giving a resolution limit of about 20 Å.

Figure (d) shows a zero tilt taken without any prior alignment. This low dose pattern shows orders out to 10 Å. Figure (e) shows a $+15^{o}$ tilt, with the Laue zones (parallel to the tilt axis) indicated by arrows. Figure (f) shows the -15^{o} tilted pattern confirming the position of the zone with opposite tilt.

During the goniometric determination of the restriction enzyme co-crystals, it was noticed that the tilt angle to maximise the intensity of a given lattice layer would increase slowly with time. In the case of the example in Figure (b) this increased from 14^{o} to 24^{o}. This corresponded to a reduction in c value from 114 Å to 64 Å. Using the Laue zone method the lowest dose showed an initial value of 124 Å. The effect of dose on 'c' is shown in the graph on the next page. The size of the unit cell was calculated from the tilt angle at increasing dose.

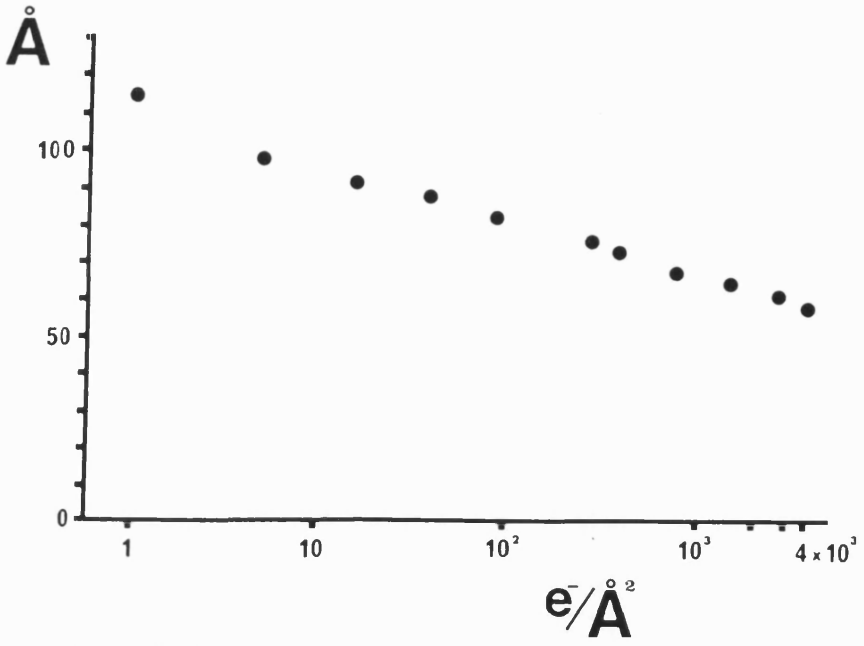

The figure below shows a negatively stained yolk platelet crystal. This gave an untilted diffraction pattern as seen in the left example of the set.

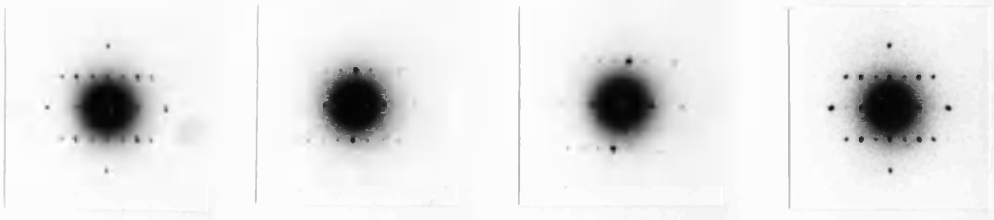

The projected unit cell dimensions are '<u>a</u>' = 85 Å and '<u>b</u>' = 175 Å. The crystal was tilted about the b axis of the crystal (horizontal on the page). The next pattern, from the left, shows the maximum for the next row of spots. This was at a tilt angle of 25°, giving through the division of the '<u>a</u>' unit cell size by the tangent of the tilt angle, a value of 182 Å for '<u>c</u>'. The third diffraction pattern shows the same projection as before, but after irradiation with 10^3 $e^-/Å^2$. The tilt angle had increased to 44°, giving a value of 88 Å for the '<u>c</u>' unit cell. The increase in the size of the reciprocal lattice can be seen in the separation of the lines of reflections which mark out the diagonal. The last pattern shows the pattern after dosing with no tilt.

The combined results of about fifty experiments to determine '<u>c</u>' using different crystals and different negative stains are shown in the graph below. The percentage reduction is plotted against the exposed radiation density.

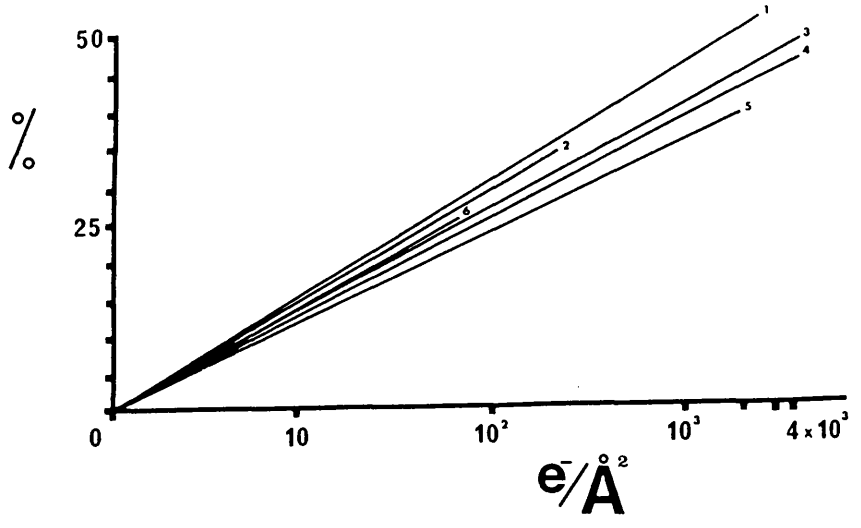

The numbers on the graph refer to different samples as follows: 1, Yolk platelet crystal stained with uranyl formate. 2, Ferritin, apoferritin and glutamine synthetase, stained with uranyl acetate. 3, Catalase stained with uranyl acetate, uranyl formate, PTA, and barium acetate. 4, Eco RV-decanucleotide crystal stained with uranyl acetate. 5, Eco RV-octanucleotide crystal stained with uranyl acetate. 6, Scanning transmission electron microscope mass loss curves [133].

The unit cell dimension '*c*', in negatively stained crystals, reduces exponentially with dose to about 50% of the starting value. In all cases of crystals supported on carbon films, a final zero tilt image of the area which had been irradiated showed no changes in '*a*' and '*b*', the crystal shrinkage having taken place entirely in the direction at right angles to the plane of the grid.

(b) For single particles

Uranyl acetate negatively stained preparations were made of ferritin, apoferritin and glutamine synthetase. Micrographs were taken under low and high dose conditions with the specimen tilted at 45°. The figure on the next page shows in (a) and (b), a low and high dose pair from an experiment with ferritin. The low dose image has a three dimensional appearance, whilst the the high dose is flat. The scale bar represents 0.15 μm.

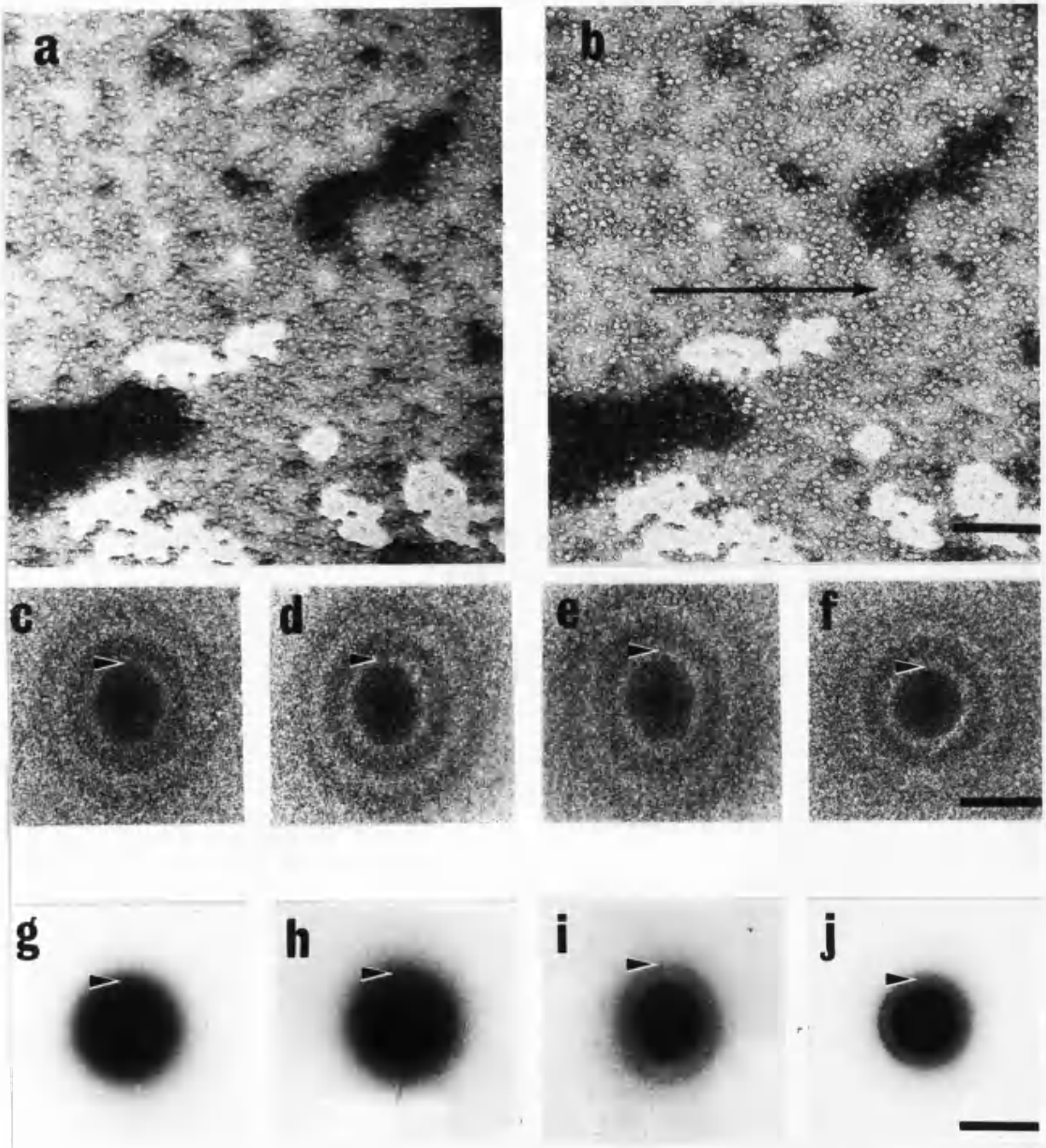
a
b
c
d
e
f
g
h
i
j

After dosing, the grid was returned to 0^{o} (carefully keeping the area irradiated centred) and imaged again. Figure (c), (d) and (e) show the optical diffractograms of a 45^{o} image dose set, taken after doses of 1, 10, and 100 $e^{-}/Å^{2}$. These can be seen to have increasing ellipticity. Figure (f) is the diffractogram of the same area returned to 0^{o} and shows the circular outline of an oblate spheroid in projection. This gives a pattern which, using the Airy disk approximation, fitted a J_1 Bessel function to the minima (arrow shows the 1st.) corresponding to discs of 124 Å diameter. This did not change with dose. The optical diffraction patterns show an increase in the radius of the minima parallel to the tilt axis with dose. This represented a reduction in height from 120 Å to 80 Å. The 30% reduction in thickness with dose was plotted in the compilation graph on page 138. Figures (g) to (j) show electron diffraction patterns of a 10 μm selected area of negatively stained ferritin particles tilted at 45^{o}. The diffraction patterns were taken with only 0.1 $e^{-}/Å^{2}$. The first pattern in this series is thus one tenth the dose of the first in the image series. The pattern is quite circular and becomes elliptical with dose (to Figure (i)). Figure (j) shows the pattern from the same region tilted back to 0^{o}. The second maximum is marked by the arrow. The scale bars represent 50 Å in (c) to (f) and 25 Å in (g) to (j).

(c) For unsupported crystals

Crystals of catalase were negatively stained and dried on to carbon films with holes. The image below shows the result of irradiation.

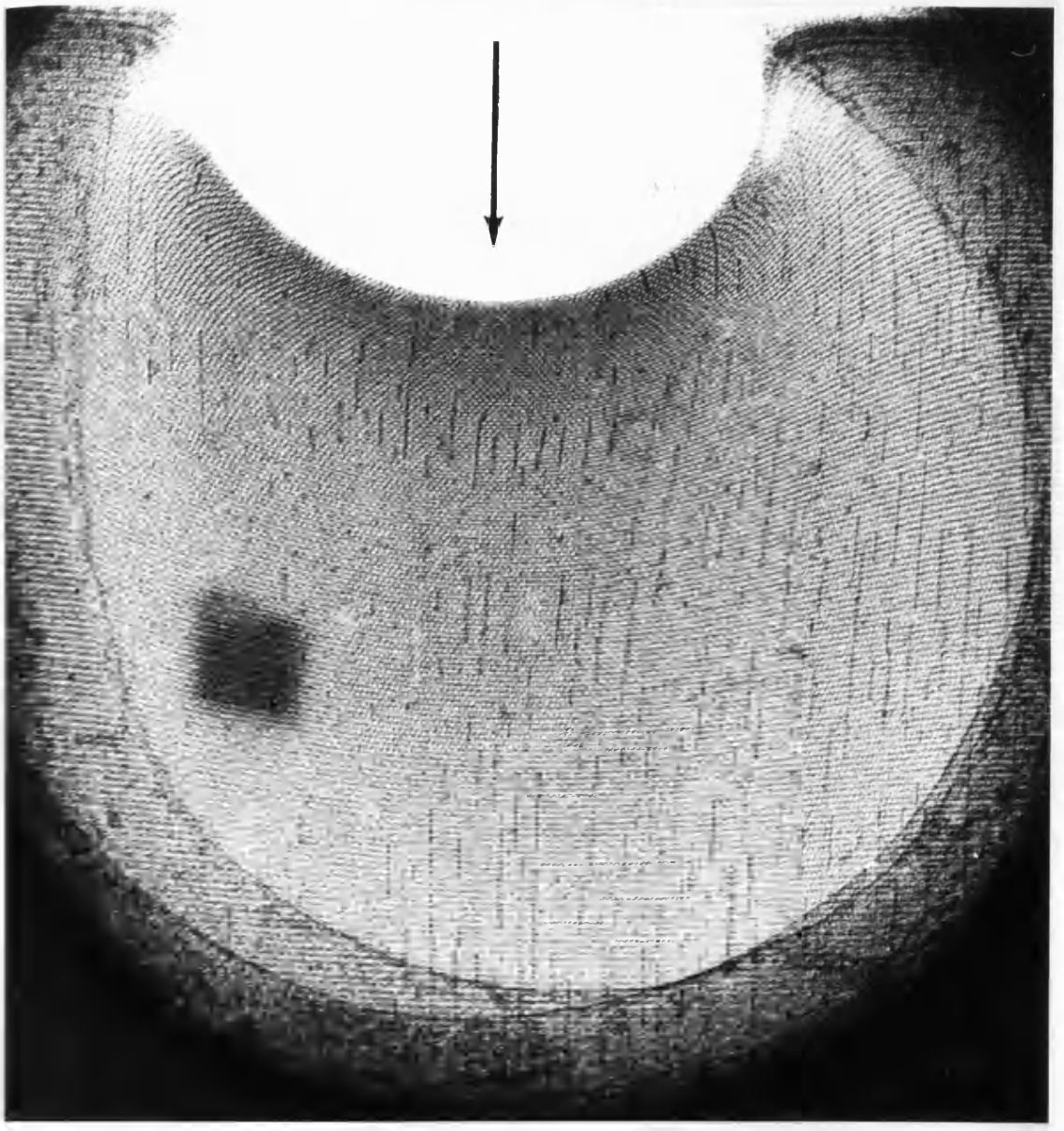

A crystal edge crossing a hole showed a pronounced movement in the direction of the arrow as the crystal contracted. Such a crystal can be considered as being supported only normal to the arrow at the edge (in this case the unit cell 'a' direction) and contraction had taken place along the 'b' direction (arrowed) at the edge where it is least supported. The crystal projection unit cell area has been reduced by about 30%, packing the stain into a smaller area and increasing the density. The reduction in the unit cell axes was measured by optical diffraction of small areas across the micrograph.

Figures (a) and (b) on the next page show the low and high dose (respectively) pair of a uranyl acetate stained crystal spanning a hole. The change, as in the previous image, showed a 30% reduction of one unit cell dimension. Figures (c) and (d) show a crystal corner that was unsupported. The contraction in this case was isometric and gave a 20% reduction on both crystal axes. With unstained crystals embedded in glucose, figures (e) and (f), it was not possible to measure changes in unit cell parameters, but dose-induced shape changes of unsupported crystals were essentially the same. The doses used were 1 $e^-/Å^2$, for the low and 100 $e^-/Å^2$ for the high dose images. The scale bar represents 0.1 μm in each pair.

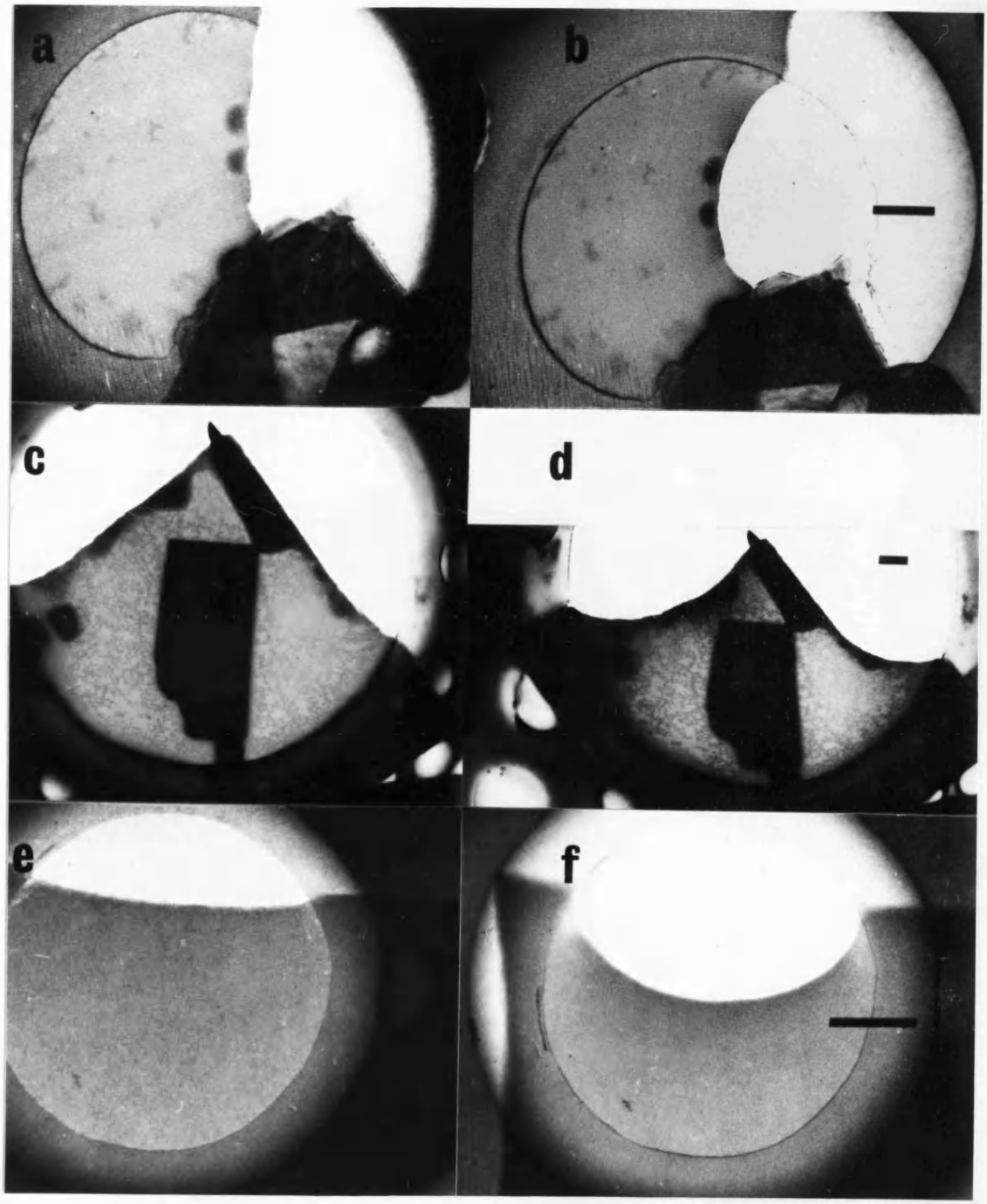
a
b
c
d
e
f

6.3.2 Absolute thickness of stained and unstained specimens

Catalase forms very well characterised crystals for electron microscopy and was chosen to test the methods used. As described above, a 50% relative reduction in '<u>c</u>' was found for the negatively stained crystals. At low dose, the maximum value was 145 Å, while the expected value was 206 Å [125]. Thus, although the reduction in '<u>c</u>' agrees well with a study of sectioned, negatively stained (and dosed) catalase crystals [126], the starting value is still 30% less than the value for hydrated crystals.

Glucose embedding has been shown to give high resolution diffraction patterns. The projection unit cell sizes were unchanged in glucose and the Laue zone method for determining '<u>c</u>' was used in low dose electron diffraction of tilted glucose embedded crystals.

The set of diffraction patterns on the next page show a tilt set from one crystal. The Laue zones are shown parallel to the tilt axis (arrows). The patterns were recorded with 0.2 $e^-/Å^2$ each, and although the strength of the pattern was reduced by radiation damage, the Laue zones were distinct throughout. The goniometer settings were -3^o, 0^o, and $+3^o$. The scale bar represents a spacing of 5 Å. Using the average '<u>c</u>' values the actual tilt angles were calculated and this simple iterative step was used for a best fit to the data.

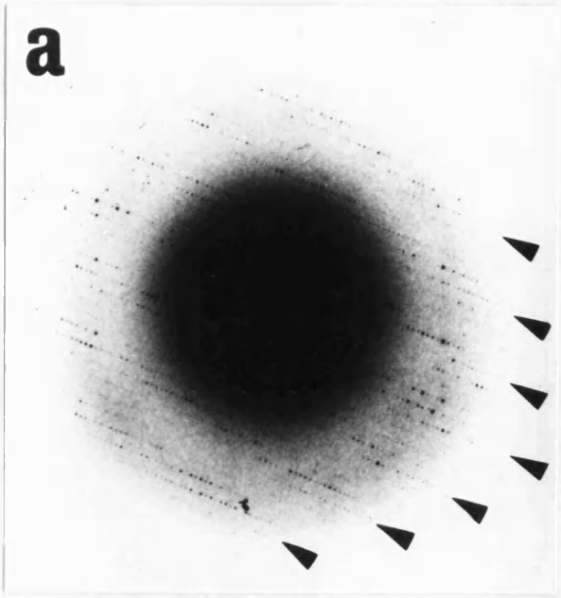
a

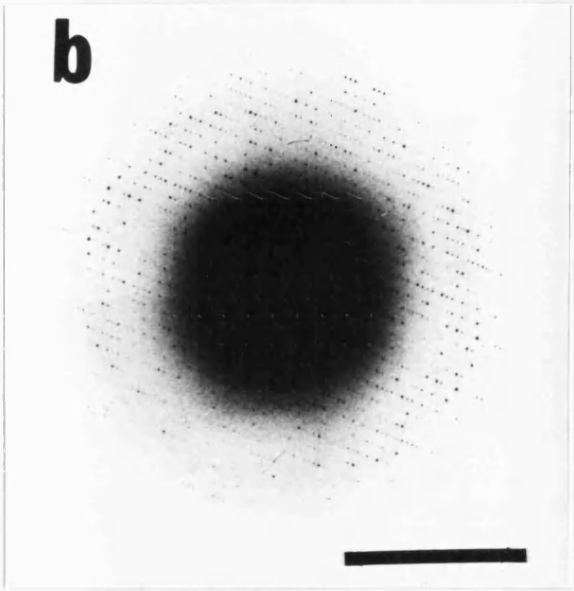
b

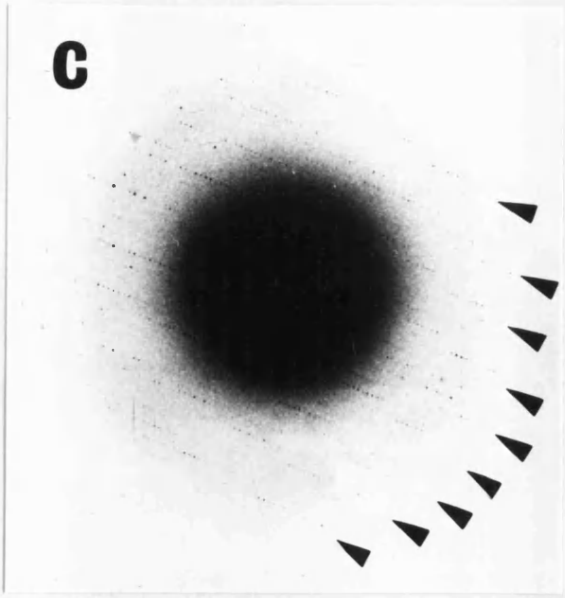
c

The results of twenty tilt sets gave an average value for '<u>c</u>' of 160 Å. This represents a reduction of 20% from the hydrated state. In order to check that the spacing did not change with dosing, crystals were irradiated at a fixed angle. The patterns below show the effect of dose on the low angle part of the glucose embedded catalase tilted diffraction. The faint signs of the Laue zones are arrowed in the high dose, 1 $e^-/Å^2$, pattern.

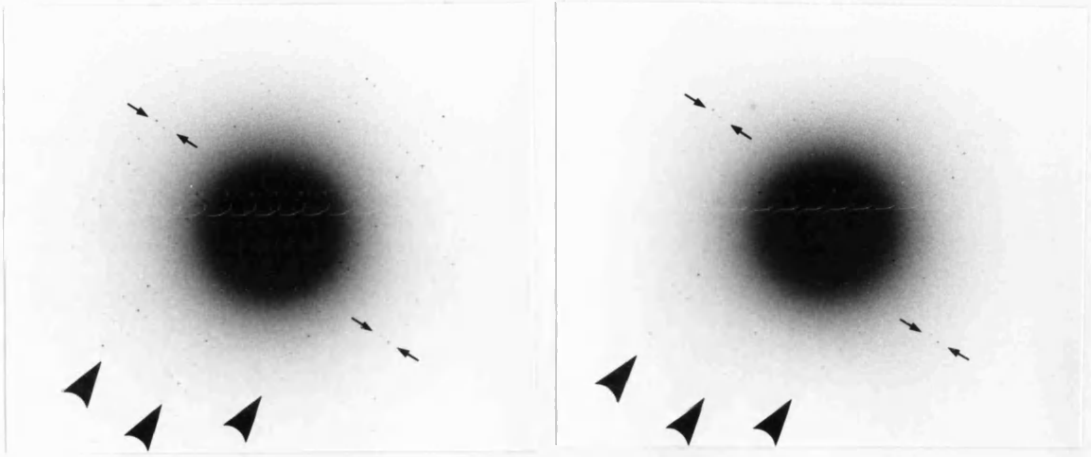

Laue zone measurements were made on frozen hydrated crystals and an example is shown in the figure below with tilts, of -3°, 0°, and +3°.

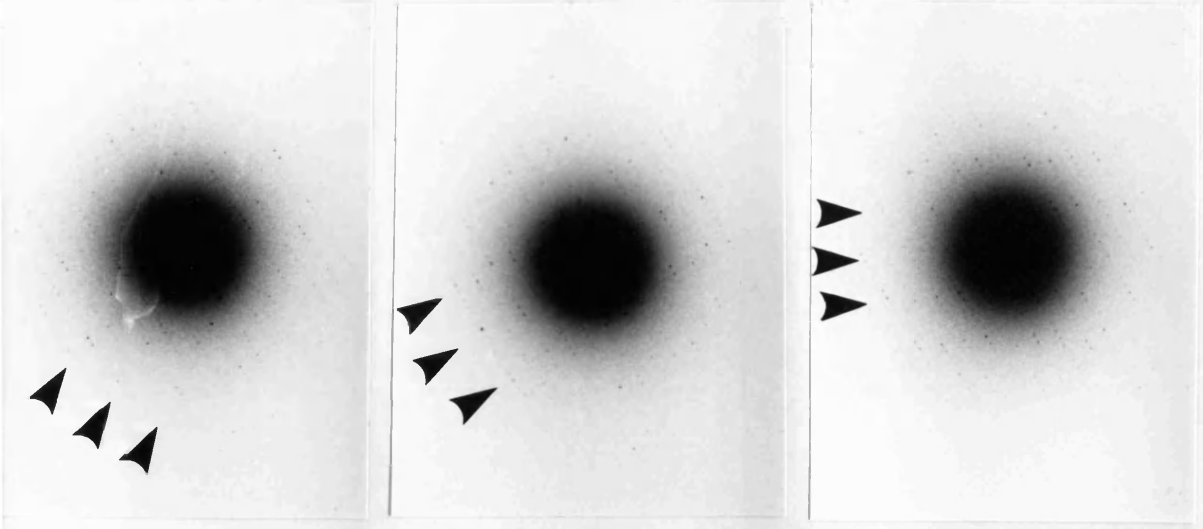

The orientation of the Laue zones was seen to rotate as the crystal was tilted. The zero tilt showed zones running at right angles to the tilt axis of the microscope stage. This showed that the cold stage was tilted about an axis at right angles to the tilt axis. The measurement could not be made directly but by using a computer program to obtain a best fit for the data, a value of 175 Å was obtained for '<u>c</u>' from an average of six experiments.

When dried negatively stained crystals were observed on the cold stage there was no evidence of the reduction in thickness which had been found at room temperature. The angle of tilt required to maintain maximum intensity of the electron diffraction pattern remained constant over a wide dose range. After about 1000 $e^-/Å^2$ the pattern had deteriorated in resolution but all unit cell dimensions were unchanged (within the experimental accuracy of 5%).

These measurements were made with a modified cold trap which restricted tilting. This was removed for tilting above 30^o with the result that the specimen behaved quite differently, the electron diffraction patterns fading very quickly. By 10 $e^-/Å^2$ the pattern had disappeared completely. Examination of images under these conditions showed that the specimen had become coated by a thin layer (presumably water vapour) and rapid destruction of the crystal by 'bubbling' took place, as shown in the images (a) to (d) on the next page.

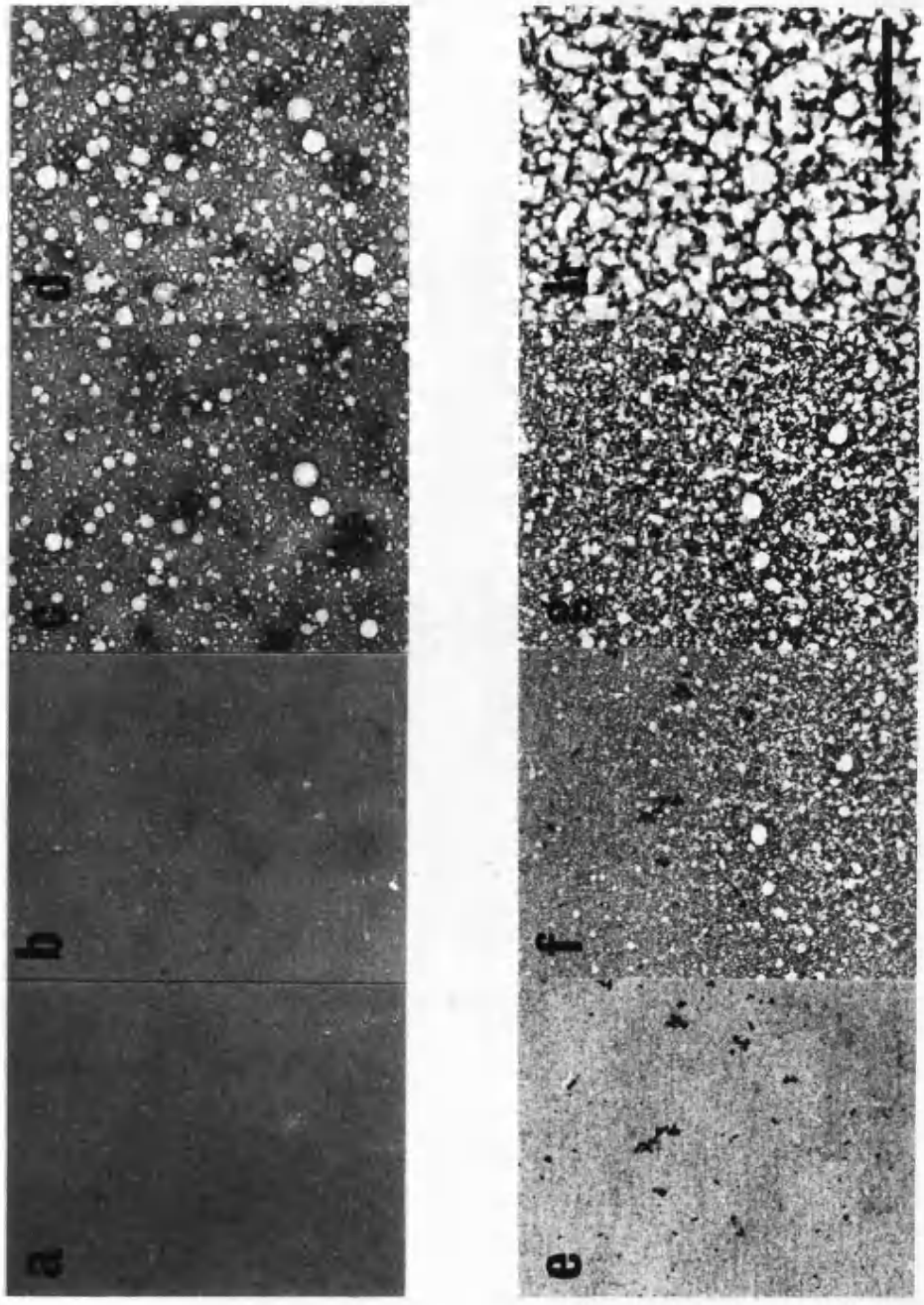
a
b
c
d
e
f

The bubbling may either be caused by some aggressive property of frozen water vapour in combination with electron irradiation, or by a simple trapping of active species such as radiation induced free-radicals by the layer. In order to discriminate between these possibilities, a dried negatively stained grid of catalase crystals was half covered with a 3 nm thick carbon film. The grid was then observed cold with the cold trap in place. The uncoated crystals did not bubble and gave diffraction patterns that were very stable. The crystals that were carbon-coated were rapidly destroyed by bubbling. Figures (e) to (h) on the previous page show a dose set from the carbon coated half. The cold trap was then removed and after a short time condensation was found on the grid and the non carbon-coated crystals also bubbled. The dose set for (a) to (d) was 1, 2, 5, and 10 $e^-/Å^2$, for (e) to (f) it was 1, 5, 10 and 100 $e^-/Å^2$. The scale bar represented 0.4 μm.

The graph on the next page shows a compilation of the experiments that measured the value of the '<u>c</u>' unit cell size under different preparative conditions. It also traces the effect of irradiation on this parameter.

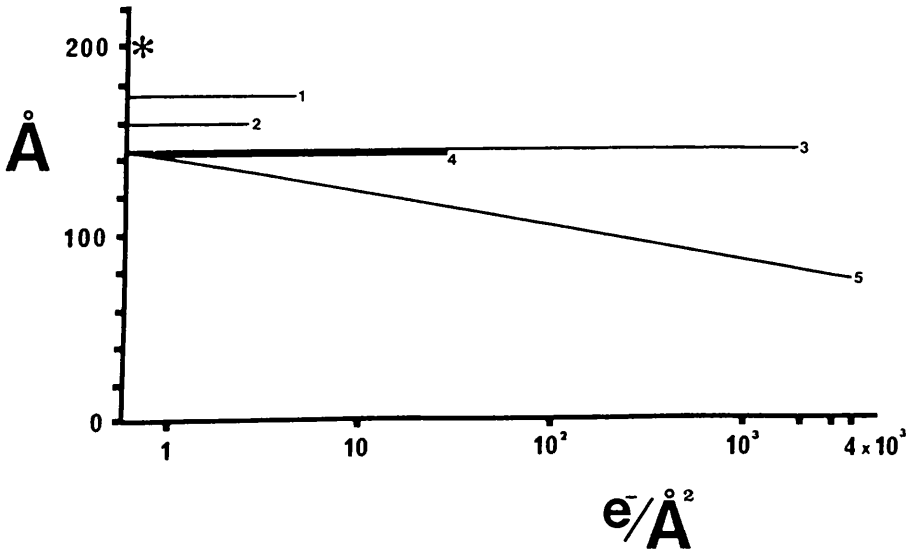

* Value of 'c' from X-ray diffraction.

1 Frozen in water at 120 °K.

2 Dried in glucose at room temperature.

3 Negatively stained at 120 °K.

4 Negatively stained at 120 °K and covered with a contamination layer of ice or a deposited carbon layer.

5 Negatively stained at room temperature.

6.3 Accuracy of the Goniometer at small angles

Since the absolute value of 'c' depends on the accuracy of the tilt angles measured, the electron microscope goniometer was checked with graphite crystals. The figure on the next page shows high angle diffraction tilt sets for graphite. (a) is a projection down c^* showing the first order Laue zone.

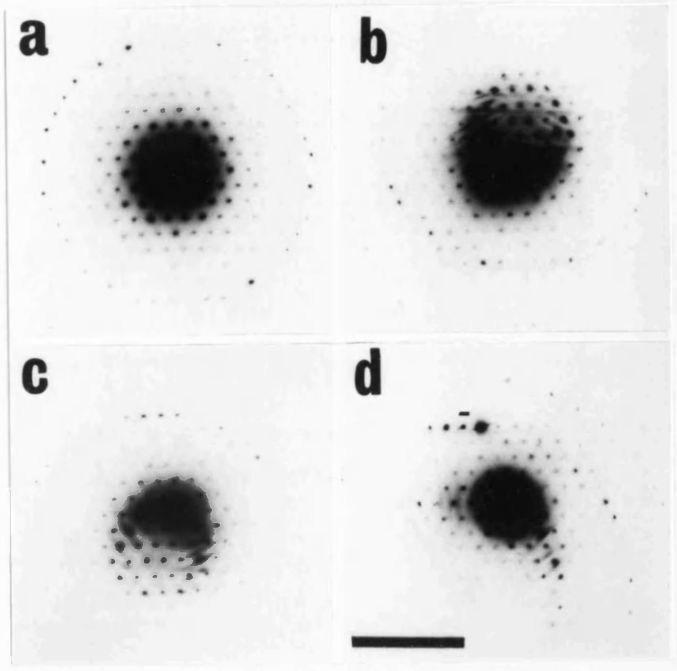

The spacing of this zone gave , using the wavelength for 80 kev electrons as 0.0418 Å, a '<u>c</u>' spacing of 3.4 Å. Figures (b) and (c) show + and - 3° tilt. The first order Laue zones are displaced in equal and opposite directions (about the tilt axis). By calculation, the positions of the Laue zones were found to agree with the tilt angles to within 5%. The scale bar represents a spacing of 0.3 Å.

6.4 Discussion

One of the first observations of an interaction between material of biological origin and an electron beam was the reduction in size of a cotton thread by

Ruska [13]. Specimen shrinkage and movement was a problem in the early days of electron microscopy which was effectively solved by supporting specimens on thin carbon films. Although this procedure prevents movement in the plane of the specimen grid, which is most important for projection imaging, it has been clear for many years the specimen becomes thinner with dose [127].

Investigations of periodic structures should detect distortions caused by changes of dimension. A study of T4 tail [128] revealed a shrinkage of the upper unsupported surface. Here the effect of dose was not investigated, and the change was ascribed to a drying artefact. The effect of radiation damage on three-dimensional reconstructions of negatively stained stacked-disc TMV protein helices [129] suggested that stain migration was taking place. This process may be just as well explained as a contraction taking place in the unsupported regions of the protein, the stain moving with the protein as it collapses. A further study of stained stacked-disc TMV and T2 phage tail [130] found that "improved" images could be recorded after a pre-irradiation of the specimen. This is certainly an optimisation of the specimen thinning rate and resolution, since both are reduced with dose.

'Thinning' by irradiation is a common method of improving the contrast of thick sections. Quantitative evidence of a reduction in thickness has been found by many investigators on such materials as pure plastics

[127], light meromyosin paracrystals [131], and in reconstructions of muscle from thin sections [132]. The thickness of the region of muscle that was studied was found to be half the value it was known to be from orthogonal sections and X-ray analysis. Grid sectioning of irradiated, negatively stained catalase crystals gave an anomalously low value for the unit cell size in the direction perpendicular to the supporting film, despite the fact that the crystals appeared to be well preserved [126].

The work described here shows that there is a marked loss of thickness for negatively stained material on irradiation, as had been found for plastic sections. By using low electron doses and electron diffraction methods for crystalline material, it was possible to show direct quantitative changes as they took place in the electron microscope. In an unsupported specimen, shrinkage occurs as an isometric process and may be related to beam-induced mass loss of the biological material. In the case of a specimen supported on a carbon film, which is the normal situation for biological electron microscopy, shrinkage is prevented in the plane of the film, with the result that there is a large shrinkage in the direction normal to it.

At the lowest doses possible, using the Laue zone method for measuring the c spacing, it would appear that dried negatively stained specimens are about 70% as thick as when hydrated. With prolonged exposure, this

reduced to only 40% of the expected value. Over the range of electron dose used in a typical continuous tilt series for three-dimensional reconstruction, the final thickness would be reduced to about 50% of the theoretical value. Studies on isolated particles, although not exhaustive, are in agreement with these results.

With unstained specimens, the starting values are somewhat better - 85% for frozen hydrated crystals and 80% for crystals dried in glucose. Since these specimens lose crystallinity on irradiation at low doses (1 to 2 $e^-/Å^2$), it was not possible to follow the change of unit cell size by diffraction, but the dimension changes in the unsupported catalase crystals in glucose suggest that the same shrinkage process was taking place.

The changes found in the volume of the specimens investigated show a similar change to the mass loss measurements described in a study on unstained specimens with a scanning transmission electron microscope (STEM) [133]. This also showed that the loss was stopped by irradiating the sample on a cold stage at liquid nitrogen temperature. The effect of bubbling of the specimen was a very unexpected result. The bubbling of specimens is normally considered to be due to carbohydrates or bound water, its observation in a dry negatively stained sample is hard to explain. In an earlier study of negatively stained catalase crystals at liquid helium temperature [134], it was found that there

was a rapid loss of resolution with electron dose. This may well have been caused by the presence of a contaminating ice layer. This phenomenon of beam-induced 'bubbling' damage may well become a limiting factor with carbon sandwiched [135], encapsulated [136] or frozen-hydrated [137] specimens below -140 ^{o}C.

The effect of beam-induced shrinkage has to be taken into account when carrying out three-dimensional reconstruction by combining tilted views of single particles or crystals. It has important consequences for both the method of collecting the tilted data and for the end result. It is clear that some degree of correction may have to be applied to the '<u>c</u>' dimensions of a reconstruction. As can be seen from the catalase crystals and single particles such as ferritin, the reconstructions may only be 50-60% as thick as the native object. This shrinkage, in a typical tilt reconstruction, is however partially compensated for by the 'missing cone' effect which tends to reduce resolution and elongate structures in the '<u>c</u>' direction. If independent orthogonal views of the projection from sectioned material are added to three dimensional reconstructions it will impose the correct thickness. It will not, however, remove the problem of combining data from objects of different thicknesses.

7. GENERAL DISCUSSION AND CONCLUSIONS

The development of electron microscopy for biological molecules has been through the application of techniques to maximise efficiency. The electron microscopist in metallurgy can investigate his specimens, either with diffraction patterns or with the images of crystal planes, with little regard to how much radiation the specimen has received. For the biological researcher it is essential to capture an image of the specimen with as little pre-irradiation as possible. The fact that the doses that the specimens are given is referred to as 'low' should not hide the fact that such a dose must be measured in thousands of mega-rads. The electron microscope can be regarded as a source of radiation which can potentially produce flux densities equal to the intensities close to atom bombs [118].

In the previous chapters the detailed analysis of a number of crystalline biological structures has been described. The application of improved specimen preparative techniques and low dose microscopy has produced new information on the organisation of the molecules studied. This would not be possible with conventional microscopy, where the natural 'milieu' is replaced with either plastic or a high density salt. The fact that both of these methods are prone to a volume reduction, which presents itself as a 'thinning', when

irradiated, will persuade future investigators to concentrate more on frozen specimens. The protocols and equipment for these techniques is continually being improved and simplified. With greater numbers of research workers in this field and an increasing number of structures solved by the method, the problems of inadequate cold traps and inflexible low dose facilities will be solved.

An important requirement for high resolution investigations is a well ordered, crystalline specimen. The best known of course is purple membrane which, after a continual effort by Henderson and colleagues, is still yielding higher resolution images [15] and insights into image analysis [138]. The fruit of this work is the correction of the many aberrations which are present in an electron microscope image by computer analysis. The progress from the original 0.7 nm map to current work at 0.28 nm is not just a matter of scale. The first images of this molecule showed the alpha-helices which were spanning the lipid membrane [50]. At high resolution the images reveal only slightly more. The reason for this is that a projection down 6 nm of coiled polypeptide superposes the chain and the side groups. In order for the structure to be interpretable the complete 3-dimensional analysis must be performed. This requires sets of images at a range of different tilts, and these are combined using computer techniques.

The first example studied in this thesis was with a sample with only poor order. Although this was prepared by an improved method of 'gentle' extraction, the negative stained results were very similar to an earlier investigation [79]. Low dose diffraction showed the orientation of coiled-coil alpha-helicies within the paracrystal. Low dose images revealed fine striations in the paracrystal which supported the model of lipoprotein being in trimeric association.This model was supported by a chemical cross-linking study [101], showing trimer formation.

The order of the paracrystals was poor because it was only possible to form them by precipitating them with salts. Crystallisation can be regarded as slow precipitation. If molecules are given sufficient time to orient when coming out of solution they will form crystals. The preparation for electron microscopy was by fast drying on to a carbon coated grid. Slow methods were tried, for instance by dialysis to remove the detergent, but the result was a large aggregate. These were examined by X-ray diffraction but were not sufficiently ordered for this. The preparation was therefore limited with regard to determinations at higher resolution. The paracrystals could not be examined unstained because they required 'stain' to form. The intractability of these problems brought my research on this molecule to an end and a new investigation was undertaken with thin crystals.

The restriction enzyme crystals that were complexed to the specific decanucleotide showed reflections that extended to 0.3 nm. This puts them in a relatively small (but growing) group of biological molecule crystals that show high resolution. It was very interesting to find that the same protein with a different oligonucleotide produced crystals with very poor diffraction. The Matthews' coefficient (V_m) for this crystal was 3.3 nm^3 / kilodalton. This is 40% higher than the value for the decanucleotide crystal. The larger solvent channels in these crystals may be easily distorted when prepared in glucose. This finding could have consequences for other crystals that have not been found to have high resolution. There may be a critical density of protein necessary to give a structure that does not distort.

The close association of the enzyme dimers in the crystals of the decanucleotide complex would also support the model of a stacking of DNA oligomers into a rod running along one of the crystal axes. The strongly hydrophobic ends of the short DNA fragments must produce highly attractive surfaces on two opposite sides of the complex. In the complex with the octameric DNA the fragment may have been too short to extend to the surface.

A complete structural analysis of the complex from this crystal still remains to be undertaken and the problems of this analysis are considerable. The first

in determining the class of the crystal formed. The fact that systematic absences are not constant prevents combining data from different crystal. This problem was shown in the case of crotoxin complex crystals [139] to be due to different numbers of layers being present in different crystals. This may be the case here but the appearance of 'forbidden' reflections may also be caused by crystal bending. If a supporting film is not sufficiently rigid then a thin crystal resting on it will bow. This will then give a diffraction pattern from a range of different orientations from different parts of the curved crystal. A diffraction pattern of a glucose embedded catalase crystal is shown below. It has been tilted about the crystal's '<u>b</u>' axis.

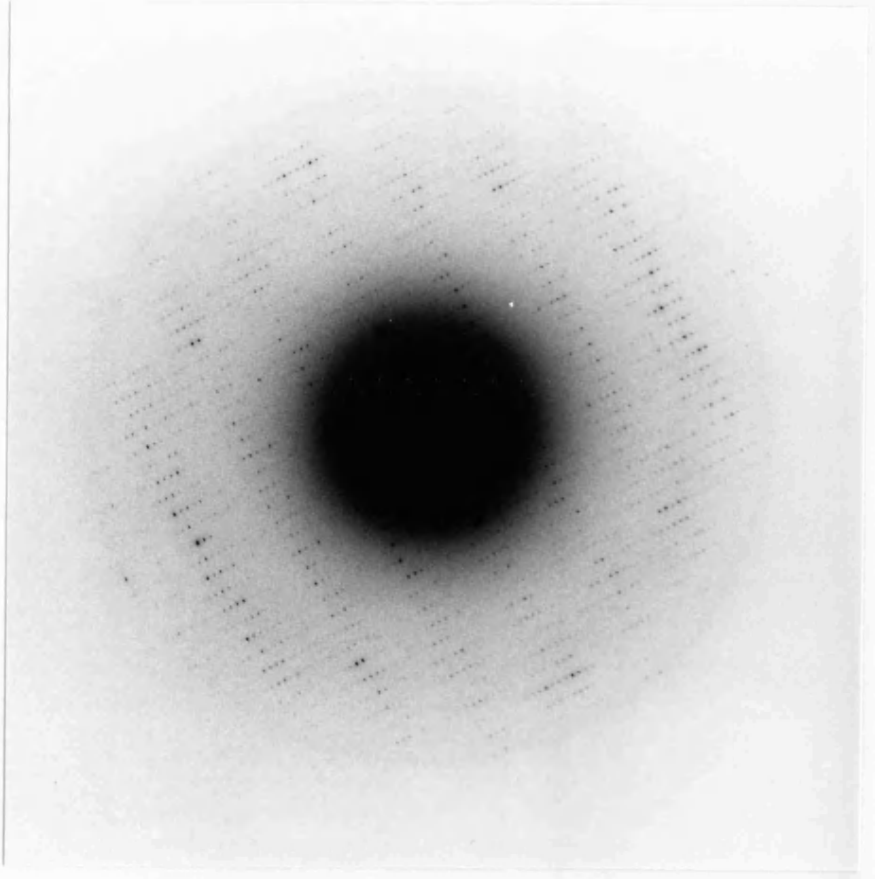

The Laue zones that cross the pattern can be seen to expand and join at high resolution. This is a consequence of the crystal being bent. The grids used in the crotoxin study have a supporting carbon film over 20 nm thick (T. W. Jeng personal communication), ten times the thickness used in this study.

In outlining the problems of high resolution structure determination, the case of the crotoxin complex is most germane to the restriction enzyme crystals. In the 0.35 nm resolution images that were obtained from crystals of this protein it was not possible to trace the protein backbone [140]. This is a consequence of superpositioning that was mentioned in the case of purple membrane. However, purple membrane is just one molecule thick, with crotoxin and the restriction enzyme crystals there are many layers and any small misalignment of tilt or curvature will degrade the image. The only solution of a high resolution structure is in a 3-dimensional reconstruction and this is an undertaking of a research group rather than an individual.

Crystallography is a rigorous discipline and has rules which are based on simple trigonometric relationships and symmetries. Electron microscopy was shown to break all the rules by having the unit cell change while it was being measured. The thinning of plastic sections was an accepted phenomenon in electron microscopy. When periodic specimens were found to have a different size, dependent on the angle of tilt required

to observe the repeating feature, it was shown to be a possible source of error [131]. When the thickness of negatively stained samples was also shown to be reducing by a similar amount (50%) it was only because the sample was crystalline that the effect could be monitored and quantified [141].

Since the publication of this work there have been investigations by other researchers which support the findings [142,143]. Also the change in thickness for plastic sections follows a very similar dose response curve to that found in the negatively stained samples [144]. There may well be the same mechanism of collapse taking place in both cases. They both have carbon-carbon atomic skeletons and have covalently bound hydrogen and side chains attached. Radiochemical evidence [25] suggests that loss of hydrogen and low molecular weight side chains is to be expected from electron irradiation. The residue then compacts as the remaining carbon core is increasingly cross-linked. The effect of lowering the temperature may be because of the retention of the side chain mass which is frozen in the sample at liquid nitrogen temperature. The bubbling being produced because of trapped hydrogen which is still a gas at this temperature.

The development of small dedicated computers controlling the operation of the electron microscope will mark an important advance for ease of operation and versatility. Progress in this direction is at an early

stage at present but, with larger memories and greater flexibility, computers will become an important feature of the future microscope. Such facilities, together with an electron detector in the microscope, would allow the storage of images and diffraction patterns digitally rather than on film.

Electron microscopy for biological specimens is currently going through a revolution because of the prospects of frozen hydrated microscopy. These are exciting times, the perfect specimen preparation that this technique offers is a wonderful opportunity for the biological investigator.

9. REFERENCES

[1] Cole,F.J., Annals of Science 2 , 1-46 and 185-235, (1937)

[2] Turner,G.L'E. and Bradbury,S., J.Roy.Micr.Soc., 85 , 435-447, (1966)

[3] Abbe,E. (1873) Arch f. Mikroscop. Anatomie 9, 413-468.

[4] Helmholtz,H. (1874) Ann. Physik u. Chemie, Jubleband 557-585.

[5] Koehler,A. (1904) Z. wiss. Mikroskopie 21, 129-165.

[6] Friedrich,W., Knipping,P. and Laue,M. Bayr. Ak. Wiss.303-322 (1912)

[7] Bragg,W.L., Nature 143 , 678, (1939)

[8] Yardley,K., Nature 122 , 810, (1928)

[9] De Broglie,L., Ann. de Physiques 3 , 22-128 (1925)

[10] Davisson,G. and Germer,L.H., Phys.Rev. 30 , 705-740 (1927)

[11] Busch,H., Ann. Phys. 81 , 974-993 (1926)

[12] Knoll,M. and Ruska,E., Ann. Physik. 12 , 607-640 (1932)

[13] Ruska,E., Z. Physik., 87 , 580-602 (1934)

[14] Ruska,E., Elektrotechn. Z., A, 531-543 (1957)

[15] Baldwin,J.M., Henderson,R., Beckman,E. and Zemlin,F. (1988 in press)

[16] Hillier,J., Knaysi,G. and Baker,R.F., J. Bact., 56 , 569-576 (1948)

[17] Hillier,J., Mudd,S., Smith,A.G. and Beutner,E.H., J. Bact., 60 , 641-654 (1950)

[18] Charlesby,A., Proc. Roy. Soc. A 215 , 187-214 (1952)

[19] Williams,R.C. and Wyckoff,R.W.G., J.A.C.S., 73 , 2057-2061 (1951)

[20] Williams,R.C., Biochim. Biophys., Acta 8 , 227-235 (1952)

[21] Hillier,J., J. Applied Phys., 19, 226-230 (1948)

[22] Bradley,D.E., Brit. J. Appl. Phys. 5 65-66 (1954)

[23] Menter,J.W., Proc. Roy. Soc. A 236 115-127 (1956)

[24] Agar,A.W., Frank,F.C. and Keller,A., Phil. Mag. 4 32-51 (1959)

[25] Reimer,L., Lab. Invest. 14 344-358 (1965)

[26] Stenn,K. and Bahr,G.F. J. Ultras. Str. Res., 31 526-550 (1970)

[27] Heidenreich,R.D., Hess,W.M., Ban,L.L., J. Appl. Cryst. 1 1-18 (1968)

[28] Franklin,R.E. and Holmes,K.C., Acta Cryst. 11 213-220 (1958)

[29] Williams,R.C.and Fisher,H.W. , J. Mol. Biol. 52 1737-1715 (1974)

[30] Glaeser,R.M. and Thomas,G. Biophys. J. 9 1073-1085 (1969)

[31] Cosslett,V.E., J. Micros. 113 113-129 (1978)

[32] Siegel,G.A., Z. Naturforsch, 27a 325-426 (1972)

[33] Taylor,K.A., J. Micros., 112 115-125 (1978)

[34] Dubochet,J. and Knapek,E., Chemica Scripta, 14 267-269 (1978)

[35] Salih,S.M. and Cosslett,V.E., J. Micros. 105 269-275 (1975)

[36] Klug,A. In: " New developments in electron microscopy ". The Royal Society, London, 89-125

[37] Rose,A. Adv. Electron 1 131-166 (1948)

[38] Kuo,I.A.M. and Glaeser,R.M., Ultramicros., 1 53-66 (1975)

[39] Unwin,P.N.T. and Henderson,R., J. Mol. Biol. 94 425-440 (1975)

[40] Jesior,J.-C., J. Ultrastruct. Res. 95 210-217 (1985)

[41] Glauert,A.M., Rogers,G.E. and Glauert,R.H., Nature 178 803 (1956)

[42] Hall,C.E., J. Biophys. Biochem. Cytol., 1 1-15 (1955)

[43] Brenner,S. and Horne,R.W., Biochim. Biophys. Acta, 34 103-110 (1959)

[44] Huxley,H.E. and Zubay,G., J. Mol. Biol. 2 10-18 (1960)

[45] Finch,J.T., J. Mol. Biol. 8 872-874 (1968)

[46] Matricardi,V.R., Moretz,R.C. and Parsons,D.F., Science 177 268-271 (1973)

[47] Valentine,R.C., Shapiro,B.M. and Stadtman,E.R., Biochemistry 7 2143-2152 (1968)

[48] Wrigley,N. J. Ultras. Res. 24 454-464 (1968)

[49] Taylor,K.A. and Glaeser,R.M., Science 186 1036-1037 (1974)

[50] Unwin,P.N.T. and Henderson,R., J. Mol. Biol. 94 425-440 (1975)

[51] Knapek,E. and Dubochet,J., J. Mol. Biol. 141 147-161 (1980)

[52] Chiu,W., Downing,K.H., Dubochet,J., Glaeser,R.M., Heide,H.G., Knapek,E., Kopf,D.A., Lamvik,M.K., Lepault,J., Robertson,J.D., Zeitler,E. and Zemlin,F., J. Microsc. 141 385-391 (1986)

[53] Dubochet,J., Lepault,J., Freeman,R., Berriman,J.A. and Homo, J.-C. J. Microsc. 128 219-237 (1982)

[54] Milligan,R.A., Brisson,A. and Unwin,P.N.T., Ultramicros. 13 1-15 (1984)

[55] Bragg,W.L., Nature 154 69-72 (1944)

[56] Unwin,P.N.T., Proc. Roy. Soc. A 329 327-359 (1972)

[57] Thon,F., Z. Naturforsch. 21A 476 (1966)

[58] Bragg,W.H., Trans. Roy. Soc. A 215 (1915)

[59] Klug,A. and Berger,J.E., J. Mol. Biol. 10 565-569 (1964)

[60] Klug,A. and De Rosier,D.J., Nature 212 29-32 (1966)

[61] De Rosier,D.J. and Moore,P.B., J. Mol. Biol. 52 355-362 (1970)

[62] Ten Eyck,L.F., Acta Cryst. A29 183-191 (1973)

[63] De Rosier,D.J. and Klug,A. Nature 217 130-134 (1968)

[64] Berriman,J.A., Bryan,R.K., Freeman,R. and Leonard,K.R., Ultramicrosc. 13 351-364 (1984)

[65] Namork,E. and Johansen,B.V., Ultramicrosc. 7 321-330 (1982)

[66] Reissig,M. Orrell,S.A., J. Ultras. Res. 32 107-119 (1970)

[67] Chui,W., Knapek,E., Jeng,T.W. and Dietrich,I., Ultramicrosc. 6 291-296 (1981)

[68] Glauert,A.M. and Thornley,M.J., Ann. Rev. Microbiol. 23 159-198 (1969)

[69] Weidel,W. and Pelzer,H. Adv. Enzymol. 26 193-232 (1964)

[70] Rosenbusch,J.P., J. Biol. Chem. 249 8019-8029 (1974)

[71] Braun,V., Biochem. Biophys. Acta. 415 335-377 (1975)

[72] Manstein,D.J., Berriman,J.A., Leonard,K., Rosenbusch,J.P., J. Mol. Biol. 189 701-707(1986)

[73] Nakamura,K., Masui,Y. and Inouye,M., J. Mol. Biol. 98 285-304 (1982)

[74] Bradford,M.M., Analyt. Biochem. 72 248-254 (1976)

[75] Doyle,B.B.. Hukins,D.W.L., Hulmes,D.J.S., Miller,A. and Woodhead-Galloway,J., J. Mol. Biol. 91 79-99 (1975)

[76] Reynolds,J.A. and Tanford,C., J. Biol. Chem. 245 5161-5165 (1970)

[77] Tanford,C. (1973). The Hydrophobic Effect. New York: J.Wiley & Sons Inc. pp. 143-145

[78] Garavito,R.M. and Rosenbusch,J.P., Methods in Enzymol. 125 309-328 (1986)

[79] Inouye,S., Takeischi,K., Lee,N., De Martini,M., Hirushima,A. and Inouye,M., J. Bacteriol. 127 555-563 (1976)

[80] Chapman,D. (1965). The Structure of Lipids. New York: J.Wiley & Sons Inc. p.291

[81] Pauling,L. and Corey,R.B., Nature 171 59-61 (1953)

[82] Crick,F.H.C., Acta Cryst. 6 689-697 (1953)

[83] Suzuki,E., Crewther,W.G., Fraser,R.D.B., McRae,T.P. and McKern,N.M. J. Mol. Biol. 73 275-278 (1973)

[84] Crick,F.H.C., Acta Cryst. 6 685-689 (1953)

[85] Cohen,C. and Holmes,K.C., J. Mol. Biol.6 423-432 (1963)

[86] Sodek,J, Hodger,R.S., Smillie,L.B. and Turasek,L., Proc. Nat. Acad. Sci. 69 3800-3804 (1972)

[87] Henderson,R., J. Mol. Biol. 93 123-138 (1975)

[88] Inouye,M., Proc. Nat. Acad. Sci. 71 2396-2400 (1974)

[89] Crick,F.H.C., Acta Cryst. 6 689-697 (1953)

[90] Philips,G.N., Filles,J.P. and Cohen,C., Biophys. J. 32 485-502 (1980)

[91] Lowey,S., Slayter,H.S., Weeds,A.G. and Baker,H., J. Mol. Biol. 42 1-29 (1969)

[92] Olander,J., Emerson,M.F. and Holtzer,A., J. Amer. Chem. Soc. 89 308-309 (1967)

[93] Geisler,N. and Weber,K., EMBO J. 1 1649-1656 (1982)

[94] Woods,E.F. and Inglis,A.S., Int. J. Biol. Macromol. 6 277-283 (1984)

[95] Steinert,P.M., Steven,A.C. and Roop,D.R., Cell 42 411-419 (1985)

[96] Philips,G.N., Flicker,P.F., Cohen,C., Manjula,B.N. and Fischetti,V.A. Proc. Nat. Acad. Sci. 78 4689-4693 (1981)

[97] Wilson,L.A., Sekehel,J.J. and Wiley,D.C., Nature 289 373-378 (1981)

[98] Doolittle,R.F., Goldbaum,D.M. and Doolittle,L.R., J. Mol. Biol. 120 311-325 (1978)

[99] Steven,A.C., Trus,B.L., Maizel,J.V., User,M., Parry,D.A.D., Wall,J.S., Hainfield,J.F., and Studier,F.W., J. Mol. Biol. (in press)

[100] Mack,J.W., Torchia,D.A. and Steinert,P.M., Biophys. J. 51 86a (1987)

[101] Yu,F., Furukawa,H., Nakamura,K. and Mizushima,S., J. Biol. Chem. 259 6013-6018 (1984)

[102] Watson,J.D. and Crick,F.H.C., Nature 171 737-738 (1953)

[103] Dussoix,D. and Arber,W., J. Mol. Biol. 5 37-49 (1962)

[104] Rosamund,J., Endlich,B. and Linn,S., J. Mol. Biol. 129 619-635 (1979)

[105] Kelly,T.J. and Smith,H.O., J. Mol. Biol. 51 393-409 (1970)

[106] Schildkraut,L., Banner,C.D.B., Rhodes,C.S. and Parekh,S., Gene 27 327-337 (1984)

[107] Bougeleret,L., Tenchini,M.L., Botterman,J. and Zabeau,M., Nucleic Acids Res. 13 3823-3839 (1985)

[108] D'Arcy,A, Brown,R.S., Zabeau,M., Wijnaendts,R. and Winkler,F.K. J. Biol. Chem. 260 1987-1990 (1985)

[109] Greene,P.J., Heyneker,H.L., Bolivar,F., Rodriguez,R.L., Bletlach,M.C., Covarrubias,A.A., Backman,K., Russel,D.J., Tait,R. and Boyer,H.W., Nucleic Acids Res. 5 2373-2380 (1978)

[110] Sproat,B.S., Beijer,B., Rider,P. and Neuner,P., Nucleic Acids Res. 15 4837-4848 (1987)

[111] Leonard,K., Wingfield,P., Arad,T. and Weiss,H., J. Mol. Biol. 149 259-274 (1981)

[112] Halford,S., Lovelady,B.M. and McCallum,S.A., Gene 41 173-181 (1986)

[113] Matthews,B.W., J. Mol. Biol. 33 491-497 (1968)

[114] Moras,D. (ed) (1985). Crystallography in Molecular Biology. London: Plenum Press. pp. 345-352. Winkler,F.K., Brown,R.S., Leonard,K. and Berriman,J.

[115] Kendrew,J.C., Dickerson,R.E., Strandberg,B.E., Hart,R.G., Davies,D.R., Phillips,D.C. and Shore,V.C., Nature 185 422-427 (1960)

[116] Anderson,J.E., Ptashne,M. and Harrison,S.C., Nature 326 846-852 (1987)

[117] McClarin,J.A., Frederick,C.A., Wang,B., Greene,P., Boyer,H.W., Grable,J. and Rosenberg,J., Science 234 1526-1536 (1987)

[118] Grubb,D.T., J. Mat. Sci. 9 1715-1736 (1974)

[119] Stenn,K. and Bahr,G.F., J. Ultrastruct. Res. 31 526-550 (1970)

[120] Laue,M.v., Ann. Physik (Leipzig) 26 55-60 (1931)

[121] Bragg,W.L. and Kirchner,F., Nature 127 738-740 (1931)

[122] Dorset,D.L. and Parsons,D.F., Acta Cryst. A31 210-215 (1975)

[123] Henderson,R. and Unwin,P.N.T., Nature 257 28-32 (1984)

[124] Parsons,D.F., J Appl. Phys. 46 938 (1975)

[125] Unwin,P.N.T., J. Mol. Biol. 98 235 (1975)

[126] Jesior,J.-Cl., EMBO J. 1 1423-1428 (1982)

[127] Cosslett,A., J. Roy. Micros. Soc. 79 263-276 (1960)

[128] Moody,M.F., J. Mol. Biol. 25 167-200 (1967)

[129] Unwin,P.N.T., J. Mol. Biol. 87 657-670 (1974)

[130] Johansen,B.V., Micron 7 145-156 (1976)

[131] Bennett,P.M., J. Cell Sci. 15 693-701 (1974)

[132] Luther,P.K. and Crowther,R.A., Nature 307 566-568 (1984)

[133] Freeman,R. and Leonard,K.R., J. Microsc. 122 275-286 (1981)

[134] Glaeser,R.M. and Hobbs,L.W., J. Microsc. 103 209-214 (1975)

[135] Fryer,J.R. and Holland,F., Ultramicrosc. 11 67-70 (1983)

[136] Jaffe,J.S. and Glaeser,R.M., Ultramicrosc. 13 373-378 (1984)

[137] Dubochet,J., Chang,J.-J., Freeman,R., Lepault,J. and McDowall,A.W. Ultramicrosc. 10 55-62 (1982)

[138] Baldwin,J. and Henderson,R., Ultramicrosc. 14 319-336 (1984)

[139] Jeng,T.W. and Chiu,W., J. Mol. Biol. 164 329-346 (1983)

[140] Jeng,T.W., Chiu,W., Zemlin,F. and Zeitler,E., J. Mol. Biol. 175 93-97 (1984)

[141] Berriman,J. and Leonard,K.R., Ultramicrosc. 19 349-366 (1986)

[142] Jesior,J.-Cl. and Wade,R.H., Ultramicrosc. 21 313-320 (1987)

[143] Seymour,J. and DeRosier,D.J., J. Microsc. 148 195-210 (1987)

[144] Luther,P.K., Lawrence,M.C. and Crowther,R.A., Ultramicrosc. 24 7-18 (1988)

9. PUBLICATIONS

The paper on changes of specimen thickness is styled as part II of an overall study of methods to determine thickness in electron microscope samples. The earlier, part I, publication is included with this set for completeness.

J. Mol. Biol. (1986) 189, 701-707

Ultrastructure of Native Lipoprotein from *Escherichia coli* Envelopes

D. J. Manstein†, J. Berriman‡, K. Leonard and J. P. Rosenbusch§

European Molecular Biology Laboratory (EMBL)
Postfach 10.2209, 6900 Heidelberg
Federal Republic of Germany

(Received 29 November 1985, and in revised form 3 March 1986)

The free form of the major lipoprotein from *Escherichia coli* cell envelopes has been purified to homogeneity by gentle extraction procedures and conventional chromatographic separations in a non-ionic detergent. The morphology of paracrystals obtained from homogeneous protein was investigated by low-dose electron microscopy. Electron diffraction of the paracrystals was consistent with α-helices arranged perpendicularly to the main cross-band with a periodicity of 20 nm.

1. Introduction

The major lipoprotein of Gram-negative bacteria is a small, well-characterized polypeptide consisting of 58 amino acid residues (Braun & Rehn, 1969). There has been considerable interest in this protein since its characterization by Braun (1975). It occurs about $7{\cdot}5 \times 10^5$ copies per cell (De Martini *et al.*, 1976) and expression and processing of its precursors have been studied extensively (Vlasuk *et al.*, 1984). Structurally, it has several unique features: the protein lacks histidine, tryptophan, glycine, proline and phenylalanine. The N-terminal cysteine is linked by a thioether to glycerol, to which two fatty acids are attached by ester linkage and a third is covalently attached to the terminal α-amino group of the cysteine residue Braun & Bosch, 1972). The ε-amino group of the C-terminal lysine is linked to the carboxyl group of every 10th to 12th mesodiaminopimelic acid residue of the peptidoglycan (Braun & Sieglin, 1970). The latter bond occurs in one third of all lipoprotein molecules present. The other two thirds exist in an unlinked or free form (Inouye *et al.*, 1972). It is believed that the lipoprotein plays an important role in stabilizing the cell envelope and in altering the functional properties of various outer membrane and possibly periplasmic proteins by physically interacting with them. A prerequisite for the understanding of these interactions is the knowledge of the native structure of the proteins involved. Former purifications of lipoprotein were based on extracting cell envelopes by boiling them in 4% (w/v) sodium dodecyl sulphate and fractionation with organic solvents. Such treatment is, of course, strongly denaturing, with conversion of the native conformation to a predominantly α-helical structure (Reynolds & Tanford, 1970). The observation that lipoprotein consisted of about 70% α-helices (Braun *et al.*, 1976) therefore required independent evidence. Here we describe a gentle extraction procedure, followed by standard purification techniques. Paracrystals (Inouye *et al.*, 1976; De Martini *et al.*, 1976) of the apparently native form have been studied by electron microscopy. We have also estimated the secondary structure of lipoprotein from our preparation by circular dichroism. The low-resolution structural information has been used to build a model for the molecular interactions of lipoprotein. Structural analysis at higher resolution was performed by applying low-dose electron diffraction techniques to the paracrystals.

2. Materials and Methods

(a) *Culture conditions*

Escherichia coli strain JA221 *lpp-/F'lac* i^q/pKEN 125 (Nakamura *et al.*, 1982) was grown in L-broth containing 50 mg ampicillin/l (5×10^8 to 8×10^8 cells/ml). When cell growth reached the end of the exponential

† Present address and author to whom correspondence should be sent: Max-Planck-Institut für Medizinische Forschung, Abteilung Biophysik, Jahnstrasse 29, D-6900 Heidelberg, F.R.G.

‡ Present address: University of Bath, Claverton Down, Bath, England.

§ Present address: Biozentrum, Klingelbergstrasse 70, CH-4056 Basel, Switzerland.

0022-2836/86/120701-07 $03.00/0

phase, 0·1 mM-IPTG (isopropyl-β-D-thiogalactopyranoside) was added. After 15 min of incubation, cells were harvested by centrifugation, frozen immediately and stored at −80°C. Approximately 1·4 g of cells (wet weight) were obtained per litre of culture medium.

(b) *Protein determination*

In most experiments, protein concentrations were measured by the method of Bradford (1976). The Biuret reaction was routinely used for protein analysis in the early stages of purification and amino acid analysis for precise determinations.

(c) *Electrophoresis*

Proteins were separated by discontinuous sodium dodecyl sulphate/polyacrylamide gel electrophoresis following the procedure of Laemmli (1970). The samples and standards were run on 15% (w/v) acrylamide gels after denaturation in incubation buffer at 100°C. Protein was stained with Coomassie brilliant blue R250/G250 (4 : 1, w/w).

(d) *Purification procedure*

In a typical purification, 60 g of frozen cell paste was thawed in 230 ml of distilled water containing 1 mM-EDTA. After centrifugation (20 min at 500 ***g***), cells were resuspended in 100 ml of breaking buffer (50 mM-sodium phosphate, pH 7·6) containing 3 mM-NaN_3 0·1 M-NaCl, 5% (w/v) sucrose, 2 mM-$MgCl_2$ and 2 mg each of ribonuclease and deoxyribonuclease. Cells were broken in a French pressure cell. Cell envelopes were pelleted by centrifugation (60 min at 24,000 ***g***) and resuspended in 65 ml of 0·1 M-KP_i (pH 6·6) containing 10 mM-$MgSO_4$ and 2·5 mg each of ribonuclease and deoxyribonuclease. After 30 min of incubation at 37°C, this suspension was centrifuged at 38,000 ***g*** for 30 min. The final membrane fraction was pre-extracted once by suspending the pellet in extraction buffer containing 10 mM-sodium phosphate (pH 5), 5 mM-citric acid, 3% (v/v) octyl-POE (octyl-polydisperse-oligooxyethylene), 3 mM-NaN_3, 0·2 mM-dithiothreitol and immediately centrifuged for 30 min at 37,000 ***g***. Pellets were extracted repeatedly as follows. The cells were resuspended in 60 ml of extraction buffer and incubated for 45 min. The suspension was then centrifuged at 30,000 ***g*** and extractions repeated until no more lipoprotein could be extracted, as judged by polyacrylamide gel electrophoresis. Solubilization was complete after 4 to 6 extractions. The extracts containing most of the lipoprotein were concentrated by pressure dialysis using an Amicon PM-10 membrane. After dialysis against buffer A (25 mM-imidazole·HCl (pH 7), 1% octyl-POE, 0·2 mM-dithiothreitol, 3 mM-NaN_3), the concentrate containing 4 to 5 mg protein/ml was loaded onto a column of Whatman DE52 (5 cm × 25 cm). The bound protein was eluted at 65 ml/h with 1·5 l of a linear gradient from 0 to 0·3 M-NaCl in buffer A. Fractions containing lipoprotein were pooled and concentrated by pressure dialysis as described above. The concentrated solution was dialysed against buffer A and then loaded onto a chromatofocusing column (1·5 cm × 34 cm) pre-equilibrated with buffer A. Lipoprotein was eluted with a polybuffer gradient from pH 7 to 4, which contained 1% octyl-POE and 0·2 mM-dithiothreitol. Lipoprotein-containing fractions were collected, concentrated by pressure dialysis and stored at 4°C. Polybuffer was removed from lipoprotein using a Sephadex G75 column.

(e) *Organic phosphate determination*

The method of Fiske & Subbarow (1925) was used to determine the organic phosphate content of the native lipoprotein.

(f) *Circular dichroism measurements*

Circular dichroism spectra were measured with a CNRS Roussel Jouan Dichrographe III spectropolarimeter. Spectra were analysed by the method of Provencher & Glöckner (1981). The concentrations of the lipoprotein solutions used were determined by amino acid analysis.

(g) *Amino acid analysis and digestion by carboxypeptidase*

Amino acid analysis was carried out with a Durrum D500 set to a sensitivity of 2·5 nmol amino acid. Samples containing approximately 0·1 mg of lipoprotein were hydrolysed in trifluoracetic acid and concentrated HCl (1 : 2, v/v) for 25 min and 50 min, following the procedure of Tsugita & Scheffler (1982). Glyceryleysteine was determined after formic acid oxidation of the lipoprotein (Hirs, 1967). D-Glucosamine content was estimated after hydrolysis in constant boiling (6 M) HCl at 106°C for 24 h in sealed, evacuated tubes. Carboxypeptidase digestion was carried out in pyridine/acetate/collidine buffer (pH 8·5) using DFP (diisopropyl-fluorophosphate)-treated carboxypeptidase A and B (Sigma). Samples were incubated for 16 h at 37°C (Tsugita & van den Broek, 1980).

(h) *Electron microscopy*

Preparations were made by drying the detergent-solubilizing protein (1 mg protein/ml in 1% octyl-POE) in the presence of the stains 1% (w/v) UAc (uranyl acetate) 1% (w/v) PTA (phosphotungstic acid), brought to pH 7·0 with KOH, or 1% (w/v) CaAc (calcium acetate) on carbon/collodion grids. These were examined in a Philips EM301 electron microscope at 80 kV. Images were taken at 25,000-fold magnification, calibrated using negatively stained catalase. Selected area electron diffraction was carried out in the standard conditions with the intermediate lens switched off. The camera length (966 mm) was calibrated against a thallous chloride specimen. Measurements were accurate to within 1%. Low-dose techniques were developed from earlier work (Unwin & Henderson, 1975; Jeng & Chiu, 1983). The dose rates were measured using the optical density of exposed Kodak SO-163 (4463) film developed for 12 min in full strength D19 developer, and using a value of $1e^-/Å^2$ for optical density 2·2. Diffraction patterns were taken with 0·1 to 0·75 $e^-/Å^2$ and images with between 3 and 4 $e^-/Å^2$.

3. Results

(a) *The native state of lipoprotein*

The results of the purification procedure are summarized in Table 1. In a typical preparation, as described in Materials and Methods, 35 mg of pure lipoprotein were obtained from 60 g of wet cells. The lipoprotein was homogeneous as indicated by the single protein band on analytical gel electrophoresis and by comparison of the amino acid composition of the purified lipoprotein with those determined for the bound (Braun, 1975) and the free form (Inouye *et al.*, 1976) of lipoprotein.

Table 1
Purification of lipoprotein

Step	Volume (ml)	Protein concn (mg/ml)	Total (mg)
Crude extract supernatant†	120	9·0	1100
Extracts			
1	65	4·4	286
2	69	2·0	138
3	69	0·35	24
4	61	0·38	23
5	60	0·33	20
6	56	0·26	15
Pooled extracts 2–6	315	0·7	220
DE52 pool	176	0·4	70
Chromatofocusing pool	59	0·6	35

† From 60 g of cells, wet weight.

A significant difference from previous reports was that lipoprotein from our preparation contained one lysine residue less per molecule. Enzymatic degradation with DFP-treated carboxypeptidases A and B revealed that the lipoprotein we isolated lacked the C-terminal lysine that is involved in the linkage to murein in the murein–lipoprotein complex. When treated with carboxypeptidases A and B, the molar ratios of the amino acids released were: Arg, 0·35; Tyr, 0·34; Lys, 0·31 (Nakamura *et al.*, 1980). Carboxypeptidase A alone did not release any amino acid. Preparations were not contaminated with the bound form since diaminopimelic acid and D-glucosamine could not be detected in purified lipoprotein. The phosphate content was less than 0·05 mol of phosphate per mol of the lipoprotein, indicating that the purified protein was essentially free of phospholipids and lipopolysaccharides.

The α-helical content estimated by circular dichroism was 87 (±10)%. This value was measured in the presence of 0·5%, 1% and 2% octyl-POE and 50 mM-sodium phosphate (pH 7·6). An influence of Mg^{2+} on the secondary structure of the lipoprotein, as described by Lee *et al.* (1977), could not be detected.

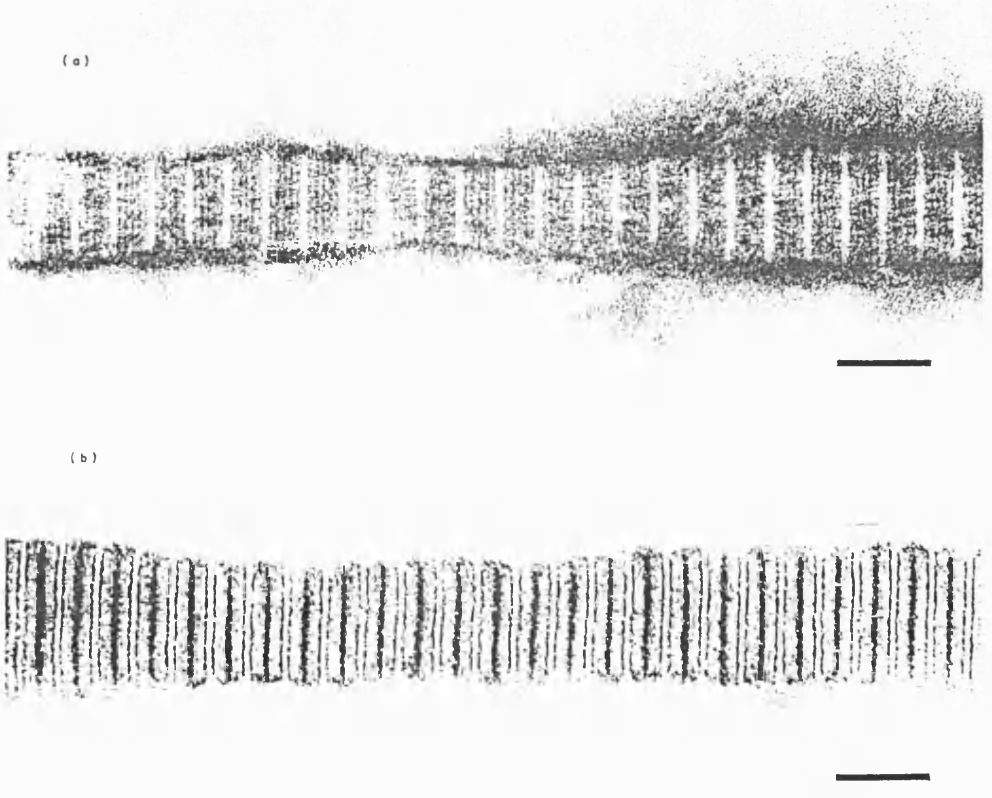

Figure 1. Paracrystals formed by drying in (a) uranyl acetate and (b) potassium phosphotungstate. The scale bars represent 50 nm. Notice the similarity of the overall morphology with those observed previously (De Martini *et al.*, 1976).

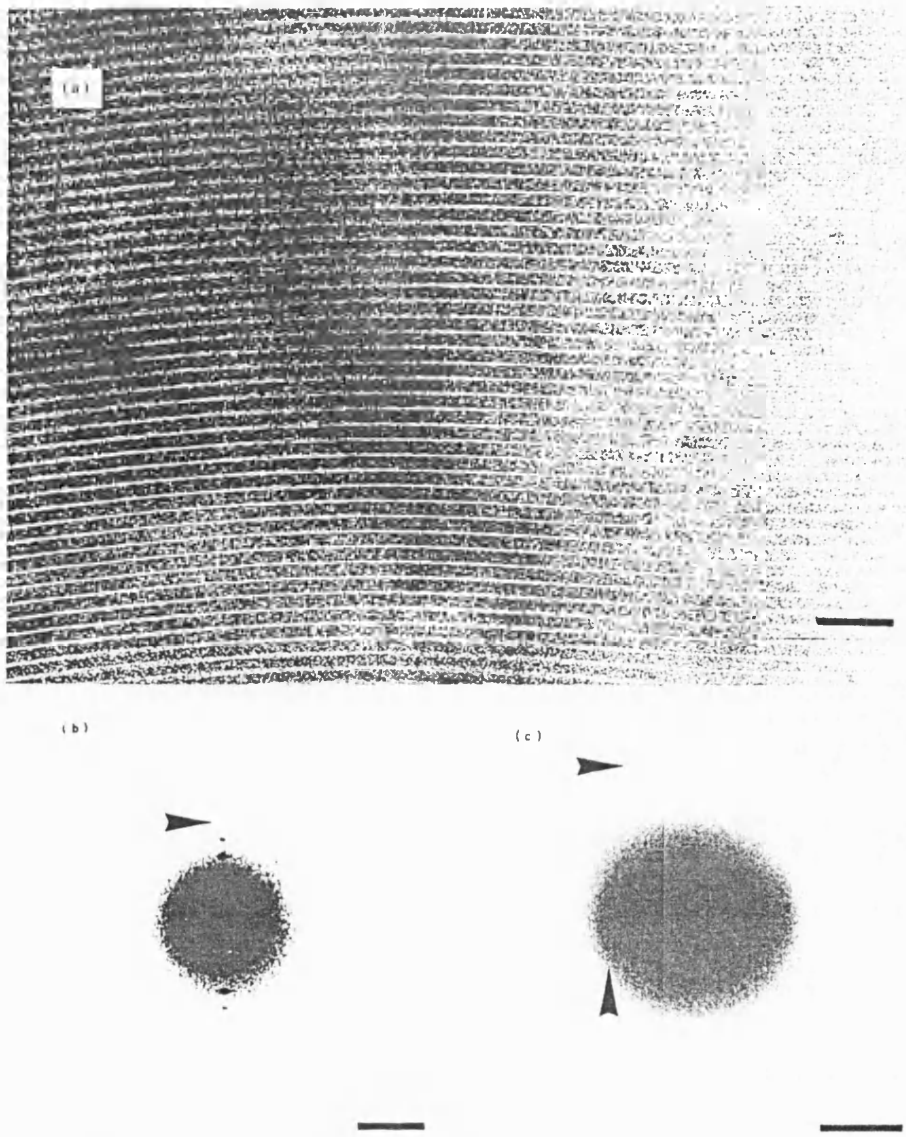

Figure 2. (a) Part of a large paracrystal formed by drying in calcium acetate. The scale bar represents 100 nm. (b) Electron diffraction pattern of a paracrystal as in (a) of a low exposure, optically enlarged so that the scale bar represents 0·2 nm^{-1}. (c) As in (b) but with a longer exposure time and a smaller optical enlargement so that the scale bar represents 1·0 nm^{-1}.

Lipoprotein, when mixed with uranyl acetate and dried, produced stained paracrystals (Fig. 1(a)). The periodicity was found to be 20 nm, with a bright, stain-excluding region 3 nm wide, alternating with a darker banded region of 17 nm width. The light region is likely to correspond to lipid and the darker regions to protein, with the banding pattern arising from positive staining of anionic acid residues. With PTA as the stain, paracrystals with the same periodicity and stain-excluding region were formed but with a different banding pattern reflecting the (positive) staining of cationic residues with the

Figure 3. An area of paracrystals formed with a low concentration (0·01%) of PTA and dried with calcium acetate (1%). The arrows point towards regions where the cross-striations are easily seen. The scale bar represents 100 nm. The insertion (bottom right) is at 2·75× higher optical magnification.

anionic dye (Fig. 1(b)). With both UAc and PTA, the banding patterns showed mirror symmetry at right angles to the axis of the paracrystal.

When calcium acetate was used, larger paracrystals up to 5 μm in diameter were formed, which were thin enough for electron microscopy (Fig. 2). These showed the same 20 nm periodicity but banding was less apparent. Electron diffraction from such a paracrystal gave, at low exposure (0·1 $e^-/Å^2$) and 20 nm periodicity extending to the seventh order (Fig. 2(b)). This resolution limit was presumably due to long-range disorder caused by bending of the planes. At an exposure of 0·75 $e^-/Å^2$, the paracrystals gave diffraction patterns showing high-resolution organization (Fig. 2(c)). This pattern is oriented as in Figure 2(b) and shows arcs at 1(±0·1) nm equatorially (perpendicular to the 20 nm spacing of the paracrystal) and arcs at 0·5 nm meridionally (parallel to the 20 nm spacing). These patterns faded with increasing electron dose and had disappeared after 1·0 $e^-/Å^2$.

A double-staining experiment performed on the lipoprotein with PTA at low concentrations (0·01%) did not yield paracrystals on drying. If calcium acetate was present, small and very thin paracrystals formed during drying (Fig. 3). These images again had the overall banding pattern characteristic for PTA staining, but in addition, revealed a 2 nm cross-striation. This fine structure, indicated by arrows in the Figure, was radiation-sensitive (see above) and was only present in the first exposure from any region.

4. Discussion

The only direct indication of structural integrity in proteins that lack measurable biological activity, such as murein–lipoprotein, consists of monitoring their spectral and chemical properties. Combined with structural studies, they may indicate the native conformation and possible changes thereof. Murein–lipoprotein, purified by the procedure of Braun or Inouye and examined by circular dichroism measurements, gave an α-helical content of over 80%. It is known that boiling in dodecyl sulphate tends to cause a shift of proteins into α-helicity (Reynolds & Tanford, 1970) regardless of their native conformation (Tanford, 1973). Since this method was originally used for the purification,

it could not be excluded that the resulting structure was an artifact of the preparation rather than reflecting the native conformation. For this reason, we developed the new purification procedure, all steps of which were known not to affect the function and structure of other *E. coli* outer membrane proteins such as the porins (Garavito & Rosenbusch, 1986). We show here that ellipticity measurements with protein prepared by the method applied here give us a high α-helix content, although this, as pointed out, cannot be used as affirmative evidence. Unlike earlier studies (Inouye *et al.*, 1976), the purified lipoprotein lacked the C-terminal lysine residue. The observation appears to be of particular interest since this residue is responsible for the linkage to the peptidoglycan in the bound form of the lipoprotein. At present it is not clear whether this processing occurs in the cell by the exo- and transpeptides present in the bacterial envelope as a significant process in the formation of a stable form of this structure.

In spite of this reserve, our results are in good agreement with the model proposed by De Martini *et al.* (1976) for the overall organization of lipoprotein molecules within the paracrystal. It is particularly noteworthy that the staining patterns one would predict from the amino acid sequence for cationic and anionic stains are in good agreement with a head-to-head association. One difference between our and their observations is the periodicity of the paracrystals, which is 20 nm in our preparations rather than 22 nm in theirs. This difference does not appear to be due to an error in measurement, but mainly to the thickness of the stain-excluding region (3 nm for our preparation against 4·6 nm in theirs), which presumably consists of lipid and detergent. This could be explained by the different detergents used in the formation of paracrystals. As we have not observed the 0·42 nm acyl chain packing periodicity, typical or a bilayer, and which would be expected on the equator of the electron diffraction pattern, it appears unlikely that the stain-excluding region is a bilayer as has been suggested. A gap of 3 nm is indeed too small to accommodate two palmitoyl chains in extended form in a single bilayer, but could well be due to interdigitation of fatty acyl residues and some detergent.

The 0·52 nm meridional arcs found by electron diffraction are at a spacing typical for coiled-coil arrangements of α-helices (Pauling & Corey, 1953; Cohen & Holmes, 1963), as they have been found in α-keratin (Suzuki *et al.*, 1973), paramyosin (Cohen & Holmes, 1963), tropomyosin (Sodek *et al.*, 1972) and bacteriorhodopsin (Henderson, 1975). The last example is of particular relevance here as the 0·52 nm spacing may be coming from a lipid phase. A 0·15 nm spacing would confirm a protein origin of the meridional reflections. Our failure to observe this is likely to be due to radiation damage that limits the resolution. Tilting has not yet been performed and it may be that curvature of the Ewald sphere was important. The extension of the reflection measured as the width of half intensity implies that features with this periodicity are about 20 nm long on average. This is consistent with the reflection being from coiled-coil α-helices aligned within the paracrystal.

The differences in banding patterns seen with cationic (UAc) and anionic (PTA) staining are similar to those observed for collagen (Doyle *et al.*, 1975) and are related to the distribution of negative and positive charges along the sequence. The presence of a mirror plane in the patterns strongly suggests that there is a regular head-to-head, tail-to-tail arrangement of lipoprotein molecules along the axis of the paracrystal.

A choice exists for the number of α-helices that make up the complex. Two models have been advanced for lipoprotein on the basis of heptad repeats in its amino acid sequence. Inouye (1974) proposed a hexameric form while McLachlan (1978) favoured a dimeric coiled-coil structure. In principle, a triple coiled-coil also seems possible. The 2 nm striations, which we report in the paracrystals shown here, would be compatible with either a double or triple-helix-stranded coiled-coil (Dobb, 1966).

Detailed analyses revealed double helix coiled-coil interactions in tropomyosin (McLachlan & Stewart, 1975), and myosin (McLachlan & Karn, 1982). Wilson *et al.* (1981) described triplet-stranded α-helical coiled-coils in the high-resolution X-ray analysis of haemaglutinin of influenza virus, which also exhibits the heptad arrangement of hydrophobic residues. Three-stranded ropes had been observed earlier in fibrinogen (Doolittle *et al.*, 1978). For the lipoprotein, a firm distinction between these alternatives is not possible on the basis of the diffraction data obtained with dried material.

We thank Drs P. Green and M. Inouye for their generous gift of the strain used in this work, Professor Akira Tsugita for carrying out amino acid analyses, and C. Barber for expert secretarial assistance.

References

Bradford, M. M. (1976). *Anal. Biochem.* **72**, 248–254.
Braun, V. (1975). *Biochim. Biophys. Acta*, **415**, 335–377.
Braun, V. & Bosch, V. (1972). *Proc. Nat. Acad. Sci., U.S.A.* **69**, 8154–8159.
Braun, V. & Rehn, K. (1969). *Eur. J. Biochem.* **10**, 426–438.
Braun, V. & Sieglin, H. (1970). *Eur. J. Biochem.* **13**, 336–346.
Braun, V., Rotering, H., Ohm, J. P. & Hagemaier, H. (1976). *Eur. J. Biochem.* **70**, 601–610.
Cohen, C. & Holmes, K. C. (1963). *J. Mol. Biol.* **6**, 423–432.
De Martini, M., Inouye, S. & Inouye, M. (1976). *J. Bacteriol.* **127**, 564–571.
Dobb, M. G. (1966). *J. Ultrastruc. Res.* **14**, 294–299.
Doolittle, R. F., Goldbaum, D. M. & Doolittle, L. R. (1978). *J. Mol. Biol.* **120**, 311–325.
Doyle, B. B., Hukins, D. W. L., Hulmes, D. J. S., Miller,

A. & Woodhead-Galloway, J. (1975). *J. Mol. Biol.* **91**, 79–99.
Fiske, C. H. & Subbarow, Y. (1925). *J. Biol. Chem.* **66**, 375–400.
Garavito, R. M. & Rosenbusch, J. P. (1986). *Methods Enzymol.* **125**, in press.
Henderson, R. (1975). *J. Mol. Biol.* **93**, 123–138.
Hirs, C. M. W. (1967). *Methods Enzymol.* **11**, 197–203.
Inouye, M. (1974). *Proc. Nat. Acad. Sci., U.S.A.* **71**, 2396–2400.
Inouye, M., Shaw, J. & Shen, C. (1972). *J. Biol. Chem.* **247**, 8154–8159.
Inouye, S., Takeischi, K., Lee, N., De Martini, M., Hirushima, A. & Inouye, M. (1976). *J. Bacteriol.* **127**, 555–563.
Jeng, T. W. & Chiu, W. (1983). *J. Mol. Biol.* **164**, 329–346.
Laemmli, U. K. (1970). *Nature (London)*, **227**, 680–685.
Lee, N., Cheng, E. & Inouye, M. (1977). *Biochim. Biophys. Acta*, **465**, 650–656.
McLachlan, A. D. (1978). *J. Mol. Biol.* **122**, 493–506.
McLachlan, A. D. & Karn, J. (1982). *Nature (London)*, **299**, 226–231.
McLachlan, A. D. & Stewart, M. (1975). *J. Mol. Biol.* **98**, 295–304.
Nakamura, K., Pirtle, R. M., Pirtle, I. L., Takaishi, K. & Inouye, M. (1980). *J. Biol. Chem.* **255**, 210–216.
Nakamura, K., Masui, Y. & Inouye, M. (1982). *J. Mol. Appl. Genet.* **1**, 289–299.
Pauling, L. & Corey, R. B. (1953). *Nature (London)*, **171**, 59–61.
Provencher, S. W. & Glöckner, J. (1981). *Biochemistry*, **20**, 33–37.
Reynolds, J. A. & Tanford, C. (1970). *J. Biol. Chem.* **245**, 5161–5165.
Sodek, J., Hodger, R. S., Smillie, L. B. & Turasek, L. (1972). *Proc. Nat. Acad. Sci., U.S.A.* **69**, 3800–3804.
Suzuki, E., Crewther, W. G., Fraser, R. D. B., McRae, T. P. & McKern, N. M. (1973). *J. Mol. Biol.* **73**, 275–278.
Tanford, C. (1973). *The Hydrophobic Effect*, pp. 143–145. John Wiley and Sons, Inc., New York.
Tsugita, A. & Scheffler, J.-J. (1982). *Eur. J. Biochem.* **124**, 585–588.
Tsugita, A. & van den Broek, R. (1980). *Methods in Peptide and Protein Sequence Analysis*, pp. 356–369. Elsevier, North-Holland Biomedical Press.
Unwin, P. N. T. & Henderson, R. (1975). *J. Mol. Biol.* **94**, 425–440.
Vlasuk, G. P., Inouye, S. & Inouye, M. (1984). *J. Biol. Chem.* **259**, 6195–6200.
Wilson, I. A., Skehel, J. J. & Wiley, D. C. (1981). *Nature (London)*, **289**, 366–373.

Edited by H. E. Huxley

STRUCTURAL STUDIES OF ECO RV ENDONUCLEASE AND OF ITS COMPLEXES WITH SHORT DNA FRAGMENTS

Fritz K. Winkler, Raymond S. Brown, Kevin Leonard and John Berriman

European Molecular Biology Laboratory
Meyerhofstr. 1, Postfach 10.2209, 6900 Heidelberg
Federal Republic of Germany

INTRODUCTION

Many bacteria restrict the expression of foreign DNA introduced through phage infection, conjugation or transformation. At the molecular level such host-controlled restriction is the result of an endonuclease activity which cuts foreign DNA and a modification activity which protects the host's DNA against this cleavage.
Of the three types of restriction-modification systems usually distinguished the type II systems are the simplest and consist of two separate enzymes, an endonuclease and a methylase which recognize the same sequence of typically 4 to 6 base pairs. The endonucleases cleave double stranded DNA at these recognition sites in the presence of Mg^{2+} ions. Their remarkable specificity and its modulation by various factors make them attractive systems for structurally oriented studies of protein nucleic acid interactions (for a recent review see Modrich and Roberts[1]).

THE SPECIFICITY OF TYPE II RESTRICTION ENDONUCLEASES

Of the approximately 400 known type II endonucleases only the Eco RI enzyme has been studied in great detail. Quantitative data on its accuracy under normal buffer conditions have recently been measured by Pingoud and Alves[2]. They find that the canonical site (-GAATTC-) is attacked 3000 and 9000 times faster than the two most labile non-canonical sites which are present on the DNA fragments used in their studies. In the presence of spermidine cleavage at non-canonical sites becomes even slower[3]. The opposite trend, i.e. enhanced cleavage at non-canonical sites, is observed under non-optimal buffer conditions[4,5]. These so-called * conditions are high pH, low ionic strength, the presence of polar organic solvents or the replacement of Mg^{2+} by Mn^{2+}. Together this means that the accuracy of Eco RI endonuclease, expressed as the relative cleavage rate at the canonical site versus that at the most labile non-canonical site(s), ranges from 10 to 100 under * conditions to 10^6 or more under optimal conditions. Qualitatively similar observations have been made with most type II endonucleases so far examined[3]. Understanding the structural basis of this remarkable specificity requires the determination of the three-

dimensional structures of enzyme DNA complexes. Such complexes with DNA carrying a canonical site (cognate DNA) can only be studied in the absence of Mg^{2+}. It is therefore important that binding studies[6,7] have shown a strong preference for canonical sites in the absence of Mg^{2+} meaning that the formation of specific interactions is not dependent on the presence of Mg^{2+}. First results of the crystal structure analysis of a complex between Eco RI endonuclease and a tridecameric DNA fragment have been reported by Frederick et al.[8]. Although the protein DNA interface has not yet been analysed in detail major deviations of the DNA fragment from a B-DNA like conformation are observed. This raises interesting questions such as whether bound non-cognate DNA fragments are similarly or less distorted or wether the enzyme undergoes large conformational changes too. In addition to the structure of a complex with cognate DNA one therefore also needs to know the structure of the free enzyme and that of a complex with non-cognate DNA. In the following account of our work with Eco RV endonuclease and small DNA fragments we show that this system is well suited to provide such information in the near future.

STRUCTURAL STUDIES OF ECO RV ENDONUCLEASE AND OF ITS COMPLEXES WITH DNA FRAGMENTS

Eco RV endonuclease, a dimeric enzyme of 2 x 29000 dalton, cleaves double stranded DNA at the sequence 5'-GAT/ATC and produces blunt ended fragments[9,10]. Its DNA derived amino acid sequence (245 residues) shows no significant homology to that of Eco RI endonuclease[11] and the same holds true for the two corresponding methylases. Large amounts of pure RV endonuclease have become available through the construction of an inducible overproducing strain[12] and have made it possible to grow crystals of the enzyme and of its complexes with various short DNA fragments.

Studies by X-ray Crystallography

Four crystal forms of Eco RV endonuclease have been obtained by precipitation with polyethylene glycol 4000[13] two of which diffract to about 2 Å resolution. They both have space group $P2_12_12_1$ with one dimer in the asymmetric unit and show similar cell dimensions of 58.2 (59.9), 71.7 (74.5) and 130.6 (121.8) Å for a, b and c of crystal form A and (B) respectively. Complexes of the enzyme with short self-complementary oligonucleotides were crystallized under rather similar conditions. Those with cognate DNA had to be crystallized in the absence of Mg^{2+} to prevent cleavage. Careful characterization of washed redissolved cocrystals by UV absorption and HPLC showed the presence of 1:1 complexes (1 RV dimer per DNA double strand) and no cleavage of the DNA fragments. Crystallographic parameters of these cocrystals are given in Table 1 (full details of their growth and characterization will be given elsewhere[14]). As can be seen structure determinations appear feasible for both types of complexes.

Thus far our efforts have concentrated on determining the structure of the free enzyme partly since we hope to be able to use molecular replacement methods to solve the structures of its complexes with DNA fragments. Data to 2.5 Å resolution were collected for native and Pb-derivative form A crystals by the oscillation method using synchrotron radiation at the EMBL outstation at DESY in Hamburg. The films were processed using A. Wonacott's film processing system MOSCO and good merging R-factors of 0.055 and 0.075 for native and derivative intensities respectively were obtained.

Table 1

Crystallographic parameters of complexes of Eco RV endonuclease with self complementary deoxy-oligonucleotides
(series I-n for cognate DNA fragment and series II-n for non-cognate DNA fragments)

Oligonucleotide Form	Sequence (5'-3')	Space-group	Unit cell parameters a	b	c (Å)	Diffraction limit (Å)	Crystal morphology
I-1	GGATATCC	n.d.				3.2	small prisms
I-2	GGGATATCCC and GCGATATCGC	$C222_1$	59.7	77.1	367.0	2.7	thick plates
I-3[a]	CCGATATGGC	n.d.	54	64	~160	3.0	very thin platelets
II-1	CGAATTCG	I222	84.0	146.1	74.0	3.2-4.0	plates
II-2	CGAATTCG	$C222_1$	84.0	127.3	74.0	3.2-4.0	plates
II-3	CGAATTCG	$P2_12_12_1$	90.3	61.7	251.3	4.5	prisms
II-4	CGAGCTCG	$P2_1$	65.5	78.4 ß = 106°	71.3	3.0	thick plates

a) These crystals were only investigated by electron microscopy and the c-periodicity has been estimated by tilting experiments.

Two major Pb sites, already identified in a 6 Å resolution difference Patterson synthesis calculated with diffractometer data, were refined using centric terms only. A low resolution diffractometer data set was also collected for a $Au(CN)_2^-$-derivative which could not be used for phasing beyond 6 Å resolution but proved very helpful to determine the position and orientation of the noncrystallographic twofold and the correct enantiomorph. Molecular replacement techniques as described by Bricogne[15] were used to produce electron density maps at 6 and 2.5 Å resolution. Initial best phases were derived from the isomorphous differences of the Au- (to 6 Å only) and the isomorphous and anomalous differences of the Pb-derivative. The molecular envelope traced in the first averaged 6 Å map was updated after a few cycles at low resolution and used without further change at higher resolution. Figure 1 shows a few sections of the final unaveraged 2.5 Å electron density map obtained after 10 cycles of molecular replacement. Two α-helices of 4 to 5 turns related by the molecular twofold are clearly recognizable but show poorly defined side chain density. Altogether the map has proved difficult to interprete and no chain tracing has yet been achieved. Different ways to improve the map are currently underway. Apart from continuing the search for more derivatives we are trying to extend the molecular replacement to crystal form B for which a 2.5 Å data set has been collected and processed. As the initial heavy atom phases might be rather poor beyond 3 Å resolution the procedure is also

being repeated at somewhat lower resolution. Position and orientation of the molecular twofold were derived from the refined coordinates of the two sets of major sites occupied in the two derivatives. Although they appear well determined, – the two heavy atom-heavy atom vectors are almost at right angles and are about 22 Å apart along the twofold –, we cannot exclude that they are somewhat in error.

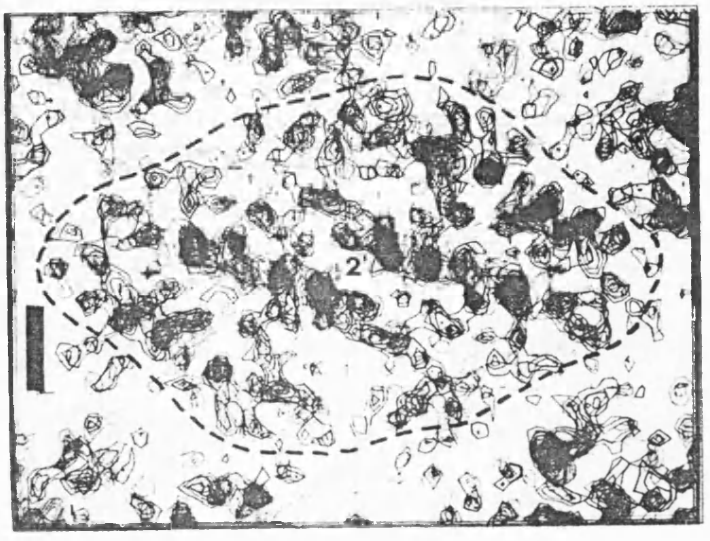

Fig. 1 2.5 Å electron density map
Eight sections spaced at 1 Å of the final unaveraged density map are shown. The view down the noncrystallographic twofold axis shows 2 symmetry related α-helices lying approximately in the plane and forming part of the dimer contact near the twofold in the center. The molecular boundary is indicated (- - -) and the bar represents 10 Å.

The presumed twofold symmetry of RV endonuclease DNA complexes leaves only few possibilities to dock a DNA fragment onto the protein. A balsa wood model of the dimer derived from the 6 Å electron density map and a simple wire model of the backbone of double stranded B-form DNA were used for this purpose. Only the arrangement illustrated in Fig. 2 satisfied a number of properties that such a complex is expected to have. The RV dimer as shown in this side view is about 60 by 60 Å across and 30 to 35 Å deep (see Fig. 5b for a view down the twofold). The bottom part of the molecule forms a tight dimer contact but its pointed end does not show any complementarity to DNA. At the top the dimer splits into two lobes leaving a depression around the twofold axis. The crude DNA model fits quite well into this depression when the major groove faces the protein. At the same time the two scissile phosphodiester bonds are in reasonable proximity to protein density. Contacts with the sugar phosphate backbone would be almost exclusively on the 3'-side of the scissile bond and could extend over 4 to 5 backbone moieties on each side (see Fig. 5b). Although we believe that this

overall arrangement is correct, conformational changes of the DNA and of the protein could yield a much tighter complex in which the two lobes might have moved more into the major groove. These questions can only be answered by solving the structures of the complexes with DNA fragments. For the cocrystals with the decamer GGGATATCCC a 3 Å data set has been collected and processed and we hope to solve its structure soon after that of the native enzyme.

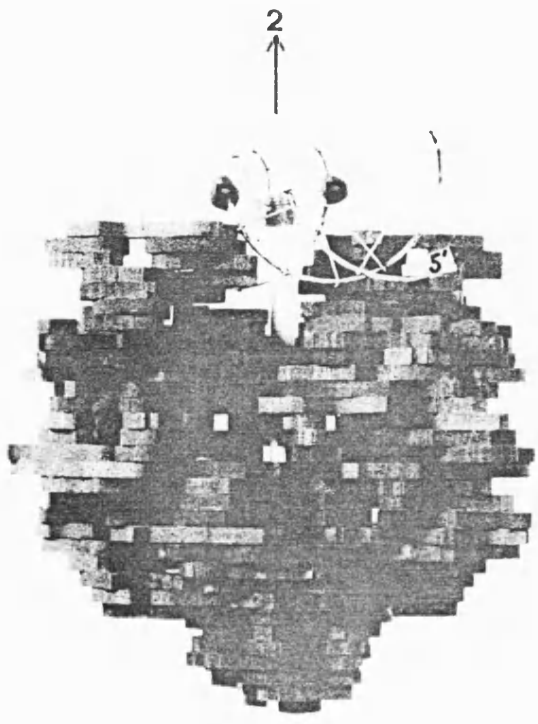

Fig. 2 Balsa wood model derived from 6 Å map
A side view of an Eco RV dimer is shown. A possible binding mode of DNA is illustrated by a wire model of a B-form double helix about 14 base pairs long. The scissile phosphodiester bonds (marked P) are near density protrusions at the top of the molecule. The bar represents 20 Å.

Studies by Electron Microscopy

The first cocrystallization attempts carried out with the cognate DNA decamer CCGATATCGG yielded crystalline platelets too thin to be studied by X-rays but very suitable for imaging in the electron microscope. Electron diffraction patterns of frozen hydrated or glucose dried cocrystal specimens extended to 3 Å resolution (Fig. 3). The hkO projection shown has almost perfect p2gg plane group symmetry but many specimens show violations of the absencies along b*.

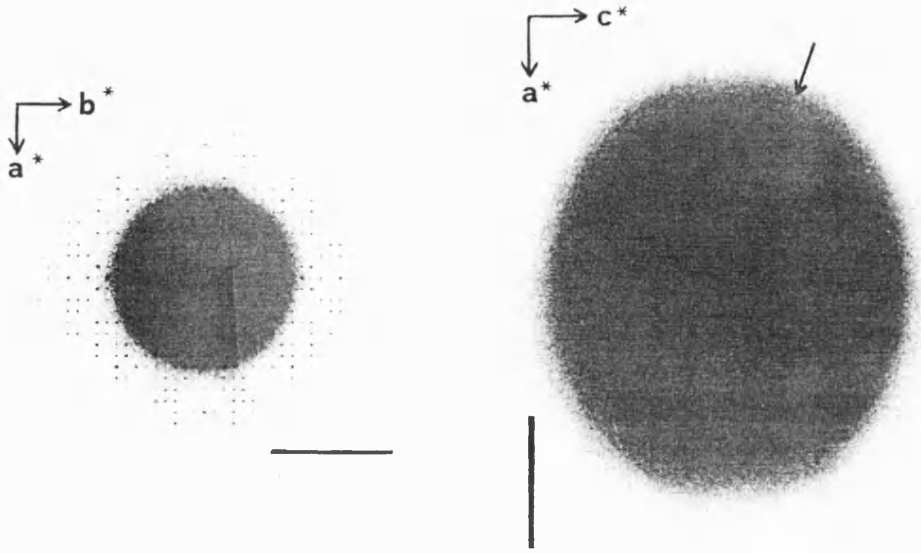

Fig. 3 (left) Electron diffraction of Eco RV-CCGATATCGG cocrystals
Thin cocrystals dried in glucose yield diffraction patterns extending to about 3 Å resolution. The bar indicates 0.2 $Å^{-1}$.

Fig. 4 (right) Electron diffraction of Eco RV-CGAATTCG cocrystals
Thin cocrystals with this non-cognate DNA octamer dried in glucose yield only poor diffraction patterns (hidden in the central black area due to overexposure) but show faint arcs at about 3.4 Å resolution centered at about +/- 20° from a*. The bar indicates 0.2 $Å^{-1}$.

We believe that a unit cell translation along c, estimated to be 140 to 160 Å from tilting experiments, comprises two molecular layers which are related by a twofold screw axis along b. Thin crystals with an odd number of layers would then not show strict absencies along b*. A two-dimensional image reconstruction from negatively stained specimens showed rather featureless, ellipsoidal density peaks. The double layer structure causes overlap in this projection and we have not yet unambiguously resolved the molecular packing. These crystals appear very suitable to develop methods of three-dimensional image reconstruction from unstained specimens of multilayered crystals.

Crystalline platelets of the complex with the non-cognate DNA octamer GGAATTCC were examined by X-ray diffraction and electron microscopy. They proved much more fragile and diffraction patterns from glucose dried specimens extended at best to about 6 Å resolution. Negatively stained specimens of multilayered crystals show c2mm plane group symmetry but single layers with p2gg symmetry could be generated by diluting the crystal mother liquor prior to staining. Fig. 5a shows the result of a two-dimensional image reconstruction from such single layers. The molecules are well resolved and the projected density suggests that we are looking down the molecular twofold axis. This was confirmed by a subsequent three-dimensional reconstruction which yielded molecular dimensions very comparable to those obtained in the X-ray analysis. Due to the low resolution of about 30 Å of this reconstruction no detailed features could be compared and no density was seen where DNA is expected to be bound. This could be due to positive staining of the nucleic acid but also due to loss of the DNA on dilution of the mother liquor needed to generate single layers.

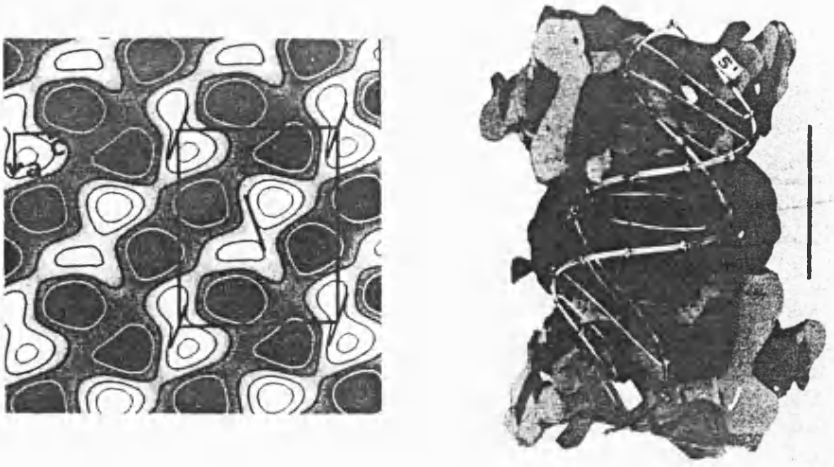

a b

Fig. 5 Orientation of DNA helix axis in RV endonuclease DNA complexes.
a) Two-dimensional image reconstruction from single layers of negatively stained RV-CGAATTCG cocrystals. Two RV dimers viewed down the twofold are clearly recognizable in one unit cell (no p2gg symmetry has been imposed). For one choice of the orientation of the DNA helix axis (marked by lines for some of the dimers) good agreement is observed to the orientation postulated from model building.
b) View down the molecular twofold of the balsa wood model of Fig. 2. The long dimension of the projected dimer is approximately aligned with the corresponding dimension in the image reconstruction. The bar represents 20 Å.

Since the DNA can hardly be involved in intra-layer contacts this appears easily possible. Some information on the orientation of the DNA in these cocrystals could however be derived from the diffraction of multilayered crystals dried in glucose. As shown in Fig. 4 faint arcs at about 3.4 Å resolution can be seen and they are centered at about 20° to the a axis of the crystal (the lattice is not visible due to overexposure necessary to bring out the arcs). Assuming that these are due to the DNA base stacking the helix axis can be chosen at + or -20° from $\underset{\sim}{a}$ with respect to a particular dimer. One of these choices gives quite good agreement with the orientation derived from model building. In both cases the angle between the helix axis and the line connecting the centers of the projected monomer densities is around 45°. Analysis of the molecular packing in these cocrystals has told us that the space group of crystal form II-2 is 1222 (and not $12_12_12_1$), that form II-3 represents simply a different stacking of the layers along the b-axis and will also help the X-ray crystallographic analysis.

Acknowledgement

We thank M. Gait (MRC, Cambridge), J. van Boom (University of Leiden) and H. Blöcker and R. Frank (GBF, Braunschweig) for their generous gifts of some of the oligonucleotides used in the cocrystallization experiments.

References

(1) P. Modrich and R.J. Roberts, in: "Nucleases", M. Linn and R.J. Roberts, eds., Cold Spring Harbor Laboratory, New York (1982).
(2) A. Pingoud and J. Alves, personnel communication.
(3) A. Pingoud, Eur. J. Biochem. 147 : 105 (1985).
(4) B. Polisky, P. Greene, D. Garfin, B. McCarthy, H. Goodman and H. Boyer, Proc. Natl. Acad. Sci. USA 72 : 3310 (1975).
(5) R.C. Gardner, A.J. Howarth, J. Messing and R.J. Sheperd, DNA 1 : 109 (1982).
(6) B.J. Terry, W.E. Jack, R.A. Rubin and P. Modrich, J. Biol. Chem., 258 : 9820 (1983).
(7) A.D. Frankel, G.K. Ackers and H.O. Smith, Biochemistry 24 : 3049 (1985).
(8) C.A. Frederick, J. Grable, M. Melia, J. Samudzi, L. Jen-Jacobsen, B.-C. Wang, P. Greene, H.W. Boyer and J.M. Rosenberg, Nature 309 : 327 (1984).
(9) G.V. Kholmina, B.A. Rebentish, Y.S. Skoblov, A.A. Mironov, Y. Yankovskii, Y.I. Kozlov, L.I. Glatman, A.F. Moroz and V.G. Debabov, Dokl. Akad. Nauk. SSSR 253 : 495 (1980).
(10) I. Schildkraut, C.D.B. Banner, C.S. Rhodes and S. Parekh, Gene 27 : 327 (1984).
(11) L. Bougueleret, M. Schwarzstein, A. Tsugita and M. Zabeau, Nucleic Acids Res. 12 : 3659 (1984).
(12) L. Bougueleret, M.L. Tenchini, J. Botterman and M. Zabeau, Nucleic Acids Res. 13 : 3823 (1985).
(13) A. D'Arcy, R.S. Brown, M. Zabeau, R. Wijnaendts van Resandt and F.K. Winkler, J. Biol. Chem. 260 : 1987 (1985).
(14) F.K. Winkler, J. van Boom, H. Blöcker and R. Frank, in preparation for J. Mol. Biol.
(15) G. Bricogne, Acta Cryst. A32 : 832 (1976).

Ultramicroscopy 13 (1984) 351–364
North-Holland, Amsterdam

METHODS FOR SPECIMEN THICKNESS DETERMINATION IN ELECTRON MICROSCOPY

J. BERRIMAN, R.K. BRYAN, R. FREEMAN * and K.R. LEONARD

European Molecular Biology Laboratory (EMBL), Meyerhofstrasse 1, D-6900 Heidelberg, Fed. Rep. of Germany

Received 5 April 1984

A new method is described for specimen thickness determination in transmission electron microscopy. This is carried out by marking specimens with gold particles and analysing the images of a tilt series by computer. The method makes it possible to distinguish populations of particles on different planes and calculate the distance between the planes with statistical variation. We have applied it to carbon films as test objects and compared the results with those obtained by transverse sectioning, STEM mass measurement, optical density and frequency change of a quartz crystal oscillator. We have then used the method for thickness measurement of multilayered protein crystals and thin sectioned cells.

1. Introduction

The thickness of objects seen in projection in the electron microscope is a parameter which is difficult to obtain directly but which can be of some importance, as for example when attempting to establish a three-dimensional structure. For this reason, we have required a reliable method for thickness determination of small protein crystals, both for negatively stained multilayers or for sections cut from three-dimensional crystals.

With the introduction of more quantitative methods of electron microscopy in cell biology, a knowledge of section thickness is important in estimating cell volumes, the efficiency of antibody labelling and the accessibility of antigenic sites.

The most reliable and direct method of thickness measurement for very thin objects which has been employed to date is undoubtedly embedding in plastic, followed by electron microscope observation of transverse sections [1,2]. Optical density measurements have also been used to measure carbon film thickness [1,3–6] and generally a linear relationship between optical density and thickness was found. However, considerable differences between the various results indicate that thickness depends on evaporation conditions, and different calibrations are required for each set of conditions [6,7].

Electron scattering can also be used to determine mass thickness, and hence specimen thickness [8]. This method can be applied successfully in bright field transmission electron microscopy (TEM) using a Faraday cage to calibrate the exposure meter reading from the fluorescent screen. Below thicknesses of 50 nm the TEM method is less reliable [1], and more accurate results can be obtained using scanning transmission electron microscope (STEM) dark field images. This technique has been applied in mass determination of protein molecules, viruses, filaments, etc. [9]. It is equally valid when used to measure thickness and can do so to an accuracy of better than 10%.

Finally, specimen thickness can be estimated by shadowing with a thin layer of metal from a low, fixed angle. Although convenient, this method relies on the presence of a clear edge along the specimen to cast a sharp shadow, which is often not the case.

In this paper we describe a new trigonometric method using an image tilt series to obtain the thickness after marking the specimen surfaces with small gold particles. Carbon films have been used to test the method and the results compared with those obtained by transverse sectioning, electron

* Present address: JEOL (UK) Ltd., Grove Park, Colindale, London NW9 0JN, UK.

0304-3991/84/$03.00

scattering and the change in frequency of a quartz crystal oscillator during evaporation. The trigonometric method was then applied to negatively stained multilayered crystals of cytochrome c reductase and to ultra-thin cryo-sections of Chinese hamster ovary cells which had been air-dried.

The normal procedure for making thin carbon films is evaportion from an incandescent arc between two sharpened carbon or graphite rods. This method is, however, somewhat unpredictable in producing films of equal thickness. Thickness is often simply deduced by a "rule of thumb" method such as comparing the colour on filter paper with a shaded region or on a white tile around an oil drop. Use of a quartz crystal monitor inside the evaporator makes the method more quantitative, but the large amount of heat radiated by the arc may disturb the measurement of frequency change. We have used a new method which produces little heat and gives good results with a quartz crystal monitor (Balzers QSG 201D with a QSK 113 Detector) producing reproducible thicknesses of evaporated carbon.

2. Methods

2.1. Sample preparation

2.1.1. Carbon films

Carbon films were produced on mica sheets from graphite and carbon rods by the conventional method, and by a new method using carbon thread as a source. Balzers supply carbon thread to be used for evaporation within their SEM preparation apparatus. Clean carbon support films can be prepared from the thread if it is used in a high vacuum evaporator (T. Arad and K. Leonard, unpublished results). We have now adapted a Fullam evaporation source to accept a standard 1 cm length of thread. The ceramic separators normally supplied were replaced with shorter ones made out of teflon and secured with screws so that the jaws are 1 cm apart (fig. 1). To prepare a carbon film, the carbon thread was clamped across the jaws which were mounted inside a high vacuum evaporator (Edwards 306) at the required height. A removable shield was placed between the thread and a freshly cleaved mica sheet. At a vacuum better than 1.33×10^{-3} Pa (1.0×10^{-5} Torr), the thread was outgassed by heating to red heat for a few seconds. When the vacuum recovered, the shield was removed and an evaporation made by setting the voltage to 15 V and switching on the current. The thread glowed white hot for about one second before breaking.

To allow a comparison to be made between the new method and the standard arc method, carbon and graphite rods were also used, evaporation being carried out in short bursts. This kept the thermal drift to a minimum and allowed an approximate thickness value to be measured with the quartz crystal oscillator.

Carbon films of a fixed ratio of thickness were

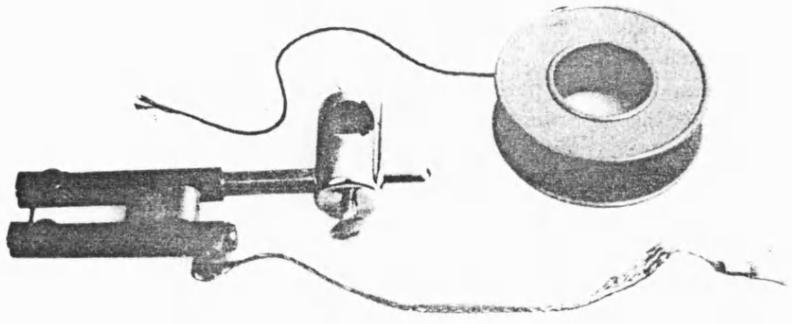

Fig. 1. The adapted evaporation source is shown together with a roll of carbon thread. A short length of the thread has been clamped between the jaws.

made by simultaneously evaporating onto mica sheets positioned at different distances from the source.

2.1.2. Protein crystals

Tubes and multilayered crystals of cytochrome reductase were prepared as described previously [10]. They were negatively stained on carbon-coated collodion grids with 1% uranyl acetate, air dried and surface-coated with gold particles for thickness measurement as described below.

2.1.3. Sections

Ultrathin cryosections of glutaraldehyde-fixed Chinese hamster ovary cells (kindly supplied by Dr. G. Griffiths, EMBL) were collected on carbon-coated formvar grids, washed and air dried [11]. They were then coated on both surfaces with gold by evaporation.

2.2. Thickness measurement

All specimens were measured by the trigonometric method. For comparison, carbon films were also measured by STEM and by thin sectioning.

2.2.1. The trigonometric method

The specimen surfaces were marked with gold, either by evaporation from a heated tungsten wire at about 13.3 Pa, at which pressure clusters of around 5 nm diameter are produced (a better vacuum giving finer particles), or with a solution of colloidal gold, again about 5 nm diameter, as used for antibody labelling experiments [12].

An area with a good distribution of marker particles was imaged at a selected magnification in a Philips 400T electron microscope. A tilt series normally of 0°, ±20° and ±40° was then recorded. The method does not require specific angles or that they be in pairs but a number of tilts are required to give statistically significant results and to refine the tilt parameters if necessary (see appendix for the mathematical basis of the method).

The same area of the specimen on each negative was then digitized using an Optronics drum densitometer and the images stored on disk. The magnification and densitometer raster were chosen to give a pixel size well within the required resolution. For example, for carbon films down to 5 nm thick a magnification of 45000 and a raster size of 25 μm was used, giving a pixel size of 0.5 nm. Images were displayed on a frame-store grey scale monitor and measured interactively using a trackball controlled cursor. A hard-copy printout was usually made at the same time to aid in identifying the particles on different images. About 50 small particles were selected and numbered and their x, y coordinates recorded. Large particles or aggregates were avoided. This procedure was repeated for each image in the tilt series and the data set was then analyzed to give a direct measurement of the thickness. It was also convenient to display the particle positions as two orthogonal projections parallel to the fitted planes. In this way variations in thickness could be seen directly.

2.2.2. Sectioning

The carbon films were scored with a needle to make 1 mm squares and then floated off the mica onto water. Formvar coated 2 × 1 mm single-hole slot grids were then used as a support and the carbon was positioned over the hole in the grid and picked up. A second film could be picked up onto the same grid when direct comparison was necessary. After embedding in Araldite and polymerisation, the block was mounted for ultramicrotomy and the copper trimmed away with a scalpel blade, care being taken not to shear the resin surface from the carbon surface. The block face, with the carbon film running horizontally, was cut on a Reichert Ultratome OmU3 with a diamond knife. Silver-coloured sections (in the range 50–70 nm thick) were collected onto the same coated single-hole grids. These were mounted in a rotational holder and observed in a Philips 400T with ±60° eucentric goniometer stage. Because the bond between resin and carbon was not strong, the sections were frequently split, and it was necessary to search many sections to find intact regions. The sectioned carbon was rotated until it was parallel with the tilt axis and then tilted until a sharp image of the carbon film was seen. Precautions were taken to record images close to focus and under conditions for reproducible magnification. A Joyce Loebl microdensitome-

ter 3CS was used to measure the film thickness from the micrographs.

2.2.3. STEM mass measurement

Carbon film thicknesses were measured using a VG HB5 STEM by the comparative technique with TMV as an internal mass standard as previously described [9]. In this work measurements were made from images recorded in the dark field mode, with the annular (elastic) dark field signal normalized by the beam current monitored at the objective aperture.

Small pieces of carbon film were floated off mica onto a dilute suspension of TMV, then washed in distilled water and picked up on 600 mesh grids. In some cases carbon films of 3 different thicknesses which had been evaporated simultaneously were manipulated together and picked up on the same grid. Thickness measurements made on these multiple layers of carbon films used a single layer as background (fig. 2). A series of images of each carbon film, which also contained a number of TMV particles, were recorded and stored on computer disk.

To carry out integration and background subtraction, images were first redisplayed using a grey-scale monitor reading from a 512 × 512 pixel frame-store interfaced to the computer (Nord 10S). Areas for measurement were then selected interactively using a manual cursor and integration carried out as described previously [9]. The mass thickness of the carbon films was calculated relative to the known mass/length of the TMV particles (131,000 D/nm).

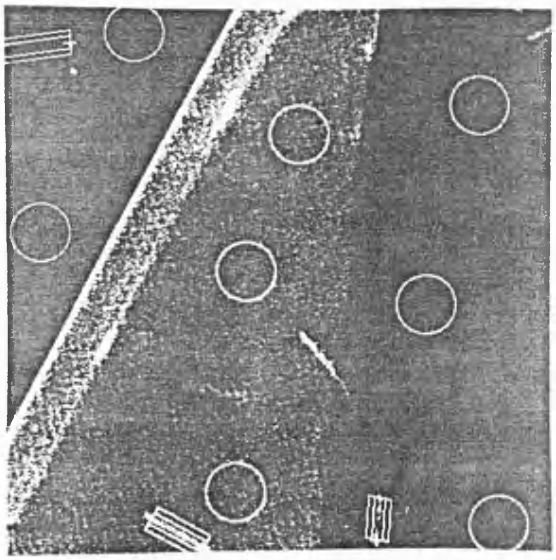

Fig. 2. This shows a typical STEM dark field image with multilayers of carbon and unstained TMV particles. Areas which have been selected for integration and background subtraction are outlined. Scale bar (bottom left) represents 250 nm.

3. Results

3.1. Carbon film thickness measurement

3.1.1. Thickness measured by the trigonometric method, compared with sectioning and frequency change of a quartz crystal monitor

Carbon thread evaporation produced a very consistent film thickness. This was measured initially with a quartz crystal oscillator positioned 5 cm from the thread. The mean frequency change at this distance was 135 Hz ± 10%. Carbon films of varying thickness were then obtained by positioning mica at different distances from the evaporation source. An inverse square law relationship for carbon deposition with distance was obeyed, as confirmed by placing two crystal oscillators at different distances in the bell jar during evaporation and by the results of sectioning.

Fig. 3a shows a cross-section of such a carbon film. Gold particles have been evaporated onto both surfaces for the trigonometric method of thickness determination. In fig. 3b, computer projections of the positions of measured particles for single and double layers are shown. The particles fall on clearly defined parallel planes.

The results of the three thickness estimates for several films are summarised in table 1. The thickness value obtained by trigonometry represents the separation of two planes of gold particles. When measurements were made on a single layer it was therefore necessary to subtract the effective particle diameter to obtain the true film thickness. This can be determined by comparing the thickness values obtained for single and double layers (fig. 3c).

The mean value for the frequency change of the

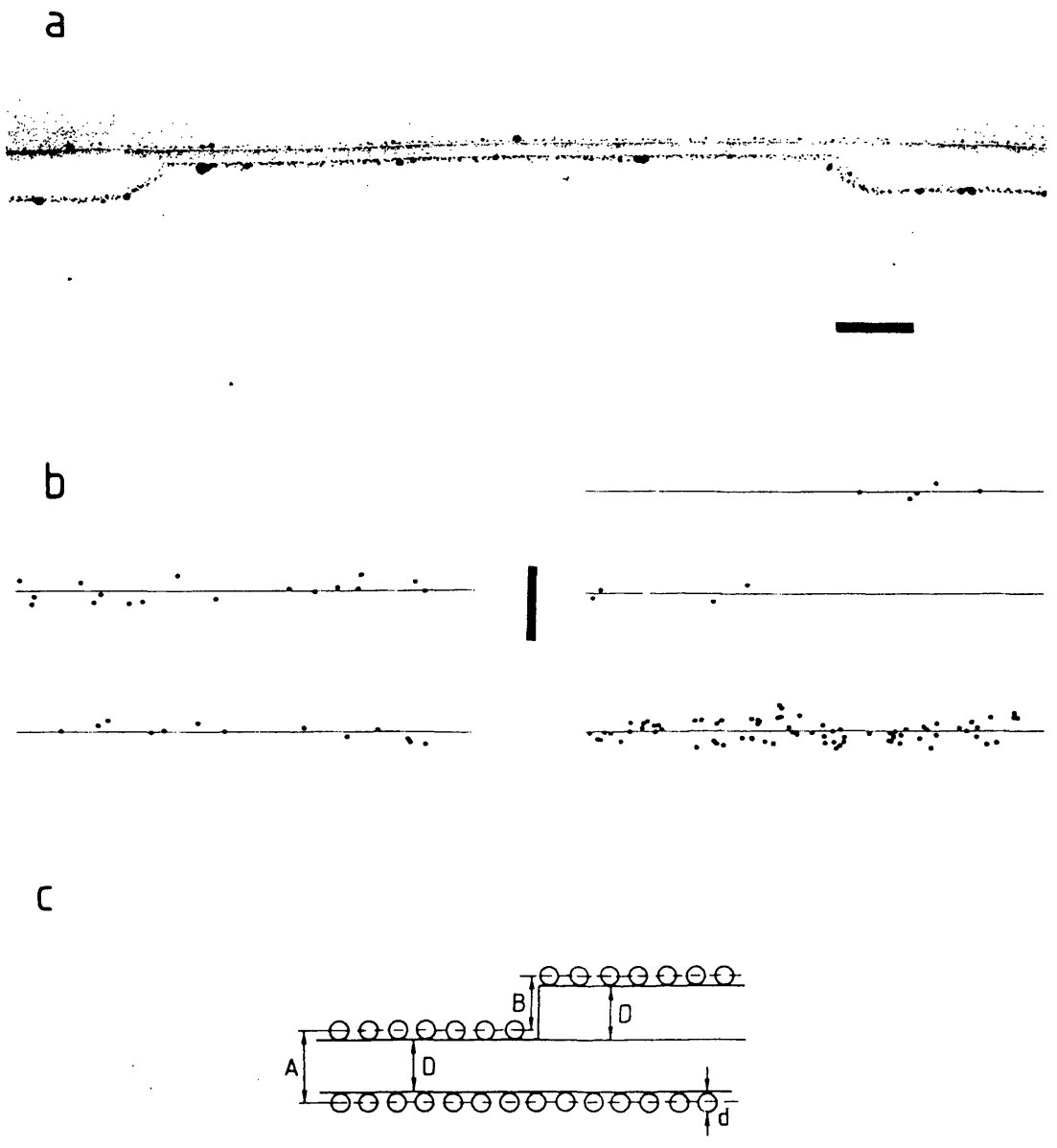

Fig. 3. (a) A thin section of a gold-coated carbon film spanning a hole in a formvar film. The carbon film, which has a thickness of 12.5 nm, has been prepared by evaporation from the thread source at 5 cm. There is a narrow gap between the gold particles and the carbon surface which may be a contaminating layer. The scale bar represents 100 nm. (b) Computer-calculated particle distributions for a single layer carbon film and for a film with two thicknesses of carbon. The vertical scale bar represents 10 nm. (c) Interpretation of film thickness from the separation of planes of markers. In the single layer, the separation of the planes is the sum of the film thickness and the mean marker diameter is $A = D + d$. For a double layer, $B = D$. Thus $d = A - B$, allowing determination of the effective marker diameter.

Table 1

Film	Change of frequency of quartz crystal monitor (Hz)	Thickness by the trigonometric method (nm)		Thicknesses by sectioning (nm)
		Separation of planes [a]	Film thickness [b]	
Single layer thread carbon deposited at 5 cm	138	16.0 ± 0.3 (A)	12.0 ± 0.3	12.5 ± 0.5
Double layer thread carbon deposited at 5 cm	138	16.3 ± 0.3 (A)	12.3 ± 0.3	12.5 ± 0.5
Double layer thread carbon deposited at 5 cm	138	12.4 ± 0.4 (B)	12.4 ± 0.4	12.5 ± 0.5
Single layer thread carbon deposited at 5 cm	125	15.2 ± 0.4 (A)	11.2 ± 0.4	10.0 ± 0.5
Single layer thread carbon deposited at 7 cm	63	9.9 ± 0.5 (A)	5.9 ± 0.5	5.0 ± 0.5
Single layer rod carbon deposited at 7 cm	70	10.6 ± 0.4 (A)	6.6 ± 0.4	6.7 ± 0.5

[a] (A) and (B) refer to fig. 3.
[b] A value of 4 nm has been subtracted from the plane heights as the effective marker thickness.

quartz crystal monitor from these results was 11 Hz/nm for carbon thread evaporation.

3.1.2. *STEM mass measurement compared with sectioning*

The values of mass thickness obtained for a number of carbon films plotted against thickness as measured by transverse sectioning (fig. 4) show a linear relationship, within experimental error. The thread carbon measurements were intermediate between those for the carbon rod and graphite arc values. The slope of the least-squares line fitted to the thread carbon points is a measure of the carbon density and was found to be 1000 D/nm^3 or 1.7×10^3 kg/m^2. The positive intercept for zero thickness may indicate the presence of a contaminating layer on the carbon surface.

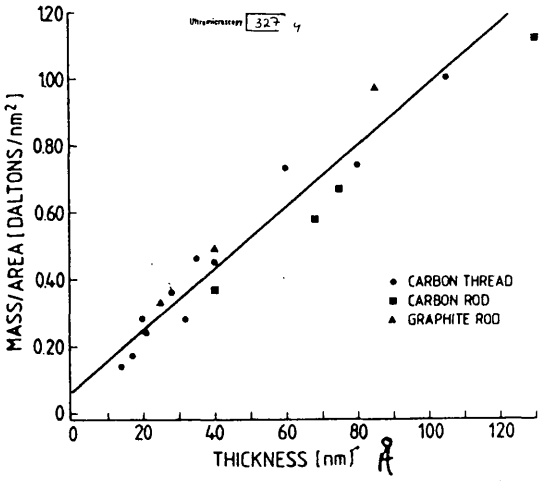

Fig. 4. Graph showing the variation of mass per unit area of several carbon films (relative to TMV) against the thickness measured by sectioning. The line is a least-squares fit to the carbon thread measurements.

3.2. *Crystal thickness measurement for cytochrome reductase.*

Fig. 5 shows a multilayered crystal marked with gold by evaporating onto the upper surface only. The boxed regions were densitometered and the trigonometric method used to analyse the distribution of gold particles. Those on the top surface of the crystal and on the supporting carbon film (box B) fitted to single, parallel planes with a separation between the the crystal surface and the supporting carbon of 24.2 ± 1.2 nm. Box A gave only a single plane with the particles fitting to within 1 nm.

This crystal has broken at the edges and shows steps in density which can be measured with a densitometer to give an estimate of the number of crystal layers. Assuming equal staining throughout the crystal, there are in this case four distinguish-

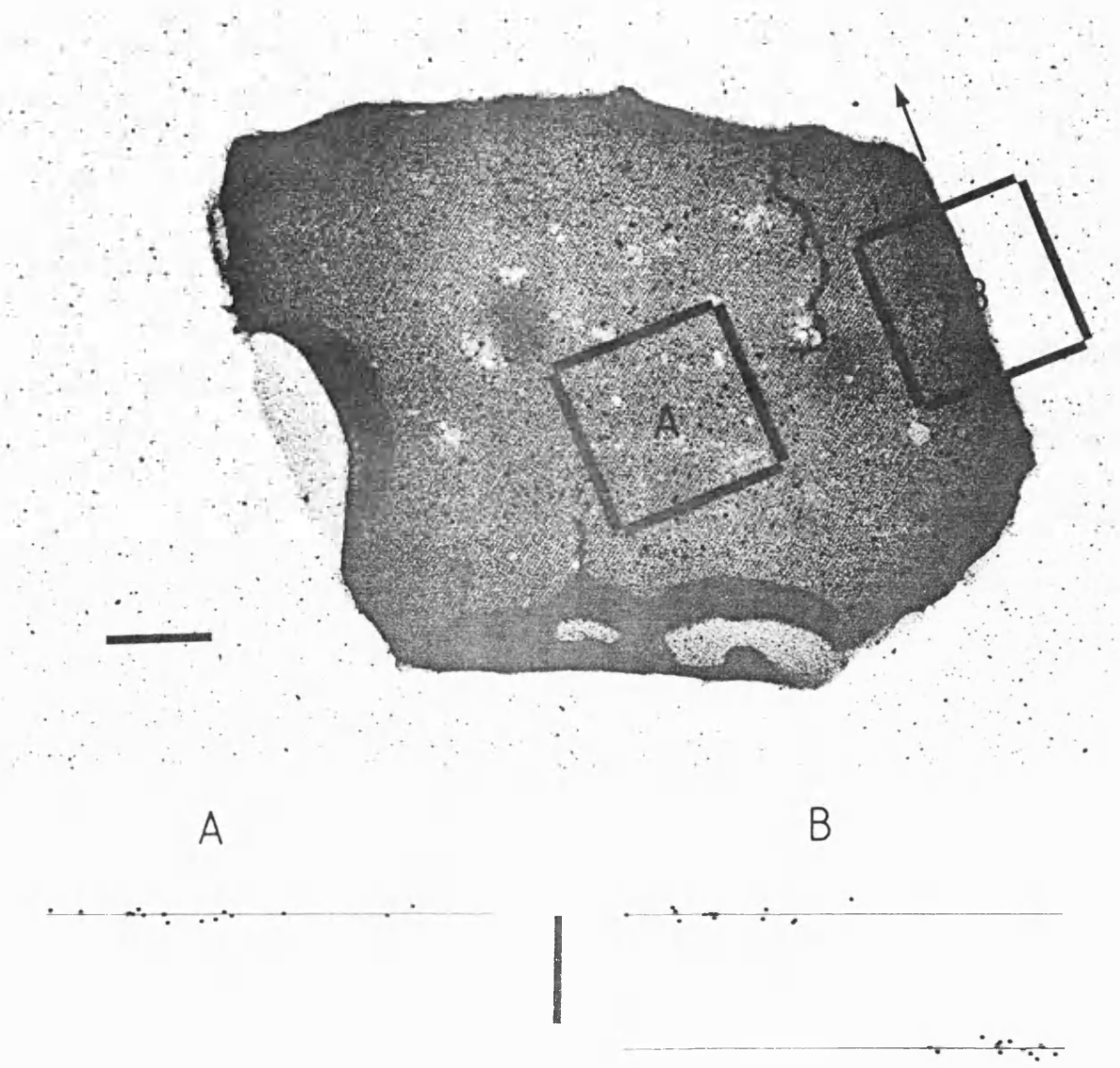

Fig. 5. A multi-layer cytochrome reductase crystal negatively stained with uranyl acetate and marked with gold by evaporation on one surface. The boxes indicate the areas digitized and the arrow the tilt axis direction. Scale bar represents 250 nm. The corresponding computer projections of the gold particles for the two areas are also shown. Vertical scale bar is 20 nm.

able layers and thus the height of one layer is about 6 nm.

To rule out the possibility that the crystal could be partially depressed into the supporting film, the method was repeated with gold markers on both surfaces of the specimen. Fig. 6a shows such an image with, in figs. 6b and 6c, the distribution of gold particles calculated for the surfaces. All the particles on the carbon film lower surface lie on one plane, indicating that the film is essentially flat.

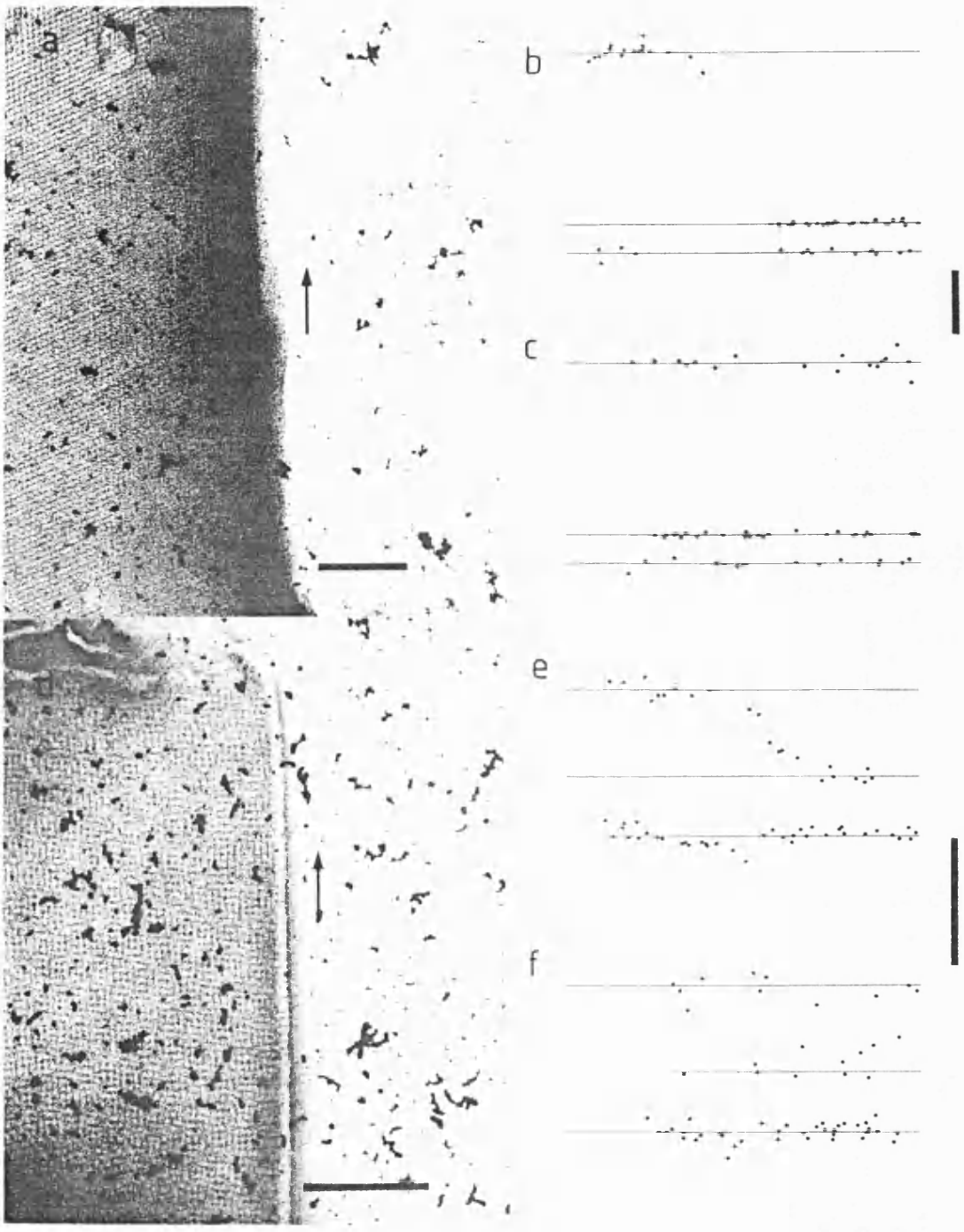

Fig. 6. (a) This shows the analysed region of a negatively stained multi-layer cytochrome reductase crystal marked on both sides of the grid with gold particles. (b) The computer projection for the separation of the markers viewed along the edge of the crystal. (c) The corresponding view of the markers seen at right angles to the edge of the crystal. (d) A cytochrome reductase tube negatively stained and marked with gold on both surfaces of the grid. (e) Computer projection of markers parallel to the edge of the tube. (f) Projection of markers at right angles to the edge of the tube. The scale bars on the micrographs represent 100 nm and the arrows indicate the tilt axis direction. The vertical scale bars on the computer projection represent 20 nm.

Fig. 6d shows a crystalline tube which has dried down on to the support film to give two overlapping single crystalline layers which are not in register. The computer-calculated distribution of gold particles projected onto lines parallel to the tube surface (fig. 6e) has one step for the carbon and a second larger step, measuring 13.0 ± 0.5 nm, for the tube, or about 6.5 nm for one layer.

The thickness results for several crystals are presented as a graph (fig. 7) with the best fit for the number of unit cells. The measured thickness increment is about 13.5 nm, but the results for the tube, where two layers must be present, and for crystals where the number of layers can be estimated (e.g. fig. 5) suggest that the single layer increment is only 6.7 nm.

3.3. Thickness of cryo-sections

Figs. 8a and 8b show cryo-sections of Chinese hamster ovary cells which have been marked with gold particles on both surfaces. These sections are not embedded in a surrounding medium, the frozen sucrose solution in which they were cut having been washed away. They thus lie isolated on the supporting film.

For this type of specimen, the plane heights show clearly that the sections have depressed the supporting film. In fig. 8a the thickness of the section is 27.4 nm and the film thickness is 11.2 nm; in fig. 8b the section thickness is 29.5 nm and the supporting film 11.3 nm.

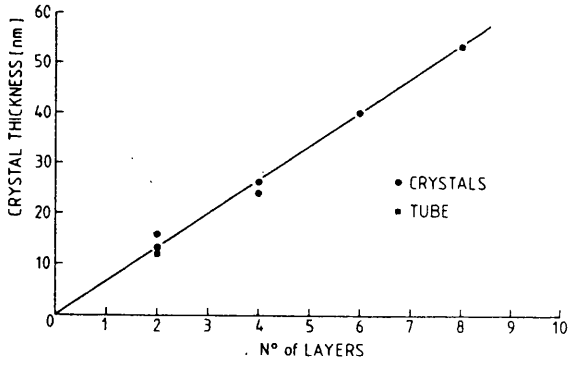

Fig. 7. Graph of crystal thickness plotted against number of layers. The abscissa represents multiples of a single layer thickness of 6.7 nm which gave the best least-squares fit to the crystal and tube thickness values.

4. Discussion

Preparation of carbon films using the carbon thread method was found to be both consistent and reliable. With the evaporation source described here films of any thickness up to 14 nm can be made by placing the mica substrate at an appropriate distance from the thread. The quartz crystal oscillator thickness monitor can then be relied on to give a good indication of carbon film thickness, taking the change of frequency as a direct reading of thickness.

Measurement of mass thickness in the STEM also confirms the consistency of this method of film preparation, giving a measured carbon film density of 1.7×10^3 kg/m^3. Compared with carbon thread, films prepared by arc evaporation from carbon rods have slightly lower density, and those from graphite rods slightly higher. These results reflect the densities of bulk material which are lower (1.8 to 2.1) for amorphous carbon than for graphite (1.9 to 2.3). The slightly lower value of 1.7 which we obtain probably reflects a loose packing of the films. Differing amounts of graphite in films prepared from different sources has also been cited [6] as the reason for discrepancy between the reported optical methods for determining carbon film thickness.

The graph for mass thickness against thickness, showing a small finite value of 500 D/nm^2 for zero thickness, indicates the presence of an extra component contributing to the total electron scattering. Very thin additional layers can sometimes be seen in transverse sections of films (e.g. fig. 3a), and these may be a contaminant deposited on the mica before carbon evaporation or on the carbon film during the later stages of sample preparation. Such a layer is likely to be present on films exposed to a normal laboratory atmosphere.

In measuring thin carbon films by photometric absorption, two other groups report that there is a linear relationship between thickness and optical density, where $T = \mathrm{OD} \times 100$ in nm [1,3]. When tested with our films made by thread evaporation, this simple rule was in excellent agreement with the measured thickness and could form the basis of a method for thickness calibration of carbon

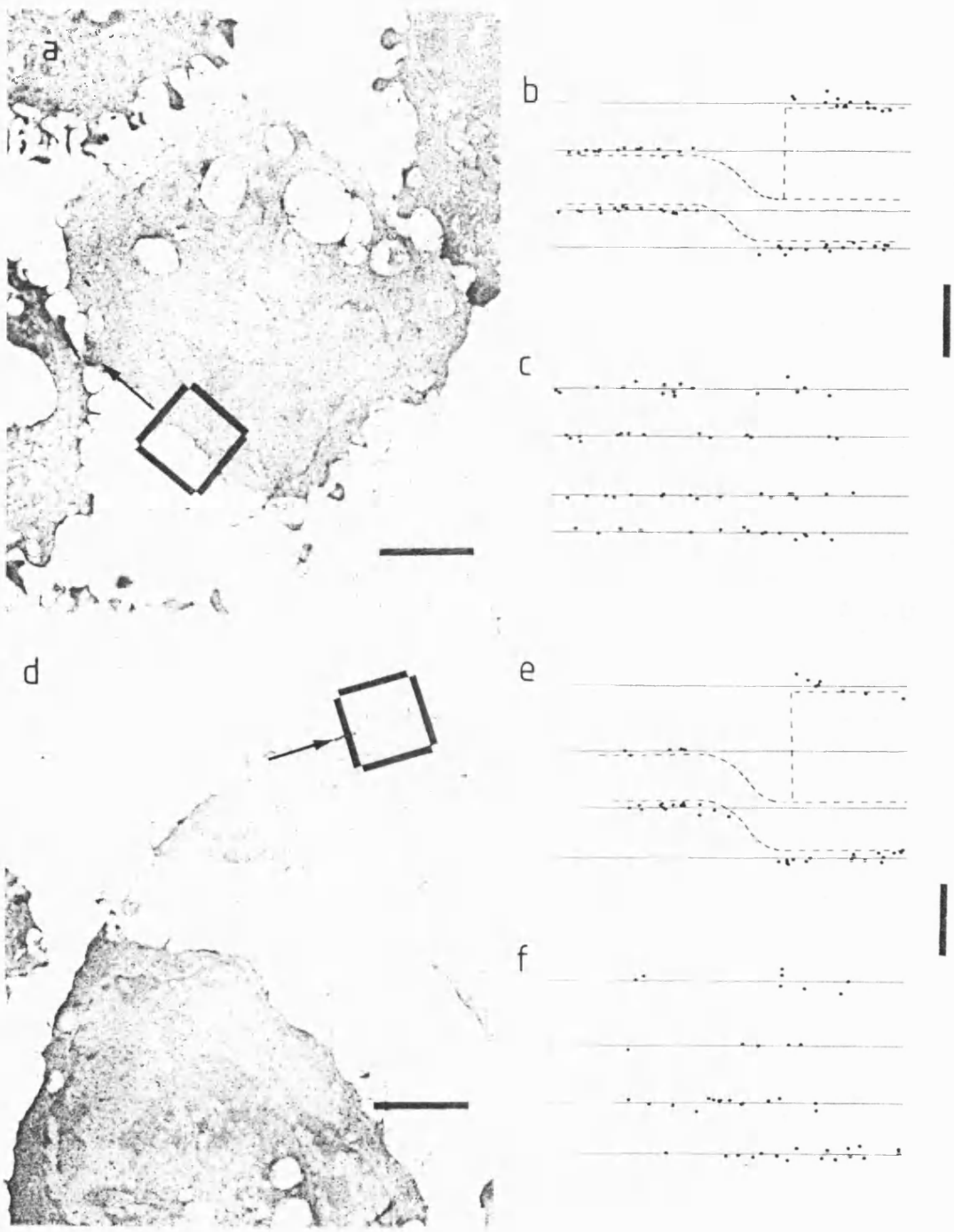

Fig. 8. (a) and (d) show sections of Chinese hamster ovary cells marked with gold by evaporation. The boxes indicate the areas digitised and the arrows the tilt axes. The same convention as fig. 6 has been used to show the analysis of the marker plane heights. The position of the section relative to the supporting film is shown by the broken lines. The scale bars on the micrographs represent 2.5 μm, and on the computer projections the vertical scale bars represent 20 nm.

films in the thickness range 1–20 nm.

It is interesting to note that a carbon film which is clearly visible as a faint brown layer when deposited on filter paper is in fact only about 2 nm thick as measured by the methods described here. Under good conditions – correct illumination of a water container with a non-reflecting base – it is also possible to see such a film floating on a water surface. Furthermore, it proves to be strong enough to be self-supporting when picked up on a fine (600) mesh grid.

The values obtained for cytochrome reductase membrane crystals, giving a thickness of about 6.7 nm for the stacking repeat, are significantly less than those found from three-dimensional reconstruction of single layers. This was originally reported to be to be 15 nm [13], but re-calculation of the three-dimensional data now indicates a value of about 10 nm for well stained specimens, or about 8 nm for weakly stained specimens such as those observed here.

In an attempt to corroborate this low value for the monolayer thickness, we have also used the method of measuring Laue zones [14] in the optical diffraction patterns of tilted multilayer crystals. Preliminary results suggest that under low dose conditions (less than 400 e^-/nm^2) the crystal thickness periodicity is about 12 nm and that this contracts to about 6 nm after a higher electron dose (about 1000 e^-/nm^2), equivalent to that required to record a normal exposure. The tilt series thus measures the thickness of a fully irradiated object.

"Height loss" as first a precursor, then a part of mass loss, has been reported for unstained, freeze-dried samples [15] and in stained catalase crystals [2]. These results serve to re-emphasise the problem of determining detail in the Z direction in three-dimensional structures calculated from tilted images.

Determination of the thickness of cryo-sections was carried out in order to estimate changes in thickness during preparation. A surprising result was the finding that the sections had apparently sunk into the supporting film. We did not find this with cytochrome reductase crystals even for crystals more than 50 nm in thickness. A possible conclusion from this result is that carbon–formvar films are much more plastic that carbon–collodion films and deform either on drying or from surface tension effects. Alternatively, radiation damage may cause preferential mass loss from the formvar which introduces shrinkage in the film, pulling the sections down into the film plane. This phenomenon, termed "wrapping", has been described previously [16] but has not been correlated with the supporting film. Our results suggest that "wrapping" occurs when formvar–carbon support films are used. Other work which has shown this phenomenon directly [2,17] has also been carried out with formvar–carbon grids.

5. Conclusion

The results for carbon films show that triangulation is an accurate method for determining specimen thickness in the electron microscope. The correlation between thicknesses measured by triangulation and by sectioning is excellent, and if sufficient numbers of particles and tilted images are used the error will be small. Only when the thickness to be measured becomes less than the average particle size (i.e., in this work, less than 5 nm) does the error become significant.

Appendix (by R.K. Bryan)

Calculation of three-dimensional coordinates of points from their projections

Each tilt of the series provides the two-dimensional projected coordinates of the gold particles. From these data we wish to calculate the three-dimensional coordinates, and then to interpret these positions in terms of particles lying on the surfaces of the specimen. The two-dimensional coordinates y_{pt}, of point p on tilt t, are related to its three-dimensional coordinates x_p, by

$$y_{pt} = P_t x_p - c_t, \quad (1)$$

where P_t is a projection matrix and c_t an origin shift. P_t depends on four parameters: three to define the orientation of the projections, and a fourth for the magnification of the image (relative,

say, to the zero tilt as a standard). The three angles defining the orientation can be conveniently taken as the tilt axis direction θ, which is common to all the tilts: ϕ_t, the angle of tilt; and ψ_t, a final rotation of the image [18]. We denote the magnification by m_t, and to define the overall coordinate system, take $m_1 = 1$, $\phi_1 = \psi_1 = 0$. P_t can be constructed from rotations about the coordinate axes as

$$m_t P_z R_3(\psi_t) R_3(\theta) R_1(\phi_t) R_3(-\theta), \tag{2}$$

where $R_i(\alpha)$ represents a clockwise rotation through an angle α about the ith axis, and P_z projects down the z-axis. We shall assume in the first instance that each point p appears in every tilt.

In principle, only two tilts suffice for the calculation of the particle coordinates, if the tilt parameters are known accurately. However, while the tilt angles and magnification are usually fairly precisely known, the tilt axis direction and image rotation are dependent on, for example, the orientation of the film in the scanner, and so are only known approximately. Accordingly, they also need to be calculated from the measured particle coordinates, in which errors can also arise, principally from the limited resolution of the digitised image (accurate to 1 pixel) and from mistakes in identifying the corresponding particle on the various tilts. Therefore, in practice, more than two tilts are required, as a cross-check on the accuracy of the tilt parameters and the measured particle coordinates. A least-squares solution is found, and incorrectly measured points or inaccurate tilt parameters can be identified by the resulting large residuals, and eliminated or refined respectively.

The least-squares solution is found by minimising

$$F = \tfrac{1}{2} \sum_{pt} \left(P_t x_p - c_t - y_{pt} \right)^2. \tag{3}$$

The solution occurs when the derivatives of F are zero. Differentiating with respect to c_t and x_p and equating to zero gives

$$P_t \sum_p x_p - N c_t - \sum_p y_{pt} = 0, \tag{4}$$

$$\sum_t P_t^{\mathrm{T}} \left(P_t x_p - c_t - y_{pt} \right) = 0. \tag{5}$$

Eq. (4) shows that c_t is simply the offset between the projection of the centre of mass of the points and the centre of mass on the projection. If we take all coordinates relative to the centre of mass, we can eliminate c_t entirely. Eq. (5) then gives

$$x_p^* = \left(\sum_s P_s^{\mathrm{T}} P_s \right)^{-1} \sum_t P_t^{\mathrm{T}} y_{pt}, \tag{6}$$

for x_p^*, the solution for x_p, given that the tilt parameters are known, and is the usual form of solution for a linear least-squares problem. Substituting this into the expression for F, eq. (3), we obtain

$$F = \tfrac{1}{2} \sum_{pt} \left[P_t \left(\sum_s P_s^{\mathrm{T}} P_s \right)^{-1} \sum_r P_r^{\mathrm{T}} y_{pr} - y_{pt} \right]^2,$$

which is in terms of the tilt parameters only. This is now a nonlinear least-squares problem, which we solve iteratively by using the Gauss–Newton approximation to the Hessian matrix and the Levenberg–Marquardt method to limit the step size at each iteration [19].

The expressions for the derivatives of F and the Hessian matrix are given by the following: Let $f_{pt} = P_t x_p^* - y_{pt}$, and α, β represent any two of the parameters θ, ϕ_t, ψ_t, m_t. Then

$$\frac{\partial F}{\partial \alpha} = \sum_{pt} f_{pt}^{\mathrm{T}} \frac{\partial f_{pt}}{\partial \alpha} = \sum_{pt} f_{pt}^{\mathrm{T}} \left(\frac{\partial P_t}{\partial \alpha} x_p^* + P_t \frac{\partial x_p^*}{\partial \alpha} \right)$$

$$= \sum_{pt} f_{pt}^{\mathrm{T}} \frac{\partial P_t}{\partial \alpha} x_p^*, \tag{7}$$

(using eq. (5)), and

$$\frac{\partial^2 F}{\partial \beta \, \partial \alpha} = \sum_{pt} f_{pt}^{\mathrm{T}} \left(\frac{\partial^2 P_t}{\partial \beta \partial \alpha} x_p^* + \frac{\partial P_t}{\partial \alpha} \frac{\partial x_p^*}{\partial \beta} \right)$$

$$+ \left(\frac{\partial P_t}{\partial \beta} x_p^* + P_t \frac{\partial x_p^*}{\partial \beta} \right)^{\mathrm{T}} \frac{\partial P_t}{\partial \alpha} x_p^*. \tag{8}$$

The term involving $\partial^2 P_t / \partial \beta \partial \alpha$ is ignored in the Gauss–Newton approximation. Differentiating eq. (6), we obtain

$$\frac{\partial x_p^*}{\partial \alpha} = \left(\sum_s P_s^{\mathrm{T}} P_s \right)^{-1} \sum_t \left[\frac{\partial P_t^{\mathrm{T}}}{\partial \alpha} y_{pt} - \left(\frac{\partial P_t^{\mathrm{T}}}{\partial \alpha} P_t + P_t^{\mathrm{T}} \frac{\partial P_t}{\partial \alpha} \right) x_p^* \right], \tag{9}$$

and we can simplify (8) to

$$\frac{\partial^2 F}{\partial\beta\,\partial\alpha} = \sum_{pt} x_p^{*T} \frac{\partial P_t^T}{\partial\beta} \frac{\partial P_t}{\partial\alpha} x_p^* - \sum_p \frac{\partial x_p^{*T}}{\partial\alpha} \left(\sum_t P_t^T P_t \right) \frac{\partial x_p^*}{\partial\beta}. \quad (10)$$

The derivatives of P_t can easily be evaluated from their defenition, eq. (2). Note that the dimensionality of this problem is equal to the number of parameters defining the tilts. This is very much less than the total number of unknowns, which also includes all the three-dimensional point coordinates. If some of the tilt parameters are fixed (e.g. magnifications all the same) then they disappear entirely from these equations.

The covariance matrix of the solution is estimated in the usual way, by a linear approximation at the solution. Assuming equal errors in the data points y_{pt}, their variance is given by

$$s_y^2 = \frac{2F_{\min}}{N_d - N_e}, \quad (11)$$

where N_d is the number of data points $= 2 \times N_t \times N_p$ and N_e is the number of parameters estimated:

$N_e = 2 \times N_t$ (centre of mass)
$+ 1$ (axis direction)
$+ 3 \times N_t$ (tilt angles)
$+ 3 \times N_p$ (three-dimensional coordinates).

The errors in the solution can then be estimated as

$$\mathrm{cov}(x_p) = s_x^2 \left(\sum_s P_s^T P_s \right)^{-1}, \quad (12)$$

$$\mathrm{var}(c_t) = \frac{1}{N_p} S_x^2 \quad (13)$$

$$\mathrm{cov}(\alpha) = S_x^2 \left(\sum_{pt} X_{pt}^T X_{pt} \right)^{-1} \quad (14)$$

where $X_{pt} = \partial f_{pt}/\partial\alpha$, and α is the vector of tilt parameters.

We have usually found sufficient points appearing on every tilt to give reliable results. However, it is also possible to solve the problem when some points are missing on some tilts (usually the high-angle ones). The offsets c_t cannot then be eliminated at the start of the calculation, and have to be included in the least-squares calculation with the x_p and tilt angles. The resulting equations are more extensive than those above, and will not be reproduced here.

Finally, we wish to find the positions of a set of parallel planes which contain the calculated positions of the points. The procedure is first to try to fit one plane through all the points. The distances of the points from the plane give an indication of how they should be grouped into sets, each of which lies in a single plane. The number of planes is increased until the residual distances are sufficiently small.

Suppose the points are in N sets, such that $\{x_{pk}: p = 1,\ldots,N_k\}$, $k = 1,\ldots,N$ are the N_k points on plane k. The set of parallel planes are represented as

$$r \cdot a = h_k, \quad |a| = 1, \qquad k = 1,\ldots,N, \quad (15)$$

and the least-squares fit is given by the minimum of

$$G = \sum_{pk} (x_{pk} \cdot a - h_k)^2, \quad |a| = 1. \quad (16)$$

Differentiation with respect to h_k gives

$$2 \sum_p (x_{pk} \cdot a - h_k) = 0, \quad (17)$$

so

$$h_k = \frac{1}{N_k} a \cdot \sum_p x_{pk}, \quad (18)$$

hence

$$G = \sum_{pk} \left(x_{pk} \cdot a - \frac{1}{N_k} a \cdot \sum_q x_{qk} \right)^2 = a \cdot B \cdot a, \quad (19)$$

where

$$B = \sum_{pk} \left(x_{pk} - \frac{1}{N_k} \sum_q x_{qk} \right)^T \left(x_{pk} - \frac{1}{N_k} \sum_q x_{qk} \right). \quad (20)$$

Clearly the minimum of G is achieved when a is the (unit) eigenvector of the matrix B with least eigenvalue. When the resulting minimum value of

G is sufficiently small, we assume that the points have been divided into enough plane sets. Although the process of dividing the points into sets could be automated, in this application the number of planes is only 2 or 3, so that it is more convenient and reliable to group the points by hand, particularly when the populations are offset in x–y from each other. The differences between the h_k give the required thickness measurements in terms of pixels. The normal vector a indicates the relation of the plane of the film to the nominal zero tilt position.

References

[1] R.C. Moretz, H.M. Johnson and D.F. Parsons, J. Appl. Phys. 39 (1968) 5421.
[2] J.-C. Jesior, EMBO J. 1 (1982) 1423.
[3] A.W. Agar, Brit. J. Appl. Phys. 8 (1957) 35.
[4] K. von Graf, Optik 18 (1961) 120.
[5] J. de Boer and G.J. Brakenhoff, J. Ultrastruct. Res. 49 (1974) 224.
[6] A. Cosslett and V.E. Cosslett, Brit. J. Appl. Phys. 8 (1957) 374.
[7] B. Kwiecinska and E. Scott, J. Microscopy 109 (1977) 289.
[8] E. Zeitler and G.F. Bahr, J. Appl. Phys. 33 (1962) 847.
[9] R. Freeman and K.R. Leonard, J. Microscopy 122 (1981) 275.
[10] S. Hovmöller, M. Slaughter, J. Berriman, B. Karlsson, H. Weiss and K. Leonard, J. Mol. Biol. 165 (1983) 401.
[11] G. Griffiths, A. Mc Dowall, R. Back and J. Dubochet, in preparation.
[12] J. Roth, The Colloidal Gold Marker System for Light Electron Microscopic Cytochemistry, in: Techniques in Immunocytochemistry, Vol. II (Academic Press 1983) pp. 218–284.
[13] K. Leonard, P. Wingfield, T. Arad and H. Weiss, J. Mol. Biol. 149 (1981) 259.
[14] D.L. Dorset and D.F. Parsons, Acta Cryst. A31 (1975) 210.
[15] A. Engel, W. Baumeister and W.O. Saxton, Proc. Natl. Acad. Sci. USA 79 (1982) 4050.
[16] E. Kellenberger, M. Häner and M. Wurtz, Ultramicroscopy 9 (1982) 139.
[17] J.-C. Jesior, Ultramicroscopy 8 (1982) 379.
[18] H. Goldstein, Classical Mechanics (Addison-Wesley, 1950) p. 107.
[19] D.W. Marquardt, SIAM J. Appl. Math. 11 (1963) 431.

Ultramicroscopy 19 (1986) 349–366
North-Holland, Amsterdam

METHODS FOR SPECIMEN THICKNESS DETERMINATION IN ELECTRON MICROSCOPY

II. Changes in thickness with dose *

John BERRIMAN ** and Kevin R. LEONARD

European Molecular Biology Laboratory (EMBL), Postfach 10.2209, Meyerhofstrasse 1, D-6900 Heidelberg, Fed. Rep. of Germany

Received 16 May 1986

The electron diffraction patterns of tilted thin crystals were used to determine the unit cell size in the direction normal to the supporting film. The method revealed a considerable dose-dependent thinning or shrinkage. Using a variety of specimens and stains, we found that this amounted to a 50% reduction in volume and could be attributable to two causes. Firstly, the specimen is held to the supporting film so that volume changes can only occur through changes in thickness. Secondly, the decrease in volume is associated with a dose-induced mass loss which is greatly suppressed at liquid nitrogen temperatures.

1. Introduction

Radiation damage in the electron microscope is a subject of wide interest and of particular concern to those investigating the ultrastructure of polymers and biological macromolecules [1,2]. The application of low or minimum-dose techniques [3] has improved image resolution and made molecular (unstained) imaging possible [4]. Investigations of unstained specimens in water [5], glucose [4] and at low temperature [6] have concentrated on periodic arrays either in two or three dimensions. This has stimulated the use of electron diffraction which, because of its quantitative nature, allows assessment of specimen preservation with respect to preparation and radiation damage [7]. Thin protein crystals pose special problems in interpreting their diffraction patterns because of the small number of unit cells present across the crystal thickness. This problem was theoretically treated by M. von Laue [8] and is of particular relevance to the analysis of electron diffraction patterns [9].

Proteins often produce crystals too small for X-ray crystallography. With platelet-type microcrystals, electron diffraction patterns can give 0.3 nm or better resolution [4]. The development of electron crystallography would be of interest to those investigating biological structures and should complement X-ray analysis and low resolution electron microscopy.

In our earlier paper [10] we found a reduction in crystal unit cell size normal to the supporting film. This we attributed to a change caused by electron damage. Here we extend and develop an investigation into this phenomenon and describe concepts necessary to understand the three-dimensional nature of thin protein crystals. In this paper we will use c to refer to the unit cell dimension normal to the supporting film.

2. Materials and instruments

EcoRV restriction enzyme-DNA oligonucleotide crystals were made according to Winkler et al.

* Part I: Ultramicroscopy 13 (1984) 351.

** Present address: University of Bath, EM Centre, Claverton Down, Bath BA2 7AY, UK.

0304-3991/86/$03.50

[11], catalase crystals by the method of Dorset and Parsons [5] and yolk platelet crystals from Pelvicachromis [12] kindly supplied by the late Dr. R.N. Lange. Single particles used were ferritin, apoferritin and glutamine synthetase, all supplied by Sigma, washed and diluted into physiological saline (0.9% NaCl).

Specimens were stained with aqueous solutions of 1% uranyl acetate, uranyl formate, barium acetate and phosphotungstic acid.

The microscopes used were a Philips 400T and 400, both with $\pm 60°$ goniometer stages. The 400 was adapted for low temperature work using an improved blade-type anticontamination device [13] and a liquid nitrogen cooling holder (Philips type PW6591). Magnification and electron diffraction camera lengths were standardized against catalase [14] and cross-checked in diffraction with thallous chloride powder patterns.

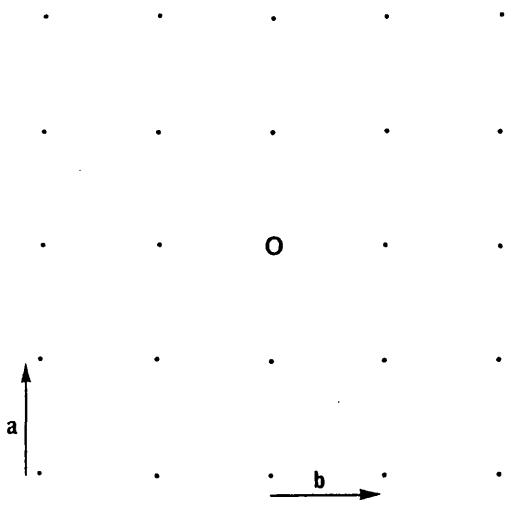

Fig. 1. A two-dimensional array of points representing a real space square lattice with $a = b$. As a reciprocal lattice the axes become a^* and b^* and the zero order or origin is shown marked as 0.

3. Methods

3.1. The determination of c for thin crystals, the unit cell dimension normal to the supporting film

Two methods were used to determine this spacing, both relying on the change in electron diffraction patterns on tilting the crystals.

3.1.1. Goniometric measurements

Fig. 1 shows a square lattice of points. This can be taken as a small part of a real lattice where the points represent centres of repeating motifs in a two-dimensional array. The points can also be considered to represent the reciprocal lattice or diffraction pattern of the real lattice. The central point then becomes the origin or zero order of the diffraction pattern. In fig. 2 the real (or reciprocal) lattice has been extended to three dimensions, taking the simplest example of a cubic lattice. Taking it to be a reciprocal lattice, the origin has been placed at the bottom left and two orders in a^*, b^* and c^* are shown. When the diffraction plane is normal to c^* (i.e., the case for an untilted specimen) the square diffraction pattern or $hk0$ projection is obtained (fig. 1). The dimensions a^* and b^* can be measured after calibration of the diffraction camera length with a compound of known lattice spacing. If the crystal is tilted with respect to the incident beam (the arrow in fig. 2) diffraction will be seen only at those points in the three-dimensional reciprocal lattice which intersect a central plane, normal to the incident beam. The tilt axis is parallel to the lines of the intersecting plane shown and, in this case, is shown at right angles to the diagonal between a^* and b^*. The crystal (rather than the beam as shown) is rotated about the tilt axis, so that the center of the 110 reflection is lost (centre spot in the bottom plane of nine spots) and the 111 reflection found (centre spot in the intersecting plane). The tilt angle is then recorded and c is determined trigonometrically. The disadvantage of this method, over the Laue zone method (see below), is that electron irradiation of the specimen is unavoidable during the "trial and error" procedure of adjusting the tilt angle to bring in the reflections.

3.1.2. Laue zone measurements

As described above, a three-dimensional crystal with many unit cells in each of the lattice directions gives rise to a reciprocal lattice consisting of discrete reflections. For very thin crystals, there is an effect of crystal shape on the diffraction pat-

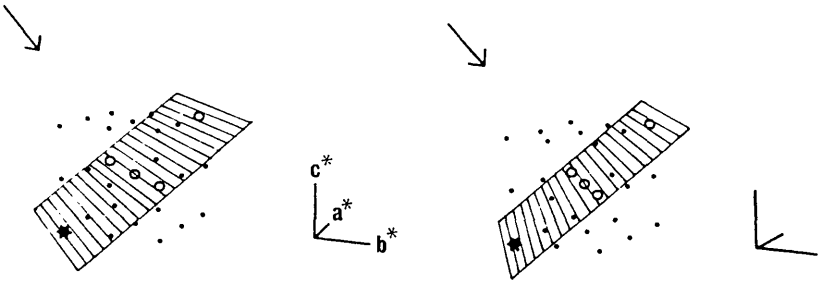

Fig. 2. A stereo pair of a three-dimensional cubic lattice of points. As a reciprocal lattice those points which are on a plane which is normal to the incidence of illumination (arrow) and which passes through the origin (bottom left) appear in the diffraction pattern (circles). In this example the tilt axis is at right angles to the diagonal of the unit cell a and b dimensions. Here c can be determined by measuring the 110 spacing (central point in the bottom plane) and the angle of tilt needed to bring the 111 reflection (central point in the middle plane) into the diffracting condition. With θ = tilt angle and $x = 110$ spacing, $c = x/(\tan\theta)$.

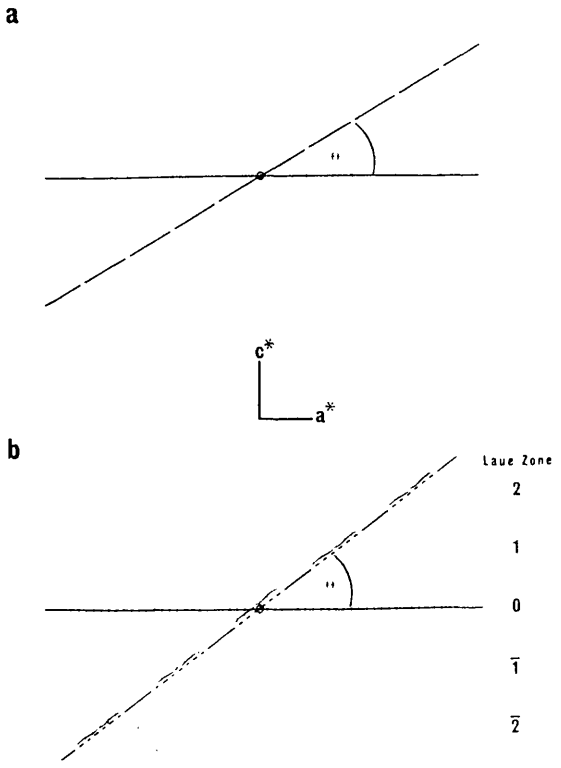

Fig. 3. This shows the 010 projections (down the b axis) of crystals which are one unit cell thick (a) and a few unit cells thick (b) along c. 0 marks the origin or zero order. In (a) the diffraction intensities are continuous spikes which can be recorded by tilting to any angle. In (b) the spikes are broken into bands with a periodicity equal to c^*. Increasing the number of unit cells gives shorter spikes and ultimately they become the points of a three-dimensional crystal. When tilted, (b) gives bands of reflections parallel to the tilt axis. Their centre-to-centre separation is dependent on c^* and the tangent of the angle of tilt.

tern which was considered theoretically by Laue [8] and reference made to observations obtained from electron diffraction of thin crystals. The limiting case of a thin crystal is one which is a single unit cell in thickness in the c direction. The three-dimensional reciprocal lattice of such a two-dimensional real lattice has continuous diffraction "spikes" parallel to c^* (fig. 3a). Tilting the specimen then samples the spikes at different points, and reconstruction of the repeating unit can be achieved by combining data from image tilt sets [15].

With a very thin three-dimensional crystal, containing a small number of unit cells in c, an intermediate situation exists, where the diffraction points are extended into short spikes parallel to c^* (fig. 3b). The separation of the planes of spikes is related to the inverse of the size of the c unit cell dimension and the length of the spike is inversely related to the thickness of the crystal or the number of unit cells along c. On tilting the crystal, the diffraction patterns show bands of reflections or Laue zones. Knowing the tilt angle, c can be calculated trigonometrically from the separation of the centres of these zones. The thickness of the crystal can also be calculated from the width of the zones [16]. Using this method it is possible to deduce c from tilted diffraction patterns without prior orientation of the crystal, thus permitting low dose measurements.

3.2. Measurement of the angular accuracy of the goniometer

As small tilt angles (up to 9°) were used in the above measurements, it was necessary to check the accuracy and reproducibility of the goniometer specimen holder within these limits. This is best done with a crystal which is not radiation sensitive and which has a known c spacing. Protein crystals have relatively large spacings but none were found which could provide a reliable standard. Thin graphite crystals were therefore used which diffract to a resolution of 0.1 Å and which have a well-established interlayer spacing of 3.4 Å [17]. Since these measurements were made at higher resolution, the effect of the curvature of the sphere of interaction, or Ewald sphere, becomes important.

Fig. 4, an Ewald construction, shows a high resolution reciprocal lattice and the intersection, at 0° tilt and θ° tilt, of the Ewald sphere, whose radius is inversely proportional to the electron wavelength. This can be regarded as a reduction of fig. 3b, where a flat plane is a reasonable approximation, by a factor of about 20 times. For example, in fig. 3b the unit cell dimension a would be about 80 Å and extend to 3 Å, whilst in fig. 4, a would be about 4 Å and extend to 0.15 Å. In the zero tilt the separation betwen the Ewald sphere and the reciprocal lattice increases with distance from the origin until reflections in this plane are no longer intersected. Eventually, with increasing reciprocal distance the Ewald sphere intersects the next layer of the reciprocal lattice, giving a circle of reflections known as the first-order Laue zone. The radius of this circle R is related to the unit cell dimension c and the wavelength of the electron beam λ via the expression

$$R = \sqrt{2/\lambda c} \quad (\lambda \ll c).$$

At zero tilt, it is possible to determine the camera length (from the projected unit cell dimensions a and b) and the c dimension (from the radius of the first-order Laue zone and the electron wavelength). A tilt set at small angles then produces Laue zone patterns which can be used to verify the tilt angles.

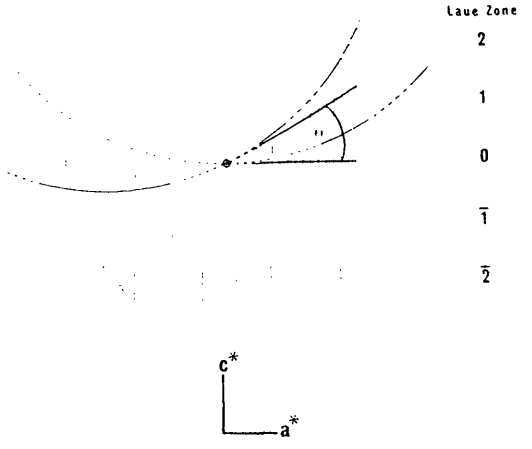

Fig. 4. The finite wavelength of electrons produces a curvature of the diffraction plane (Ewald sphere). At high resolution fig. 3b alters to the pattern shown here. The untilted diffraction plane curves out of the zero order Laue zone and through the first order. Tilting the intersection of a curved surface with parallel planes produces a complex distribution of intensities.

3.3. Preparation of low temperature specimens

Specimens in water were applied to carbon-collodion coated copper grids, blotted quickly with filter paper and frozen in liquid nitrogen. Samples were inserted into the microscope by cold transfer with the specimen holder at liquid nitrogen temperature. The sample was then observed in the microscope either with or without an anticontaminator. Negatively stained specimens were dried, inserted into the microscope and then cooled. In order to determine the effect of a contaminating layer, dried negatively stained grids were partially coated with carbon on the upper surface, by shielding one half with a metal strip. To identify the coated area a small amount of gold was sputtered onto the surface with the uncoated half still shielded.

3.4. Preparation of partly supported crystals

Crystals of catalase were applied to holey carbon films and negatively stained with uranyl acetate. After taking a series of micrographs with increasing electron dose, changes in the unit cell in different areas of the crystal were measured with an optical diffractometer using an aperture to sample small regions of the negative.

3.5. Determination of the thickness of single particles

An area of negatively stained, approximately spherical and similar-sized particles is diffracted, either directly with the electron beam or optically from an image. Each individual particle acts as a diffracting disk, and a random distribution of such particles will then produce a combined Fraunhofer diffraction pattern. This "Airy disk" pattern has an intensity distribution which depends primarily upon the projected outline of the object. The central maximum is surrounded by a dark ring which corresponds to the first zero of the J_1 Bessel function. Thus from such diffraction patterns the average radius of the particles can be determined using Bessel function tables.

If the specimen is tilted in the microscope, a truly spherical particle will always have a circular projection and the diffraction pattern will also be circular. Should the particle be compressed (i.e. reduced in thickness normal to the supporting film), the projection will increase in ellipticity as the angle is increased. Correspondingly, the diffraction pattern will cease to be circular and become elliptical, the major axis of the ellipse in reciprocal space being generated by the reduced thickness of the compressed particle. The minor axis of the ellipse remains constant during tilting since there is no change in real space along the tilt axis around which the spheroid is being rotated. Fig. 5 shows a sphere becoming progressively oblate. Viewing from A (the normal direction of electron microscopy) would give no difference. From C the change in thickness would be easily measured. At B the thickness change is found through the sine of the angle of observation. To measure changes in thickness with electron dose, a series of images of the same area of specimen tilted to 45° were taken, followed by a final image at 0° tilt. The images were then analysed with an optical diffractometer and the degree of ellipticity determined for the diffraction pattern produced by each image. Alternatively, electron diffraction of a large selected area (10 μm) was carried out at 45° tilt and a series of patterns photographed with increasing dose. A final 0° tilt pattern was again taken. In each case, changes in the diffrac-

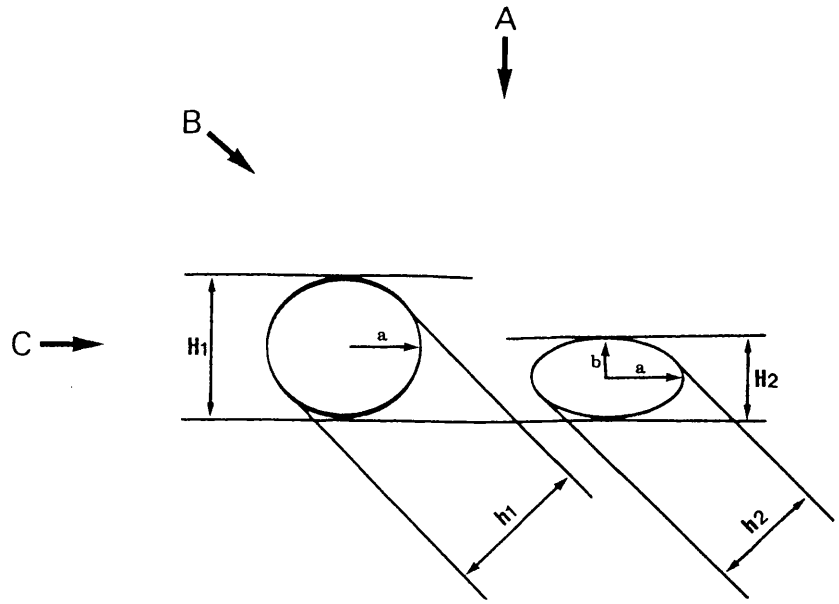

Fig. 5. Shows two oblate spheroids representing single particles flattened to different extents and seen parallel to the supporting film of an electron microscope grid. The direction A is that of normal observation for which no difference is measurable. From B, a tilted view of the reduction in height ($H_1 - H_2$) produces a corresponding reduction in projected diameter ($h_1 - h_2$) and measurement is possible using the sine of the angle of tilt.

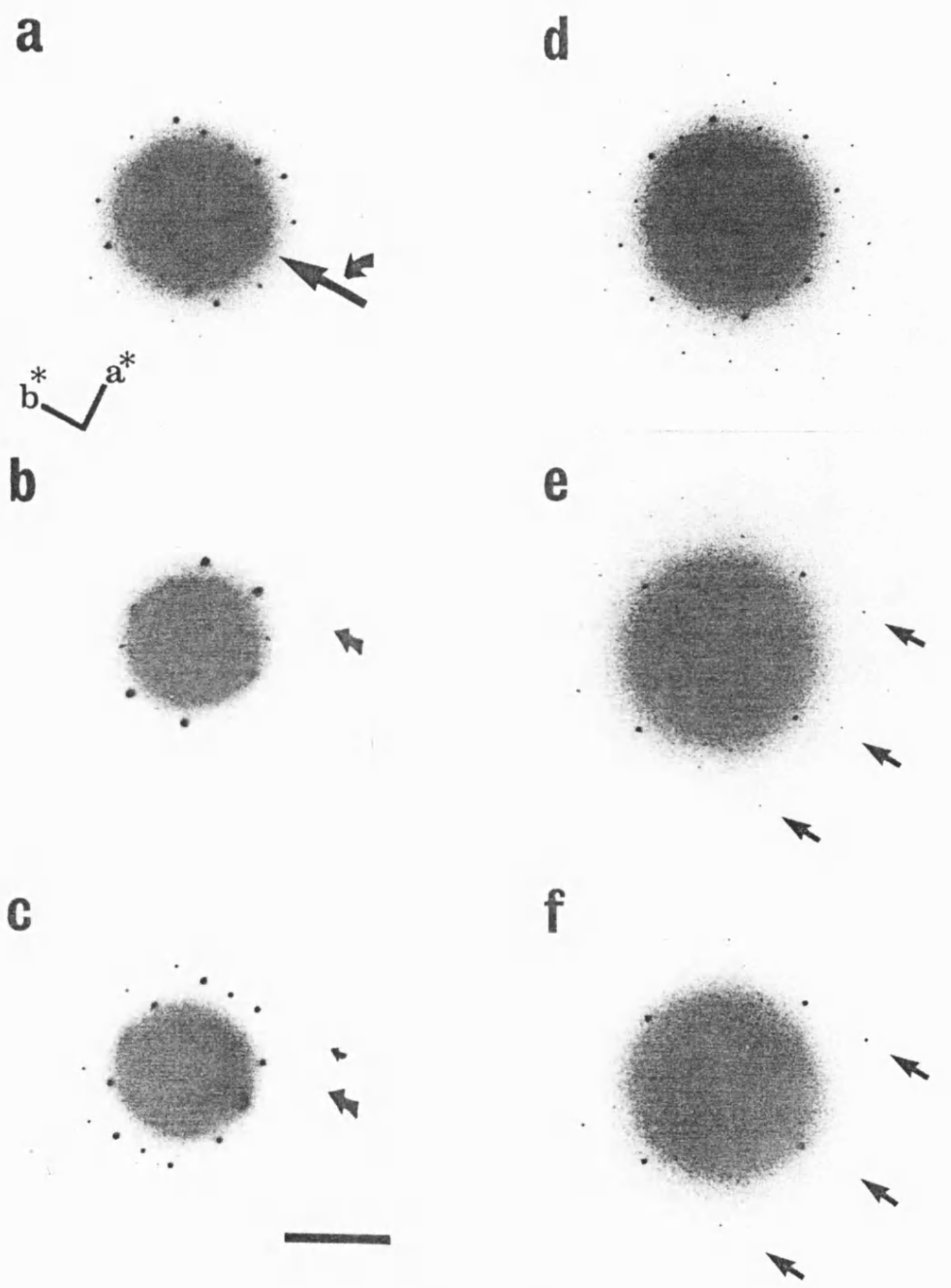

Fig. 6. Diffraction patterns from negatively stained EcoRV-10o crystals as described in the text. The tilt axis is shown by the large arrow in (a) and the same axis orientation has been used in all subsequent patterns. (a) to (c) show a tilt set where the crystal ***b*** axis has been aligned with the tilt axis. (d) to (f) show a tilt set where the crystal has not been aligned but the zero, plus and minus tilts were recorded sequentially. The Laue zones (parallel to the tilt axis) are shown arrowed. All patterns are to the same scale and the bar in (c) represents 0.05 A^{-1}.

tion patterns were used to determine changes in specimen thickness with electron dose.

3.6. Measurement of electron dose

Kodak SO-163 film was used, developed for 12 min in D19. This gives an optical density of 2.2 for 1 $e^-/\mu m^2$ at the film [18].

4. Results

4.1. Thickness change in negatively stained specimens

4.1.1. For thin crystals

This was measured either by direct goniometry or by the Laue zone method. As an example of the former, we show in figs. 6a–6c measurements made on a stained EcoRV-10o crystal. The crystal has been rotated in a eucentric goniometer so that the tilt axis (arrow) is parallel with b^*. Fig 6a at zero tilt shows the electron diffraction pattern of the projection down c^*. The crystal is then tilted about b^* until the pattern seen in fig. 6(b) is obtained. Here the points along the second layer line have increased to a maximum intensity (arrowed). The tilt angle is then measured and the diffraction pattern recorded. In fig. 6c the crystal has been tilted further and the first layer line now comes to a maximum (large arrow) coincident with a second maximum on the second layer line (small arrow). By using these angles and those obtained when rotating the crystal in the opposite direction, it is possible to correct for initial specimen tilt and to ensure that c is perpendicular to a and b. This procedure is one of trial and error, and the specimen therefore receives a fairly high electron dose giving a resolution limit of about 20 Å.

In figs. 6d–6f, we show an example of the use of Laue zones to determine c^* for the EcoRV-10o crystals. Fig. 6d is a zero-tilt projection and, as no alignment has been carried out, the low dose pattern extends to 10 Å. Fig. 6e shows a +15° tilt, with the Laue zones (parallel to the tilt axis) indicated by arrows. Fig. 6f shows a −15° tilted pattern confirming the position of the zone with opposite tilt

During the goniometric measurements, it was

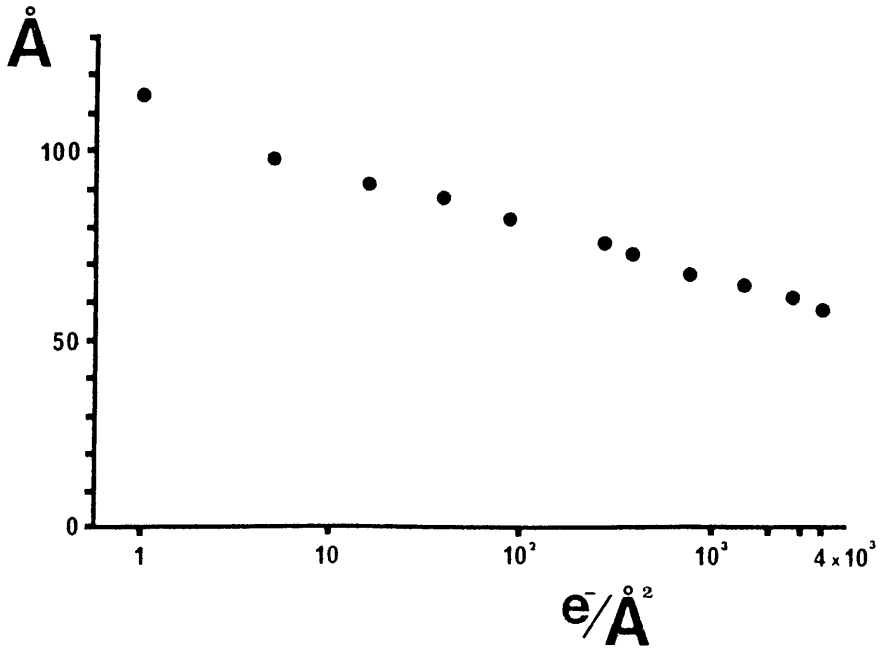

Fig. 7. Variation of the c unit cell dimension of an EcoRV-10o uranyl acetate stained crystal with accumulated dose.

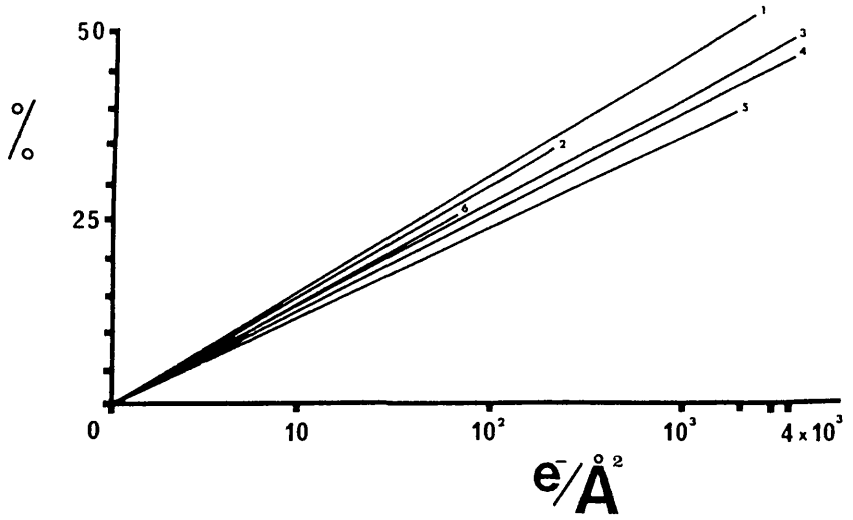

Fig. 8. Variation of the percentage reduction in the value of c dimension with accumulated dose. (1) The yolk platelet crystal stained with uranyl formate. (2) Ferritin, apoferritin and glutamine synthetase stained with uranyl acetate. (3) Catalase stained with uranyl acetate, uranyl formate, phosphotungstic acid and barium acetate. (4) Restriction enzyme EcoRV-10o DNA (decamer) co-crystal stained with uranyl acetate. (5) Restriction enzyme EcoRV-8 DNA (octamer) co-crystal stained with uranyl acetate. (6) STEM mass loss curves [31].

noticed that the tilt angle required to maximise the intensity of a given lattice layer would increase slowly with time. In the case of EcoRV 10o, for example, if a tilt was made as in fig. 6b, an initial value of 14° was recorded and this increased to 24°. This corresponded to a reduction in c value from 114 to 64 Å. Using low dose Laue zone measurements as in fig. 6e, an initial value of 124 Å was found. This was repeated with different preparations of the same crystal. The effect of electron dose on the c dimension of this crystal is shown in fig. 7.

The combined results of some fifty experiments using different crystals and negative stains are shown in fig. 8. The unit cell dimension c in negatively stained crystals reduces exponentially with dose to about 50% of the starting value. In all cases of crystals supported on carbon films, a final zero tilt image of the area which had been irradiated showed no changes in a and b, the crystal shrinkage having taken place entirely in the direction at right angles to the plane of the grid.

4.1.2. For single particles

Uranyl acetate negatively stained preparations were made of ferritin, apoferritin and glutamine synthetase. Micrographs were taken under low and high dose conditions with the specimen tilted at 45°. Figs. 9a and 9b show a low and high dose pair from the ferritin experiment. The low dose image has a three-dimensional appearance whilst the high dose is flat. After dosing, the grid is returned to 0° (carefully keeping the area irradiated centered) and imaged again (not shown). Figs. 9c–9e show show the optical transforms of a 45° image dose set. These can be seen to have increasing ellipticity. Fig. 9f is the transform of the same area returned to 0° and shows the circular outline of an oblate spheroid in projection. This gives a pattern which, using the Airy disc approximation, fitted a J_1 Bessel function to the minima corresponding to discs of 124 Å diameter. This did not change with dose. The 45° patterns 9c–9e show an increase in the radius of the minima parallel to the tilt axis with dose. This was measured initially to be 120 Å and reduced to 80 Å. This 30% reduction in thickness with dose is plotted out in fig. 8, line 2.

Figs. 9g–9j show electron diffraction patterns of a 10 μm selected area of negatively stained ferritin molecules tilted at 45°. The diffraction patterns were taken with only 0.1 e/Å and so fig.

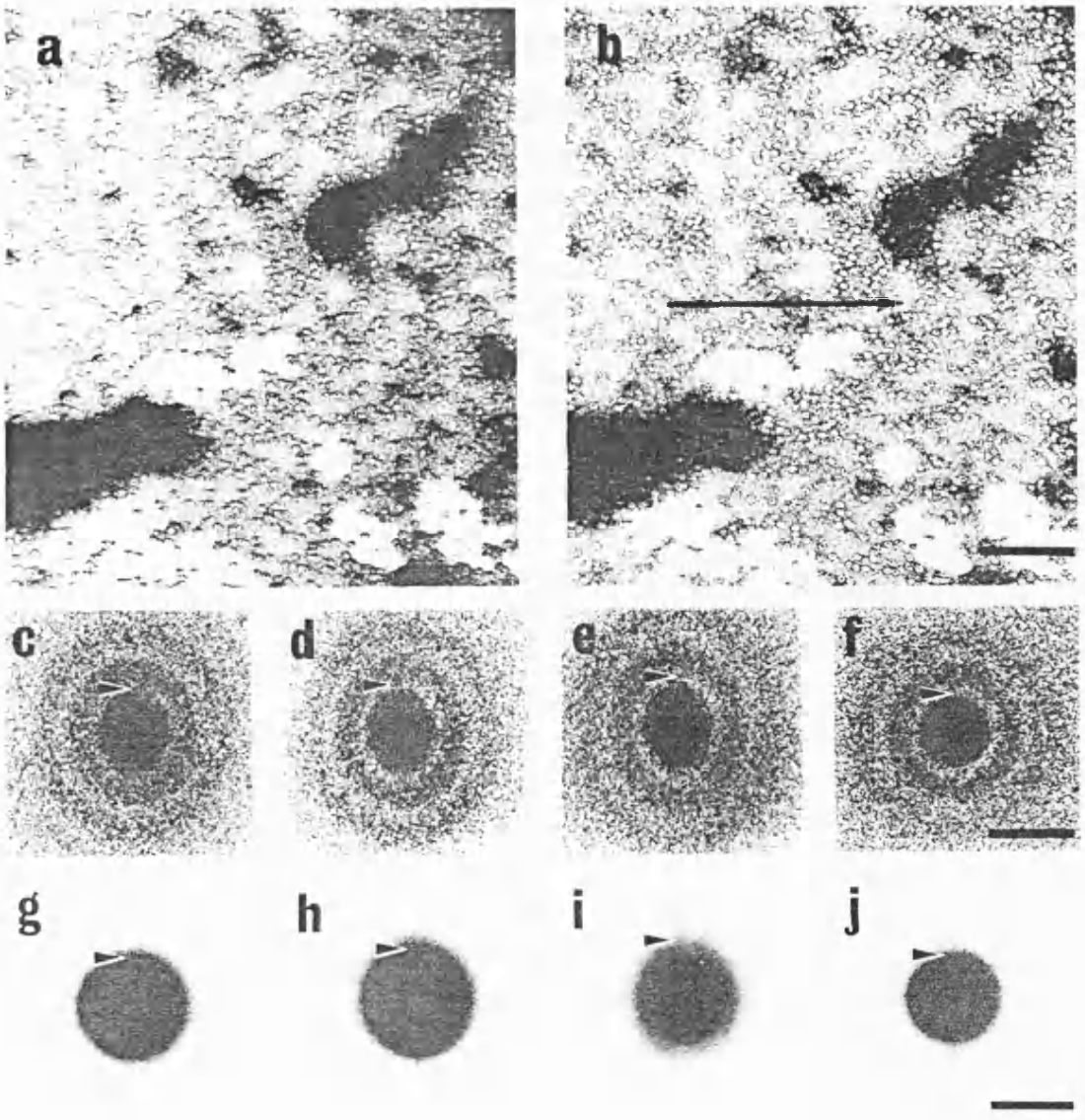

Fig. 9. Uranyl acetate stained ferritin particles. (a) and (b) are low (1 $e^-/Å^2$) and high (100 $e^-/Å^2$) dosed images taken at a tilt angle of 45°. The tilt axis is indicated by the arrow in (b) and the scale bar represents 0.15 μm. (c) is an optical transform of an area as shown in (a) taken with a dose of 1 $e^-/Å^2$. (d) is the same area after 10 $e^-/Å^2$ and (e) is after 100 $e^-/Å^2$. (f) is the transform of the dosed area on changing the tilt to 0°. In (c) to (f) the arrow indicates the first minimum of the J_1 Bessel function. The scale bar represents 0.02 $Å^{-1}$. The images were taken close to focus and the patterns are not to be confused with Thon rings. (g) and (j) are electron diffraction patterns of 10 μm selected areas of the feritin sample. (g) to (i) are at 45° tilt and taken after 0.1, 10 and 100 $e^-/Å^2$. (j) is the closed area at 0° tilt. The arrow marks the second maximum of the J_1 Bessel function which , because of inelastic scattering, is more easily resolved than the first minimum. The scale bar represents 0.04 $Å^{-1}$.

9g, the first pattern, is one tenth the dose of fig. 9a. The pattern starts quite circular and becomes elliptical with dose (to fig. 9i). Fig. 9j shows the pattern from the same region tilted back to 0°.

4.1.3. Unsupported crystals

Crystals of catalase were negatively stained and dried onto carbon films with holes. A series of images taken of a crystal edge crossing a hole showed a pronounced movement of the edge as the crystal contracted (fig. 10). Such a crystal can be considered as being supported only normal to the arrow at the edge (in this case the unit cell ***a*** direction) and contraction has taken place along the ***b*** direction (arrowed) at the edge where it is least supported. The crystal projection unit cell area has been reduced by about 30%, packing the stain into a smaller area and increasing the density. The reduction in the unit cell axes was measured by optical diffraction of small areas across the micrograph.

Figs. 11a and 11b show the low and high dose

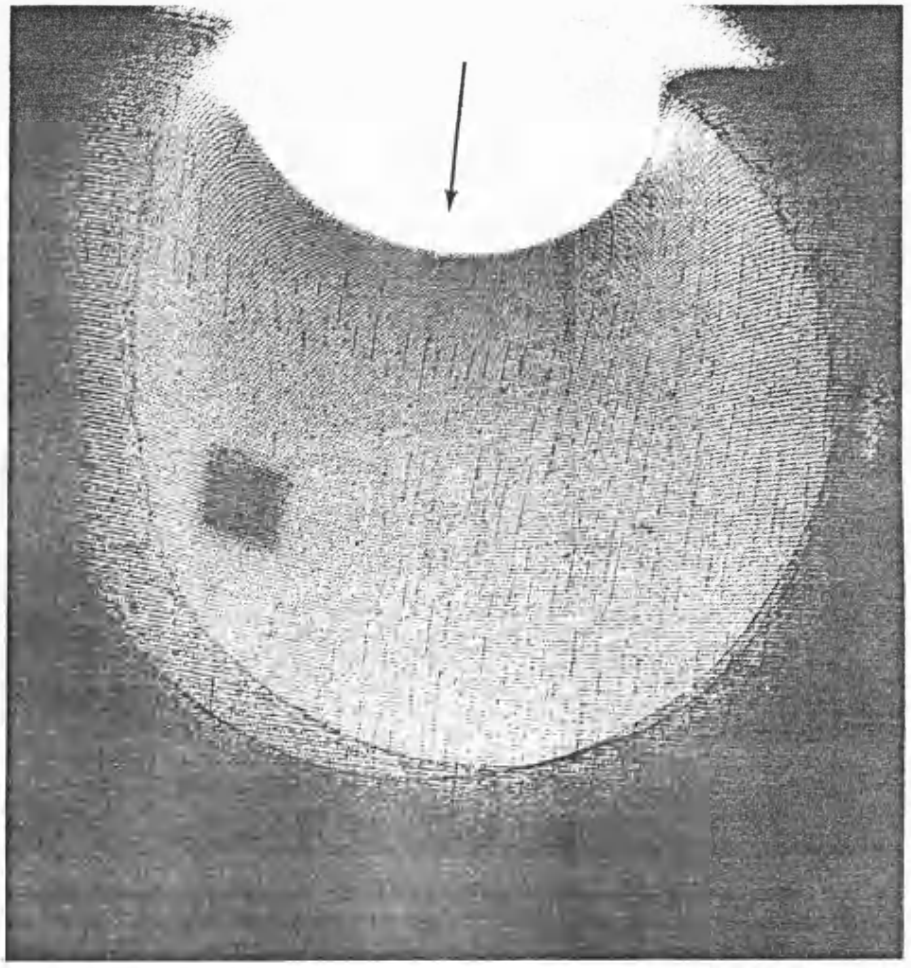

Fig. 10. An irradiated negatively stained catalase crystal which spans a hole in the supporting film. One edge was not supported and the crystal has contracted as shown by the arrow. The reduction in the ***b*** unit cell size can be seen by viewing the image close to the page at right angles to the arrow. Parallel to the arrow the ***a*** unit cell dimension is only slightly distorted. The scale bar represents 0.1 μm.

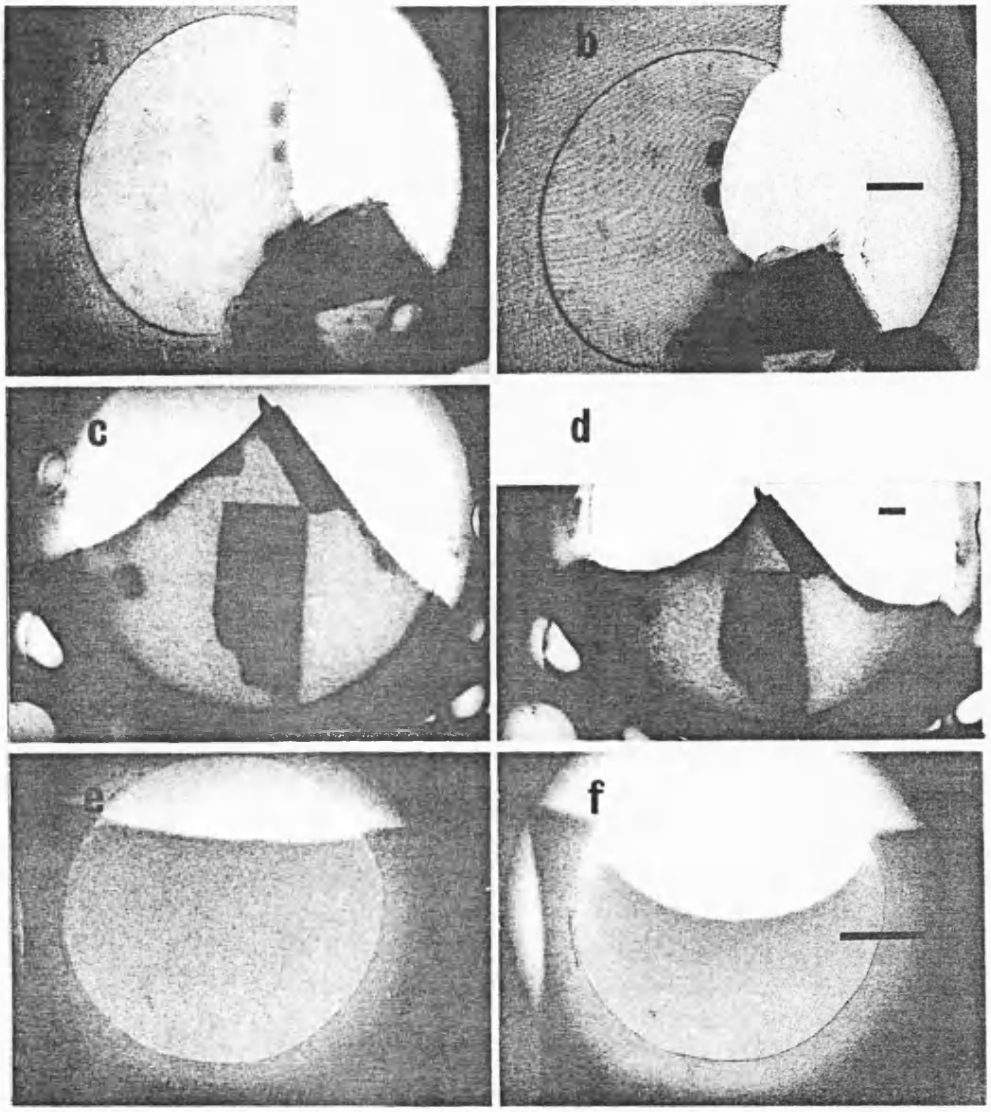

Fig. 11. Catalase crystal images of low (1 $e^-/Å^2$) and high (100 $e^-/Å^2$) accumulated dose spanning holes in the supporting film. (a) and (b) are uranyl acetate stained with an unsupported edge, (c) and (d) are with an unsupported corner and (e) and (f) are glucose-embedded with an unsupported edge. The scale bars for each pair represent 0.1 μm.

pair of a crystal as in fig. 10. The change again showed a 30% reduction of one unit cell dimension. Figs. 11c and 11d show a crystal corner that was unsupported. The contraction in this case is isometric and showed a 20% reduction on both crystal axes. With unstained crystals embedded in glucose (figs. 11e and 11f) it was not possible to measure changes in the unit cell parameters, but dose induced shape changes of unsupported crystals were essentially the same.

4.2. Absolute thickness of stained and unstained specimens

Catalase forms very well characterised crystals for electron microscopy and was therefore used as

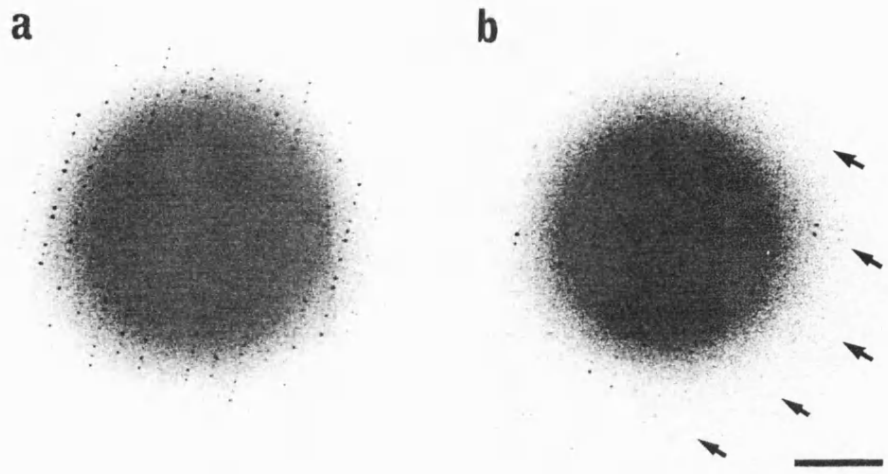

Fiig. 12. An example of the low dose Laue zone method for determining c with a negatively stained catalase crystal. Both diffraction paatterns were taken with 0.2 $e^-/Å^2$. In (b) the tilt angle was 9° and the Laue zones (parallel to the tilt axis) are arrowed. c can be calculated by dividing the separation of the Laue zones by the sine of 9°.

a test object for further investigation. As described above, a 50% relative reduction in c was found for the negatively stained crystals. At low dose, however, c was maximally 145 Å, fig. 12, a long way short of the expected vale of 206 Å [19]. Thus, although the reduction in c agrees well with a study of sectioned negatively stained (and dosed) catalase crystals [20], the starting value is still 30% less than the value for hydrated crystals.

Catalase can exist in different crystal habits and so to check the homogeneity and unit cell dimensions of our preparation, a small-angle X-ray diffffraction pattern was taken. A crystal suspension was sedimented in a quartz capillary. The X-ray pattern shown in fig. 13 was taken with unifilered radiation and can be interpreted as two patterns generated by the copper Kα and weak Kβ X-ray wavelengths. The unit cell dimensions are $68 \times 174 \times 200$ Å and $P2_12_12_1$ space group with systematic absences along the principal axes for $h + k + l$ odd. The first ring doublet is from the 011 reflections at 132 Å. The arcs oriented meridionally (arrowed) are from the 002, c, spacing at 100 Å. The orientation of this spacing is a consequence of the thin platelet crystals settling under gravity as a staggered stack. The half width of the 002 reflection gives a value of 2000 Å for the thickness of the crystals. This is about 10 unit cells and is consistent with results obtained in the electron microscope. Thus by X-ray diffraction we found our preparation to be homogeneous with a

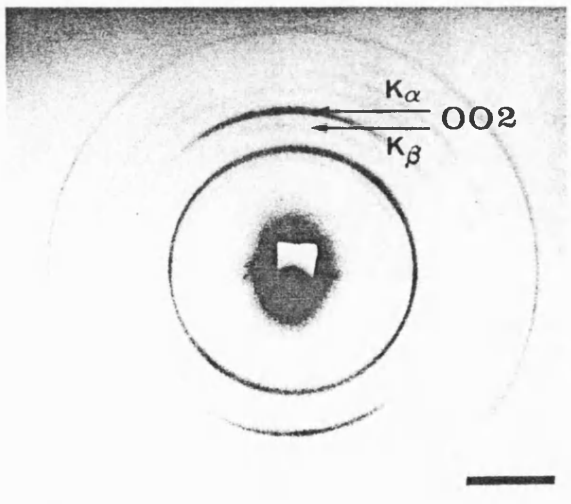

Fig. 13. The X-ray diffraction pattern of a suspension of catalase crystals which had settled in a quartz capillary. The orientation of the tube is vertical and the strong 002 arc is arrowed. The pattern corresponds to a $68 \times 174 \times 200$ Å unit cell size and a $P2_12_12_1$ space group. The scale bar represents 0.005 $Å^{-1}$ for the Cu Kα wavelength.

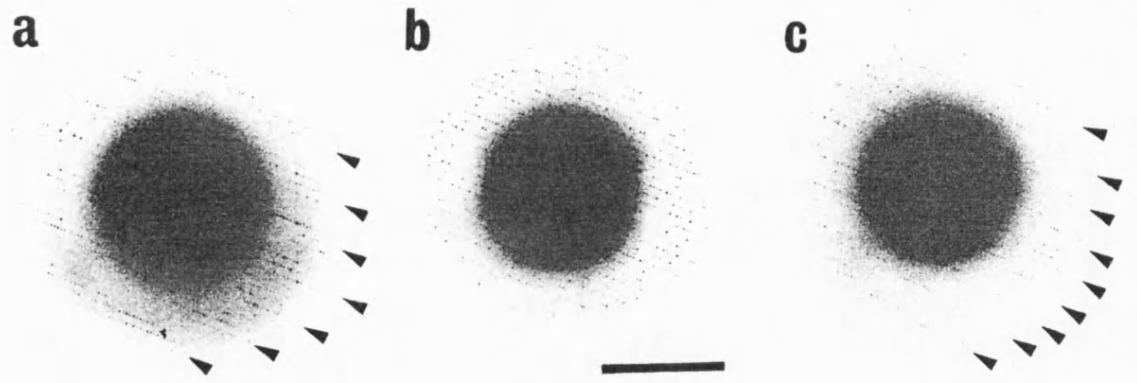

Fig. 14. An example of the low dose Laue zone method for determining c with glucose embedded catalase crystals. A dose of 0.2 $e^-/Å^2$ was used for each pattern. (a) to (c) correspond to goniometer settings of $-3°$, $0°$ and $+3°$. The Laue zones (parallel to the tilt axis) are arrowed. (a) and (c) give two different values for c because $0°$ is not exactly normal to the beam (this is confirmed by the lack of Friedel symmetry across the tilt axis in (b)). Using the average c value, the actual tilt angles can be calculated and this simple iterative step yields a best fit to the data. The scale bar represents 0.2 $Å^{-1}$.

value of c for hydrated material of 200 Å.

Glucose embedding of protein crystals gives high resolution diffraction patterns [4]. This improvement in preparation over negative staining is thought to be a result of hydrogen bonding by the carbohydrate which replaces water as it dries to a gum. The projection unit cell sizes are unchanged and the Laue zone method for determining c was used in low dose electron diffraction of tilted glucose-embedded crystals.

Fig. 14 shows a tilt set from one crystal. The Laue zones are shown parallel to the tilt axis. The patterns were recorded with 0.2 e/Å each and although the strength of the pattern reduced, the Laue zones are still distinct.

The results of twenty tilt sets gave a value of c of 160 ± 10 Å. This corresponds to a 20% reduction in c for the starting value in glucose. In order to check that the spacing did not change with dosing, crystals were irradiated at a set angle. No movement of Laue zones was found as the pattern became weaker and disappeared.

Laue zone measurements on frozen hydrated crystals were difficult to interpret directly since they showed a precession of the zones with increasing tilt. The low-temperature holder, since it is isolated with glass spheres, has a tilt which cannot be corrected with the specimen in the microscope. A computer program essentially the same as that used for analysing data for tilted layers of particles [10] showed that specimens were tilted by 4° to 6° normal to the tilt axis. The corrected Laue zone spacings then gave a mean value for the c spacing of $175 = 10$ Å from six experiments. As with glucose, the c spacing did not change on dosing but the Laue zones remained fixed while the intensities decreased.

When dried negatively stained crystals were observed on the cold stage, there was no evidence of the shrinkage which had been seen to occur at room temperature. The angle of tilt required to maintain maximum intensity of the electron diffraction pattern remained constant over a wide dose range. After about 1000 e/Å the pattern had deteriorated in resolution but all unit cell dimensions were unchanged (within the experimental accuracy of 5%).

These measurements were made with a modified cold trap close to the specimen [13] which restricts tilting. This was removed for tilting above 30° with the surprising result that the specimen behaved quite differently, the electron diffraction patterns fading very quickly. By 10 e/Å the pattern had disappeared completely. Examination of images under these conditions showed that the specimen had become coated by a thin layer (pre-

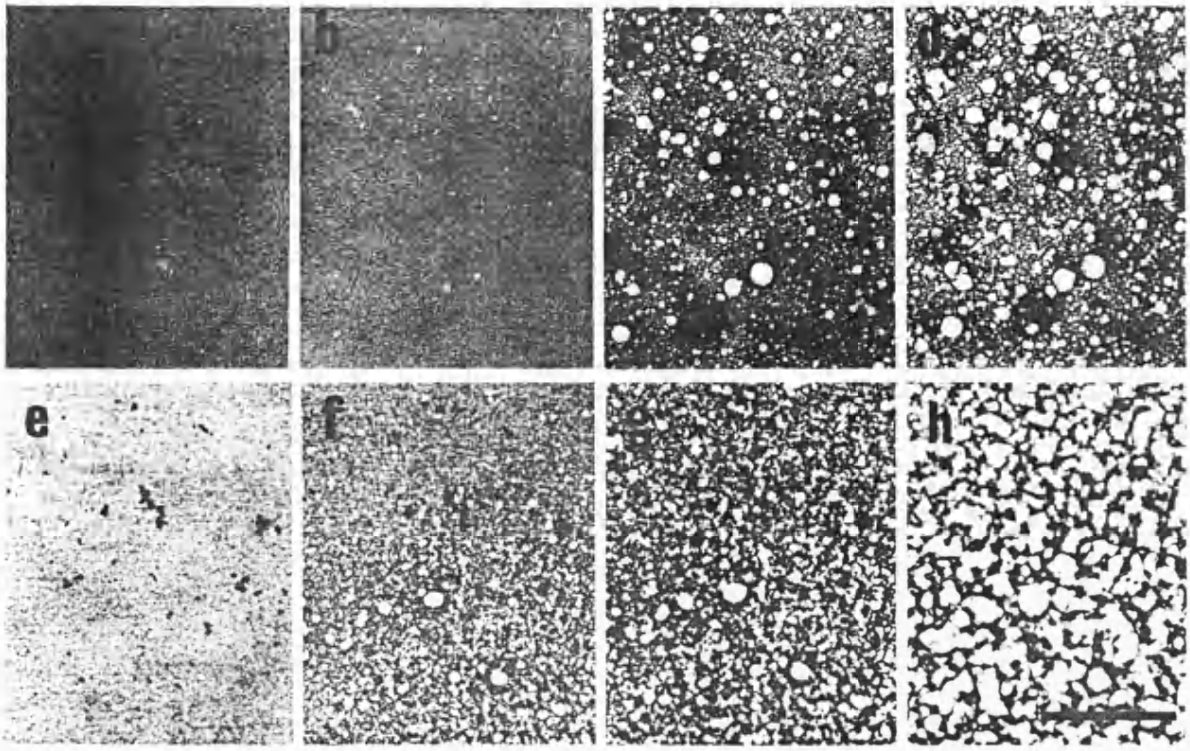

Fig. 15. Negatively stained catalase crystals cooled to 120 K and (a) to (d) coated with a thin layer of ice. The images are taken sequentially at 1, 2, 5 and 10 $e^-/Å^2$. (e) to (h) are carbon coated and marked with gold particles. This dose set is 1, 5, 10 and 100 $e^-/Å^2$. The scale bar represents 0.4 μm.

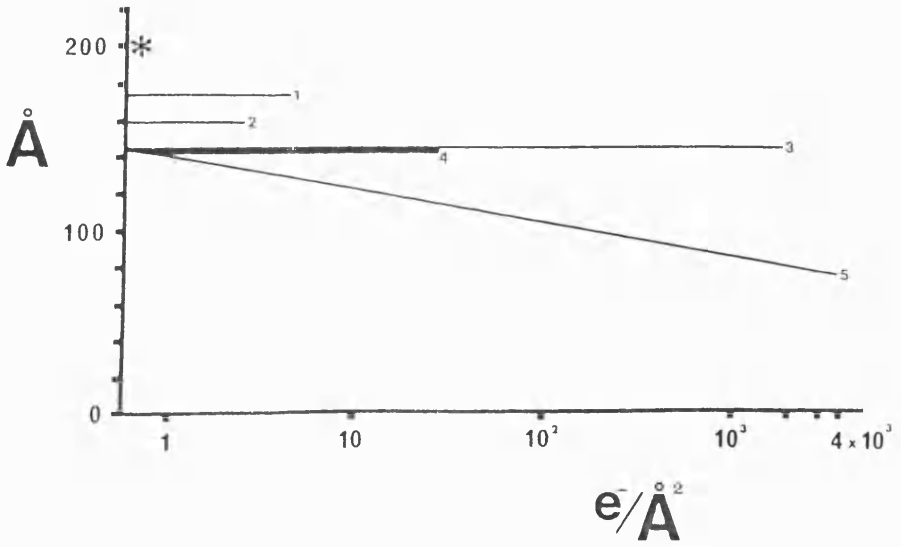

Fig. 16. Variation of catalase c^* unit cell size with accumulated dose under different experimental conditions. (*) Value by X-ray diffraction. (1) Frozen in water at 120 K. (2) Glucose-embedded at room temperature. (3) Negatively stained at 120 K. (4) Negatively stained at 120 K with a contaminating layer of ice or deposited carbon layer. (5) Negatively stained at room temperature.

sumably water vapour) and rapid destruction of the crystal by "bubbling" took place (figs. 15a–15d).

The bubbling may be caused either by some aggressive property of frozen water vapour in combination with electron irradiation or perhaps by a simple trapping of active species such as radiation-induced free-radicals, with the layer acting as a permeability barrier. In order to discriminate between these, a dried negatively stained grid of catalase crystals was half covered with a 30 Å carbon film. The grid was then observed cold with the cold finger in place. The uncoated crystals did not bubble and gave diffraction patterns that were stable for many hundreds of $e^-/Å^2$. The crystals that were carbon-coated were rapidly destroyed by bubbling. Figs. 15e–15h show a dose set from the carbon-coated half. The cold finger was then removed and after a short time condensation was found on the grid and the non-carbon-coated crystals also bubbled.

To test the effect of temperature on this damaging process, the grid was warmed by stopping the cold nitrogen supply. At 140 K the surface layer of amorphous ice is converted to cubic ice [21] and at 150 K this evaporates in a few seconds into the high vacuum of the microscope. On recooling the grid with the cold finger in place, the coated crystals were found not to bubble until the temperature was below 140 K. The experiment was repeated with a completely carbon-coated grid without the gold markers. Again below 140 K bubbling was found to occur.

Fig. 16 shows a compilation of these results for catalase.

4.3. Accuracy of the goniometer at small angles

Since the absolute value of c depends on the accuracy of the tilt angles measured, the electron microscope goniometer was checked with crystals of graphite. Fig. 17 shows a high-angle diffraction tilt set for graphite; fig. 17a is a projection down c^* showing the first-order Laue zone.

The spacing of this zone gave, using the wavelength for 80 kV electrons (0.0418 Å), a c spacing of 3.44 Å. Figs. 17b and 17c show $+3°$ and $-3°$ tilt. The first-order Laue zones are displaced in

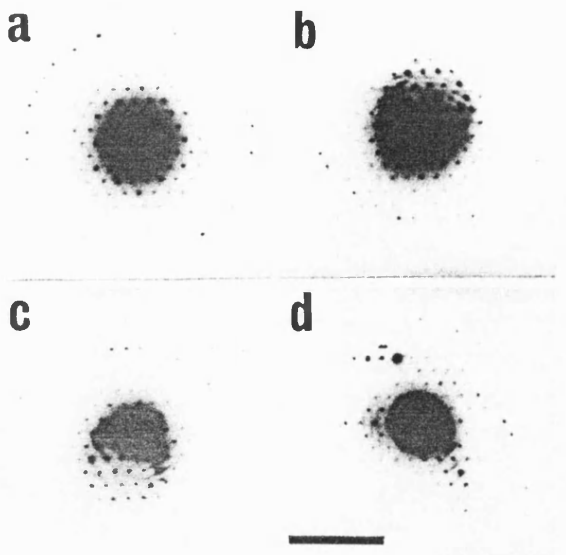

Fig. 17. Diffraction pattern tilt set for a graphite crystal taken at 80 kV: (a) 0°; (b) $=3°$; (c) $-3°$; (d) $-6°$. The scale bar represents 3.2 $Å^{-1}$.

equal and opposite directions (about the tilt axis). Fig. 17d shows a $-6°$ tilt having the first- and second-order Laue zones. By calculation, the positions of the Laue zones were found to agree with the measured tilt angles to within 5%.

5. Discussion

One of the first observations of an interaction between material of biological origin and an electron beam was the reduction in size of cotton thread [22]. Specimen shrinkage and movement was a problem in the early days of electron microscopy which was effectively solved [23] by supporting specimens on thin carbon films. Although this procedure prevents movement in the plane of the specimen grid, which is the most important for projection imaging, it has been clear for many years that the specimen can undergo a dimensional change in the direction parallel to the beam during irradiation with electrons. This becomes an important factor when attempting to extract three-dimensional information from the micrographs.

Specimen shrinkage has been discussed in a theoretical review of the effects of radiation damage [2]. A reduction in thickness of TMV particles on irradiation has also been described [24]. An argument against substantial shrinkage was that specimens could "wrap" into the supporting film [25], to give an apparent reduction in thickness (as, for example, measured by shadowing with heavy metal). Contamination was also a considerable problem in early work and the loss of thickness on irradiation could be confused with a build-up of a contaminating layer [26].

Investigation of changes in periodic structures should be independent of such uncertainty. A study of T4 tail [27] revealed a shrinkage of the upper unsupported surface. The effect of radiation damage on three-dimensional reconstructions of negatively stained stacked-disc TMV particles [28] suggested that stain migration was taking place. We would rather explain this process as a contraction of the unsupported regions of the protein, the stain moving with it to "fill in" the empty space. A further study of stained stacked-disc TMV and T2 phage [29] found that "improved" images could be recorded after a pre-irradiation of the specimen with the beam. This procedure gives the best compromise between specimen thinning rate and resolution, since both are reduced with dose.

"Thinning" by irradiation is also a common way of improving the contrast of thick sections and quantitative evidence for such a reduction was found in reconstructions from muscle sections, where the three-dimensional lattice is known [30]. Grid sectioning of irradiated, negatively stained catalase crystals gave an anomalously low value for the unit cell size in the direction perpendicular to the supporting film, despite the fact that the crystals appeared to be quite well preserved [20].

The work described here shows that there is a marked loss of thickness for negatively stained material on irradiation. By using low electron doses and electron diffraction methods for crystalline material, we have been able to make a direct quantitation of these changes as they take place in the electron microscope. In an unsupported specimen, shrinkage occurs as an isometric process and may be related to beam-induced mass loss of the biological material. In the case of a specimen supported on a carbon film, which is the normal situation for biological electron microscopy, shrinkage is prevented in the plane of the film, with the result that there is a large shrinkage in the direction normal to it, i.e. a reduction in thickness of the specimen.

At the lowest doses possible, using the Laue zone method for measuring the *c* spacing, it would appear that dried, negatively stained specimens are about 70% as thick as wet crystals. With prolonged electron irradiation, this reduces to only 40% of the expected value. Over the range of electron dose used in a typical continuous tilt series for three-dimensional reconstruction, the final thickness would be reduced to about 50% of the theoretical value. Studies on isolated particles, although not exhaustive, are in agreement with these results.

Working with unstained specimens, the starting values are somewhat better: 85% for frozen hydrated crystals and 80% for crystals dried in glucose. Since these specimens lose crystallinity on irradiation with electrons at quite small doses (up to 2.0 e/Å), it is not possible to follow further changes, but the dimension changes in unsupported catalase crystals in glucose suggest that the same shrinkage process is taking place.

It is interesting to compare these results with the extensive studies on the radiation damage of polythene crystals [1]. Here radiation damage leads to polymer backbone crosslinking together with side chain scission. There is, following loss of crystallinity, an increase in density with associated dimensional changes which depend on the degree of support these crystals have. Proteins would be expected to damage in a similar way [2]. In our investigation, we found a volume change which matched the radiation-induced mass loss described in a study on unstained specimens in the STEM [31].

An unexpected result was the effect of irradiation on negatively stained specimens at low temperatures. At liquid nitrogen temperature, no radiation-induced shrinkage could be observed over a considerable dose range. This again is in agreement with the STEM study [31], where mass loss also disappears at liquid nitrogen temperatures. This is, however, only the case if the specimen is

not covered with a surface layer of ice (i.e. if an efficient anti-contamination trap is used). In the presence of a surface layer the specimen becomes very radiation sensitive with a rapid disappearance of the electron diffraction patterns and images showing extensive damage by bubbling. Since the effect can be produced in the absence of ice, by covering the specimen surface with a thin carbon layer, it may be a result of "trapping" of volatile material produced by irradiation, which can then disrupt the specimen. Trapping of free-radicals which cause "knock-on" damage to the specimen may also occur. Bubbling is a temperature-dependent process, which only occurs if the coated specimen is below −140°C.

In a previous attempt to study negatively stained catalase crystals at liquid helium temperatures [32], it was found that there was a rapid loss of resolution with electron dose. This may well have been caused by the presence of a contaminating ice layer which would have been difficult to prevent at such low temperatures. This phenomenon of beam-induced "bubbling" damage may well become a limiting factor with carbon sandwiched [33], encapsulated [34] or frozen-hydrated [35] specimens below −140°C.

The effect of beam-induced shrinkage has to be taken into account when carrying out three-dimensional reconstruction by combining tilted views of single particles or crystals. It has important consequences for both the method of collecting the tilted data and for the end result. It is clear that some degree of correction may have to be applied to the *c* dimensions of a reconstruction. As can be seen from our results for catalase crystals and single particles such as ferritin, the reconstruction may only be 50–60% as thick as the native object. This shrinkage, in a typical tilt reconstruction, is however partially compensated for by the "missing-cone" effect which tends to reduce resolution and elongate structures in the *c* direction. If data are added for the (00*l*) axis of the reconstruction by using information from independent orthogonal views of the object, it will impose the correct thickness. It will not, however, remove the problem of combining data from objects of different thicknesses.

6. Conclusion

Electron diffraction and low dose images of tilted biological specimens has revealed a substantial thinning that is dose dependent. This effect can be halted by cooling the specimen to liquid nitrogen temperature and using an efficient anti-contaminator. Projection images and three-dimensional reconstructions would be improved both in resolution and fidelity with cooled specimens.

Acknowledgements

We would like to express our thanks to Christine Barber for secretarial help, to John Wray (Max-Planck-Institut für Medizinische Forschung, Heidelberg) for the catalase X-ray diffraction pattern, to Chris Carlson for the stereo view of a 3D lattice and to Richard Bryan for computational help in general, with the precessing Laue zones in particular and many instructive discussions.

References

[1] D.T. Grubb, J. Mater. Sci. 9 (1974) 1715.
[2] K. Stenn and G.F. Bahr, J. Ultrastruct. Res. 31 (1970) 526.
[3] A.W. Agar, F.C. Frank and A. Keller, Phil. Mag. 4 (1959) 32.
[4] P.T. Unwin and R. Henderson, J. Mol. Biol. 94 (1975) 425.
[5] D.L. Dorset and D.F. Parsons, Acta Cryst. A31 (1975) 210.
[6] K.A. Taylor, J. Microscopy 112 (1978) 115.
[7] R.M. Glaeser and G. Thomas, Biophys. J. 9 (1969) 1073.
[8] M. von Laue, Ann. Physik (Leipzig) 26 (1931) 55.
[9] W.L. Bragg and F. Kirchner, Nature 127 (1931) 738.
[10] J. Berriman, R.K. Bryan, R. Freeman and K.R. Leonard, Ultramicroscopy 13 (1984) 351.
[11] F.K. Winkler, K.R. Leonard and J.A. Berriman, in preparation.
[12] R.H. Lange, H.-P. Richter, R. Riehl, K. Zierold, T. Trandaburu and G. Magdowski, J. Ultrastruct. Res. 83 (1983) 122.
[13] J.-Cl. Homo, F. Booy, P. Labouesse, J. Lepault and J. Dubochet, J. Microscopy 136 (1984) 337.
[14] N.G. Wrigley, J. Ultrastruct. Res. 24 (1968) 454.
[15] R. Henderson and P.N.T. Unwin, Nature 257 (1975) 238.
[16] D.L. Parsons, J. Appl. Phys. 46 (1975) 938.
[17] R.D. Heidenreich, W.M. Hess and L.L. Ban, J. Appl. Cryst. 1 (1968) 1.

[18] T.W. Jeng and W. Chiu, J. Mol. Biol. 164 (1983) 329.
[19] P.N.T. Unwin, J. Mol. Biol. 98 (1975) 235.
[20] J.-Cl. Jesior, EMBO J. 1 (1982) 1423.
[21] J. Dubochet, J. Lepault, R. Freeman, J.A. Berriman and J.-Cl. Homo, J. Microscopy 128 (1982) 219.
[22] E. Ruska, Z. Physik 87 (1934) 580.
[23] M.L. Watson, J. Biophys. Biochem. Cytol. 1 (1955) 183.
[24] R.C. Williams and H.W. Fisher, J. Mol. Biol. 52 (1970) 121.
[25] E. Kellenberger, M. Häner and M. Wurtz, Ultramicroscopy 9 (1982) 139.
[26] R.C. Williams, Biochim. Biophys. Acta 8 (1952) 227.
[27] M.F. Moody, J. Mol. Biol. 25 (1967) 167.
[28] P.N.T. Unwin, J. Mol. Biol. 87 (1974) 657.
[29] B.V. Johansen, Micron 7 (1976) 145.
[30] P.K. Luther and R.A. Crowther, Nature 307 (1984) 566.
[31] R. Freeman and K.R. Leonard, J. Microscopy 122 (1981) 275.
[32] R.M. Glaeser and L.W. Hobbs, J. Microscopy 103 (1975) 209.
[33] J.R. Fryer and F. Holland, Ultramicroscopy 11 (1983) 67.
[34] J.S. Jaffe and R.M. Glaeser, Ultramicroscopy 13 (1984) 373.
[35] J. Dubochet, J.-J. Chang, R. Freeman, J. Lepault and A.W. McDowall, Ultramicroscopy 10 (1982) 55.